Nano-Optics and Nanophotonics

Shuji Sakabe
Christoph Lienau
Rüdiger Grunwald *Editors*

Progress in Nonlinear Nano-Optics

Springer

Nano-Optics and Nanophotonics

Editor-in-Chief

Motoichi Ohtsu, Tokyo, Japan

Editorial Board

Gunnar Björk, Kista, Sweden
Hirokazu Hori, Kofu, Yamanashi, Japan
Chennupati Jagadish, Canberra, ACT, Australia
Christoph Lienau, Oldenburg, Germany
Lih Y. Lin, Seattle, WA, USA
Erich Runge, Ilmenau, Germany
Frank Träger, Kassel, Germany
Masaru Tsukada, Aoba-ku, Sendai, Japan

The Springer Series in Nano-Optics and Nanophotonics provides an expanding selection of research monographs in the area of nano-optics and nanophotonics, science- and technology-based on optical interactions of matter in the nanoscale and related topics of contemporary interest. With this broad coverage of topics, the series is of use to all research scientists, engineers and graduate students who need up-to-date reference books. The editors encourage prospective authors to correspond with them in advance of submitting a manuscript. Submission of manuscripts should be made to the editor-in-chief, one of the editors or to Springer.

More information about this series at http://www.springer.com/series/8765

Shuji Sakabe · Christoph Lienau
Rüdiger Grunwald
Editors

Progress in Nonlinear Nano-Optics

Springer

Editors
Shuji Sakabe
Institute for Chemical Research,
Laboratory for Laser Matter Science
Kyoto University
Kyoto
Japan

Rüdiger Grunwald
Max Born Institute for Nonlinear Optics
and Short-Pulse Spectroscopy
Berlin
Germany

Christoph Lienau
Institut für Physik
Carl-von-Ossietzky Universität
Oldenburg
Germany

ISSN 2192-1970 ISSN 2192-1989 (electronic)
Nano-Optics and Nanophotonics
ISBN 978-3-319-12216-8 ISBN 978-3-319-12217-5 (eBook)
DOI 10.1007/978-3-319-12217-5

Library of Congress Control Number: 2014957154

Springer Cham Heidelberg New York Dordrecht London
© Springer International Publishing Switzerland 2015
This work is subject to copyright. All rights are reserved by the Publisher, whether the whole or part of the material is concerned, specifically the rights of translation, reprinting, reuse of illustrations, recitation, broadcasting, reproduction on microfilms or in any other physical way, and transmission or information storage and retrieval, electronic adaptation, computer software, or by similar or dissimilar methodology now known or hereafter developed.
The use of general descriptive names, registered names, trademarks, service marks, etc. in this publication does not imply, even in the absence of a specific statement, that such names are exempt from the relevant protective laws and regulations and therefore free for general use.
The publisher, the authors and the editors are safe to assume that the advice and information in this book are believed to be true and accurate at the date of publication. Neither the publisher nor the authors or the editors give a warranty, express or implied, with respect to the material contained herein or for any errors or omissions that may have been made.

Printed on acid-free paper

Springer International Publishing AG Switzerland is part of Springer Science+Business Media (www.springer.com)

Preface

Nanostructures can have quite amazing linear and especially nonlinear optical properties. Metallic nanoparticles, for instance, can localize visible light on a scale of a few nanometers only in the form of surface plasmon excitations. This light localization is of key importance for a plethora of fundamentally relevant applications ranging from cancer therapy and water splitting or photocatalysis in general to single molecule (bio-)sensing. When using such nanoparticles for localizing femtosecond light pulses, local field intensities are easily reached that are sufficient to generate high harmonic radiation or to propel electrons out of these particles, generating new nanoscale sources of femtosecond electron bunches of potential interest for future applications in ultrahigh time-resolution electron microscopy or diffraction. Semiconductor nanoparticles offer particularly strong optical nonlinearities and are key elements in next generation light emitting diodes and nanolasers. Moreover, they are of prime interest as biolabels. When combined with metallic nanostructures, new functionality arises, as the strong optical dipole coupling between semiconductor excitons and metal plasmons forms short-lived hybrid polariton excitations that may be useful in ultrafast switching applications or for designing new classes of photonic transistors with unprecedented sensitivity. Polymeric nanomaterials are not only forming the basis of organic photonics. When illuminated with focused femtosecond laser pulses, multiphoton polymerization is induced and this is the basis for sculpting three-dimensional structures with a spatial resolution of 100 nm or even below.

Driven by these and other exciting potential applications, nonlinear nano-optics is an extremely rapidly developing field of research in photonics. It is the aim of this small book to provide an insight into some of the current activities in this emerging field. The idea of the book was born at the 2nd International Workshop on "Nonlinear Nanostructures for Ultrafast Laser Applications" at Max-Born-Institute in Berlin 2011, which succeeded an earlier meeting with a tighter focus on ZnO and TiO_2 nanostructures. These events brought together some of the leading experts in nonlinear nanophotonics and stimulated the exchange of ideas and results on further conferences and meetings, e.g., in the community of laser-induced periodic surface structures, and in joint research projects of some of the authors.

A book project on this extremely fast developing field is inevitably faced with the difficulty of a strict selection. The editors decided to include 14 chapters covering experimental as well as theoretical studies in three different divisions: *Laser-Induced Nanostructures*, *Nonlinear Nano-Optics*, and *Advanced Theoretical Studies*. The spectrum of the contributions addresses some of the topics discussed at the Berlin Workshop as well as very recent continuing activities.

In the first division, Varlamova et al. give an overview of the self-organized pattern formation upon femtosecond laser ablation of dielectrics, and Kazansky et al. introduce the exciting prospects of polarization-shaped laser pulses for laser writing in dielectrics. Also, the remaining four chapters in this division focus on laser-induced writing in semiconductors: *Silicon* (Richter et al.), TiO_2 (Kumar Das et al.), *dielectrics* (Höhm et al.), and *metals* (Sakabe et al.).

The second division gives a broad overview of recently emerging applications in nonlinear nano-optics. Vogelgesang et al. start by introducing the very interesting optical properties of polariton excitations in strongly coupled metal/semiconductor nanostructures. Kabouraki et al. explain how to sculpt almost arbitrary three-dimensional nanostructures with sub-100 nm precision by multiphoton polymerization. Hentschel et al. give a clear presentation of the surprising success of a nonlinear oscillator model in quantitatively predicting nonlinear optical spectra of plasmonic nanoantennas. The part *Photoemission and Nonlinear Spectroscopy* in this division starts with a chapter by Herink et al., introducing recently discovered phenomena in strong field emission of electron pulses from sharp gold tips. It is followed by a presentation by Kumar Das et al. comparing linear and nonlinear optical properties of zinc oxide nanorods, and an article by Messaoudi et al. on using laser-written periodic nanostructures in metals for surface-enhanced Raman sensing of biomolecules.

The third division summarizes recent theoretical developments in this field. Manley et al. give a concise overview of the optical properties of metallic nanoparticles, their numerical simulation, and possible applications in plasmon-enhanced solar cells before, in the final chapter, Husakou et al. present a fundamentally interesting analysis of laser-driven high harmonic generation in various metallic nanoantennas.

We trust that this small collection of chapters gives an interesting overview of the current status of research in nonlinear nano-optics and will stimulate the reader to dig deeper into the rapidly growing original literature in this emerging field. We also hope that it provides a firm idea of how much more fundamental and applied research is urgently needed to uncover the full potential of nonlinear nano-optics in such diverse areas as physics, chemistry, materials science, measurement technology, and biomedicine.

We close this preface by expressing our sincere thanks to the German Ministry of Education and Research (BMBF) and to all other sponsors for financial support of this meeting and to all coauthors of this book for their important contributions to

this book. Very special thanks are also due to Claus Ascheron from Springer for his expert editorial advice and to Prof. Thomas Elsässer for very substantial support and the generous hospitality at Max-Born-Institute. Most of all, we are very grateful for having experienced the spirit of a fruitful and inspiring collaboration with colleagues from many parts of the world.

Kyoto — Shuji Sakabe
Oldenburg — Christoph Lienau
Berlin — Rüdiger Grunwald

Contents

Part I Laser-Induced Nanostructures: General Aspects and Structuring in Three Dimensions

1 Self-organized Surface Patterns Originating from Laser-Induced Instability 3
Olga Varlamova, Juergen Reif, Sergey Varlamov and Michael Bestehorn
1.1 Self-organized Laser-Induced Surface Structures 4
1.1.1 Experimental Observations 4
1.1.2 Modeling of Ripples Formation 6
1.1.3 Self-organization as Origin of LIPSS 7
1.2 Laser Polarization in the Model of Self-organization 13
1.2.1 Model 14
1.2.2 Linear Stability Analysis 19
1.2.3 Morphological Diagram for the Ripple Orientation . . . 21
1.2.4 Nonlinear Regime 23
1.2.5 Influence of Polarization 23
1.2.6 Period of Numerically Calculated Pattern 24
1.2.7 Time Evolution 25
1.3 Conclusion 27
References 27

2 Harnessing Ultrafast Laser Induced Nanostructures in Transparent Materials 31
Martynas Beresna, Mindaugas Gecevičius and Peter G. Kazansky
2.1 Introduction 31
2.2 Cylindrical Vector Beams 34
2.3 Polarization Converter 36
2.4 Fabrication and Characterization 39

2.5 5D Optical Memory 41
2.6 Conclusions 44
References. 44

Part II Laser-Induced Nanostructures: Nanostructure Formation in Semiconductors and Dielectrics

3 Nanogratings in Fused Silica: Structure, Formation and Applications. 49
Sören Richter, Matthias Heinrich, Felix Zimmermann, Christian Vetter, Andreas Tünnermann and Stefan Nolte
3.1 Introduction 50
3.2 Methodology 51
3.2.1 Nanograting Inscription 51
3.2.2 Conventional Characterization Techniques 52
3.2.3 Small Angle X-ray Scattering 53
3.3 Experimental Results. 55
3.3.1 Fundamental Structure of Nanogratings 55
3.3.2 Processing Parameter Window for Nanograting Formation 57
3.3.3 Evolutional Stages of Nanograting Growth. 58
3.3.4 Cumulative Action of Laser Pulses 61
3.4 Applications. 63
3.4.1 Retardation Control. 63
3.4.2 Wave Plates 65
3.4.3 Generation of Cylindric Vector Beams 65
3.4.4 Polarization-Coded Wave Plates 67
3.5 Summary 68
References. 69

4 Femtosecond-Laser Induced Nanostructures in TiO_2 73
Susanta Kumar Das, Hamza Messaoudi, Kiran Dasari, Wolfgang Seeber and Rüdiger Grunwald
4.1 Introduction 73
4.2 Methods of LIPSS Generation in Scanning Mode 74
4.3 Roughness and Initial Stages of fs-LIPSS in TiO_2 Bulk Crystals 75
4.4 Experimental Results with Line Focus and Moving Substrate 76
4.5 Theoretical Estimation of the Optical Constants 78
4.6 Generation of Uniform LIPSS Areas in Thin TiO_2 Films 78
4.7 Conclusions and Outlook. 81
References. 82

5 Formation of Laser-Induced Periodic Surface Structures (LIPSS) on Dielectrics and Semiconductors upon Double-Femtosecond Laser Pulse Irradiation Sequences 85
Sandra Höhm, Marcus Rohloff, Joerg Krüger, Joern Bonse and Arkadi Rosenfeld
5.1 Introduction 85
5.2 Experimental 87
5.3 Results and Discussion 88
5.3.1 Fluence Dependence of LIPSS 88
5.3.2 Pulse Number Dependence of LIPSS. 89
5.3.3 LIPSS Formation upon Double-fs-Pulse Irradiation . . . 91
5.4 Conclusions 97
References. 98

Part III Laser-Induced Nanostructures: Nanostructures Formation at Metal Surfaces

6 Scaling of Grating Spacing with Femtosecond Laser Fluence for Self-organized Periodic Structures on Metal 103
Shuji Sakabe, Masaki Hashida, Shigeki Tokita, Yasuhiro Miyasaka, Masahiro Shimizu and Shunsuke Inoue
6.1 Introduction 103
6.2 Experiments on LIPSS Production and Measurement. 105
6.3 Features of Femtosecond LIPSS on Metals. 106
6.4 Plasma Waves on Surface 107
6.5 Scaling of LIPSS Line Spacing with Laser Fluence. 111
6.6 Universal Scaling of LIPSS Line Spacing for Metal 112
6.7 Summary 113
References. 114

Part IV Nonlinear Nano-Optics: Plasmonic Nanostructures and Metamaterials

7 Interplay Between Strong Coupling and Radiative Damping in Hybrid Excitonic-Plasmonic Nanostructures 119
Ralf Vogelgesang, Wei Wang, Parinda Vasa, Robert Pomraenke, Ephraim Sommer, Antonietta De Sio and Christoph Lienau
7.1 Introduction 120
7.2 A Prototype Hybrid System 121
7.3 Experimental 124
7.3.1 Sample Fabrication 124
7.3.2 Spectral Interferometry 124

7.4 Theoretical Modelling 126
7.4.1 Linear Optical Response of Bare Dye Film 126
7.4.2 Coherent and Incoherent Coupling Mechanisms 126
7.4.3 Hybrid X-SPP Modes 127
7.5 Results 128
7.5.1 Phenomenological Description 129
7.5.2 Homogeneity of the J-Aggregates Resonance 130
7.5.3 Coherent Dynamics 131
7.6 Summary 133
References 134

8 Direct fs Laser Writing of 3D Nanostructures 137
Elmina Kabouraki, Konstantina Terzaki, Vasileia Melissinaki, Maria Manousidaki, Maria Vamvakaki and Maria Farsari
8.1 Introduction 137
8.2 Theoretical Issues of Multi-photon Polymerization 138
8.2.1 The Mechanism of Multi-photon Absorption 138
8.2.2 The Diffraction Limit 139
8.2.3 DLW Inspired by Stimulated-Emission-Depletion Fluorescence Microscopy 140
8.2.4 Diffusion-assisted DLW 140
8.3 Materials for DLW 141
8.3.1 Introduction 141
8.3.2 Photoinitiators 142
8.3.3 Organic Photopolymers 142
8.3.4 SU-8 143
8.3.5 Photosensitive Hybrid Materials 143
8.4 Biopolymers 144
8.5 Applications 145
8.5.1 Photonic Crystals 145
8.5.2 Micromechanical and Microfluidic Systems 147
8.6 Conclusions 149
References 149

9 Nonlinear Plasmon Optics 155
Mario Hentschel, Tobias Utikal, Bernd Metzger, Harald Giessen and Markus Lippitz
9.1 Introduction 155
9.2 Results and Discussion 160
9.3 The Nonlinear Harmonic Oscillator Model 170
9.4 Resonantly Enhanced Optical Nonlinearities 175
9.5 Summary and Conclusion 177
References 178

Part V Nonlinear Nano-Optics: Photoemission and Nonlinear Spectroscopy

10 Strong-Field Photoemission from Metallic Nanotips 185
Georg Herink, Daniel R. Solli, Max Gulde, Reiner Bormann and Claus Ropers
10.1 Introduction 185
10.2 Strong-Field Physics at Metallic Nanotips 186
10.3 Photoemission from Metallic Nanotips in the Mid-Infrared. . . . 187
References. 191

11 Comparison of Linear and Nonlinear Optical Properties of ZnO Nanorods 193
Susanta Kumar Das, Frank Güell, Ciarán Gray, Daragh Byrne, Prasanta Kumar Das, Rüdiger Grunwald, Günter Steinmeyer and Enda McGlynn
11.1 Introduction 194
11.2 Experimental Details 195
11.2.1 ZnO Nanostructure Growth and Structural Characterization 195
11.2.2 Linear and Nonlinear Optical Characterisation 197
11.3 Experimental Results and Discussion. 197
11.3.1 ZnO Nanostructure Growth and Structural Characterization 197
11.3.2 ZnO Nanostructure Linear and Nonlinear Optical Characterisation. 198
11.3.3 ZnO Nanorods as Frequency Converters for Third Order Pulse Characterization with iFROG 202
11.4 Conclusions 204
References. 205

12 Femtosecond-Laser Induced Periodic Surface Structures for Surface Enhanced Raman Spectroscopy of Biomolecules 207
Hamza Messaoudi, Susanta Kumar Das, Janine Lange, Friedhelm Heinrich, Sigurd Schrader, Marcus Frohme and Rüdiger Grunwald
12.1 Introduction 208
12.2 Laser-Induced Nanostructuring of Metal Substrates with Ultrashort Pulses 209
12.3 Experimental Techniques 210
12.3.1 Femtosecond-Laser Preparation of Metallic Substrates for SERS 210
12.3.2 Surface Enhanced Raman Spectroscopy. 211

12.4 Experimental Results . . . 212
12.4.1 Femtosecond-Laser-Induced Periodic Nanostructures in Ag . . . 212
12.4.2 SERS Measurements at Selected Biomolecules . . . 214
12.5 Conclusions and Outlook . . . 216
References . . . 217

Part VI Advanced Theoretical Studies: Linear Simulations

13 Design Principles for Plasmonic Nanoparticle Devices . . . 223
Phillip Manley, Sven Burger, Frank Schmidt and Martina Schmid
13.1 Plasmonic Principles . . . 223
13.1.1 Bulk Plasmons . . . 224
13.1.2 Surface Plasmon Polaritons . . . 226
13.1.3 Particle Plasmons . . . 226
13.1.4 Far Field Effects . . . 228
13.1.5 Near Field Effects . . . 230
13.2 Finite Element Method . . . 231
13.3 Shape Effects . . . 234
13.3.1 Nanoparticle Length || to E . . . 235
13.3.2 Nanoparticle Length || to k . . . 237
13.3.3 Nanoparticle Length || to H . . . 238
13.3.4 Surface Curvature . . . 239
13.4 Material Effects . . . 240
13.4.1 Nanoparticle Material . . . 240
13.4.2 Homogeneous Medium . . . 241
13.4.3 Substrate . . . 242
13.5 Designing Plasmonic Solar Cells . . . 243
References . . . 246

Part VII Advanced Theoretical Studies: Nonlinear Optics

14 High Harmonic Generation Assisted by Metal Nanostructures and Nanoparticles . . . 251
Anton Husakou, Song-Jin Im, Kwang-Hyon Kim and Joachim Herrmann
14.1 Introduction . . . 251
14.2 Theory of High-Harmonic Generation in the Vicinity of Metal Nanostructures . . . 253
14.3 Spatial Field Distribution and HHG in Gases Near a Metallic Tip and a Bow-Tie Nanostructure . . . 255

14.4 HHG in Noble Gases in the Vicinity of a Rough Metallic Surface with Fractal Properties 260
14.5 HHG in a Mixture of Nanoparticles and a Noble Gas 264
References 267

Index 269

Contributors

Martynas Beresna Optoelectronics Research Centre, University of Southampton, Southampton, Hampshire, UK

Michael Bestehorn LS Theoretische Physik II, Brandenburg University of Technology (BTU) Cottbus, Cottbus, Germany

Joern Bonse BAM Bundesanstalt für Materialforschung und -prüfung, Berlin, Germany

Reiner Bormann IV. Institute of Physics, University of Göttingen, Göttingen, Germany

Sven Burger Zuse Institute Berlin, Berlin, Germany

Daragh Byrne School of Physical Sciences, National Centre for Plasma Science and Technology, Dublin City University, Dublin, Ireland

Kiran Dasari Max Born Institute for Nonlinear Optics and Short-Pulse Spectroscopy, Berlin, Germany

Antonietta De Sio Institut für Physik, Carl von Ossietzky Universität, Oldenburg, Germany

Maria Farsari IESL-FORTH, Heraklion, Crete, Greece

Marcus Frohme Engineering Department, University of Applied Sciences Wildau, Wildau, Germany

Mindaugas Gecevičius Optoelectronics Research Centre, University of Southampton, Southampton, Hampshire, UK

Harald Giessen 4th Physics Institute and Research Center SCoPE, University of Stuttgart, Stuttgart, Germany

Ciarán Gray School of Physical Sciences, National Centre for Plasma Science and Technology, Dublin City University, Dublin, Ireland

Rüdiger Grunwald Max Born Institute for Nonlinear Optics and Short-Pulse Spectroscopy, Berlin, Germany

Frank Güell Departament d'Electrònica, Universitat de Barcelona, Barcelona, Catalunya, Spain

Max Gulde IV. Institute of Physics, University of Göttingen, Göttingen, Germany

Masaki Hashida Advanced Research Center for Beam Science, Institute for Chemical Research, Kyoto University, Uji, Kyoto, Japan; Division of Physics and Astronomy, Graduate School of Science, Kyoto University, Sakyo, Kyoto-ku, Japan

Matthias Heinrich CREOL, The College of Optics and Photonics University of Central Florida, Orlando, FL, USA

Friedhelm Heinrich Engineering Department, University of Applied Sciences Wildau, Wildau, Germany

Mario Hentschel 4th Physics Institute and Research Center SCoPE, University of Stuttgart, Stuttgart, Germany; Max Planck Institute for Solid State Research, Stuttgart, Germany

Georg Herink IV. Institute of Physics, University of Göttingen, Göttingen, Germany

Joachim Herrmann Max-Born-Institut für Nichtlineare Optik und Kurzzeitspektroskopie, Berlin, Germany

Sandra Höhm Max-Born-Institut für Nichtlineare Optik und Kurzzeitspektroskopie, Berlin, Germany

Anton Husakou Max-Born-Institut für Nichtlineare Optik und Kurzzeitspektroskopie, Berlin, Germany

Song-Jin Im Max-Born-Institut für Nichtlineare Optik und Kurzzeitspektroskopie, Berlin, Germany

Shunsuke Inoue Advanced Research Center for Beam Science, Institute for Chemical Research, Kyoto University, Uji, Kyoto, Japan; Division of Physics and Astronomy, Graduate School of Science, Kyoto University, Sakyo, Kyoto-ku, Japan

Elmina Kabouraki IESL-FORTH, Heraklion, Crete, Greece

Peter G. Kazansky Optoelectronics Research Centre, University of Southampton, Southampton, Hampshire, UK

Kwang-Hyon Kim Max-Born-Institut für Nichtlineare Optik und Kurzzeitspektroskopie, Berlin, Germany

Joerg Krüger BAM Bundesanstalt für Materialforschung und -prüfung, Berlin, Germany

Susanta Kumar Das Max-Born-Institut für Nichtlineare Optik und Kurzzeitspektroskopie, Berlin, Germany; School of Applied Sciences, KIIT University, Bhubaneswar, Odisha, India

Prasanta Kumar Das School of Applied Sciences, KIIT University, Bhubaneswar, Odisha, India

Janine Lange Engineering Department, University of Applied Sciences Wildau, Wildau, Germany

Christoph Lienau Institut für Physik, Carl von Ossietzky Universität, Oldenburg, Germany

Markus Lippitz 4th Physics Institute and Research Center SCoPE, University of Stuttgart, Stuttgart, Germany; Max Planck Institute for Solid State Research, Stuttgart, Germany

Phillip Manley Helmholtz Zentrum Berlin für Materialien und Energie GmbH, Berlin, Germany; Zuse Institute Berlin, Berlin, Germany

Maria Manousidaki IESL-FORTH, Heraklion, Crete, Greece

Enda McGlynn School of Physical Sciences, National Centre for Plasma Science and Technology, Dublin City University, Dublin, Ireland

Vasileia Melissinaki IESL-FORTH, Heraklion, Crete, Greece

Hamza Messaoudi Max-Born-Institut für Nichtlineare Optik und Kurzzeitspektroskopie, Berlin, GermanyEngineering Department, University of Applied Sciences Wildau, Wildau, Germany; Bremen Institute of Applied Beam Technology, Bremen, Germany

Bernd Metzger 4th Physics Institute and Research Center SCoPE, University of Stuttgart, Stuttgart, Germany

Yasuhiro Miyasaka Advanced Research Center for Beam Science, Institute for Chemical Research, Kyoto University, Uji, Kyoto, Japan; Division of Physics and Astronomy, Graduate School of Science, Kyoto University, Sakyo, Kyoto-ku, Japan

Stefan Nolte Institute of Applied Physics, Abbe Center of Photonics, Friedrich-Schiller-Universität Jena, Jena, Germany; Fraunhofer Institute for Applied Optics and Precision Engineering, Jena, Germany

Robert Pomraenke Institut für Physik, Carl von Ossietzky Universität, Oldenburg, Germany

Juergen Reif LS Experimentalphysik II, Brandenburg University of Technology (BTU) Cottbus, Cottbus, Germany

Sören Richter Institute of Applied Physics, Abbe Center of Photonics, Friedrich-Schiller-Universität Jena, Jena, Germany

Marcus Rohloff Max-Born-Institut für Nichtlineare Optik und Kurzzeitspektroskopie, Berlin, Germany

Claus Ropers IV. Institute of Physics, University of Göttingen, Göttingen, Germany

Arkadi Rosenfeld Max-Born-Institut für Nichtlineare Optik und Kurzzeitspektroskopie, Berlin, Germany

Shuji Sakabe Advanced Research Center for Beam Science, Institute for Chemical Research, Kyoto University, Uji, Kyoto, Japan; Division of Physics and Astronomy, Graduate School of Science, Kyoto University, Sakyo, Kyoto-ku, Japan

Martina Schmid Helmholtz Zentrum Berlin für Materialien und Energie GmbH, Berlin, Germany; Freie Universität Berlin, Berlin, Germany

Frank Schmidt Zuse Institute Berlin, Berlin, Germany

Sigurd Schrader Engineering Department, University of Applied Sciences Wildau, Wildau, Germany

Wolfgang Seeber Otto-Schott-Institut für Glaschemie, Friedrich-Schiller-Universität Jena, Jena, Germany

Masahiro Shimizu Advanced Research Center for Beam Science, Institute for Chemical Research, Kyoto University, Uji, Kyoto, Japan; Division of Physics and Astronomy, Graduate School of Science, Kyoto University, Sakyo, Kyoto-ku, Japan

Daniel R. Solli IV. Institute of Physics, University of Göttingen, Göttingen, Germany

Ephraim Sommer Institut für Physik, Carl von Ossietzky Universität, Oldenburg, Germany

Günter Steinmeyer Max-Born-Institut für Nichtlineare Optik und Kurzzeitspektroskopie, Berlin, Germany

Konstantina Terzaki IESL-FORTH, Heraklion, Crete, Greece

Shigeki Tokita Advanced Research Center for Beam Science, Institute for Chemical Research, Kyoto University, Uji, Kyoto, Japan; Division of Physics and Astronomy, Graduate School of Science, Kyoto University, Sakyo, Kyoto-ku, Japan

Andreas Tünnermann Institute of Applied Physics, Abbe Center of Photonics, Friedrich-Schiller-Universität Jena, Jena, Germany; Fraunhofer Institute for Applied Optics and Precision Engineering, Jena, Germany

Tobias Utikal 4th Physics Institute and Research Center SCoPE, University of Stuttgart, Stuttgart, Germany; Max Planck Institute for Solid State Research, Stuttgart, Germany

Maria Vamvakaki IESL-FORTH, Heraklion, Crete, Greece

Sergey Varlamov LS Theoretische Physik II, Brandenburg University of Technology (BTU) Cottbus, Cottbus, Germany

Olga Varlamova LS Experimentalphysik II, Brandenburg University of Technology (BTU) Cottbus, Cottbus, Germany

Parinda Vasa Institut für Physik, Carl von Ossietzky Universität, Oldenburg, Germany

Christian Vetter Institute of Applied Physics, Abbe Center of Photonics, Friedrich-Schiller-Universität Jena, Jena, Germany

Ralf Vogelgesang Institut für Physik, Carl von Ossietzky Universität, Oldenburg, Germany

Wei Wang Institut für Physik, Carl von Ossietzky Universität, Oldenburg, Germany

Felix Zimmermann Institute of Applied Physics, Abbe Center of Photonics, Friedrich-Schiller-Universität Jena, Jena, Germany

Part I
Laser-Induced Nanostructures: General Aspects and Structuring in Three Dimensions

Chapter 1
Self-organized Surface Patterns Originating from Laser-Induced Instability

Olga Varlamova, Juergen Reif, Sergey Varlamov and Michael Bestehorn

Abstract Self-organized surface pattern formation upon femtosecond laser ablation is considered in framework of an adopted surface erosion model, based on the description for spontaneous pattern formation on ion bombarded surfaces. We exploit the similarity to ion-beam sputtering and extend a corresponding model for laser ablation by including laser polarization. We find that an asymmetry in deposition and dissipation of incident laser energy, related to the laser polarization, results in a corresponding dependence of coefficients in a nonlinear equation of the Kuramoto-Sivashinsky type. We present the surface morphologies obtained by this model for different polarization of the laser beam and discuss a time evolution of the nanopattern. A comparison of numerical results with experimental data shows an excellent qualitative agreement. Our results support the non-linear self-organization mechanism of pattern formation on the surface of solids.

O. Varlamova (✉) · J. Reif
LS Experimentalphysik II, Brandenburg University of Technology (BTU) Cottbus,
Platz der Deutschen Einheit 1, 03046 Cottbus, Germany
e-mail: olga.varlamova@tu-cottbus.de

J. Reif
e-mail: reif@tu-cottbus.de

S. Varlamov · M. Bestehorn
LS Theoretische Physik II, Brandenburg University of Technology (BTU) Cottbus,
Platz der Deutschen Einheit 1, 03046 Cottbus, Germany
e-mail: sergev@physik.tu-cottbus.de

M. Bestehorn
e-mail: bes@physik.tu-cottbus.de

© Springer International Publishing Switzerland 2015

S. Sakabe et al. (eds.), *Progress in Nonlinear Nano-Optics*,
Nano-Optics and Nanophotonics, DOI 10.1007/978-3-319-12217-5_1

1.1 Self-organized Laser-Induced Surface Structures

1.1.1 Experimental Observations

The development of laser technologies and application of ultrashort, i.e. subpicosecond pulses in material processing, has revealed a large diversity of surface structures distinct from earlier observed LIPSS [1–4]. Along with the classical ripples with periods of about the laser wavelength, also fine nano-ripples with a feature size much smaller than the applied laser wavelength and coarse macro-ripples with a lateral size in a several microns range, as well as even more complex patterns like arrays of conical features were registered at the laser-modified area [5–21]. Very often, several different types of these structures can coexist in the same ablation spot.

Since the end of the 1990s it has been established that, typically, these structures can be generated upon irradiation of the picosecond to femtosecond range at intensities below or about the single-shot ablation threshold on surfaces of different solids (crystalline and amorphous insulators, semiconductors, and metals). The laser-induced morphology is qualitatively independent of the kind of ablated material and of their crystallographic structure. Generally, the LIPSS completely develop only after a considerable number of pulses [7, 9, 10], and positive feedback plays an important role in the ripple formation process [17, 22, 23]. The ripples period and complexity vary across the ablation spot, from fine and regular at the edge to coarse and complex in the middle, depending rather on the local pulse intensity than on the laser wavelength [10].

Pattern morphology and orientation are, typically, controlled by the polarization state of the laser electric field [24–27]. Linear high-periodic structures with multiple bifurcations or an arrangement of nanospheres are typical for linearly and circularly polarized light, respectively, as shown in Fig. 1.1a, b; a mixture of long and short

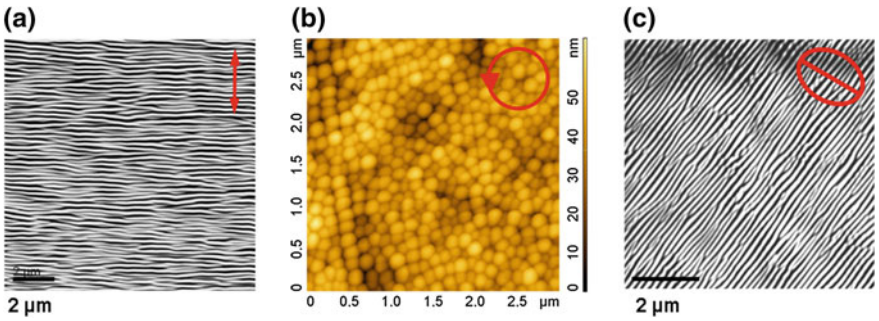

Fig. 1.1 Micrographs of sections from the *bottom* of ablation craters obtained on a CaF_2 surface. **a**, **b** and **c** show patterns generated with *linearly*, *circularly* and *elliptically* polarized irradiation (λ_{laser} = 800 nm, τ_{pulse} = 120 fs), respectively (5,000 pulses@8.1 TW/cm^2) (State of the laser polarization indicated at the *right upper corner*)

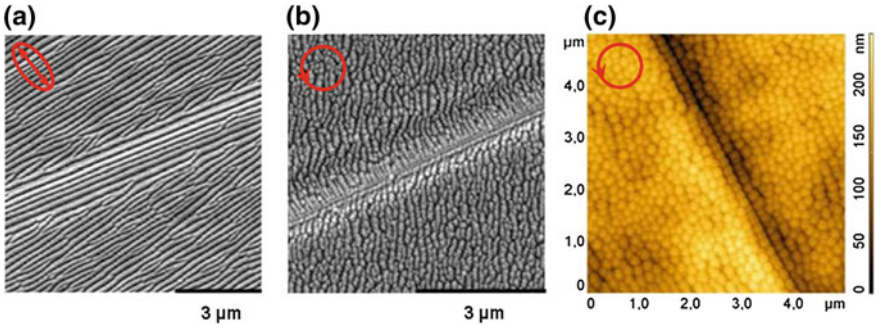

Fig. 1.2 Influence of extended surface defects (scratches, cleavage steps) on the orientation of nanostructures: **a** CaF_2 (111) irradiated with 5,000 pulses of *elliptically* polarized light at laser intensity 8.3 TW/cm^2; **b** CaF_2 (111) irradiated with 120,000 pulses of *circularly* polarized light at laser intensity 1.9 TW/cm^2; **c** NaCl (111) irradiated with 5,000 pulses of *circularly* polarized light at intensity 7.9 TW/cm^2

lines (Fig. 1.1c) is observed for elliptically polarized pulses. However, also extended macroscopic surface defects play an important role as an order parameter [28], the influence of surface defects on structure orientation is even significantly stronger than that of the polarization (Fig. 1.2).

At an increasing irradiation dose, also the superposition of several structures can be observed. Detailed inspection of the ablation spot on CaF_2, induced upon 10,000 pulses of linear polarization at intensity 8.4 TW/cm^2, reveals complex structuring of the crater walls. A coarse overstructure that is not really related to the polarization direction (Fig. 1.3a), and fine ripples with spacing less than 20 nm, directed perpendicular to the laser electric field (Fig. 1.3b), coexist in the irradiated area.

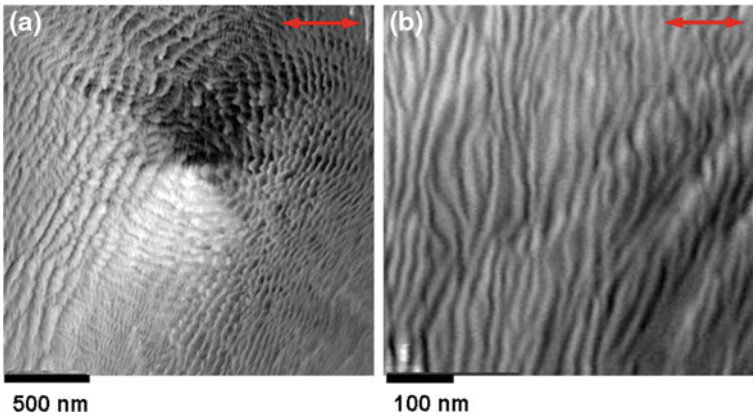

Fig. 1.3 SEM micrographs of the *central* part of an ablation crater on CaF_2 (10,000 pulses@8.4 TW/cm^2) exhibiting: **a** radial spreading coarse overstructure and **b** fine ripples

1.1.2 Modeling of Ripples Formation

Experimental observation of ripples over such wide range of materials and over a large wavelength interval has been accompanied by intensive theoretical studies; however, the underlying physical mechanisms are not yet fully understood. Presently, two basically different approaches are discussed in the literature.

The "classical" approach assumes that a lithography-like *modulated energy deposition*, caused by some optical interference, is imprinted into a corresponding ablation pattern and thus results in a modulated surface morphology, as shown in Fig. 1.4a [29–31]. In that model, ripples appear in the areas, where the absorbed energy is largest, and the formation process is lithography-like, where the irradiated material only plays a *passive* role. Another approach, schematically presented in Fig. 1.4b, known as a *self-organization model* [24, 32], is based on the dynamics of ultrashort pulse laser interaction with the target material [33, 34], and is inspired by the similarity of the laser generated patterns with those observed in very many other fields in nature, in particular in surface sputtering by energetic ions [35]. The model supposes an *active* contribution of the irradiated material: The absorbed laser energy causes a perturbation and softening of the crystal binding, leading to an unstable surface region, which relaxes via self-organization and, as a consequence of this, a spontaneous formation of surface structures in the laser-modified area [36, 37].

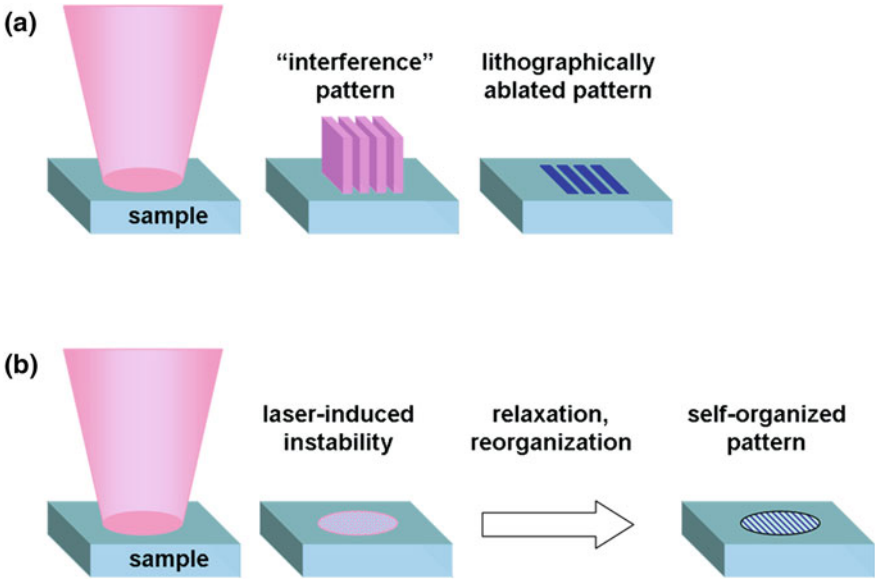

Fig. 1.4 Different approaches of LIPSS formation: **a** spatially modulated energy deposition ("interference" pattern) results in modulated ablation; **b** "self-organization model": femtosecond laser beam induces a high degree of instability at the surface; the perturbated surface relaxes through reorganization that leads to formation of self-organized pattern in the laser-affected region

1.1.2.1 Weakness of the Classical Theory

The theoretical approach based on a modulated energy deposition was in good agreement with many experimental data published at that time [4, 31]: the "interference" model described very well structures consisting of long, almost parallel lines, resembling very much a typical interference pattern, with periods close to the laser wavelength. These LIPSS are often called "LSFL" ("low spatial frequency LIPSS") [20], to be distinguished from the femtosecond laser-induced ripples, termed as "HSFL" ("high spatial frequency LIPSS"), with periods much smaller than the laser wavelength. Such fine ripples constitute the major deficiency of the "classical" approach, because they cannot be explained by an optical interference effect. To overcome this problem, additional interactions have been introduced in the model. At first, optical properties of the excited target material were taken into account by an adaptable (by an adjustable density of surface free electrons) refractive index of the surface selvedge [12, 38]. Further, the "surface scattered field" in the classical approach was modified to include short-wavelength irradiation, e.g. by the generation of higher harmonics [20, 39, 40] or excitation of high-frequency surface plasmon polaritons [18, 19, 41]. As a consequence, the actual version of the model proposes *different* interaction mechanisms for different kinds of structures.

Though some progress has been made, and the models mentioned above could approximately account for the ripple periods of subwavelength range, they are not appropriate to explain other complex features, as, e.g., the dependence of the ripple period on the absorbed laser fluence, as well as multiple bifurcations, coarsening, including period doubling, showing up in femtosecond laser ablation experiments. Despite all updating, the classical approach is, nevertheless, unable to explain a diversity of complex patterns, such as cones, "bubbles", or larger formations (macro structures), observed by femtosecond laser ablation. In particular, patterns induced by circularly polarized irradiation cannot at all be interpreted in framework of this model.

1.1.3 Self-organization as Origin of LIPSS

Analysis of the experimental observations, especially the variety of typical structures shapes and sizes, as well as their complex morphology indicates that femtosecond LIPSS are very similar to other self-organized patterns originating from instabilities such as, e.g., ripples produced by ion beam sputtering (IBS) [42].

A detailed comparison of surface morphologies generated by IBS and fs laser ablation (see Fig. 1.5) reveals very strong similarity in the shapes (bifurcating long linear structures) and ripples wavelength ($\Lambda \sim 200 \div 300$ nm). Additionally to the visual affinity of the patterns, other common features are found such as, for instance, the dependence of the ripples period on the irradiation dose, namely, on ions' energy and irradiation time for IBS [43] and laser intensity and number of pulses in case of laser ablation [10, 44]; or the important role of positive feedback in

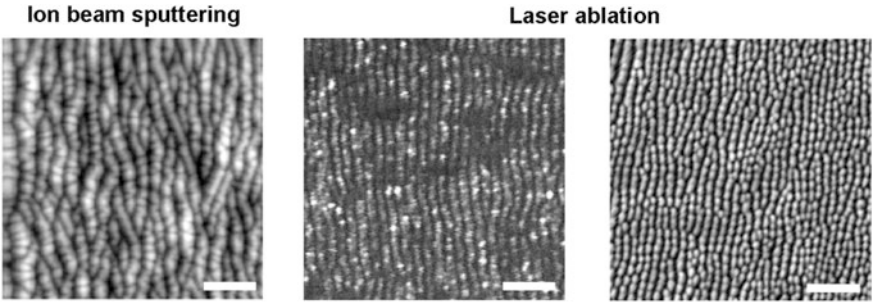

Fig. 1.5 Ripples induced upon *Ion beam sputtering* and femtosecond *Laser ablation*. The *left image*: AFM micrograph of ripple pattern generated on silicon with Ar+ ion beam [42]; in the *middle*: SEM image of ripples structures at the *bottom* of an ablation crater produced on silicon with 60,000 pulses at 0.4 TW/cm^2 [13]; the *right image*: SEM micrograph of the ripples induced on CaF_2 surface upon 5,000 pulses, 8 TW/cm^2. The *bar scale* at the micrographs indicates 1 μm

the development and formation of the pattern [23, 42]; or the coexistence of coarse and fine ripples with stepped changing of the periodicity ("period doubling") [26]. All this suggests to assume a similar mechanism of ripples formation by energetic ion beam and ultrashort pulsed laser irradiation.

1.1.3.1 Patterns Originating from Instability

Pattern formation from instability is very well known as a general natural phenomenon, and it has been intensively studied in various areas of basic and applied science. In nature, ripples can be observed in sandy deserts [45] and on the sea-bottom [46] as a result of interaction between sand grains and wind or shallow wavy water, and even on Mars [47]. In physics, the pattering behavior can be found in different areas of material processing, such as ion-beam sputtering [42], thin film deposition [48], or as in our case, as a result of femtosecond pulse laser ablation.

After a physical system has been driven into instability, i.e. a state which is not in thermodynamic equilibrium, the system has to move toward a new stable state by some intrinsic nonlinear mechanisms involving positive feedback. The physics of pattern formation can be described within the theoretical framework of nonlinear dynamics. Spatial and temporal evolution of a perturbed system is generally represented by nonlinear partial differential equations, for example equations of the Kuramoto-Sivashinsky/Kardar-Parisi-Zhang type [49–51]. The solution of such equations with corresponding boundary conditions results in the pattern formation. Understanding of the physical background in the patterning behavior must include the study of mechanisms how some small effects can govern the dynamics of pattern formation. That is the great scientific challenge.

Attributing the "femtosecond" ripples to the universal phenomenon of spontaneous pattern formation arising from instabilities, we want first to review the well known description of surface pattering by IBS.

1.1.3.2 Pattern Formation Upon Ion-Beam Sputtering (Review)

When a high-energetic ion beam impacts on a target surface, it will penetrate into the solid and transfer its kinetic energy and momentum to the lattice atoms through cascades of collisions [52]. The volume excited by these ballistic processes is approximately an ellipsoid with the major axis along the incident ion beam direction (Fig. 1.6). During this process, lattice atoms can be displaced from their equilibrium position or, if the transferred energy is sufficient to overcome binding energy, ejected or sputtered from the target.

The volume perturbed by the collisions depends on the energy and mass of the bombarding ions and on the mass of the target atoms. The amount of sputtered atoms, or sputtering yield, is a function of the incident ion flux and of the local surface curvature. Erosion of a corrugated surface by an ion beam is shown in Fig. 1.6a. Let us consider the dissipation of energy, deposited at point P, to the target surface. The average energy transferred to O' is greater than at O, $\mathrm{E}(O') > \mathrm{E}(O)$, that means that the erosion velocity of the valleys is larger than at the crests, $\upsilon(O') > \upsilon(O)$ [55]. Thus, the inhomogeneous erosion increases the amplitude of the corrugation and leads to an instability. To complete the surface evolution, thermal atomic self-diffusion activated by the irradiation should be taken into account. These competing processes, surface erosion and diffusion of target atoms, result in ripple pattern formation.

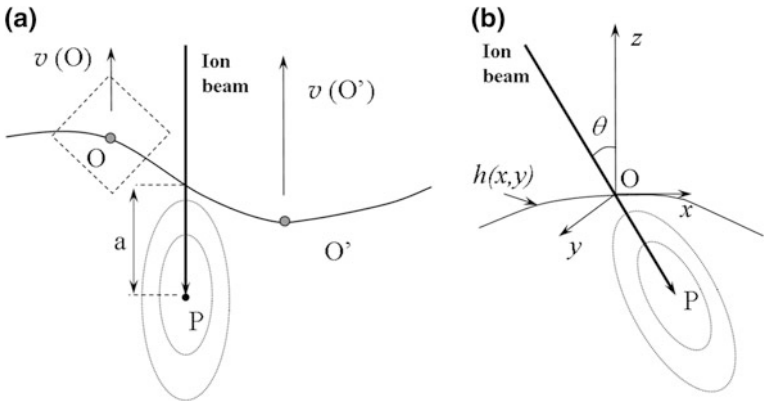

Fig. 1.6 Erosion of a corrugated surface by an ion beam. **a** The incident ion beam (*bold solid arrow*) penetrates an average distance a inside the solid and will be stopped at point P due to collisions, losing kinetic energy. O and O' are surface atoms on the crest and in the valley, correspondingly. P is the point of energy deposition; the *dotted ellipses* show contours of equal energy deposition (after [53]). **b** Ion erosion at point O (indicated with a *dashed square* in (**a**)) is shown in *local* coordinates (after [54])

The first theoretical approach, describing ripple formation by ion-beam sputtering, has been proposed by Bradley and Harper [55]. The modeling exploits the dependence of the erosion velocity [52], υ, on the average energy deposited at a point P(x, y, z) by an ion (Fig. 1.6b). Taking into account that the erosion velocity, υ, is a function of incidence angle, θ, and a local surface curvature, R, and adding a surface self-diffusion term, we obtain the time evolution of the growing surface profile $h(x, y)$:

$$\frac{\partial h}{\partial t} = -\upsilon(\theta, R)\sqrt{1 + (\nabla h)^2} - K\nabla^2\left(\nabla^2 h\right) \tag{1.1}$$

Now, let us consider the first term on the right-hand side of (1.1). As indicated in Fig. 1.7, removal takes place in a direction locally normal to the interface. When a particle is removed, the increment, $\upsilon\Delta t$, projected along the h axis is Δh. Following the geometry of the problem, from a right triangle we find Δh as (cf. Fig. 1.7):

$$\Delta h = \left[(\upsilon\,\Delta t)^2 + (\upsilon\,\Delta t\,\tan\alpha)^2\right]^{1/2} \tag{1.2}$$

Taking into account that $\tan\alpha = \frac{dh}{dx}$, (1.2) results in the first term of (1.1):

$$\frac{\partial h}{\partial t} = \upsilon\left[1 + (\nabla h)^2\right]^{1/2} \tag{1.3}$$

The second term on the right-hand side in (1.1) describes the surface self-diffusion of atoms, where the diffusion coefficient K is given by

$$K = \frac{D_S \gamma v}{n^2 k_B T}\exp\left(-\frac{\Delta\varepsilon}{k_B T}\right) \tag{1.4}$$

Here D_S is the surface self-diffusivity, γ the surface free energy per unit area, v the real density of diffusing atoms and $\Delta\varepsilon$ the activation energy for surface self-diffusion [55].

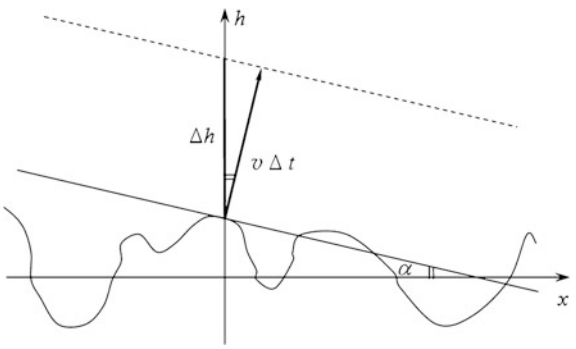

Fig. 1.7 Influence of a surface local curvature on the erosion velocity $\upsilon(h)$ (analogous to [51])

Equation (1.1) is an equation of Kardar-Parisi-Zhang type, and its solution predicts the formation of periodic surface structures with orientation and wavelength Λ depending on the incident angle of the ion beam, θ, and, in special cases, depending on the surface temperature, T, diffusion coefficient, K, and the activation energy for surface self-diffusion, $\Delta\varepsilon$:

$$\Lambda(\theta) \propto \frac{K}{\sqrt{T}} \exp\left(-\frac{\Delta\varepsilon}{k_B T}\right) \tag{1.5}$$

1.1.3.3 Ultrashort Pulsed Laser Induced Surface Instability

The physical processes of femtosecond laser ablation indicate the generation of a considerable instability at the irradiated surface. The rapid excitation of electrons by the incident laser electric field induces a softening of the atomic bonds [56] through redistribution of the deposited energy on a time scale about of several 100 fs leading to a destabilization of the crystal lattice [57]. Additionally, the surface equilibrium order can be disturbed due to emission of individual components (ions, atoms, clusters). As a result, the target lattice is strongly perturbed on a very short time scale,[1] i.e. the system is strongly unstable and very far from thermodynamic equilibrium. This nonequilibrium in the system must rapidly relax via a macroscopic material removal and surface restructions. The rapid relaxation is provoked by a steep gradient in crystalline order to the surrounding material and is too fast for any thermal processes [58].

Like a pattern induced by surface bombardment with an energetic ion beam, we attribute such structure formation to a surface self-organization from a high degree of instability induced by irradiation with an ultrashort laser beam. But, in contrast to ion sputtering, when the erosion of the surface takes place *during* ion bombardment and proceeds continuously, femtosecond laser ablation is a pulsed process. Energy input and desorption/rearrangement of massive particles are temporally well separated. Consequently, the impact of intense ultrashort pulse on solid surface results in a few different regimes shown in Fig. 1.8.

This scheme shows the time scales of secondary processes activated in a transparent dielectric crystal by irradiation with a 120-fs laser pulse of 800 nm at intensity well below the single-shot ablation threshold [59]. The incident light first only excites the electrons of the system, their appreciable emission is observed during the pulse. In a second, presumably delayed step, the actual ejection of fast ions (Coulomb/phase explosion) occurs, after a transfer of electronic excitation to the lattice. With the emission of slow/thermal ions begins the last step, namely, the thermal relaxation on a larger timescale through thermal conductivity effects/thermal self-diffusion of atoms.

[1] Similar to a melt, but not relaxed to thermodynamic equilibrium.

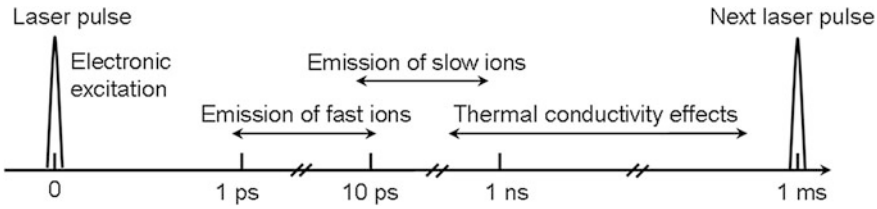

Fig. 1.8 Typical time scales of various secondary processes stimulated by irradiation of transparent dielectrics by a femtosecond laser pulse

1.1.3.4 Time Evolution of Surface Profile Upon Repetitive Irradiation

In this section we consider the creation of a thin corrugated layer on the surface of irradiated target upon multiple ultrashort laser pulses. For simplicity, let's restrict to a dielectric crystal. Initially, the surface of the target is assumed to be ideally plain.

When the laser beam hits a plain surface, a stochastic charge distribution and, hence, an ion emission from randomly located sites, resulting in the creation of the local defects, can occur in the irradiated area. A higher absorption probability in the defect states will result in a progressively inhomogeneous surface ionization upon the following laser pulses. The conception of the corrugated surface layer is shown schematically in Fig. 1.9: small symmetry breaking irregularities on the initially plain surface develop to the modulated surface layer upon multipulse irradiation. The process is highly nonlinear and boosted by a positive feedback.

After several more laser pulses, a modulated, thin surface film of thickness a and modulation height $h(x, y)$ builds up (Fig. 1.10). The absorption cross-section of the film is tending towards a more homogeneous with each subsequent pulse. Desorption, however, is not homogeneous and depends on a local surface-curvature. Assuming Coulomb explosion, e.g., as the possible ablation mechanism, we can see that for a uniform surface charge density, the ion sitting in a valley (Fig. 1.10) has the higher density of (charged) neighbors than an ion on a crest. The higher next-neighbor density results in the stronger repulsion (Coulomb) force and, consequently, in a larger escape velocity of valley-ions, υ_{valley}, compared to that

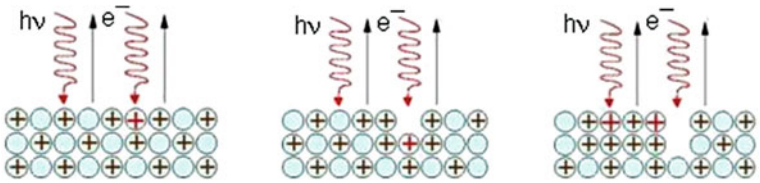

Fig. 1.9 Development of a corrugated surface layer upon multipulse laser irradiation. Incident laser light ($h\nu$) is shown with *waved arrows*; emission of photoelectrons (e^-) is indicated with *vertical arrows*

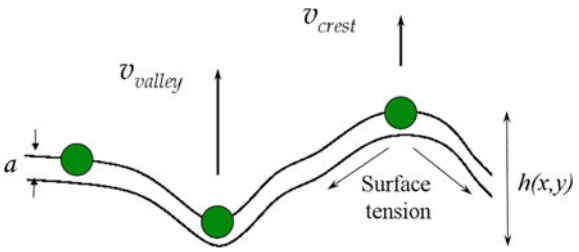

Fig. 1.10 Model for surface height evolution: a is the thickness and $h(x, y)$ is the modulation height of an unstable surface film induced upon repetitive laser irradiation. Velocities of the desorbed ions from the valley (v_{valley}) and from the crest (v_{valley}) are indicated with *arrows*

from crests, v_{crest}. So, valleys will be faster eroded than crests, this causes instability of the thin surface film, very similar to the case of ion sputtering (Fig. 1.6).

Balancing the surface erosion process, thermally activated self-diffusion tends to smooth the surface again by filling the valleys with diffused crest-atoms. Moreover, in the thin unstable layer the particle on the crest will feel a higher surface tension than in the valley. The tension gradient forces the particles to downhill moving and balances thereby the instability on the surface.

Thus, the time evolution of the growing surface profile can be described by the elementary processes taking place in the system: surface erosion (roughening) due to particle emission and smoothing due to atomic self-diffusion.

1.2 Laser Polarization in the Model of Self-organization

Numerous experimental results have revealed a strong dependence of ripples orientation on the polarization of the incident laser field. By taking into account that an ultrashort laser pulse is addressed just to the electronic system of solids and the subsequent energy transfer to the lattice occurs on the timescale of electron-phonon relaxation [60] that is significantly larger than the laser pulse duration, the understanding of the puzzling relation between pattern orientation and laser polarization, i.e. the direction of the electromagnetic field vector, becomes very important and interesting.

In the following, this dependence is analyzed within an adopted surface erosion model, based on the description of ion beam sputtering [55]. A continuum theory of erosion by polarized laser irradiation is developed. In particular, the dependence of generated patterns on the laser polarization is considered.

1.2.1 Model

The geometry of the model is illustrated in Fig. 1.11. In the figure are shown the laboratory frame (x, y, h) with h perpendicular to the *flat* substrate, the *local* surface frame (X, Y, Z) taking into account surface corrugation with radius R, and the frame (x', y', z') connected with the incident laser beam propagating in the direction parallel to z', as well as azimuthal and elevation angles connecting these frames. The laser beam is incident on the target surface and is absorbed in some point P, from where its energy is further transferred (cf. dotted ellipses in Figs. 1.11 and 1.13) to the neighboring sites. Though the incidence angle of the beam can vary (cf. Fig. 1.6b), here, for simplicity, we consider normal incidence to the flat surface.

Following Peter Sigmund's theory of ion sputtering [52], we can relate the erosion velocity normal to the surface to the energy input:

$$\upsilon \cong \xi \int_V dr^3 \psi(r) \varepsilon(r) \tag{1.6}$$

where the integration is performed over the volume V, including all points, at which the deposited energy contributes to the erosion velocity υ at the surface. ξ is a material parameter, $\psi(r)$ takes into account local variations of the deposited energy due to attenuation, refraction and reflection. In principle, $\psi(r)$ contains all information about spatial beam profile, absorption cross section, and losses along the beam pass to reach $P(r)$. ε (r) is the fraction of that energy, dissipated to the surface

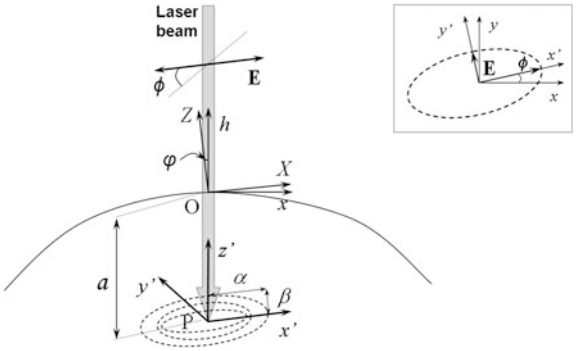

Fig. 1.11 Reference frames for the computation of the erosion velocity: (x', y', z') is the reference frame of the incoming beam, x' is parallel to the vector **E** of the electromagnetic field; (X, Y, Z) corresponds to the local coordinate frame, where Z is parallel to the local normal to the surface, while (x, y, h) denotes the laboratory frame of coordinates with h perpendicular to the flat substrate surface. The *dotted ellipse* is a Gaussian distribution of deposited energy with half-width α, β along x', y', respectively. The energy distribution along z' with half-width γ is not shown here. φ is the angle between the local and the laboratory reference frames (corrugation) and denotes the "local" incidence angle; ϕ is orientation of **E** in the plane of incidence (x, y). *Inset* View from *top* along h

after absorption at $P(r)$ and resulting in erosion. To evaluate $\varepsilon(r)$, we have to take into account the dynamics of femtosecond laser-matter interaction.

Similarity of the laser-induced instability on the target surface to the well-known hydrodynamic instability of thin liquid films (cf. Sect. 1.1.3.1) allows us to use an analogous approach as in that case and to describe the time evolution of the surface height profile $h(x, y, t)$, caused by surface erosion [35], with the (1.1), where the erosion velocity is a function not only of the local surface curvature (φ, R) and of the incident angle of the laser beam (θ) (cf. Fig. 1.7), but depends also on the orientation of the laser electric field denoted with angle ϕ in Fig. 1.11.

1.2.1.1 The Role of Anisotropic Excitation

The absorbed laser energy results only in an excitation of electrons. In dielectrics and semiconductors, electrons are excited from the valence to the conduction band. These electrons thermalize their kinetic energy first by collisions with the other conduction electrons and then, only subsequently, transfer the energy to the lattice by electron-phonon collisions.

One possible origin of an asymmetry in such energy transfer is based on the initial photoionization, i.e. the excitation from the valence into the conduction band. It is well known from the photoionization of free atoms that the electric light field results in an asymmetric distribution of electron kinetic energy: their velocity is larger in the field direction and less in all other directions. On the other hand, the electron mean free path strongly depends on their kinetic energy [61] and decreases more than one order of magnitude in the range between 0.5 and 10 eV [58], as a consequence of a reciprocal variation of collision-and thus energy transfer-probability (Fig. 1.12).

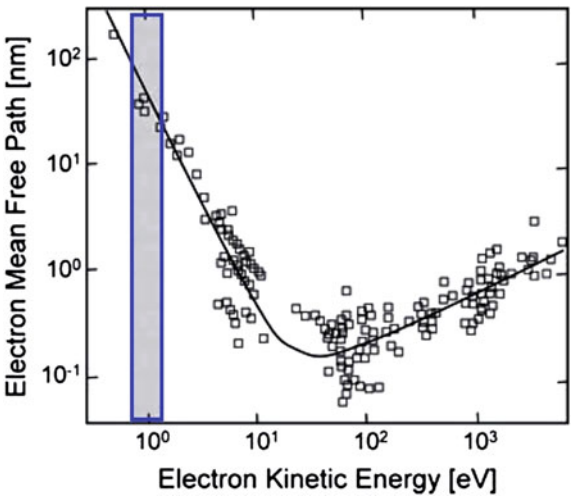

Fig. 1.12 The "Universal Curve" of electron mean free path versus electron kinetic energy. The *grey area* indicates the region of typical kinetic energies in the considered situation (from [58])

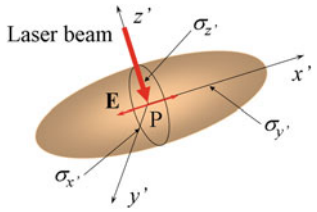

Fig. 1.13 The *ellipse* illustrates the cross sections of relative collisional energy transfer after laser excitation at point P in the frame of incoming beam (x', y', z'). *Linear* polarized *laser beam* propagates along z'; vector **E** defines the direction of linear polarization (**E**$\|x'$)

Consequently, assuming Gaussian velocity distributions for the electrons, we can approximate the contribution of energy absorbed at P to the erosion velocity:

$$\varepsilon(r') = \chi \exp\left\{-\frac{1}{l^2}\left[\left(\frac{x'^2}{\sigma_{x'}}\right) + \left(\frac{y'^2}{\sigma_{y'}}\right) + \left(\frac{z'^2}{\sigma_{z'}}\right)\right]\right\} \tag{1.7}$$

Here l is the electron mean free path at low electron energy (close to the bottom of the conduction band) and it is proportional to a in Fig. 1.11; χ is a material parameter; and σ_k are the relative energy coupling cross sections in k direction ($k = x'$, y', z') (Fig. 1.13) and thus reciprocal to the relative mean free path, α, β and γ in Fig. 1.11.

Another possible reason for the anisotropic energy transfer is the resonant excitation of surface plasmon-polaritons (SPPs) on a corrugated interface conductor/vacuum [18, 41], where absorption is largest for **E** parallel to the k-vector of the corrugation.

1.2.1.2 Equation Describing an Evolution of the Surface Profile

Let's return to the problem of the time evolution of the surface height profile as described in Fig. 1.11. Whereas in Sigmund's theory [52] the parameters α, β and γ along x', y' and z', respectively, are scaled as $\alpha = \beta \geq \gamma$, in the case of light-matter interaction we do not have anymore the same constant ratio between these three components. The relation between α and β depends on the characteristics of irradiation, absorption and dissipation; and γ is a constant that corresponds to a thin layer a (cf. Figs. 1.10 and 1.11), generally determined by the mean free path of conduction band electrons.

Following to [35, 55] we have to perform the calculation of the erosion rate in the local coordinate system (X, Y, Z). This means that we need to transform the deposited energy $\varepsilon(r)$ (1.7) from (x', y', z') to the local (X, Y, Z) reference frame by a rotation:

$$\begin{pmatrix} x' \\ y' \\ z' \end{pmatrix} = \begin{pmatrix} \cos\phi\cos\varphi & \sin\phi & \cos\phi\sin\varphi \\ -\sin\phi\cos\varphi & \cos\phi & -\sin\phi\sin\varphi \\ -\sin\varphi & 0 & \cos\varphi \end{pmatrix} \cdot \begin{pmatrix} X \\ Y \\ Z \end{pmatrix} \tag{1.8}$$

and subsequent translation along the beam direction by the value a. To simplify our consideration we restrict our calculations to the case of small incident angles θ in optically transparent materials. The local correction to the incident energy flux is now given by $\psi(r) = \mathrm{A} \cdot I_0\left(\cos\varphi + \left(\partial Z/\partial X\right)\sin\varphi\right)$, where A is the generalized absorption coefficient[2] of the material and I_0 is the laser intensity. In order to describe the surface profile in the neighborhood of O (Fig. 1.11), we take into account cross-terms of the type $\sim XY$

$$Z(X,Y) \cong -\frac{1}{2}\left(\frac{X^2}{R_X} + \frac{Y^2}{R_Y}\right) - \frac{XY}{R_{XY}} \tag{1.9}$$

As in [35] we assume that the radii of curvature R_X, R_Y and R_Z of the surface are much larger than a, which in this case means the distance from the surface to the absorption point P, so that only terms up to first order in a/R_X, a/R_Y and a/R_Z are kept. The integration results in the erosion velocity $\upsilon(\varphi, \phi, R_X, R_Y, R_{XY})$ as a function of angles φ, ϕ, and the curvatures:

$$\frac{1}{R_X} = -\frac{\partial^2 Z}{\partial X^2}, \qquad \frac{1}{R_Y} = -\frac{\partial^2 Z}{\partial Y^2}, \qquad \frac{1}{R_{XY}} = -\frac{\partial^2 Z}{\partial X \partial Y}. \tag{1.10}$$

Now, we examine the evolution of the surface corrugation $z = h(x, y, t)$ with time t, starting from an originally flat configuration ($h = 0$). We rewrite υ in terms of the laboratory coordinates (x, y, h) [35]:

$$\frac{\partial h(x,y,t)}{\partial t} = -\upsilon(\varphi, \phi, R_X, R_Y, R_{XY})\sqrt{1 + (\nabla h)^2} \tag{1.11}$$

We expand (1.11) in a Taylor series and complete it by adding surface self-diffusion (cf (1.1)) and the statistical fluctuations of initial surface roughness $\eta(x, y, z)$ (short noise). Finally, we obtain the equation of motion known as an anisotropic noisy Kuramoto-Sivashinsky [49, 50] equation:

$$\begin{aligned} \frac{\partial h}{\partial t} = &-\upsilon_0 + \nu_x \frac{\partial^2 h}{\partial x^2} + \nu_y \frac{\partial^2 h}{\partial y^2} + \nu_{xy} \frac{\partial^2 h}{\partial x \partial y} \\ &+ \frac{\lambda_x}{2}\left(\frac{\partial h}{\partial x}\right)^2 + \frac{\lambda_y}{2}\left(\frac{\partial h}{\partial y}\right)^2 + \frac{\lambda_{xy}}{2}\left(\frac{\partial h}{\partial x}\right)\left(\frac{\partial h}{\partial y}\right) \\ &- K\nabla^2\left(\nabla^2 h\right) + \eta(x,y,z), \end{aligned} \tag{1.12}$$

[2] Note that, for multiphoton absorption in transparent media, A will be of the form $\mathrm{A}_0\mathrm{I}^{n-1}$.

where the coefficients are now the complex functions of the two angles ϕ and θ. For the case of normal incidence illustrated in Fig. 1.11, the coefficients take the form:

$$\begin{aligned}
v_x &= -\frac{Fa}{2\gamma}\left(\frac{\alpha^2}{\gamma^2}\cos^2\phi + \frac{\beta^2}{\gamma^2}\sin^2\phi\right),\\
v_y &= -\frac{Fa}{2\gamma}\left(\frac{\alpha^2}{\gamma^2}\sin^2\phi + \frac{\beta^2}{\gamma^2}\cos^2\phi\right),\\
v_{xy} &= -\frac{Fa}{2\gamma}\left(\frac{\beta^2}{\gamma^2} + \frac{\alpha^2}{\gamma^2}\right)\sin 2\phi,\\
\lambda_x &= -\frac{F}{\gamma}\left[1 + \left(\frac{\alpha^2}{\gamma^2} - 1\right)\left(\frac{\alpha^2}{\gamma^2}\cos^2\phi + \frac{\beta^2}{\gamma^2}\sin^2\phi\right)\right],\\
\lambda_y &= -\frac{F}{\gamma}\left[1 + \left(\frac{\alpha^2}{\gamma^2} - 1\right)\left(\frac{\alpha^2}{\gamma^2}\sin^2\phi + \frac{\beta^2}{\gamma^2}\cos^2\phi\right)\right],\\
\lambda_{xy} &= -\frac{F}{\gamma}\left(\frac{\alpha^2}{\gamma^2} - 1\right)\left(\frac{\beta^2}{\gamma^2} - \frac{\alpha^2}{\gamma^2}\right)\sin 2\phi,\\
\upsilon_0 &= \frac{F}{\gamma}
\end{aligned} \tag{1.13}$$

and $F = \frac{I_0 \xi A}{\sqrt{2\pi}} \exp\left(\frac{\alpha^2}{2\gamma^2}\right)$.

In order to extract the physical meaning from (1.12) and (1.13), we consider, in this approach, the special case $v_{xy} = 0$ and $\lambda_{xy} = 0$. That means (1.12) and (1.13) are taken in the reference frame rotated by the angle ϕ (cf. inset in Fig. 1.11). Moreover, we neglect here the erosion velocity of the initial flat surface υi_0, which does not effect the size of ripples and can be eliminated by the transformation $\tilde{h} = h + \upsilon i_0 t$.

$$\frac{\partial h}{\partial t} = v_x\frac{\partial^2 h}{\partial x^2} + v_y\frac{\partial^2 h}{\partial y^2} + \frac{\lambda_x}{2}\left(\frac{\partial h}{\partial x}\right)^2 + \frac{\lambda_y}{2}\left(\frac{\partial h}{\partial y}\right)^2 - K\nabla^2\left(\nabla^2 h\right) + \eta(x,y,z), \tag{1.14}$$

where the coefficients are given now by

$$\begin{aligned}
v_{x,y} &= -\frac{F}{2}\sigma_\gamma \Omega_{x,y}\\
\lambda_{x,y} &= -\frac{F}{\gamma}\left[1 + \left(\sigma_\gamma^2 - 1\right)\Omega_{x,y}\right]
\end{aligned} \tag{1.15}$$

and

$$\begin{aligned}
&\Omega_{x,y} = \Delta[1 \pm \Pi]; \qquad \Delta = \frac{1}{2}\left(\frac{\sigma_\gamma^2}{\sigma_\alpha^2} + \frac{\sigma_\gamma^2}{\sigma_\beta^2}\right); \qquad \Pi = \frac{\sigma_\beta^2 - \sigma_\alpha^2}{\sigma_\beta^2 + \sigma_\alpha^2};\\
&\sigma_i = \frac{a}{i}(i = \alpha, \beta, \gamma)
\end{aligned} \tag{1.16}$$

Polarization parameter Π describes an asymmetry of energy distribution in ($x'y'$) plane, *depth parameter* Δ takes into account energy deposition also along z' axis (Fig. 1.11), connected with the direction of laser beam propagation. Combinations of Π and Δ result in *anisotropy parameter* Ω in (1.16) that determines the spatial asymmetry in energy distribution at point *P*.

1.2.2 Linear Stability Analysis

In this section the basic role of polarization and depth parameters, Π and Δ, will be explained by means of a linear stability analysis of (1.14). For this purpose, we introduce a periodic perturbation $h = h_0 \exp\{i(q_x x + q_y y - \omega t) + \sigma t\}$ and obtain the normalized growth rate

$$\frac{1}{h_0}\frac{\partial h}{\partial t} = \Sigma = -\left[v_x q_x^2 + v_y q_y^2 + K\left(q_x^2 + q_y^2\right)^2\right]. \tag{1.17}$$

From (1.15) and (1.16) follows that polarization and depth parameters contribute to the two tension coefficients $v_{x,y}$, which are negative for normal incidence and in general are not equal to each other due to the fact that Π increases v_x and reduces v_y. Figure 1.14 shows the linear growth rate Σ along perturbation wave vectors q_x and q_y for various values of parameters Δ and Π. For Δ = 0 the uniform state is stable ($v_x = v_y = 0$), whereas for nonzero Δ and Π = 0 we obtain equal instability along q_x and q_y ($v_x = v_y = -(F\sigma_\gamma/2)\Delta$). Distinct from zero, the value of Π induces an asymmetrical instability in the q_{xy}-plane with the wave vector:

$$q_{x,y}^* = \sqrt{\frac{F\sigma_\gamma}{4K}\Delta[1 \pm \Pi] - q_{y,x}^2} \tag{1.18}$$

An increase of Π shifts the instability to higher values of q_x ($v_x = -(F\sigma_\gamma/2)\Delta[1 + \Pi]$) and suppresses the instability along q_y ($v_x = -(F\sigma_\gamma/2)\Delta[1 - \Pi]$). Thus, for $\Pi \sim 1$ the instability along q_y disappears.

From the stability analysis of Fourier modes for (1.14) we expect the instability for the ripple formation with wavelength $\Lambda_i = 2\pi\sqrt{2K/|v_i|}$, where i refers to the x or y direction along which the corresponding v_i is largest. Thus, in the case of $v_x < v_y < 0$, which holds when $0 < \Pi < 1$, the ripple structure is oriented in x direction with the following wavelength of the surface modulations:

$$\Lambda_{x,y} = 4\pi\sqrt{\frac{K}{F\sigma_\gamma\Delta(1 \pm \Pi)}} \tag{1.19}$$

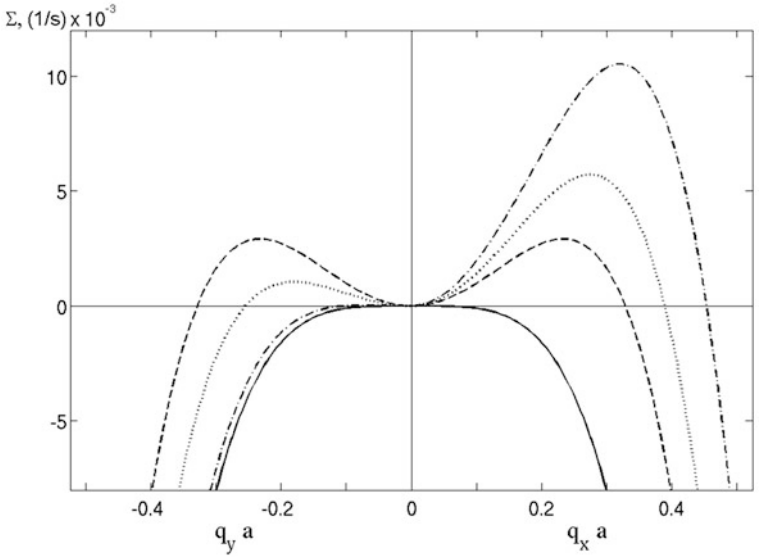

Fig. 1.14 Growth rate Σ as a function of a two dimensionless wave vectors $q_x a$ and $q_y a$ for various values of parameters Δ and Π: Δ = 0, Π = 0 (*solid line*); Δ = 1, Π = 0 (*dashed line*); Δ = 1, Π = 0.4 (*dotted line*); Δ = 1, Π = 0.9 (*dash-dotted line*)

For "zero" polarization parameter (Π = 0) the wavelength of ripple along x and y axis are equal: $\Lambda_x = \Lambda_y$. An increase of Π slightly reduces Λ_x whereas Λ_y becomes to be very large for $\Pi \rightarrow 1$. Equation (1.19) has revealed an influence of polarization parameter Π on the experimentally measured ripples characteristics Λ_x, Λ_y (period and bifurcation length). From the relation $\Lambda_x/\Lambda_y = \sqrt{(1-\Pi)/(1+\Pi)}$ the polarization parameter Π and, correspondingly, polarization of the incident laser field, can be determined.

We can consider the polarization parameter as a control parameter that represents a degree of anisotropy in the energy deposition and, therefore, the orientation of ripples formation. Indeed, from (1.16) Π = 0 corresponds to an equal energy deposition ($\alpha = \beta$, isotropic energy distribution) along x and y axes, whereas, $\Pi \sim 1$ describes the case $\alpha \gg \beta$ (energy flow in x, parallel to **E**).

To summarize, it has been shown that polarization parameter Π, characterizing the symmetry of the deposited energy distribution in the (x', y') plane (Fig. 1.11), determines orientation and also morphology of the calculated pattern. The anisotropy in the energy distribution is correlated with the vector **E** of incoming laser field in such a manner that **E** defines the preferred direction of the energy transfer. In the next subsection we discuss a morphological diagram and suppose to identify the direction of the preferred energy transfer with the vector of polarization **E**.

1.2.3 Morphological Diagram for the Ripple Orientation

Another quantity that can change the ripple orientation is the angle of incidence θ. It is very important to note, that the orientation of the ripple due to the polarization and due to the incidence angle θ can compete or work together. Such behavior is one prediction of this theory, which has been tested experimentally. The general expressions being too complicated, we present here v_x and v_y in the reference frame rotated by angle ϕ:

$$\begin{aligned} v_x &= -\frac{F\sigma_\gamma}{2\zeta^2}\left(\frac{\sigma_\gamma^2}{\sigma_\alpha^2}\right) \\ &\quad \times \left[\cos^2\theta - 2\sin^2\theta\left(1 - \frac{\sigma_\gamma^2}{2\zeta}\cos^2\theta\right)\left(\frac{\sigma_\gamma^2}{\sigma_\alpha^2}\right)\right], \\ v_y &= -\frac{F\sigma_\gamma}{2\zeta}\left(\frac{\sigma_\gamma^2}{\sigma_\beta^2}\right)\cos^2\theta, \end{aligned} \tag{1.20}$$

where $\zeta = \cos^2\theta + \left(\sigma_\gamma^2 \Big/ \sigma_\alpha^2\right)\sin^2\theta$ and by using (1.16) we express the $\sigma_\gamma^2 \Big/ \sigma_\alpha^2$ and $\sigma_\gamma^2 \Big/ \sigma_\beta^2$ in terms of Δ and Π:

$$\left(\frac{\sigma_\gamma^2}{\sigma_\alpha^2}\right) = \Delta(1+\Pi) \quad \text{and} \quad \left(\frac{\sigma_\gamma^2}{\sigma_\beta^2}\right) = \Delta(1-\Pi). \tag{1.21}$$

In contrast to ion beam sputtering [35, 55] the most important parameter that influences the orientation of ripples in our consideration is the polarization parameter Π. Therefore, we study here the (Π, θ) morphological diagram for different values of σ_y. The boundary in the diagram is defined by $v_x(\Pi, \theta) = v_y(\Pi, \theta)$ and separates the region I ($v_x < v_y$) with the ripples wave vector in y-direction and region II ($v_x > v_y$) with the ripples wave vector in x-direction.

We start to discuss the diagram from the bottom (the left Inset in Fig. 1.15), where for small θ the wave vector of ripples is aligned along **E** and is perpendicular to the component of the beam in the surface plane. Thus, for small θ the orientation of ripples is defined by **E** and the influence of the angle of incidence is not appreciable. With increasing of θ the growing angle of incidence supports the effect of polarization and the wave vector of ripples remains along **E** that is shown in the bottom of diagram in the right Inset.

In the case of weak polarization $-0.4 \leq \Pi < 0$ a reorientation of ripples in dependence on θ can be observed for $\sigma_y > 1$. Indeed, one can see from the diagram in the case of $\Pi = 0$ that the increase of θ from zero (normal incidence) to some finite values reveals two possibilities: the wave vector of ripples is aligned parallel

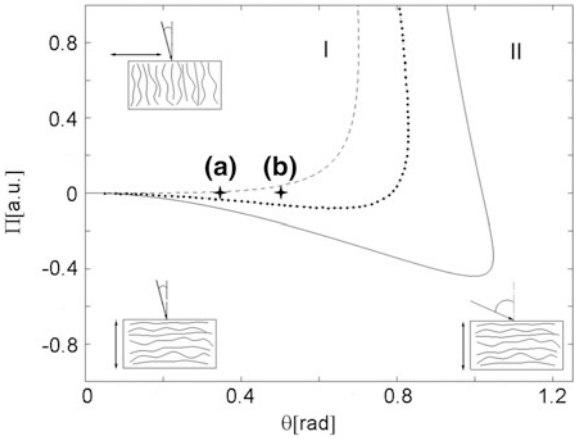

Fig. 1.15 Ripple orientation diagram presenting the boundary separating regions I ($v_x < v_y$) and II ($v_x > v_y$) for different values of $\sigma_y = 1$; 1.5; 2 (*dashed*, *dotted*, *solid line*, respectively). *Insets* show the incident angle, the direction of ripples and the vector **E** (*double arrows*). (*a*) and (*b*) correspond to the surface morphologies in Fig. 1.16

(perpendicular) to the component of incoming beam in the Region I (Region II) for $\sigma_y \leq 1$ ($\sigma_y > 1$). In the case of $\Pi = 0$ and at normal incidence some isotropic structures are expected in the model. This is also proved experimentally: at non-normal incidence an arrangement of nano-spheres typical for circular polarization (Fig. 1.1b) turns into a linear pattern with the wave vector of modulations oriented parallel to the incoming irradiation (Figs. 1.15 and 1.16). This comparison helps us to fix partially the parameter σ_γ for the following numerical calculations.

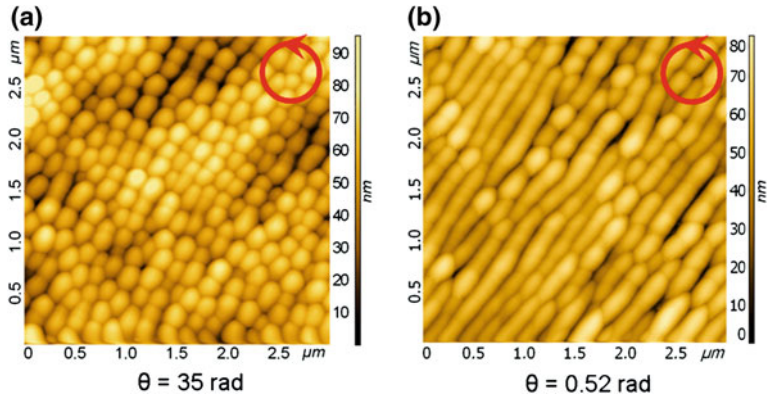

Fig. 1.16 Dependence of surface morphology on angle of incidence θ for *circularly* polarized beam: CaF_2 irradiated with 5,000 pulses at an intensity of about 8 TW/cm^2

1.2.4 Nonlinear Regime

Closer examination of (1.14) reveals that its time dependence consists of a linear part and nonlinear components. Let us consider the influence of the nonlinear terms λ_x and λ_y. As shown in [62], such separation of linear and nonlinear behavior in time assumes the existence of a crossover time t_c that separates these two regimes. In the linear regime up to t_c the nonlinear terms are negligible whereas they take over after

$$t_c \propto \left(\frac{K}{\nu^2}\right) \ln\left(\frac{\lambda}{\nu}\right) \tag{1.22}$$

and completely determine the surface morphology, which depends on the relative signs of λ_x and λ_y. The transition between linear and nonlinear regime is very abrupt and it is followed by the appearance of kinetic roughening. For $\sigma_y = 1.5$ both λ_x and λ_y are negative and depend on Π. The dependence of the crossover time on the polarization can be presented as follows:

$$t_c(\Pi) \propto \frac{t_c(\Pi = 0)}{(1 + \Pi)^2}, \tag{1.23}$$

where t_c is decreased with increasing of Π.

1.2.5 Influence of Polarization

Surface patterns obtained by numerical integration of (1.12) and corresponding Fourier images (2D-FTT) are presented in the upper row of Fig. 1.17. The morphologies are calculated for various ϕ, describing the orientation of the laser electric field $\mathbf{E}$ in the plane of incidence (x, y) (Fig. 1.11), and various values of polarization parameter Π, which can be associated with the polarization degree. The obtained numerical results show that an asymmetric energy deposition can describe the correlation of ripples orientation with laser polarization. The simulation time t is measured in arbitrary units (a.u.) and will be discussed in the next section. Note that, in contrast to the continuum evolution in the simulations, the experimental evolution is given by increasing the number of laser pulses.

In Fig. 1.17a we observe the surface morphology calculated for $\Pi = 1$, ($\sigma_\alpha \ll \sigma_\beta$), $t = 800$ a.u. and $\phi = 0$. That means the energy distribution along x' is much larger than along y'. The pattern consists of periodic parallel lines, oriented perpendicular to $\mathbf{E}$. This is similar to the ripples produced by a linearly polarized laser beam (Fig. 1.17e). By rotation of vector $\mathbf{E}$ ($\phi = 45°$) for the same values of Π and t, the ripples follow the direction of incident electrical field (Fig. 1.17b) that is also in good agreement with experiment (Fig. 1.17f).

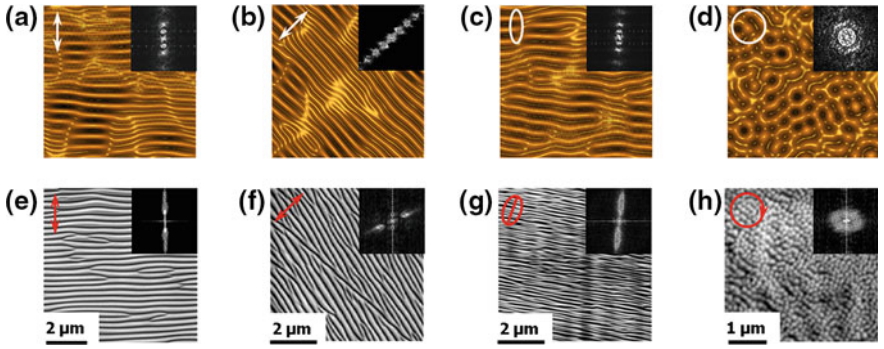

Fig. 1.17 The *upper panels* present numerically calculated surfaces of size $64\pi \times 64\pi$ in a.u., showing the surface morphologies for **a** $\phi = 90°$, $\Pi = 1$, t = 800 a.u.; **b** $\phi = 45°$, $\Pi = 1$, t = 800 a.u; **c** $\phi = 90°$, $\Pi = 0.5$, t = 1,400 a.u.; **d** $\phi = 90°$, $\Pi = 0$, t = 3,000 a.u.; *white double arrows* and *elliptical* figures define the energy distribution in the $(x'y')$-plane. The *bottom panels* exhibit ablation patterns on CaF_2 produced by 5,000 pulses at intensity 8 TW/cm^2 with *linear* (**e**, **f**), *elliptical* (**g**) and *circular* (**h**) polarization. The direction of incident electrical laser field is indicated with *double arrows*, *ellipse* and *circle*, respectively. The corresponding 2D-FFT images are presented in the *insets*

By variation of Π, between zero and one ($\sigma_\alpha < \sigma_\beta$), and fixed angle $\phi = 90°$ we create the configuration of elliptic polarization. The large axis of the polarization ellipse is oriented along y in the laboratory coordinate frame (x, y, h) (Inset in Fig. 1.11). As can be seen from Fig. 1.17c (t = 1,400 a.u.) the ripples are still aligned to the large axis of polarization ellipse, again good correlation with experiment for elliptic polarized irradiation (Fig. 1.17g). For $\Pi = 0$, ($\sigma_\alpha = \sigma_\beta$), i.e. circular polarization, we have a symmetrical energy distribution with respect to x' and y'. The calculated surface morphology for t = 3,000 a.u. does not posses linear order, the pattern is uniformly distributed (Fig. 1.17d). A similar kind of pattern, characterized by lack of linear order and consisting of arrays of uniformly distributed dots, is observed by laser ablation with circularly polarized pulses (Fig. 1.17h).

A detailed comparison and analysis of the 2D-FFT generated for the numerically simulated patterns (Fig. 1.17a–d) and for the SEM images of ablation morphologies (Fig. 1.17e–h) has revealed an excellent qualitative agreement between theory and experiment.

1.2.6 Period of Numerically Calculated Pattern

By irradiation of a flat surface with ultrashort laser pulses at intensity above a threshold value, we induce in the illuminated area a high degree of instability and pattern formation sets in. From linear stability analysis of (1.14), describing the

time profile evolution of irradiated surface, we expect the instability for the "ripple formation" with the wavelength

$$\Lambda_i = 2\pi\sqrt{\frac{2K}{|v_i|}}, \tag{1.24}$$

where K is the specific surface self-diffusion coefficient, v_i are the tension coefficients in (1.14) and i refers to the direction (x or y) with the largest v_i. Assuming the proportionality of v_i to the incident laser fluence F (1.15), we obtain that the ripple wavelength Λ depends only on the laser energy coupled into the material F and on the specific surface self-diffusion coefficient K:

$$\Lambda \propto \sqrt{\frac{K}{F}}. \tag{1.25}$$

This, on the first sight, confusing relation of the ripple wavelength with the fluence can be explained by taking into account the dependence of the specific self-diffusion coefficient K on the surface temperature T [54]:

$$K \propto \frac{1}{k_B T}\exp\left(-\frac{E_a}{k_B T}\right), \tag{1.26}$$

where E_a is the activation energy for surface self-diffusion. Assuming a linear dependence of the surface temperature T with the laser fluence F [63] and taking into account an exponential increase of the thermal surface diffusion K with the surface temperature T (1.26), we obtain exponential growth of the ripples wavelength with T.

1.2.7 Time Evolution

As it has been shown in Sect. 1.2.4, we can analyze the time evolution of the numerically generated pattern taking in account existence of the characteristic time t_c that separates linear and nonlinear regimes.

For a simulation-time much smaller than t_c we observe some periodical surface modifications (Fig. 1.18a), but the pattern has not completely developed yet. By increasing the time up to $t_c/2$ a refined surface pattern consisting of well expressed parallel lines with numerous bifurcations is observed (Fig. 1.18b, cf. also Fig. 1.17). At the time about crossover time t_c, as illustrated in Fig. 1.18c, we notice a coarsening of the ripples. Whereas Fig. 1.18a–c exhibit a progressive development of surface patterns, for times considerably above t_c (Fig. 1.18d) structures start to collapse and kinetic roughening takes place, known from nonlinear dynamics. Though in the

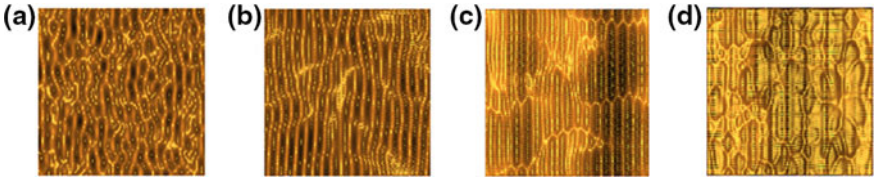

Fig. 1.18 Time evolution of numerically calculated surfaces ($64\pi \times 64\pi$) for $\Pi = 1$ and $\phi = 0$: **a** $t \ll t_c$; **b** $t = t_c/2$; **c** $t = t_c$; **d** $t = 2t_c$ (t_c = 1,600 a.u.)

model the situation is simplified and we did not investigate the pulse-to-pulse development of ripples, the numerical results show that a progressive evolution of structures occurs only in an appropriate time interval.

The effect of multipulse irradiation as well as an important role of feedback effect in ripples formation process have been established in numerous experiments. Figure 1.19 presents in more detail the time (resp. pulse-to-pulse) evolution of the central region of an ablation spot on a Si surface, produced by linearly polarized irradiation at intensity of about 2.6 TW/cm^2. With an increasing number of incident pulses up to 5,000 (Fig. 1.19a–c) the patterns become bigger and complex. This pattern coarsening effect is, again, in agreement with the simulation (Fig. 1.18a–c). At further increase of irradiation dose (Fig. 1.19d), after 10,000 pulses, we detect a collapsing of the structured region (similar to Fig. 1.18d) and the development of the deep crater with linear pattering of the walls, correlated to the direction of laser polarization.

The time evolution in experimental and numerical results allows to establish such general properties as the existence of a certain time interval for successful pattern development and the important role of feedback effect in the ripple formation process.

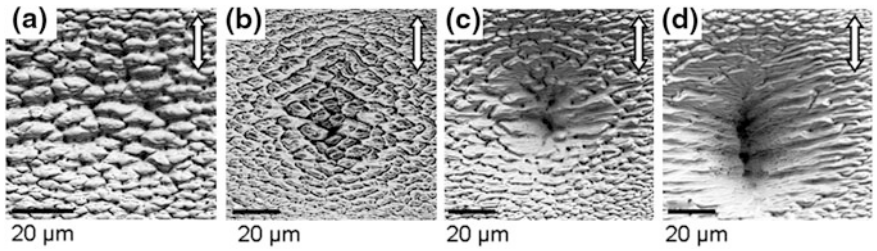

Fig. 1.19 SEM micrographs of pulse-to-pulse evolution of surface patterns at central part of ablated crater on Si by irradiation with linear polarized laser beam of intensity 2.6 TW/cm^2. **a** 1,000 pulses; **b** 3,000 pulses; and **c** 5,000 pulses; **d** 10,000 pulses. *Double arrows* indicate the direction of laser electrical field

1.3 Conclusion

The model for self-organized surface pattern formation upon femtosecond laser ablation was developed by introducing of a dependence on laser polarization. Sigmund's stochastical theory of sputtering and the model of ion-induced surface pattern formation were applied to the investigation of polarization dependent nanostructures. In this approach the laser electric field causes an asymmetry of the initial electron kinetic energy distribution and the related variation in excitation transfer probability. Polarization breaks the symmetry in electron energy transfer and aligns the surface patterns corresponding to the main direction of the energy flow.

Numerically calculated patterns are in good qualitative agreement with experiment for corresponding conditions of orientation and degree of ellipticity of the laser polarization as well as interaction times/number of incident pulses. Moreover, in the framework of this model we have quantitatively estimated the relative influence of input energy on the ripple period that make possible to minimize the size of ripples, selecting suitable parameters of a target material and laser irradiation.

Here it is necessary to note, that our explanation of anisotropic excitation upon femtosecond laser ablation is linked to asymmetric electron energy transfer as one of possible scenario. The microscopic nature of this phenomenon can be more complex and include other processes that break symmetry in the energy transfer and result in a similar effect.

References

1. M. Birnbaum, J. Appl. Phys. **36**, 3688 (1965)
2. D.C. Emmony, R.P. Howson, L.J. Willis, Appl. Phys. Lett. **23**, 598 (1973)
3. J.F. Young, J.E. Sipe, J.S. Preston, H.M. van Driel, Appl. Phys. Lett. **41**, 261 (1982)
4. J.F. Young, J.S. Preston, H.M. van Driel, J.E. Sipe, Phys. Rev. B **27**, 1155 (1983)
5. H. Varel, M. Wähmer, A. Rosenfeld, D. Ashkenasi, E.E.B. Campbell, Appl. Surf. Sci. **127–129**, 128 (1998)
6. A.M. Ozkan, A.P. Malshe, T.A. Railkar, W.D. Brown, M.D. Shirk, P.A. Molian, Appl. Phys. Lett. **75**, 3716 (1999)
7. J. Bonse, H. Sturm, D. Schmidt, W. Kautek, Appl. Phys. A **71**, 657 (2000)
8. M. Henyk, D. Wolffframm, J. Reif, Appl. Surf. Sci. **168**, 263 (2000)
9. J. Bonse, S. Baudach, J. Krüger, W. Kautek, M. Lenzner, Appl. Phys. A **74**, 19 (2002)
10. F. Costache, M. Henyk, J. Reif, Appl. Surf. Sci. **186**, 352 (2002)
11. F. Costache, M. Henyk, J. Reif, Appl. Surf. Sci. **208–209**, 486 (2003)
12. J. Bonse, K.-W. Brzezinka, A.J. Meixner, Appl. Surf. Sci. **221**, 215 (2004)
13. F. Costache, S. Kouteva-Arguirova, J. Reif, Solid State Phenom. **95–96**, 635 (2004)
14. G. Miyaji, K. Miyazaki, Appl. Phys. Lett. **89**, 191902 (2006)
15. G. Miyaji, K. Miyazaki, Appl. Phys. Lett. **91**, 123102 (2007)
16. G. Seifert, M. Kaempfe, F. Syrowatka, C. Harnagea, D. Hesse, H. Graener, Appl. Phys. A **81**, 799 (2005)
17. T. Tomita, K. Kinoshita, S. Matsuo, S. Hashimot, Appl. Phys. Lett. **90**, 153115 (2007)
18. G. Miyaji, K. Miyazaki, Opt. Express **16**, 16265 (2008)

19. J. Bonse, A. Rosenfeld, J. Krüger, J. Appl. Phys. **106**, 104910 (2009)
20. D. Dufft, A. Rosenfeld, S.K. Das, R. Grunwald, J. Bonse, J. Appl. Phys. **105**, 34908 (2009)
21. Z. Li, H. Li, J. Zhang, S. Chen, M. Huang, X. Yu, Opt. Laser Technol. **44**, 923 (2012)
22. J. Reif, Ch. 6 in *Laser Processing of Materials*, ed. by P. Schaaf (Springer, Heidelberg, 2010), p. 113
23. J. Reif, O. Varlamova, M. Ratzke, M. Schade, H.S. Leipner, T. Arguirov, Appl. Phys. A **101**, 361 (2010)
24. J. Reif, F. Costache, M. Henyk, S.V. Pandelov, Appl. Surf. Sci. **197–198**, 891 (2002)
25. O. Varlamova, F. Costache, M. Ratzke, J. Reif, Appl. Surf. Sci. **253**, 7932 (2007)
26. J. Reif, F. Costache, O. Varlamova, G. Jia, M. Ratzke, Phys. Status Solidi C **6**, 681 (2009)
27. S. Höhm, A. Rosenfeld, J. Krüger, J. Bonse, J. Appl. Phys. **112**, 014901 (2012)
28. J. Reif, O. Varlamova, F. Costache, Appl. Phys. A **92**, 1019 (2008)
29. H.M. van Driel, J.E. Sipe, J.F. Young, Phys. Rev. Lett. **49**, 1955 (1982)
30. J.E. Sipe, J.F. Young, J.S. Preston, H.M. van Driel, Phys. Rev. B **27**, 1141 (1983)
31. J.F. Young, J.E. Sipe, H.M. van Driel, Phys. Rev. B **30**, 2001 (1984)
32. M. Henyk, N. Vogel, D. Wolffframm, A. Tempel, J. Reif, Appl. Phys. A **69**, 355 (1999)
33. J. Reif, Opt. Eng. **28**, 1122 (1989)
34. J. Reif, M. Henyk, D. Wolffframm, Proc. SPIE **3933**, 26 (2000)
35. R. Cuerno, A.-L. Barabasi, Phys. Rev. Lett. **74**, 4746 (1995)
36. J. Reif, F. Costache, M. Bestehorn, Ch. 9 in *Recent Advance in Laser Processing of Materials*, ed. by J. Periere, E. Millon, E. Fogarassy (Elsevier, Amsterdam, 2006), p. 275
37. J. Reif, O. Varlamova, S. Varlamov, M. Bestehorn, Appl. Phys. A **104**, 969 (2011)
38. Q. Wu, Y. Ma, R. Fang, Y. Liao, Q. Yu, Appl. Phys. Lett. **82**, 1703 (2003)
39. J. Bonse, M. Munz, H. Sturm, J. Appl. Phys. **97**, 013538 (2005)
40. T.H.R. Crawford, H.K. Haugen, Appl. Surf. Sci. **253**, 4970 (2007)
41. F. Garrelie, J.-P. Colombier, F. Pigeon, S. Tonchev, N. Faure, M. Bounhalli, S. Reynaud, O. Parriaux, Opt. Express **19**, 9035 (2011)
42. J. Erlebacher, M.J. Aziz, E. Chason, M.B. Sinclair, J.A. Floro, Phys. Rev. Lett. **82**, 2330 (1999)
43. E. Chason, T.M. Mayer, B.K. Kellerman, D.T. McIlroy, A.J. Howard, Phys. Rev. Lett. **72**, 3040 (1994)
44. O. Varlamova, M. Ratzke, J. Reif, Solid State Phenom. **156–158**, 535 (2010)
45. C. Misbah, A. Valance, Eur. Phys. J. E **12**, 523 (2003)
46. J.L. Hansen, M. van Hecke, A. Haaning, C. Ellegaard, K.H. Andersen, T. Bohr, T. Sams, Nature **410**, 324 (2001)
47. M.C. Malin, M.H. Carr, G.E. Danielson, M.E. Davies, W.K. Hartmann, A.P. Ingersoll, P.B. James, H. Masursky, A.S. McEwen, L.A. Soderblom, P. Thomas, J. Veverka, M.A. Caplinger, M.A. Ravine, T.A. Soulanille, J.L. Warren, Science **279**, 1681 (1998)
48. C. Teichert, J.C. Bean, M.G. Lagally, Appl. Phys. A **67**, 675 (1998)
49. Y. Kuramoto, T. Tsuzuki, Prog. Theor. Phys. **55**, 356 (1977)
50. G.I. Sivashinsky, Acta Astronaut. **6**, 569 (1979)
51. M. Kardar, G. Parisi, Y.-C. Zhang, Phys. Rev. Lett. **56**, 889 (1986)
52. P. Sigmund, Phys. Rev. **184**, 383 (1969)
53. P. Sigmund, J. Mater. Sci. **8**, 1545 (1973)
54. M.A. Makeev, R. Cuerno, A.-L. Barabasi, Nucl. Instr. Meth. Phys. Res. B **197**, 185 (2002)
55. R.M. Bradley, J.M.E. Harper, J. Vac. Sci. Technol. **6**, 2390 (1988)
56. H.O. Jeschke, M.E. Garcia, M. Lenzner, J. Bonse, J. Krüger, W. Kautek, Appl. Surf. Sci. **197–198**, 839 (2002)
57. A.M. Lindenberg, S. Engemann, K.J. Gaffney, K. Sokolowski-Tinten, J. Larsson, P.B. Hillyard, D.A. Reis, D.M. Fritz, J. Arthur, R.A. Akre, M.J. George, A. Deb, P.H. Bucksbaum, J. Hajdu, D.A. Meyer, M. Nicoul, C. Blome, T.H. Tschentscher, A.L. Cavalieri, R.W. Falcone, S.H. Lee, R. Pahl, J. Rudati, P.H. Fuoss, A.J. Nelson, P. Krejcik, D.P. Siddons, P. Lorazo, J.B. Hastings, Phys. Rev. Lett. **100**, 135502 (2008)

58. J. Reif, Ch. 2 in *Laser-Surface Interactions for New Materials Production. Tailoring Structure and Properties*, ed. by A. Miotello, P.M. Ossi (Springer, Heidelberg, 2010), pp. 19–41
59. J. Reif, F. Costache, S. Eckert, M. Henyk, Appl. Phys. A **79**, 1229 (2004)
60. V. Hertel, R. Stoian, A. Rosenfeld, D. Ashkenasi, E.E.B. Campbell, Riken Rev. **32**, 23 (2001)
61. A. Zangwill, *Physics at Surfaces* (Cambridge University Press, Cambridge, 1988)
62. S. Park, B. Kahng, H. Jeong, A.-L. Barabasi, Phys. Rev. Lett. **83**, 3486 (1999)
63. A. Cavalleri, K. Sokolowski-Tinten, J. Bialkowski, M. Schreiner, D. von der Linde, J. Appl. Phys. **85**, 3301 (1999)

Chapter 2
Harnessing Ultrafast Laser Induced Nanostructures in Transparent Materials

Martynas Beresna, Mindaugas Gecevičius and Peter G. Kazansky

Abstract Self-organized nanogratings are generated with a focused femtosecond laser beam in the bulk of fused silica. Such sub-micron structures exhibit form birefringence with a retardance of several hundreds of nanometers. The spatial orientation of the nanostructures is induced by polarization management. The ability to control the direction of the slow axis and induce high retardance levels leads to the engineering of unique optical devices with spatially varying birefringence.

2.1 Introduction

The first observation of laser induced ripples dates back to the sixties when Birnbaum reported ripple formation on the surface of a semiconductor [1]. Since then, ripple formation was observed on virtually any material surface from dielectrics to metals and polymers. The phenomenon could be observed in a vast variety of different conditions, with the wavelength of irradiation ranging from UV to mid-infrared and over different operating regimes from continuous wave (CW) to femtosecond lasers.

In 2003, a new type of self-organized nanostructure was observed inside of SiO_2 glass after undergoing ultrafast laser irradiation [2]. It was found to be responsible [3] for the induced anisotropy and propeller shape scattering reported 4 years earlier [4, 5]. Under certain irradiation conditions, highly ordered subwavelength structures with features smaller than 20 nm could be formed in the irradiated volume (Fig. 2.1). There is also an indication that nanogratings are constituted from

M. Beresna (✉) · M. Gecevičius · P.G. Kazansky (✉)
Optoelectronics Research Centre, University of Southampton,
Highfield, SO17, 1BJ Southampton, Hampshire, UK
e-mail: mxb@orc.soton.ac.uk

P.G. Kazansky
e-mail: pgk@orc.soton.ac.uk

© Springer International Publishing Switzerland 2015

S. Sakabe et al. (eds.), *Progress in Nonlinear Nano-Optics*,
Nano-Optics and Nanophotonics, DOI 10.1007/978-3-319-12217-5_2

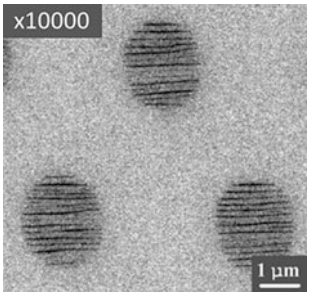

Fig. 2.1 Back scattering electron image of nanogratings induced in the bulk of silica glass. Surface of silica glass is polished close to the depth of the focal spot. *Source* Shimotsuma et al. [2]

nanoporous material [6]. As opposed to surface ripples, nanostructures inside the material are reported only for a handful of materials: fused silica, quartz, sapphire and several other crystalline materials. However, nanogratings induced in the volume were reported to continuously transform into surface ripples when the laser focus moves out of the sample [7]. As a result, some theories on nanostructure formation attempt to reconcile surface ripple and volume nanograting formation [8].

Since the first observation of nanogratings in the bulk of fused silica, numerous applications of these structures have been demonstrated [9] including anisotropic microreflectors [10], polarization sensitive holograms [11] and waveguides [12]. In this chapter, we will focus on polarization controlling devices written in fused silica with self-assembled nanogratings.

Conventional anisotropic optical elements, such as linear polarizers or wave plates, are uniform in the transverse direction (i.e. their optical properties are spatially invariant). These elements are widely used to manipulate light polarization: purify, rotate or transform. However, there is an increasing interest in producing spatially variant birefringent optical elements, where anisotropic properties will vary across the structure. Spatially variant polarization elements can be seen as analogous to conventional diffractive optics, which have found numerous applications from complex beam shapers to Fresnel lenses in LED flash within mobile phones. Instead of phase or amplitude these elements affects the polarization state of the transmitted or reflected light. A multitude of functional devices based on spatially varying anisotropy have been already demonstrated including beam splitters [9, 13], azimuthal and radial polarization state converters [14–16] and coronographs [17]. Interesting results can be achieved by simultaneous control of the phase and polarization of the laser beam, allowing point spread function engineering in the focus of a high numerical aperture objective [18]. In certain cases, a single spatially variant polarization element can effectively replace a group of conventional optical elements. For instance, a polarization diffraction grating enables both selectivity of polarization and angular dispersion thus effectively replacing a polarizer and diffraction grating [12, 19, 20]. Another potential application of spatially variant birefringent optical elements is instantaneous read-out of the birefringent optical data storage [21, 22]. Currently, spatial polarization control is achieved through several

technologies: spatial light modulators [13, 18], segmented linear polarizers or waveplates [23], subwavelength gratings [12, 19], or materials with photo-aligning chromophores [24].

Probably, the most popular method for spatial polarization manipulation is based on spatial light modulators. The main advantage of spatial light modulators is their ability to dynamically change optical properties of the light on a time scale of less than 200 ms. However, liquid crystals, which are the basis of most spatial light modulators, can modulate only one polarization component at a time. Essentially, a liquid crystal based spatial light modulator is an array of waveplates, where retardance can be arbitrarily set for each waveplate. The slow axis for liquid crystal cells, however, is uniform across the array and cannot be manipulated. As a result, full control of polarization requires the light to impinge on a spatial light modulator at least twice, making the configuration of the experiment non-trivial. Additional optical elements must be included to achieve the desired result, e.g. radial polarization [25]. In simple cases, only one spatial light modulator can be used. However, several light modulators must be combined for full polarization control. This inevitably introduces higher losses. Additionally, they are expensive and operate only at moderate laser fluences (200 mJ/cm^2 at 10 ns). Devices based on liquid crystals also tend to suffer from thermal drift leading to undesired error of the induced phase shift.

Passive spatially variant birefringent elements with simple geometries can be fabricated by joining small segments of polarizers or waveplates. The advantage of such elements is the broadband operation and ability to sustain high power of laser irradiation. In comparison to spatial light modulator-based set-ups, this technique allows the production of much more compact and easy to use polarization control elements. The segmentation technique, however, suffers from low resolution, leading to intensity losses due to diffraction and additional spatial filtering required for purifying the laser beam after passing the polarization element. The fabrication of such elements is costly as it requires high manufacturing precision and involves time consuming procedures such as polishing, gluing and aligning separate parts into the final optical element.

Birefringent elements can also be fabricated using materials with azobenzene. The birefringence is induced in an initially isotropic material by axis selective *trans-cis-trans* photoisomerization and the subsequent orientation of the azobenzene groups along the laser beam polarization [26]. It is possible to write a polarization diffraction grating directly by exposing the material to the interference pattern of two circularly polarized beams [24]. Thus the technique is viable for fast mass production, leading to potentially low manufacturing costs. However, such polymeric substances, currently, are instable and tend to return to the random molecule distribution even at the room temperature.

Finally, spatially variant birefringent elements can be produced via material nanostructuring. A photolithographic technique was used to create a subwavelength grating, which exhibits form birefringence [12, 19]. Metal stripes (Ti and Au) via contact photolithography and lift-off are formed on the surface of a GaAs wafer into a subwavelength structure. Although this method allows for complex geometries

with easily controlled final parameters, the restriction of available resolution and the requirement for a high aspect ratio, allowed demonstration of prototypes only at 10 μm. Recently, a similar technique was used to fabricate devices operating in the NIR (1 μm) [27]. However, demonstrated optical quality is strongly compromised with the nanostructure resolution.

In this respect the femtosecond laser direct writing is an attractive alternative due to the possibility of energy deposition within the focal volume with a resolution of few hundred nanometres. The femtosecond laser self-assembly of nanostructures in fused silica offers a flexible and simple alternative for fabrication of polarization sensitive devices for the visible spectral range [11, 20, 28].

2.2 Cylindrical Vector Beams

One of the applications of spatially variant polarization optics is related to cylindrical vector beams. The cylindrical vector (CV) beams are vector-beam solutions of Maxwell's equations that obey axial symmetry in both amplitude and phase [29, 30]. Comparison of beams with spatially homogenous and spatially variant polarization states is illustrated in Fig. 2.2. If the polarization of a beam is aligned in the radial direction, it is called radial polarization (Fig. 2.2g). Similarly, if the electric field is in the tangential direction, we get azimuthal polarization (Fig. 2.2h). A linear superposition of these two modes can produce a beam with even more complex polarization distribution (Fig. 2.2i). Spatially homogenous polarization modes can also exhibit instantaneous electric fields, which are directed into

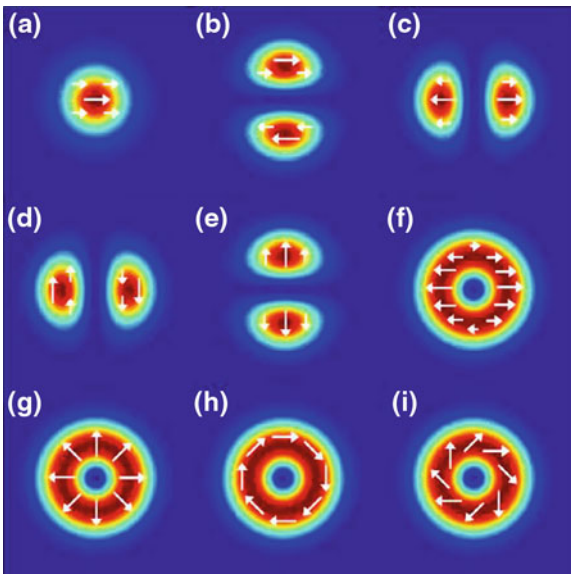

Fig. 2.2 Spatial distributions of intensity and vector fields for different polarization modes: **a** x-polarized fundamental Gaussian mode; **b** x-polarized HG_{01} mode; **c** x-polarized HG_{10} mode; **d** y-polarized HG_{10} mode; **e** y-polarized HG_{01} mode; **f** x-polarized LG_{01} mode (vortex); **g** radially polarized mode; **h** azimuthally polarized mode; **i** linear superposition of (**g**) and (**h**)

opposite directions as a result of inhomogeneous phase distribution across the beam, but there is no axial symmetry.

The solutions for the beams with spatially homogeneous states of polarization are obtained by solving the scalar Helmholtz equation for electric field:

$$\left(\nabla^2 + k^2\right)E = 0,$$

where k is the wavenumber. In Cartesian coordinates, the general solution for the electric field has the form:

$$E(x, y, z, t) = u(x, y, z)\exp[i(kz - \omega t)],$$

where ω is frequency of light.

For the slowly varying envelope approximation, the Hermite-Gauss modes (HG_{mn}) solution is the following:

$$u(x, y, z) = E_0 H_m\left(\sqrt{2}\frac{x}{\omega(z)}\right)H_n\left(\sqrt{2}\frac{y}{\omega(z)}\right)\frac{w_0}{w(z)}\exp[-i\varphi_{mn}(z)]\exp\left[i\frac{k}{2q(z)}r^2\right],$$

where $H_m(x)$ denotes Hermite polynomials, E_0 is a constant electric field amplitude, $w(z)$ is the beam size, w_0 is the beam size at the waist, $q(z)$ is complex beam parameter and $\varphi_{mn}(z)$ is the Gouy phase shift.

For the beams with spatially variant polarizations, the full vector wave equation has to be used:

$$\nabla \times \nabla \times \vec{E} - k^2\vec{E} = 0.$$

Considering a cylindrically symmetric, azimuthally polarized field:

$$\vec{E}(r, z) = U(r, z)\exp[i(kz - \omega t)]\vec{e}_{\phi_0},$$

where $\vec{e}_{\phi_0}$ is the unit vector in the azimuthal direction. $U(r, z)$ satisfies the following equation:

$$\frac{1}{r}\frac{\partial}{\partial r}\left(r\frac{\partial U}{\partial r}\right) - \frac{U}{r^2} + 2ik\frac{\partial U}{\partial z} = 0.$$

The solution of this equation corresponds to an azimuthally polarized vector Bessel-Gauss beam:

$$\vec{E}(r, z) = -E_0 J_1\left(\frac{\beta r}{1 + \frac{iz}{z_0}}\right)\exp\left[\frac{\frac{i\beta^2 z}{2k}}{1 + \frac{iz}{z_0}}\right]\frac{w_0}{w(z)}\exp[-i\varphi(z)]\exp\left[i\frac{k}{2q(z)}r^2\right]\exp[i(kz - \omega t)]\vec{e}_{\phi_0}.$$

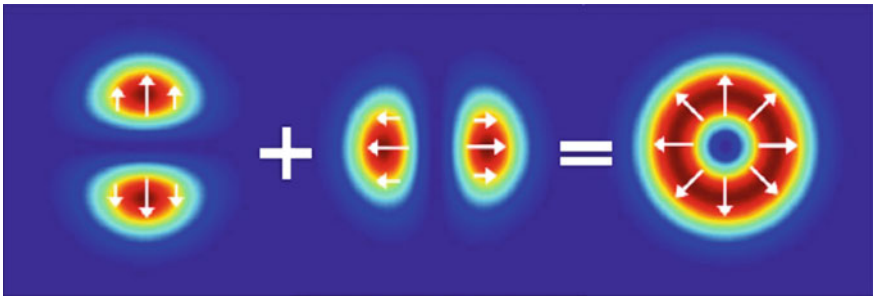

Fig. 2.3 Radial polarization as a superposition of two orthogonally polarized HG modes

where β is a constant scale parameter, z_0 is the Rayleigh range, $\varphi(z)$ is the Gouy phase shift and $J_1(x)$ is the first-order Bessel function of the first kind. Instead of the vector Bessel-Gauss solution, in many applications, the simplified electric field distribution can be used [30]:

$$\vec{E}(r,z) = Ar\,\exp\left(-\frac{r^2}{w^2}\right)\vec{e}_{r,\phi},$$

where A is the amplitude of an electric field. Alternatively, vector beams can be described as a superposition of two orthogonally polarized Hermite-Gauss HG_{01} and HG_{10} modes. For instance, a radially polarized beam can be expressed as follows (Fig. 2.3):

$$\vec{E}_r = HG_{10}\vec{e}_x + HG_{01}\vec{e}_y.$$

2.3 Polarization Converter

The cylindrical vector beams can be produced by polarization converters created based on spatially variant subwavelength gratings, which would generate azimuthally symmetric polarization from conventional linearly or circularly polarized Gaussian modes (Fig. 2.4).

The working principle of such optical elements is similar to the segmented half-wave plates, where several segments of half-wave plates are glued together with an appropriately arranged slow axis. The advantage of subwavelength gratings is that the slow axis orientation is changing continuously, thus pure radial/azimuthal polarization can be generated by a single optical element. Photolithography, which is usually used for fabrication of such elements, has a limited resolution that restricts the wavelength of operation to the infrared (<10 μm). In this respect, the nanogratings induced by femtosecond lasers are a perfect choice for devices operating in the visible and near-infrared. Depending on the induced retardance,

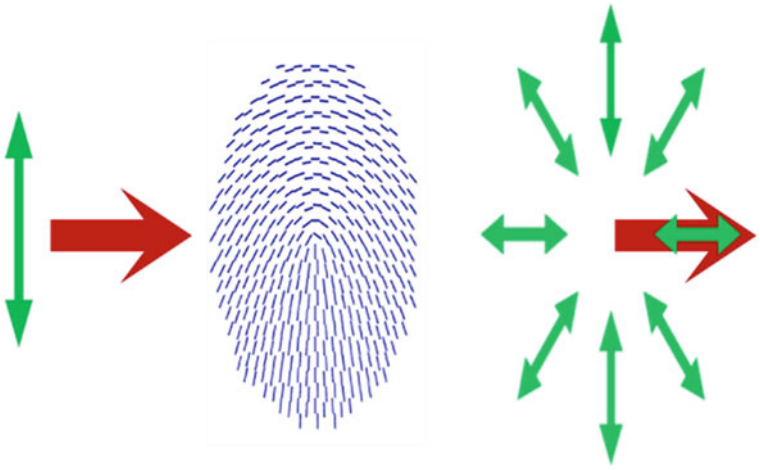

Fig. 2.4 Principle of radial polarization converter. Incident linearly polarized light is converted into radially polarized light due to the spatially varying slow axis direction. The *blue dashes* schematically represent spatial orientation of subwavelength gratings in the half-wave polarization converter

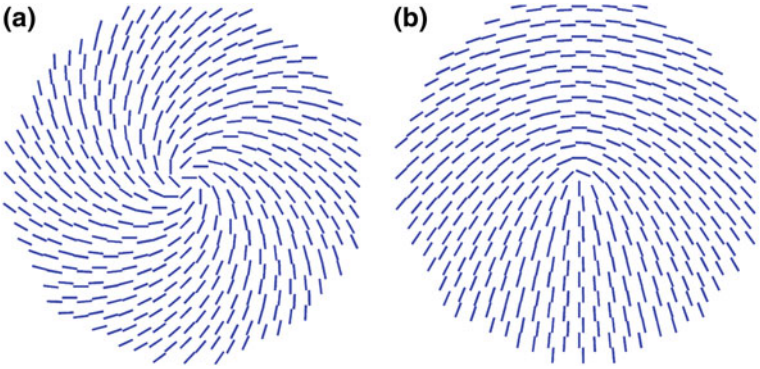

Fig. 2.5 Schematic drawings of nanograting distribution in quarter- (**a**) and half-wave (**b**) polarization converters. The *blue dashes* indicate the direction of the nanogratings

two types of converters can be constructed (Fig. 2.5). The first type is a spatially variant quarter wave plate, which converts an incident, circularly polarized beam into a radially or azimuthally polarized optical vortex. The second type is a spatially variant half-wave plate, which converts linearly or circularly polarized incident light into radial/azimuthal polarization or an optical vortex respectively. Both types differ by the amount of required retardance and orientation of the slow axis (Fig. 2.5).

Using Jones matrix formalism, a rotation operation can be applied to the matrix of a quarter wave plate. Then the spatially variant quarter wave plate can be described by the following matrix:

$$M_{QW} = \begin{pmatrix} \cos^2\theta + i\sin^2\theta & (1-i)\cos\theta\,\sin\theta \\ (1-i)\cos\theta\,\sin\theta & i\cos^2\theta + \sin^2\theta \end{pmatrix},$$

where $\theta = \phi + \pi/4$ and ϕ is a polar angle in the polar coordinate system. Multiplying a vector describing the left handed circular polarization by this matrix, the following expression is derived:

$$\vec{E}_{AZI} = M_{QW}\frac{1}{\sqrt{2}}\begin{pmatrix} 1 \\ i \end{pmatrix} = \begin{pmatrix} -\sin\phi \\ \cos\phi \end{pmatrix} e^{i\phi} e^{i\frac{\pi}{4}}.$$

The first term of the product represents azimuthal polarization while the second term indicates the presence of the orbital angular momentum ($l = 1$). Similar calculations made for the right handed incident polarization yield radial polarization with the orbital momentum $l = -1$. The appearance of the orbital momentum is the result of the Pancharatnam–Berry geometrical phase [31, 32]. As a result, a combination of the radial/azimuthal polarization and orbital momentum yields a complex electric field distribution. A pure radial polarization with a flat phase front can be generated by adding a vortex phase plate, which would compensate the orbital momentum.

If the rotation operator is applied to a spatially homogeneous half-wave plate, the following Jones matrix expression for a spatially variant half-wave plate is obtained:

$$M_{HW} = \begin{pmatrix} \cos\phi & \sin\phi \\ \sin\phi & -\cos\phi \end{pmatrix}.$$

This is essentially the same rotation operator, where the incident polarization is rotated by the angle ϕ. The only difference is that the angle used here is also the azimuth of the polar coordinates. Then for the incident horizontally polarized light, the radial polarization emerges:

$$\vec{E}_{RAD} = M_{HW} \cdot \vec{E}_{LVP} = M_{HW}\begin{pmatrix} 0 \\ 1 \end{pmatrix} = \begin{pmatrix} \sin\phi \\ -\cos\phi \end{pmatrix}.$$

Similarly for the incident vertically polarized light, the azimuthal polarization is derived. In this case, as opposed to a spatially variant quarter-wave plate, a half-wave plate converts linear polarization into a pure radial polarization state without the presence of orbital momentum. The superposition of two cylindrically symmetric polarization states can be easily produced by rotating the incident beam polarization with respect to the spatially variant half-wave plate. An interesting

result follows if a circularly polarized light is transmitted through the half-wave converter:

$$\vec{E}_{VOR} = M_{HW} \cdot \vec{E}_{RCP} = M_{HW} \frac{1}{\sqrt{2}} \begin{pmatrix} 1 \\ i \end{pmatrix} = \frac{1}{\sqrt{2}} \begin{pmatrix} \cos\phi + i \sin\phi \\ \sin\phi - i \cos\phi \end{pmatrix} = e^{i\phi} \begin{pmatrix} 1 \\ -i \end{pmatrix}.$$

From this expression it is obvious that circularly polarized incident light changes its handedness and acquires a spatially varying phase factor $e^{i\phi}$, which directly indicates the presence of an optical vortex. As a result, the same converter can be used for the production of azimuthally symmetric polarization states and optical vortices.

2.4 Fabrication and Characterization

The polarization converters were fabricated with a PHAROS femtosecond laser system (Light Conversion Ltd.) based on direct diode pumped Yb:KGW (Yb-doped potassium gadolinium tungstate) crystal. The system operates at 1,030 nm and delivers pulses of 270 fs, which can be stretched to 8 ps. The repetition rate was set to 200 kHz.

The orientation of the nanogratings is controlled with the polarization of the writing beam, which is rotated with a half-wave plate mounted onto a motorized rotation stage. The focusing is performed with relatively low numerical aperture lenses (NA = 0.16–0.35), which have sufficiently long Rayleigh ranges to induce high retardance values required for polarization converters. After the writing procedure, the fabricated structures are analysed with the Abrio birefringence measurement system (CRi Inc.) and Olympus BX51 optical microscope (Fig. 2.6).

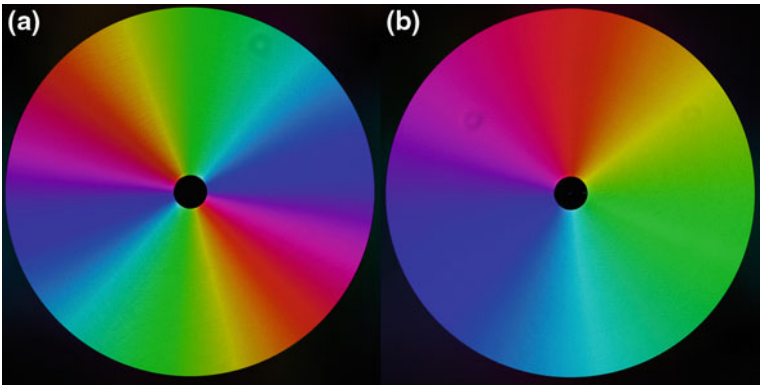

Fig. 2.6 Quantitative birefringence measurements of femtosecond laser written radial polarization converters for circular (**a**) and linear (**b**) incident polarizations. The *brightness* represents the retardance magnitude while the *colour* indicates the direction of the slow axis

The first converters were demonstrated for 532 nm [28, 33]. Later, high quality polarization converters were also fabricated for 1,030 and 1,550 nm. As the birefringence of nanogratings is constant for longer wavelengths, the required retardance was achieved by stacking several birefringent layers together, while using the same focusing optics and laser power as for the elements operating at 532 nm.

The ability of a half-wave retardance converter to generate an optical vortex with circular polarization was examined by observing the self-interference pattern on a CCD camera. The interference pattern was formed by overlapping two replicas of the laser beam (532 nm) after it passed through the converter. As both beams were incident at an angle, the intensity gained a 'sine' wave like modulation. In the interference pattern, two forks can be clearly seen, confirming the presence of an optical vortex (Fig. 2.7).

The contrast of the generated optical vortex was of about 3 %. However, it was improved by more than one order of magnitude by inserting a linear polarizer after the converter. As a result, a high quality optical vortex with a contrast >0.1 % was produced. The measurement of the exact value of the contrast was limited by the dynamic range of the beam profiler used for the characterization.

A constant value of retardance with the continuously varying direction of the slow axis was measured across the whole structure. The transmission losses for the converters of corresponding wavelengths are 40 % at 532 nm, 20 % at 1 μm and 10 % in the telecom wavelengths (1,550 nm). The measurements made in the far-field were found to be in good agreement with the model based on the Jones matrix formalism and Fourier propagation (Fig. 2.8).

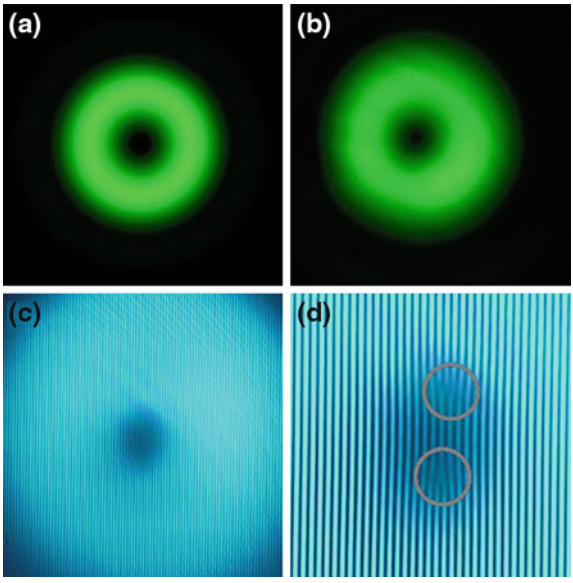

Fig. 2.7 **a** Modelled and **b** measured vortex intensity profiles, **c** diffraction pattern of two interfering vortices, **d** zoomed central part. *Red circles* indicate a 'fork' pattern formed due to a phase discontinuity present in the interfering electric field

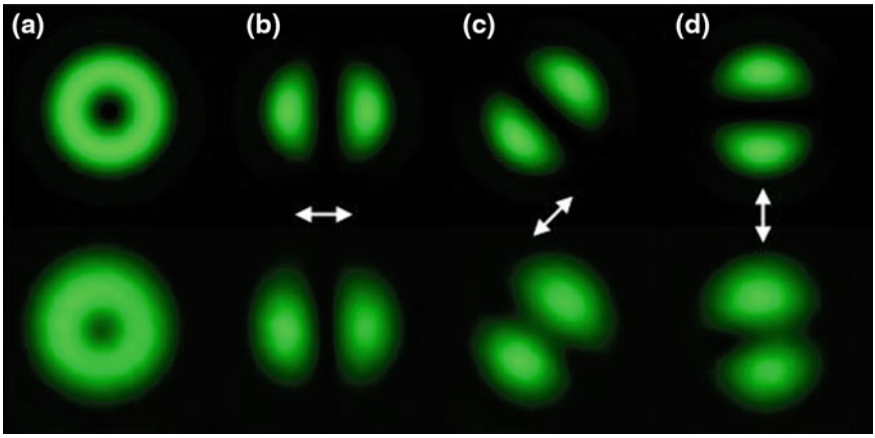

Fig. 2.8 Modelled (*top*) and measured (*bottom*) profiles of generated radial polarization directly after the converter (**a**) and after polarizer (**b–d**). *White arrows* indicate the transmission axis of the polarizer inserted between the converter and a CCD camera

The damage threshold of the converter for 532 nm was characterized by Altechna Ltd. following the procedure according to ISO 11254–2 standard. Such an element had a damage threshold of 22.8 J/cm^2 at 1,064 nm, τ = 3.5 ns, f = 10 Hz.

2.5 5D Optical Memory

Another interesting application of a femtosecond laser pulse induced birefringence is multi-dimensional optical memory. The growing hunger of information fuels the race for continuous advances in data storage. Additionally, the development of cloud technologies will also require the reliable storing of tremendous amounts of data in a single location. As a result, the need for increasing storage capacity demands the development of new approaches, such as storing more than a single bit per one physical location of optical storage. Here a novel approach of multiplexing the data storage is demonstrated by femtosecond laser induced nanostructures.

Optical data storage is based on the manipulation of optical properties in the storage medium. Typically, in such storages, the reflectivity of the surface is manipulated to achieve a two level intensity signal system, e.g. CD, DVD and Blue-Ray. The data is recorded using the linear absorption of the material, thus only the surface can be modified in this case. This is so-called 2D optical memory, as the data is stored only on the surface of the carrying medium. Employing a nonlinear absorption mechanism, such as two photon absorption, 3D optical memory can be constructed [34], where optical properties of the medium can be manipulated in the confined volume and thus extending the possible storage capacity by at least 10 times. The theoretical capacity limit of 3D optical memory is about 3.5 Tbit/cm^3.

Still this optical recording technology is based on two level intensity signal encoding. Thus in a single memory cell, or voxel, only 1 bit can be stored. In order to further expand the potential storage capacity, multiple research groups started investigating the possibility of storing more than one bit in a single voxel. This can be implemented in media which is sensitive not only to the intensity of the laser beam but also to its other properties. The signal can then be read in several channels, thus enabling multiplexing of the data. One of the most popular ways is to explore birefringent or dichroic properties of the materials, i.e. recording and reading the polarization of the light beam [21].

More than a decade ago, the potential of ultrafast laser writing of isotropic modification for three-dimensional optical memory was demonstrated [35]. Later it was found that the ultrashort laser pulses could also induce anisotropic modifications related to self-assembled nanograting formation [3]. This anisotropy can be characterized by two independent parameters: retardance and slow axis orientation (Fig. 2.9), which can be rewritten with successive pulse sequences [22, 36]. Recently, it was proposed that using these two parameters, optical recording can be extended beyond the three spatial dimensions [22]. As a result, femtosecond laser induced self-assembled nanostructures can be employed as a method for rewritable five-dimensional optical memory.

A nanograting is a structural modification which can withstand temperatures of 1,000 °C [37]. Additionally, the femtosecond laser pulse induced nanograting is formed inside of silica glass, which itself is known for high stability and chemical resistance. This altogether makes the described optical memory ideal for archiving high volumes of important information. It was also shown that such nanostructures can be successfully rewritten or deleted with ultrashort light pulses, which remodifies an otherwise stable structure. As the nanogratings are induced by non-linear absorption of intense femtosecond pulses, they are written selectively in the focal volume of the laser beam. The ability to record and read several layers of information by the nanogratings was successfully demonstrated by Shimotsuma et al. [22].

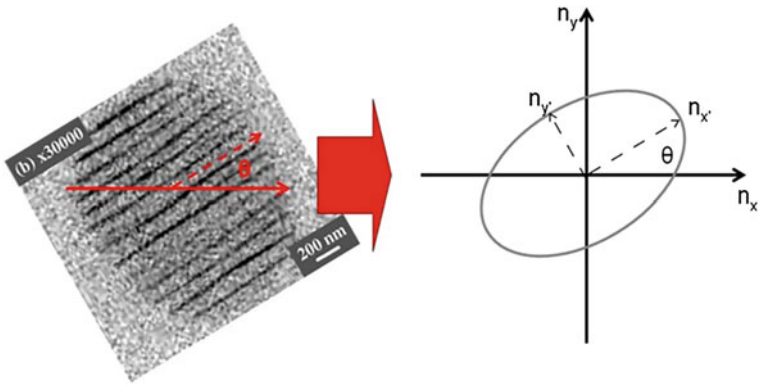

Fig. 2.9 Schematic description of two parameters describing birefringence: slow axis angle θ and retardance $(n_{x'} - n_{y'}) \cdot d$, ($d$—length of birefringent structure)

During the recording procedure, the number of pulses and the azimuth of their polarization can independently control retardance and the slow axis direction. By quantifying both parameters, one can encode the information by using both parameters. The capacity of the storage will depend on the precision with which the retardance and slow axis can be written and read. Currently, during the recording procedure, the retardance can be controlled with a precision of about 10 nm, while the slow axis angle can be defined with a precision of a few degrees. For the read-out procedure, the Abrio polarization measurement system (CRi Inc.) is employed, which can measure both parameters with a precision of less than 1 nm and 1° respectively.

As a demonstration of multidimensional optical data storage, the portraits of two great scientists, Maxwell and Newton, were recorded in a piece of silica glass by continuously controlling exposure and polarization during the writing process. For encoding, both greyscale (256 grey levels) portraits were first matched in pixel size. The Newton portrait was split into 8 layers and later combined with Maxwell's image using a MATLAB code. Finally 8 greyscale images were generated and each separately recorded with different polarization orientations.

The greyscale values of each layer were directly expressed into the number of pulses. The polarization rotation is performed by mechanically rotating a half-wave plate. As a result, the Maxwell portrait was encoded with varying strength of birefringence and Newton's was done by varying the slow-axis orientation. Later, using the Abrio system, images were decoupled, clearly demonstrating the potential of the proposed information recording technique (Fig. 2.10).

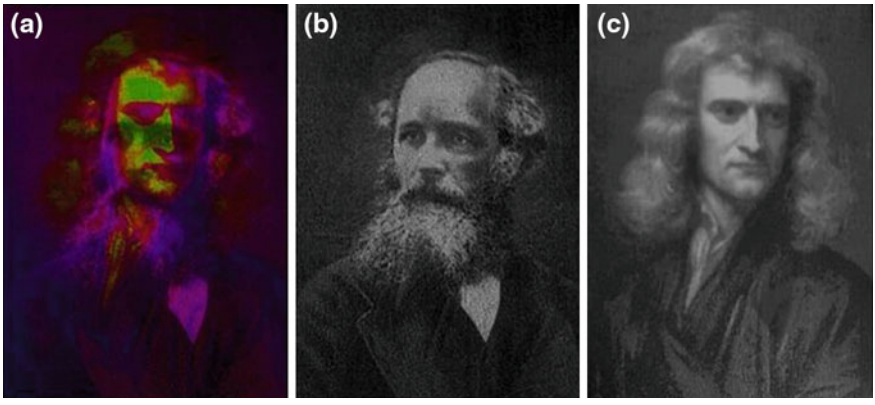

Fig. 2.10 **a** The Abrio image representing in *false colours* the recorded information in slow axis and retardance. **b** and **c** Decoupled images of Maxwell and Newton (no additional operations on images were performed afterwards)

2.6 Conclusions

A femtosecond laser beam focused into the bulk of fused silica can produce self-organized nanogratings. This structure, with a sub-micron period, exhibits form birefringence with a retardance of several hundreds of nanometers. Manipulation of the writing laser beam's polarization allows control of the spatial orientation of the nanostructure and, as a result, the orientation of the optical axes of induced birefringence. The ability to control the direction of the slow axis and induce high retardance levels leads to the engineering of unique optical devices with spatially varying birefringence.

The devices can be operated in the visible and near-infrared. These optical elements allow the efficient conversion of linear polarization into radial/azimuthal polarization. Additionally, a circularly polarized beam can be converted into an optical vortex, where the charge sign is defined by the handedness of the incident circular polarization. This effect is related to Pancharatnam–Berry geometrical phase. The quality of the converted beam is comparable to commercially available radial polarization generation techniques. A high damage threshold allows applications of these converters, where high power lasers are used.

Finally, 5D optical recording has been demonstrated based on femtosecond laser induced nanostructures in the bulk of fused silica. The additional channels for memory multiplexing were retardance and birefringence, which can be independently recorded and read. As a demonstration, two images were recorded into the same plane and then successfully decoupled using a quantitative birefringence measurement system. Potentially, high capacity and stable optical storage could benefit large storage infrastructures, where large amounts of information need to be stored in a compact and reliable form.

References

1. M. Birnbaum, Semiconductor surface damage produced by ruby lasers. J. Appl. Phys. **36**, 3688 (1965)
2. Y. Shimotsuma, P. Kazansky, J. Qiu, K. Hirao, Self-organized nanogratings in glass irradiated by ultrashort light pulses. Phys. Rev. Lett. **91**, 247405 (2003)
3. E. Bricchi, B.G. Klappauf, P.G. Kazansky, Form birefringence and negative index change created by femtosecond direct writing in transparent materials. Opt. Lett. **29**, 119–121 (2004)
4. P. Kazansky, H. Inouye, T. Mitsuyu, K. Miura, J. Qiu, K. Hirao, F. Starrost, Anomalous anisotropic light scattering in ge-doped silica glass. Phys. Rev. Lett. **82**, 2199–2202 (1999)
5. L. Sudrie, M. Franco, B. Prade, A. Mysyrowicz, Writing of permanent microlayers in bulk fused silica with femtosecond laser pulses. Opt. Commun. **171**, 279–284 (1999)
6. J. Canning, M. Lancry, K. Cook, A. Weickman, F. Brisset, B. Poumellec, Anatomy of a femtosecond laser processed silica waveguide [Invited]. Opt. Mater. Express **1**, 998 (2011)
7. J. Gottmann, D. Wortmann, M. Hörstmann-Jungemann, Fabrication of sub-wavelength surface ripples and in-volume nanostructures by fs-laser induced selective etching. Appl. Surf. Sci. **255**, 5641–5646 (2009)

8. R. Buividas, L. Rosa, R. Sliupas, T. Kudrius, G. Slekys, V. Datsyuk, S. Juodkazis, Mechanism of fine formation on surfaces of (semi)transparent materials via a half-wavelength cavity feedback. Nanotechnology **22**, 055304 (2011)
9. E. Hasman, Z. Bomzon, A. Niv, G. Biener, Polarization beam-splitters and optical switches based on space-variant computer-generated subwavelength quasi-periodic structures. Opt. Commun. **209**, 45–54 (2002)
10. J.D. Mills, P.G. Kazansky, E. Bricchi, J.J. Baumberg, Embedded anisotropic microreflectors by femtosecond-laser nanomachining. Appl. Phys. Lett. **81**, 196 (2002)
11. W. Cai, A.R. Libertun, R. Piestun, Polarization selective computer-generated holograms realized in glass by femtosecond laser induced. Opt. Express **14**, 3785 (2006)
12. K. Mishchik, G. Cheng, G. Huo, I.M. Burakov, C. Mauclair, A. Mermillod-Blondin, A. Rosenfeld, Y. Ouerdane, A. Boukenter, O. Parriaux, R. Stoian, Nanosize structural modifications with functions in ultrafast laser irradiated bulk fused silica. Opt. Express **18**, 24809 (2010)
13. J.A. Davis, J. Adachi, C.R. Fernández-Pousa, I. Moreno, Polarization beam splitters using diffraction gratings. Opt. Lett. **26**, 587 (2001)
14. Z. Bomzon, V. Kleiner, E. Hasman, Formation of radially and azimuthally polarized light using space-variant subwavelength metal stripe gratings. Appl. Phys. Lett. **79**, 1587 (2001)
15. R. Yamaguchi, T. Nose, S. Sato, Liquid crystal polarizers with axially symmetrical properties. Jpn. J. Appl. Phys. **28**, 1730–1731 (1989)
16. M. Stalder, M. Schadt, Linearly polarized light with axial symmetry generated by liquid-crystal converters. Opt. Lett. **21**, 1948–1950 (1996)
17. D. Mawet, P. Riaud, J. Surdej, J. Baudrand, Subwavelength surface-relief gratings for stellar coronagraphy. Appl. Opt. **44**, 7313 (2005)
18. F. Kenny, D. Lara, O.G. Rodríguez-Herrera, C. Dainty, Complete and phase control for focus-shaping in high-NA microscopy. Opt. Express **20**, 14015 (2012)
19. J.E. Ford, F. Xu, K. Urquhart, Y. Fainman, Polarization-selective computer-generated holograms V-pol input. Opt. Lett. **18**, 456–458 (1993)
20. M. Beresna, P.G. Kazansky, Polarization diffraction grating produced by femtosecond laser nanostructuring in glass. Opt. Lett. **35**, 1662 (2010)
21. P. Zijlstra, J.W.M. Chon, M. Gu, Five-dimensional optical recording mediated by surface plasmons in gold nanorods. Nature **459**, 410 (2009)
22. Y. Shimotsuma, M. Sakakura, P.G. Kazansky, M. Beresna, J. Qiu, K. Miura, K. Hirao, Ultrafast manipulation of self-assembled form birefringence in glass. Adv. Mater. **22**, 4039–4043 (2010)
23. F. Gori, Measuring stokes parameters by means of a grating. Opt. Lett. **24**, 584–586 (1999)
24. G. Cipparrone, A. Mazzulla, S.P. Palto, S.G. Yudin, L.M. Blinov, Permanent gratings in photosensitive Langmuir-Blodgett films. Appl. Phys. Lett. **77**, 2106 (2000)
25. H. Ono, H. Wakabayashi, T. Sasaki, A. Emoto, T. Shioda, N. Kawatsuki, Vector holograms using radially polarized light. Appl. Phys. Lett. **94**, 071114 (2009)
26. G. Cipparrone, P. Pagliusi, C. Provenzano, V.P. Shibaev, Polarization holographic recording in amorphous polymer with photoinduced linear and circular birefringence. J. Phys. Chem. B **114**, 8900 (2010)
27. T. Kampfe, S. Tonchev, G. Gomard, C. Seassal, O. Parriaux, Hydrogenated amorphous silicon microstructuring for 0th-order polarization elements at 1.0–1.1 μm wavelength. IEEE Photonics J. **3**, 1142–1148 (2011)
28. M. Beresna, M. Gecevičius, P.G. Kazansky, Polarization sensitive elements fabricated by femtosecond laser nanostructuring of glass [invited]. Opt. Mater. **1**, 10117–10124 (2011)
29. D.G. Hall, Vector-beam solutions of Maxwell's wave equation. Opt. Lett. **21**, 9 (1996)
30. Q. Zhan, Cylindrical vector beams: from mathematical concepts to applications. Adv. Opt. Photonics **1**, 1–57 (2009)
31. S. Pancharatnam, Generalized theory of interference and its applications. Part II. Partially coherent pencils. Proc. Indian Acad. Sci. **44**, 247–262 (1956)

32. M.V. Berry, Quantal phase factors accompanying adiabatic changes. Proc. R. Soc. A: Math. Phys. Eng. Sci. **392**, 45–57 (1984)
33. M. Beresna, M. Gecevičius, P.G. Kazansky, T. Gertus, Radially polarized converter created by femtosecond laser nanostructuring of glass. Appl. Phys. Lett. **98**, 201101 (2011)
34. E. Walker, P.M. Rentzepis, Two-photon technology: a new dimension. Nat. Photonics **2**, 406–408 (2008)
35. E.N. Glezer, M. Milosavljevic, L. Huang, R.J. Finlay, T.H. Her, J.P. Callan, E. Mazur, Three-dimensional optical storage inside transparent materials. Opt. Lett. **21**, 2023–2025 (1996)
36. W. Yang, E. Bricchi, P.G. Kazansky, J. Bovatsek, A.Y. Arai, Self-assembled periodic sub-wavelength structures by femtosecond laser direct writing. Opt. Express **14**, 10117 (2006)
37. E. Bricchi, P.G. Kazansky, Extraordinary stability of anisotropic femtosecond direct-written structures embedded in silica glass. Appl. Phys. Lett. **88**, 111119 (2006)

Part II
Laser-Induced Nanostructures: Nanostructure Formation in Semiconductors and Dielectrics

Chapter 3
Nanogratings in Fused Silica: Structure, Formation and Applications

Sören Richter, Matthias Heinrich, Felix Zimmermann, Christian Vetter, Andreas Tünnermann and Stefan Nolte

Abstract We investigate the formation of periodic subwavelength structures, so-called nanogratings, in the volume of fused silica. These self-organized structures emerge upon irradiation with ultrashort laser pulses at intermediate intensities. Using Small Angle X-ray scattering and Focused Ion Beam milling we could prove that they consist of hollow cavities, whose arrangement give rise to the overall periodicity. The formation of the grating structure undergoes three distinct stages of growth from initially randomly distributed nanostructures to extended domains with uniform periodicity after several hundreds of laser pulses. The experiments revealed that the cumulative action of subsequent laser pulses is mediated by dangling-bond type defects. On shorter time scales, transient self trapped excitons may significantly enhance the formation process. The periodic subwavelength structure of nanogratings leads to form birefringence, which can be utilized to implement optical functionalities. Wave plates based on nanogratings offer a great deal of flexibility and precision regarding their retardation as well as the orientation of their optical axis.

S. Richter · F. Zimmermann · C. Vetter · A. Tünnermann · S. Nolte (✉)
Institute of Applied Physics, Abbe Center of Photonics, Friedrich-Schiller-Universität Jena, Max-Wien-Platz 1, 07743 Jena, Germany
e-mail: stefan.nolte@uni-jena.de

M. Heinrich
CREOL, The College of Optics and Photonics University of Central Florida, 4000 Central Florida Blvd., Orlando, FL 32816, USA

A. Tünnermann · S. Nolte
Fraunhofer Institute for Applied Optics and Precision Engineering, Albert-Einstein-Straße 7, 07745 Jena, Germany

© Springer International Publishing Switzerland 2015

S. Sakabe et al. (eds.), *Progress in Nonlinear Nano-Optics*, Nano-Optics and Nanophotonics, DOI 10.1007/978-3-319-12217-5_3

3.1 Introduction

The interaction of ultrashort laser pulses with transparent materials has been the subject of intense research in the last decades [1–3]. A particularly versatile platform for the induction of various structural modifications is fused silica. At moderate pulse energies, isotropic changes of the refractive index can be induced [1, 4]. If the laser focus is moved through the sample, three-dimensional complex systems of waveguides can be realized [5, 6]. In contrast, using high pulse energies it is also possible to generate voids with diameters of only a few hundred nanometers through microexplosions [7, 8]. At intermediate pulse energies, Kazansky et al. discovered anisotropic light scattering in Ge-doped silica glass [9]. Birefringent modifications were also observed by Sudrie et al. in the bulk of fused silica [10]. The underlying nature of this peculiar phenomenon was revealed in 2003: Shimotsuma et al.: self-organized periodic subwavelength structures are formed which induce form birefringence [11]. The period of these so-called nanogratings scales with the applied laser wavelength λ, as can be seen in Fig. 3.1. The planes of the nanogratings are always oriented perpendicular to the laser polarization [12, 13].

Although several possible explanations were put forward to explain the formation of nanogratings [11, 14], the actual self-organization mechanism is not yet fully understood. The initial theory was based on the interference of the incident light field with the induced plasma. However, the applied laser energy is insufficient to satisfy the required plasma temperature and density [13]. A more current approach tries to describe the evolution of the periodic structure from randomly distributed spherical nanoplasmas into sheets and eventually into a homogeneous grating [14]. This nanoplasmonic model predicts a grating period of $\lambda/2n$ (with λ the wavelength of the inscription laser and n the refractive index of the material), but cannot explain the observed continuous dependence of the period on the applied pulse number [11, 15, 16].

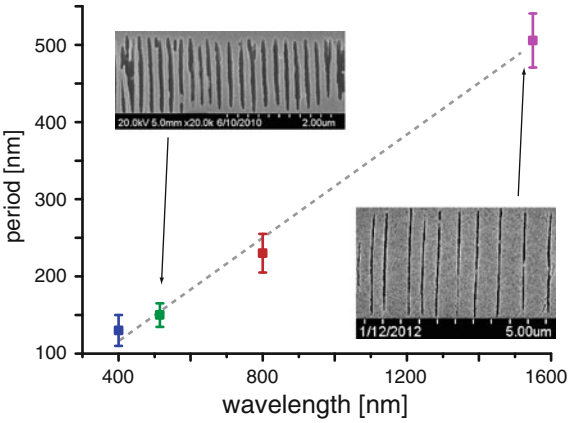

Fig. 3.1 The period of nanogratings is proportional to the wavelength λ of the inscription laser. Exemplary SEM micrographs of nanogratings inscribed at λ = 515 and 1,550 nm are shown as *insets*

3.2 Methodology

3.2.1 Nanograting Inscription

In order to investigate the formation of nanogratings with respect to the processing parameters we used different laser systems. Most of the experiments were performed with a femtosecond laser oscillator (Amplitude Systemes, t-pulse 500) delivering 450 fs pulses at a wavelength of 1,030 nm with a repetition rate of 9.4 MHz and an average output power of 5 W. For the inscription, the pulses were converted to the second harmonic (λ = 515 nm) in an LBO crystal. We used an external acousto-optic modulator (AOM) and a half-wave plate followed by a polarizer, to select the repetition rate and change the pulse energy, respectively. An aspheric lens (f = 4.5 mm) with a numerical aperture of 0.55 served to focus the laser pulses into the sample (see Fig. 3.2).

In addition we employed a regeneratively amplified Ti:Sapphire laser system (RegA, Coherent, Inc.) delivering 150 fs pulses with a repetition rate of R = 100 kHz and an average power of up to 3 W. Both the fundamental wavelength of λ = 800 nm and the second harmonic at 400 nm were used to generate nanogratings. Here, a 20x microscope objective (NA of 0.35) served as the focusing optic. To affirm the general dependence of the grating period on the laser wavelength (see Fig. 3.1), we also realized nanogratings using a wavelength of 1.55 µm (Smart Light 50, Raydiance) at a pulse duration of 800 fs and a repetition rate of 400 kHz.

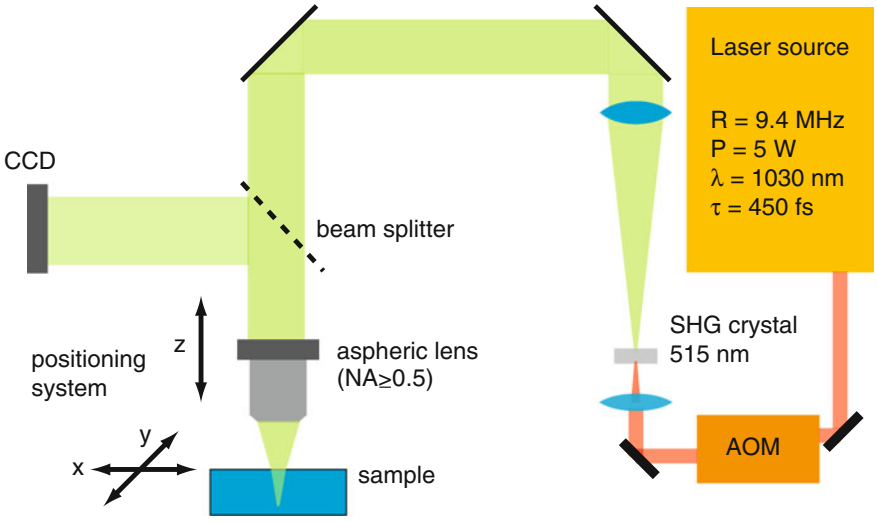

Fig. 3.2 Experimental setup for the inscription of nanogratings. Laser pulses of a femtosecond oscillator are converted to a wavelength of 515 nm. To control the repetition rate an external acousto optic modulator (AOM) was utilized. The beamsplitter and camera (CCD) were used to adjust the focus position in the sample

In all experiments, computer controlled positioning systems (Aerotech ABL1000) were used to translate the sample. The total number of pulses per spot contributing to the formation of nanogratings was adjusted through the translation velocity v and the repetition rate R: $N = R \cdot d/v$, where d is the diameter of the focal spot. For all experiments, we used commercially available high purity fused silica.

3.2.2 Conventional Characterization Techniques

The anisotropic character of the nanogratings is induced by form birefringence due to the different refractive indices (n_1 and n_2) of the grating planes, see Fig. 3.3. Thus, the birefringence is related to the widths w_1 and w_2 of the individual layers and to their refractive index contrast $\delta n \equiv n_2 - n_1$. If the period $\Lambda = w_1 + w_2$ is smaller than the wavelength of the incident light, the structure acts as a homogeneous effective medium [14]. Nanogratings behave similar to an uniaxial negative crystal with its optical axis perpendicular to the grating planes. Consequently the fast axis of this birefringent material is parallel to the optical axis and thus parallel to the polarization of the writing laser beam [17]. In the case of $w_1 \ll w_2$, the overall birefringence $\Delta n \equiv n_o - n_e$ can be approximated as

$$\Delta n \approx \frac{2}{\Lambda}\left(\frac{\delta n^2}{n_2} + \frac{\delta n^3}{n_2^2}\right). \tag{3.1}$$

Several approaches exist for the characterization of nanogratings. The simplest method is polarization contrast microscopy, which allows to measure the form birefringence. The transmission T of a birefringent element between two crossed polarizers, is given by [18]:

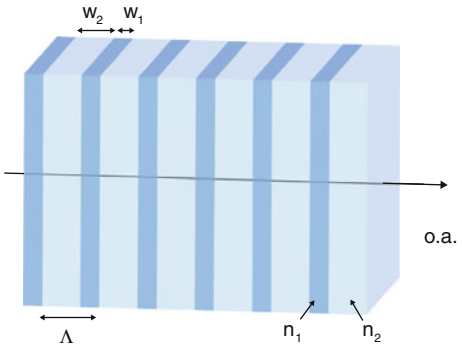

Fig. 3.3 Schematic of the grating structure comprising alternating planes of different refractive indices, which give rise to the form birefringence. The optical axis (o.a.) is perpendicular to the planes [15]

$$T = \frac{1}{2}\sin^2(2\vartheta)[1 - \cos(\delta)] \tag{3.2}$$

where δ is the retardation of the birefringent structure and ϑ is the angle between its optical axis and the transmission axis of the first polarizer. Thus, 3.2 allows simple measurements of the retardation of the birefringent structures. However, additional structural information is required to determine even the grating period from such a measurement.

To resolve structures well below optical wavelengths scanning electron microscopy (SEM) is the method of choice. To allow for the use of this technique, the samples have first to be polished down to reveal the nanogratings. Since ultrashort pulse modified fused silica exhibits an increased etch rate for hydrofluoric acid (HF), this can be utilized to excavate nanogratings and reveal their structure [19, 20]. The resulting structure can be studied with SEM. However, a certain broadening of the nanograting contours inevitably occurs in this invasive type of sample preparation: Although material removal is greatly accelerated in the laser-affected volume the bulk material is slightly etched, too. Consequently, the finest structures with a size of only few nanometers are erased, leaving only the coarse structure of the nanogratings. By cleaving samples containing nanogratings it was shown that the nanograting lamellas indeed exhibit a sub-structure [14, 21], which is destroyed by the polishing and the subsequent etching of the sample.

We used polishing and HF-etching for the characterization of nanogratings with respect to their period. The mean period of the nanogratings was obtained by a discrete Fourier transformation of the SEM images and evaluation of the spatial frequencies of the structures. The Fourier component with the highest amplitude was measured for multiple longitudinal sections. Images with strongly varying periods corresponding to perturbed regions of the gratings were discarded. The measured periods are subject to an error corresponding to one pixel. Due to the limited field of view of the SEM, we chose pixel sizes between 5 and 10 nm to minimize the systematic errors while at the same time ensuring sufficient reproducibility by incorporating a large number of grating periods. For our analysis of the period, we considered the nanostructures formed in the upper region of the focal volume, as these modifications are the most homogeneous structures [15, 16].

An alternative method for the excavation of nanogratings that leaves their fine structures intact is Focused Ion Beam (FIB) milling [22]. Thereby it is possible to selectively remove material with nanometer precision while leaving the surrounding region unaffected [23]. For this approach, we used a commercial FIB milling device (Zeiss Neon 60, current 50 pA, accelerating voltage 30 kV).

3.2.3 Small Angle X-ray Scattering

To reveal the substructure of nanogratings in a contactless, nondestructive manner we investigated the X-ray scattering pattern of nanogratings. Small angle X-ray

scattering (SAXS) is capable to investigate density inhomogeneities down to the nanometer scale [24] and can be applied to embedded structures without any preparation steps.

The distribution of the scattering intensity $I(q)$ represents the Fourier transformation of the local scattering length density contrast profile $\Delta\rho(\vec{r}) = \rho(\vec{r}) - \rho_0$:

$$I(q) \propto N \left| \int_V \Delta\rho(\vec{r}) \exp(iqr) d\vec{r} \right|^2 . \tag{3.3}$$

It is a function of the angle-dependent scattering vector $q = 4\pi \sin(\vartheta)/\lambda$ and invariant to the sign of the density contrast [25]. The so-called generalized description [26, 27] is a formalism that allows the evaluation of scattering patterns arising from broad-range ensembles of particles:

$$I(q) = \sum_i B\left(q_i^*\right)^{-d_{f,i}} + \sum_i N_i \Delta\rho_i^2 V_i^2 \exp\left(-q^2 R_{g,i}^2/3\right). \tag{3.4}$$

The ensemble of multiple particles average smears out the distinct features of single objects, resulting in a simple power-law decay (first term in 3.4, $d_{f,i} = 4$ for compact objects [27]). The second term accounts for the contributions of different size populations following the Guinier approximation [27] with the respective radii of gyration $R_{g,i}$ and number densities N_i, the density contrasts $\Delta\rho_i$ and volumes V_i. A very useful quantity is the shape-independent Porod Invariant, which is proportional to the integrated scattering length contrast:

$$P = \int_0^\infty I(q) q^2 dq = 2\pi^2 \Delta\rho^2 \Phi(1 - \Phi) \tag{3.5}$$

with Φ being the particle filling fraction. For a porous material with a filling fraction $\Phi \ll 1$ the Porod Invariant is proportional to the total pore volume. Consequently P corresponds to the total scattering strength of the modifications within the probed volume.

We performed SAXS experiments at the cSAXS beamline at Swiss Light Source (Villigen, CH). The principle setup is shown in Fig. 3.4b. At first, we inscribed a 3 × 3 mm pattern of nanogratings (3,000 lines with a distance of 1 μm) into the fused silica sample. One single line is shown in Fig. 3.4a. The probe beam (photon energy 13.6 keV, beam dimensions $6 \times 23\,\mu m^2$ at the target) is scattered at the sample and the pattern is recorded by a large direct converting pixel detector (Pilatus 2M, Dectris). The typical intensity distribution shows a pronounced anisotropy along the direction of the grating planes [22], see scattering pattern in Fig. 3.4b. Standard image corrections were applied before the intensity was integrated to obtain $I(q)$ along the main axes x and z of the scattering pattern [28, 29].

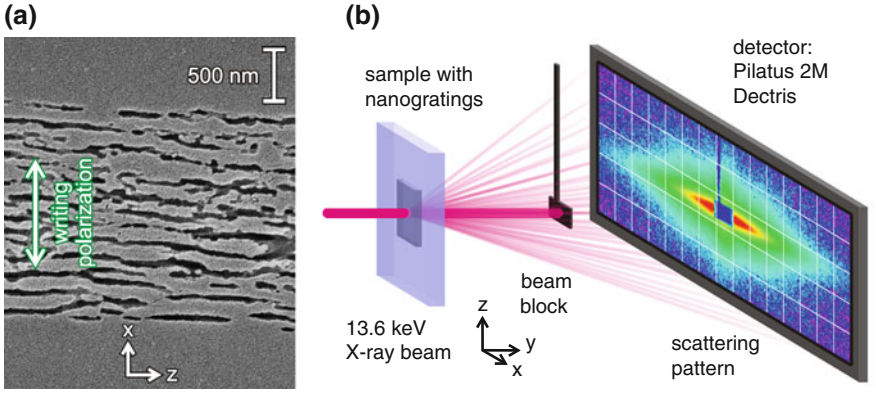

Fig. 3.4 **a** SEM micrograph of nanogratings revealed by etching with hydrofluoric acid. **b** Schematic of the SAXS measurement. The nanograting sample is placed in the *beam line*. The orientation of the nanogratings accords the SEM micrograph. The grating is lying in the *x*-*z* plane. After blocking the main beam, the scattering pattern is recorded on a direct converting pixel detector [22]

3.3 Experimental Results

3.3.1 Fundamental Structure of Nanogratings

With Small Angle X-ray scattering we could determine the we could determine the structure size of the fundamental pattern giving rise to the nanogratings. The observed scattering distributions are strongly anisotropic, which means different structural dimensions along x and z axis (compare Fig. 3.4). The polarization of the writing laser was parallel to the x-axis, the resulting grating can be seen in the SEM image of Fig. 3.4a.

Along the x-axis (Fig. 3.5a) two distinct populations with different diameters $D = 2\sqrt{5/3}\,R_g$ exist. Those two diameters, $D_1 = 6\,\text{nm}$ and $D_2 = 28\,\text{nm}$ respectively, are roughly independent of the number of applied laser pulses, see Fig. 3.5a. In addition, we could not observe any pulse energy dependence. This indicates that no significant growth takes place parallel to the laser polarization after the structures have formed. We analyzed the aspect ratio of the scattering pattern to obtain information of the structure size along the z direction. A direct evaluation of the scattering pattern along the z axis is hindered by the large beam stop, which blocks the low scattering vectors. Along the z direction (which is perpendicular to the laser polarization) we found significant changes only during the first ≈100 laser pulses [22]. Within the first 100 pulses the structure size along z direction increases with the number of applied laser pulses and eventually an aspect ratio between the structure size along x and z axis of ≈7 is reached. Figure 3.5b shows the evolution of the Porod Invariant P, which yields information on the overall pore volume. The Porod Invariant increases for the first ≈750 laser pulses. On the contrary, the

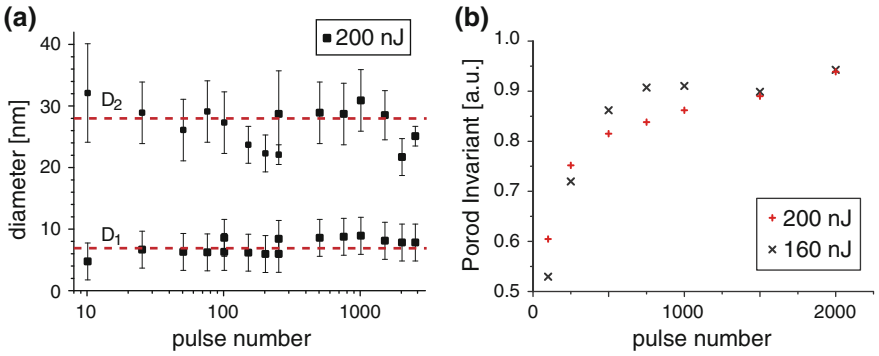

Fig. 3.5 Results of the SAXS measurements. **a** Along the *x* axis, two distinct size populations with respective diameters nearly independent on the laser exposure parameters have been observed. **b** The increase of the Porod Invariant takes longer to saturate, signifying a growing overall pore volume during the first ≈1,000 pulses

transversal growth of the individual structures ceases after ≈100 pulses. Thus, any further change in P has to result from either an increase in the number of pores or a longitudinal growth (along y axis) of the existing structures. We suppose that a growing number of pores is responsible for the increase in P, as this behavior corresponds well to the observed decrease of the grating period during prolonged laser exposure [15].

Our SAXS measurements have shown that nanogratings consist of pores with characteristic dimensions of 6 and 28 nm along x and about 200 nm along z. However, the actual material composition of the structures remains unknown.

Therefore, in addition to the SAXS measurements, we used FIB milling to dissect (slice thickness of 12.5 nm) a volume of $5 \times 10 \times 1\,\mu m^3$ of nanogratings fabricated with 500 pulses per spot. The laser writing polarization was perpendicular to the sample translation. An exemplary SEM image is shown in Fig. 3.6a. The single dark spots are hollow cavities, which exhibit a width of about 30 nm along the x direction, which fits to the diameter D_2 predicted by the SAXS data in Fig. 3.5a. However, we could not observe any smaller hollow features, which would match to the D_1 population. These SAXS signatures most likely correspond to density modulations around the pores or within the pristine glass.

In a next step we constructed a three-dimensional model of the pores within the dissected volume, by analyzing all SEM micrographs. Figure 3.6b shows a projection of all data on the x–y-plane. The nanograting period of 150 nm can clearly be seen. These grating planes are partially filled with individual pores [22]. The transverse dimensions (z direction) of the pores are significantly larger than their thickness, in agreement to the SAXS results. To summarize the characteristic feature dimensions we created a schematic sketch, see Fig. 3.6c. The pores have a thickness of ≈30 nm and exhibit similar sizes along y (≈300 nm) and z (≈200 nm) with a slight elongation along the direction of the writing beam. The sheet like arrangement of the pores forms the well known periodicity, here with a period of 150 nm.

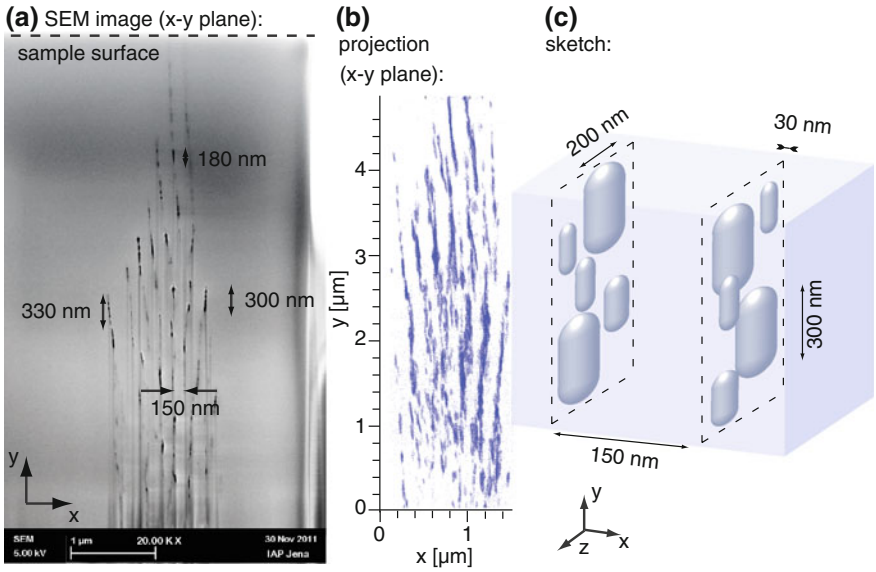

Fig. 3.6 Three-dimensional structure of nanogratings. **a** Representative SEM micrograph of a FIB slice in the *x-y* plane. Despite the lack of etching, hollow structures exist within the surrounding material. **b** Projection of the 3D pore configuration within the dissected volume onto the *x-y* plane. The grating planes consist of isolated sheet-like pores. Note that the structures have not been etched by HF. **c** Schematic sketch illustrating the characteristic feature dimensions

3.3.2 Processing Parameter Window for Nanograting Formation

As the formation mechanism of nanogratings is still not fully understood, it is important to clarify at first the required processing parameters to form nanogratings in fused silica. A fundamental processing parameter for the efficient generation of nanogratings is the laser repetition rate, since it allows the direct scaling of the accessible processing velocity. Thus, we investigated the nanograting formation in fused silica for repetition rates from 50 kHz to 9.4 MHz with different pulse energies. To this end, we used a femtosecond oscillator (Amplitude t-pulse 500) at a wavelength of 515 nm and pulse duration of 450 fs. We repeated the inscription process for different translation velocities between 1 and 1,000 mm/min for every parameter set to determine the parameters at which stable nanogratings are formed. It can be seen in Fig. 3.7 that the formation of nanogratings occurs within a well-defined range of processing parameters (yellow area). Below the absorption

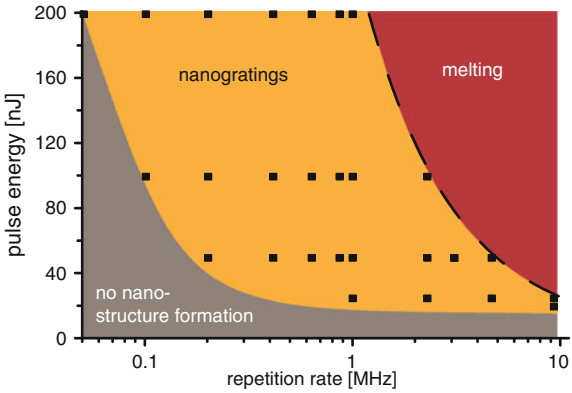

Fig. 3.7 The type of material modification within fused silica is mainly determined by pulse energy and repetition rate. The formation of nanogratings was only observed at intermediate laser powers (*yellow shaded area*). The *dashed line* exhibits the limit of average power (230 mW) where melting starts to occur. For inscription a wavelength of 515 nm and pulse duration of 450 fs was used

threshold no modification was observed (gray shaded area in Fig. 3.7). Due to incubation and cumulative effects, the minimal pulse energy to obtain nanogratings also depends on the repetition rate. With increasing pulse energy, the formation of birefringent modifications was observed. When using high laser powers (e.g. pulse energy above 100 nJ and several MHz repetition rate), heat accumulation of subsequent laser pulses and the accompanied melting of the material occurs [30]. Within this parameter range no nanogratings could be found. Therefore, melting due to heat accumulation poses an upper limit on the average power deposited into the material. Consequently, the maximum usable repetition rate is inversely proportional to the pulse energy (see dashed graph in Fig. 3.7). The maximum average power for the formation of nanogratings in these experiments is thus limited to 230 mW (translation velocity between 10 and 100 mm/min). As the upper limit for the nanograting formation is given by the applied average power for melting of the material, the pulse energy parameter window gradually narrows towards high repetition rates. Nevertheless, nanograting formation was observed up to the maximum available repetition rate of the laser system of 9.4 MHz, which allows the efficient and rapid inscription of nanogratings at high translation velocities.

3.3.3 Evolutional Stages of Nanograting Growth

In order to understand the self organizing process of the formation of nanogratings within fused silica, the regularity and separation of the induced nanostructures with respect to the number of applied laser pulses were investigated. Figure 3.8 shows

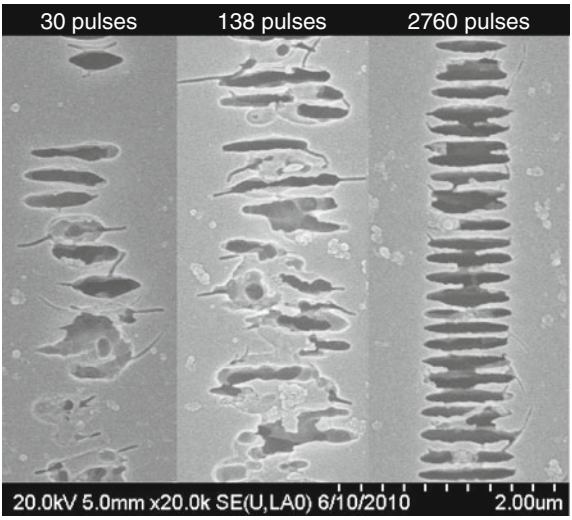

Fig. 3.8 The growth of the nanostructures is dependent on the number of pulses irradiating the sample. The different evolutional stages of the nanograting formation from disordered nanostructures to periodic nanogratings can be seen. We used a laser wavelength of 515 nm, pulse duration of 450 fs and pulse energy of 50 nJ

different nanostructures obtained while changing the translation velocity (from 1 to 200 mm/min) for fixed repetition rate (2.3 MHz) and pulse energy (50 nJ) at a wavelength of 515 nm. The different translation velocities result in different numbers of pulses N irradiating the same spot of the sample. We assumed a spot diameter of one micron, in agreement with the calculated value from the focussing conditions as well as the width of the nanostructures observed with the SEM (compare Fig. 3.8).

The measurements show distinct stages in the evolution of nanograting formation. During the first tens of pulses, the induced nanostructures are already oriented perpendicular to the writing polarization but still contain a high fraction of non-modified regions in the trace of the focus. These structures exhibit no visible periodicity and their size is irregular. In the following, we will designate this regime of isolated nanomodifications as stage I of the growth process. With increasing number of incident pulses periodic structures emerge. During stage II, the vacancies between the isolated nanomodifications start to vanish. Consequently, by selecting specific domains, it becomes possible to measure a grating period. During stage III, starting at several hundred pulses, isolated domains have linked up and a continuous decrease of the grating period with the number of pulses applied can be observed. Comparative measurements with inversely varying repetition rate and writing velocity confirm that not one of these parameters alone is the determining factor for the grating period, but rather the total number of pulses applied. These three stages of nanograting formation occur throughout a wide range of pulse energies; however, the specific number of pulses required to reach the next stage

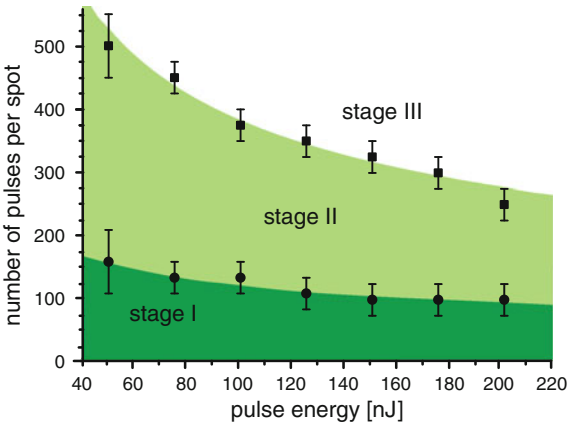

Fig. 3.9 Number of pulses required to reach each stage of the nanograting formation as a function of the pulse energy. The stages are separated by *trend lines*

decreases notably with increasing pulse energy (see Fig. 3.9). This can easily be explained by an increased number of excited electrons at higher pulse energies: due to the increased electron density the induced structural change is enhanced. As discussed in Sect. 3.3.4, defect generation plays an important role in the formation of nanogratings. At larger pulse energies more defects are generated and consequently the formation process of nanogratings is enhanced. Therefore, stage III is reached at lower pulse numbers for higher pulse energies.

Interestingly, the period of a nanograting depends also mainly on the incident number of pulses. In order to demonstrate this, the period was measured for different repetition rates and translation velocities (fixed irradiation wavelength of 515 nm), see Fig. 3.10. A significant change in the period with the number of pulses can be observed. The lower limit of pulse number is given by the onset of regular

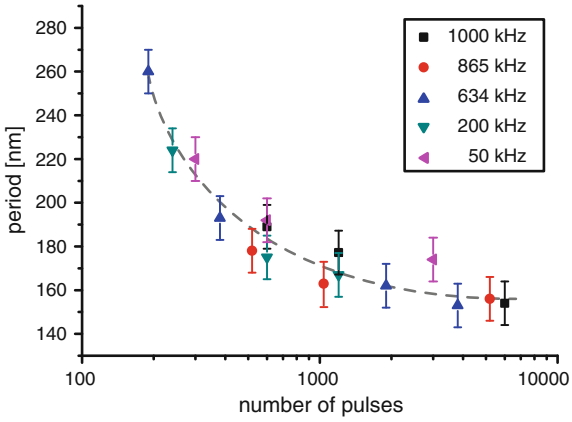

Fig. 3.10 Dependence of the nanograting period in fused silica on the number of laser pulses incident per spot. Laser wavelength was 515 nm, pulse duration was 450 fs and pulse energy was 200 nJ. The *dashed line* is a *trend line* of all data points

grating formation within selected regions at the end of stage II. Here, the grating period starts at about 260 nm and decreases continuously with increasing number of pulses, which is in agreement with previous results [11, 15]. After approximately 3,000 pulses the period saturates at a minimal value of about 150 nm. This is significantly smaller than the prediction based on the nanoplasmonic model [14], which yields a period of $\lambda/(2n)$ = 176 nm for 515 nm and n = 1.46 (refractive index of bulk fused silica). In order to accommodate a period of 150 nm, a refractive index of 1.7 would be required.

3.3.4 Cumulative Action of Laser Pulses

As discussed in Sect. 3.3.3 numerous pulses are required for the formation of nanogratings. However, it is still unknown how individual pulses with µs to ms temporal separation can contribute to the formation of nanogratings. The laser induced plasma clearly cannot be responsible for the coupling of the individual pulses, as the electronic recombination time inside the glass is only about 150 fs [31, 32]. To investigate the influence of the temporal pulse separation on nanograting formation over almost ten orders of magnitude (between 500 fs and several ms) two experiments were designed [33]. The first experiment examined pulse separations between 500 fs and 1 ns, with a Mach-Zehnder interferometer geometry to generate symmetric double pulses with a defined pulse delay τ. Here, a regeneratively amplified Ti:sapphire laser system (150 fs, 800 nm, 100 kHz) was used. For the fabrication of the nanogratings we used a translation velocity of 12 mm/min. To characterize the induced modification quantitatively polarization contrast microscopy was used. The polarization contrast intensity (*PCI*, transmission trough sample between two crossed polarizers) is roughly proportional to the retardation δ for values of $\delta \lesssim \pi/4$: $PCI \backsim \sin\delta$ [15]. Afterwards the modifications were polished, etched and imaged with a SEM to reveal the nanograting structure.

Figure 3.11 shows the dependence of PCI on the temporal separation τ of the double pulses for different pulse energies. The stated pulse energies refer to the energy of one pulse within the double pulse train. Generally, the PCI is increased for higher pulse energies. We observed an enhanced PCI for pulse separations shorter than 200 ps and about 20 ps for pulse energy of 560 and 132 nJ, respectively. After these delay time the PCI decreases significantly. The inset of Fig. 3.11 shows SEM pictures according to the marked points within the graph. Using 132 nJ pulses, a homogeneous formed nanograting (stage 3) can only be found for a pulse separation of 0.5 ps, while with increasing delay time (e.g. 1,024 ps) the nanostructure obtained exhibits a large number of defects and an increasing grating period, indicating that the formation process is still in its early stages.

The observed dependence on the pulse separation may be explained by the formation of Self Trapped Excitons (STEs) and their respective decay into point defects within several 100 ps [33]. After the nonlinear absorption of the femtosecond laser pulse, excitons are formed [34]. An exciton can be trapped by its own

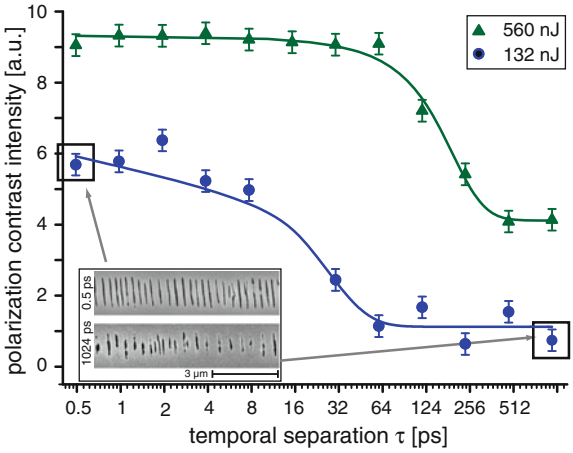

Fig. 3.11 Decrease of the polarization contrast intensity (PCI) with increasing temporal separation τ for a double pulse experiment with pulse separation between 500 fs and 1 ns. The *solid lines* serve as guide to the eye. The inserted SEM images correspond to the marked data points

distortion field at a lattice site initially free of defects [35], leading to a so-called self trapped exciton (STE). The STEs relax to permanent defects like E'-centers and non-bridging oxygen hole centers (NBOHCs) [31, 36, 37]. The decay time for this relaxation was deduced by Wortmann et al. to about 400 ps [34]. This decay time fits to the measured curve using a pulse energy of 560 nJ. For pulse separations shorter than the decay time the presence of STEs increases the absorptivity of the modified material. Thus, the absorption of the following laser pulse is increased and consequently more energy is coupled into the material, enhancing the formation of nanogratings and leading to a more pronounced PCI signal. If the pulse separation exceeds the lifetime of the STEs, this mechanism ceases as confirmed by the polarization contrast measurements (Fig. 3.11). The generally reduced PCI for lower pulse energies is explained by the energy dependent formation of STEs reported in [38]. The different decay times with respect to the pulse energies can be attributed to a different amount of induced STEs and thus varying STE decay machanisms after the irradiation with low intense laser pulses [39].

However, the investigated temporal pulse separations are significantly shorter than typical pulse separations for nanograting inscription (e.g. a repetition rate of 100 kHz corresponds to a delay time of 10 µs [14]). To investigate the pulse separation influence on a longer timescale we sampled down a frequency-doubled oscillator (Amplitude t-pulse 500) with an external acousto optical modulator. Thus, we obtained repetition rates in the kHz range, resulting in temporal pulse separations in the µs range. Generally, we observed for increasing pulse separations a decreasing PCI [33]. This implies, that the formation of nanogratings is slowed down for longer pulse separations and more pulses are required to form a

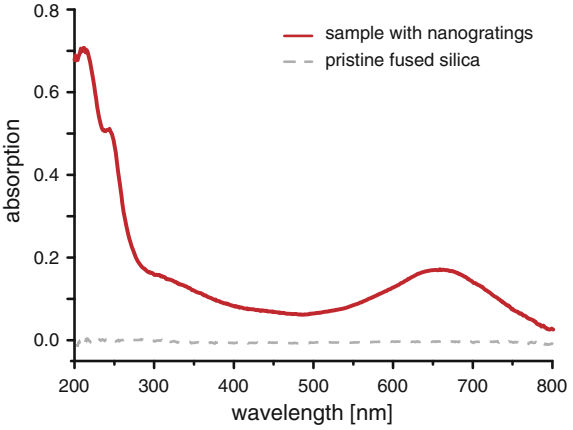

Fig. 3.12 Absorption spectra of nanogratings. The peaks originate from E'centers (212 nm) and NBOHCs (244 and 652 nm). As reference pristine fused silica is shown (*dashed line*)

homogeneous grating. Nevertheless, we observed birefringent modifications even with repetition rates as low as 0.1 Hz (τ = 10 s).

The generation of nanogratings using multiple pulses with pulse separations in the µs range or above has to be mediated by (semi)-permanent defects. Such defects arise after the irradiation with intensive laser pulses as a result of the decaying STEs [17, 40, 41]. The very important group of the dangling bond type defects (Non-bridging oxygen hole centers (NBOHCs) and E'centers) exhibit different absorption bands, which can be observed even in the absorption spectra of nanogratings [33], see Fig. 3.12. The bands at 244 and 652 nm are characteristic for NBOHCs, whereas the peak at 212 nm can be attributed to the presence of E'-centers [42]. These defects are responsible for an altered network structure, as they reduce the valence of the SiO_2 ring structure. This leads to a decrease of the average bond angle and a densification of the material [43]. Pristine fused silica shows no significant absorption peaks in the spectral range investigated. The measured dependence of the PCI on the pulse separation can be explained by the temporal decay of the laser induced defects, due to the interconversion of the defects and their recombination in the material [42, 44, 45].

3.4 Applications

3.4.1 Retardation Control

The great advantage of nanogratings is their precisely tunable birefringence, which opens the possibility to realize intricate phase elements for polarization control [46]. To this end, we conducted a detailed study to investigate the influence of the processing parameters as line separation or pulse energy [15]. Here, we worked with a Ti:sapphire laser system (RegA, Coherent Inc.) delivering 150 fs pulses with

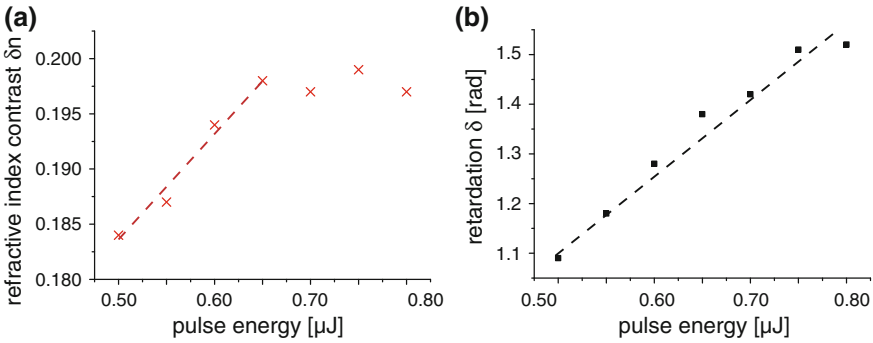

Fig. 3.13 Dependence of the **a** refractive index contrast and **b** retardation of the nanograting waveplates for different pulse energies. The NA of the focusing objective was 0.35. Repetition rate was 100 kHz and pulse duration 150 fs. The line separation was 0.5 μm

a repetition rate of 100 kHz at a wavelength of 800 nm. For focusing a microscope objective with NA of 0.35 was used. We inscribed macroscopic quasiuniform layers (line separation ≤0.5 μm to avoid diffraction) of nanogratings with a dimension of 2×2 mm^2. Subsequently, we measured the transmission of the birefringent devices in a polarization contrast setup at a wavelength of 633 nm and determined the period of the nanogratings via HF-etching and electron microscopy. Using (3.2) we determined the retardation δ of the induced structures. Yang [18] showed, that the retardation of a birefringent material mainly depends on the birefringence $\Delta n = n_o - n_e$ and the thickness d of the birefringent region: $\delta = \Delta n \cdot k \cdot d$, where $k = 2\pi/\lambda$ (λ is the probing wavelength). The birefringence is connected with the refractive index contrast $\delta n = n_2 - n_1$ by (3.1). The maximal index contrast is given by the difference between the refractive index of the bulk material and the refractive index of the low density grating planes, which consist of the nanocavities as reported in Sect. 3.3.1. We could prove, that an increasing overlap of adjacent lines primarily influences the birefringence through an enhancement of the local index contrast between the grating planes [15]. The most convenient parameter to adjust the retardation of nanogratings is the pulse energy, as can be seen in Fig. 3.13. Here, the influence of self-focusing (P_{th} = 4.3 MW in fused silica [47] for a wavelength of 800 nm, corresponding to 0.65 μJ for 150 fs pulses) becomes important. Below 0.65 μJ, the index contrast (and also birefringence) scales linearly with the pulse energy, whereas at larger energies Δn remains largely constant. However, the retardation scales linearly with the pulse energy throughout the whole investigated range (see Fig. 3.13b). This suggests, that the increase of the retardation is induced by an elongation of the modified volume, due to the self-focusing. The measured maximal index contrast is about 0.2. However, the two-layer model (Fig. 3.3) assumes a constant refractive index n_1 in the low density planes. In contrast, the FIB measurement have shown that the low-density planes consist of hollow cavities embedded in the bulk material (see Fig. 3.6). Thus, the measured index contrast of 0.2 corresponds to an average quantity and is a reasonable value.

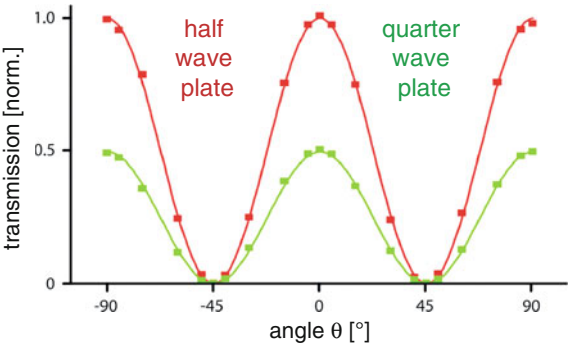

Fig. 3.14 Normalized angle-dependent transmission through crossed polarizers for a quarter-wave plate and half-wave plate

An upper limit of the usable pulse energy is imposed by the formation of microvoids and cracks, the presence of which tends to dramatically increase the scattering losses.

3.4.2 Wave Plates

We fabricated wave plates with a pulse energy of 0.47 μJ, writing velocity of 48 mm/min and a line separation of 0.5 μm (wavelength 800 nm, repetition rate 100 kHz, pulse duration 150 fs) [15]. At those parameters, a single layer yielded scattering losses of approximately 10 % and a retardation of $\pi/4$ (probe wavelength of 633 nm). In a next step, multiple layers were combined to achieve the retardations required for quarter- and half-wave plates, see Fig. 3.14. The measured transmission through crossed polarizers are in very good agreement with the theoretical behavior (continuous lines). These wave plates illustrate the high degree of precision attainable in retardation control by using nanogratings.

3.4.3 Generation of Cylindric Vector Beams

In addition to wave plates with a fixed optical axis, nanogratings can also be used to realize polarization converters, which transform incident linear or circular polarized light into radially or azimuthally polarized light. These so-called cylindric vector beams exhibit polarization symmetry to the optical axis and have a helical phase front which results in a phase singularity or optical vortex on the axis. Thus, destructively interfering field components cause a central dark spot. It was shown by Bozom et al., that sub-wavelength structures can be utilized to transform circular polarized light into radial or azimuthal polarized light [48]. Consequently a special arrangement of nanogratings can be used to generate cylindrical-vector beams, too [49, 50]. An incident circular-polarized beam can be transformed into a radial or

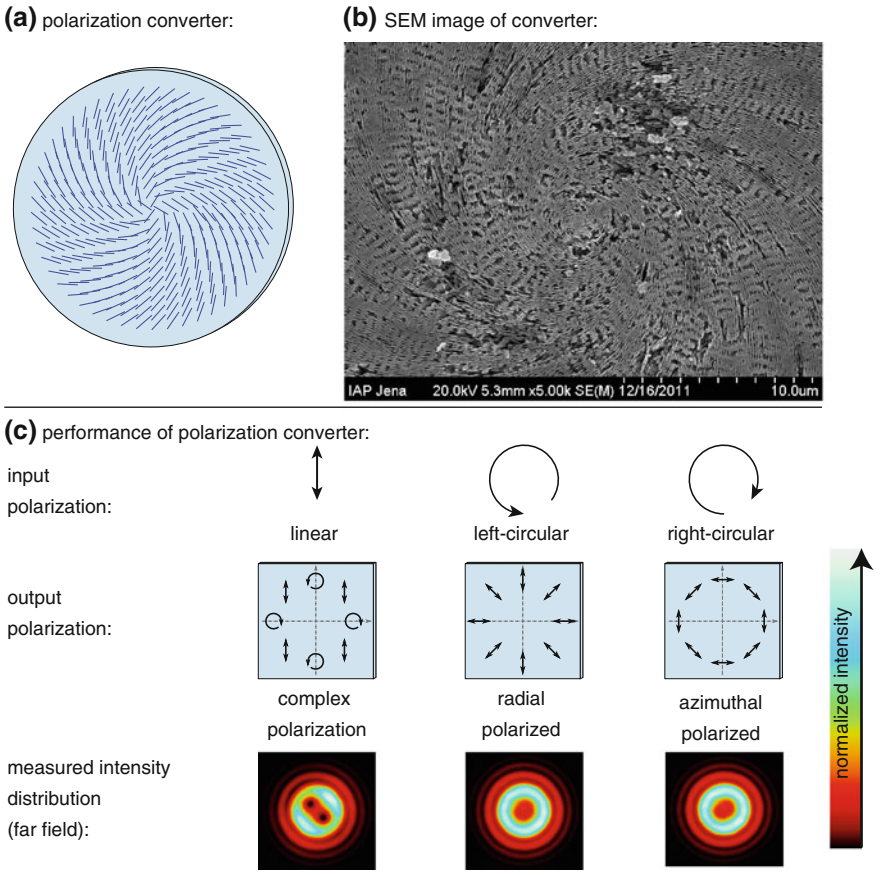

Fig. 3.15 **a** Sketch of the polarization converter, **b** SEM image of inscribed nanogratings after HF etching, **c** performance of the polarization converter for different input polarizations. The intensity distribution was measured without an additional analyzer

azimuthal polarized beam by a special quarter wave plate with a screw-shaped alignment of nanogratings, see Fig. 3.15a. To inscribe these structures with high precision we mounted a rotation stage on the positioning system such that the initial focal position coincided with the rotation axis. While rotating the sample, the focal spot was moved outwards while maintaining the track speed. The result is a spiral grating structure with uniform grating pitch, as shown in an SEM image of the HF-etched central region (Fig. 3.15b). For the fabrication we used a wavelength of 515 nm, repetition rate of 1 MHz, 170 nJ pulse energy, a line separation of 0.2 µm and 100 mm/min tangential translation velocity in combination with an aspheric lens with NA of 0.55.

Figure 3.15c shows the performance of the polarization converter for different input polarizations. For incident linear polarization the polarization state of the output beam depends on the position and the far-field intensity distribution exhibits

two maxima. Circular polarized light is transformed into a cylindric vector beam with a central singularity and a circular intensity maximum. As no polarizer was placed behind the polarization converter, left-circular and right-circular incident polarization yield the same intensity distribution. The difference between these two vector beams can seen in their polarization orientation: incident left-circular light is transformed into a radial polarized vector beam, whereas right-circular light is transformed into an azimuthal polarized vector beam. This difference can be made visible in the far field using a polarizer, resulting in a typical "s" pattern of the intensity distribution [49].

3.4.4 Polarization-Coded Wave Plates

The observation of fast processes remains a problem in modern biology. Confocal microscopy, which may achieve the necessary resolution, is limited in its acquisition rate due to the required scanning procedure. Wicker and Heintzmann proposed a homogeneous but polarization-coded structured illumination, which allows for a single-shot acquisition of images at resolutions rivaling those achieved by confocal microscopy [51]. To this end, a polarization-coded wave plate can be used. The wave plate changes the polarization state from circular to linear with a locally changing orientation, depending on the local orientation of the optical axis of the wave plate. The reflected light of the sample is analyzed with respect to the polarization state. To realize wave plates with the required continuously varying orientation of birefringence, we used the same laser parameters as described in Sect. 3.4.3. As a result, the pitch angle of the nanogratings changes linearly with the position on the waveplate, as can be seen in Fig. 3.16. A very smooth orientation of

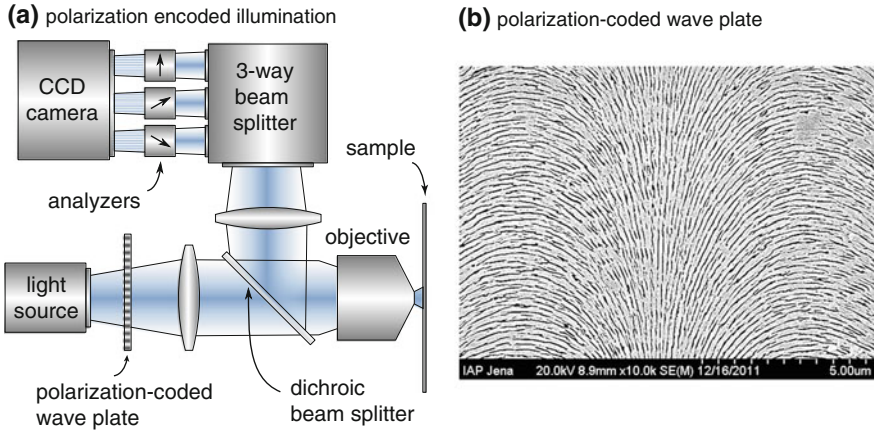

Fig. 3.16 **a** Sketch of polarization encoded illumination [51], **b** SEM image of inscribed nanogratings. The orientation of the writing polarization has been changed by 4° per line

the nanogratings can be observed, although the angle of the writing polarization was changed by four degrees per line. This indicates, that grating elements within the overlap area will already be reorientated by the ensuing line. Thus, nanogratings are perfectly suited to inscribe arbitrary grating geometries.

3.5 Summary

Using Small Angle X-ray Scattering and Focused Ion Beam milling we were able to show that nanogratings consist of periodically arranged cavities with characteristic dimensions of $30 \times 200 \times 300$ nm^3. The three-dimensional arrangement of these cavities give rise to the well known periodicity of nanogratings. We extended the viable parameter window for the inscription of nanogratings to repetition rates of about 10 MHz, thereby enabling the rapid fabrication of birefringent components based on nanogratings. Our experiments revealed that the formation of nanogratings occurs in three distinct stages. With increasing number of incident laser pulses, the structures evolve from isolated nanostructures in stage I to homogenous nanogratings in stage III. Continued exposure to laser pulses then leads to a continuous decrease of the grating period, which eventually saturates after about 3,000 laser pulses. We identified different coupling mechanisms mediating the cumulative action of laser pulses during the formation of nanogratings. Directly after the absorption of the laser pulse, the presence of self trapped excitons (STEs) may significantly enhance the formation of nanogratings. These STEs decay within several hundreds of picoseconds. For longer pulse separations, the coupling mechanism is provided by (semi-)permanent dangling bond type defects, such as E'-centers and nonbridging oxygen hole centers as confirmed by spectroscopic measurements. We demonstrated the high degree of control over the birefringent structures. By varying the retardation we realized embedded quarter and half-wave plates. Finally, we utilized nanogratings to fabricate polarization converters to generate radial and azimuthal vector beams as well as polarization-coded wave plates for structured illumination in microscopy.

Acknowledgments The authors gratefully acknowledge financial support by Deutsche Forschungsgemeinschaft (priority programme 1327). Sören Richter was supported by the Hans L. Merkle Stiftung. Matthias Heinrich was supported by the German National Academy of Sciences Leopoldina (Grant No. LPDS 2012-01). We thank Dr. Anton Plech from the Institute for Synchrotron Radiation, Karlsruhe Institute of Technology for the support by the SAXS measurements and analysis. We acknowledge Rainer Heintzmann from the Institute of Physical Chemistry, Friedrich-Schiller-Universität Jena, for his suggestions on the polarization coded microscopy.

References

1. K. Itoh, W. Watanabe, S. Nolte, C. Schaffer, Ultrafast processes for bulk modification of transparent materials. MRS Bull. **31**, 620 (2006)
2. M. Ams, G.D. Marshall, P. Dekker, M. Dubov, V.K. Mezentsev, I. Bennion, M.J. Withford, Investigation of ultrafast laser-photonic material interactions: challenges for directly written glass photonics. IEEE J. Quantum Elect. **14**, 1370 (2008)
3. R.R. Gattas, E. Mazur, Femtosecond laser micromachining in transparent materials. Nat. Photonics **2**, 219–225 (2008)
4. K.M. Davis, K. Miura, N. Sugimoto, K. Hirao, Writing waveguides in glass with a femtosecond laser. Opt. Lett. **21**, 1279–1731 (1996)
5. A. Szameit, S. Nolte, Discrete optics in femtosecond laser-written photonic structures. J. Phys. B. **43**, 163001 (2010)
6. M. Heinrich, R. Keil, F. Dreisow, A. Tünnermann, A. Szameit, S. Nolte, Nonlinear discrete optics in femtosecond laser-written photonic lattices. Appl. Phys. B. **104**, 469–480 (2011)
7. E.N. Glezer, M. Milosavljevic, L. Huang, R.J. Finlay, T.-H. Her, J.P. Callan, E. Mazur, Three-dimensional optical storage inside transparent materials. Opt. Lett. **21**, 2023–2025 (1996)
8. S. Juodkazis, S. Matsuo, H. Misawa, V. Mizeikis, A. Marcinkevicius, H.B. Sun, Y. Tokuda, M. Takahashi, T. Yoko, J. Nishii, Application of femtosecond laser pulses for microfabrication of transparent media. Appl. Surf. Sci. **197**, 705–709 (2002)
9. P.G. Kazansky, H. Inouye, T. Mitsuyu, K. Miura, J. Qio, K. Hirao, Anomalous anisotropic light scattering in ge-doped silica glass. Phys. Rev. Lett. **82**, 2199–2202 (1999)
10. L. Sudrie, A. Mysyrewicz, M. Franco, B. Prade, Writing of permanent birefringent microlayers in bulk fused silica with femtosecond laser pulses. Opt. Commun. **171**, 279–284 (1999)
11. Y. Shimotsuma, P.G. Kazansky, J. Qiu, K. Hirao, Self-organized nanogratings in glass irradiated by ultrashort light pulses. Phys. Rev. Lett. **91**, 2474051–2474054 (2003)
12. J.D. Mills, P.G. Kazansky, E. Bricchi, J.J. Baumberg, Embedded anisotropic microreflectors by femtosecond-laser nanomachining. Appl. Phys. Lett. **81**, 196–198 (2002)
13. V.R. Bhardwaj, E. Simova, P.P. Rajeev, C. Hnatovsky, R.S. Taylor, D.M. Rayner, P.B. Corkum, Optically produced arrays of planar nanostructures inside fused silica. Phys. Rev. Lett. **96**, 057404 (2006)
14. R. Taylor, C. Hnatovsky, E. Simova, Applications of femtosecond laser induced self-organized planar nanocracks inside fused silica. Laser Photon. Rev. **2**, 26–46 (2008)
15. L.P.R. Ramirez, M. Heinrich, S. Richter, F. Dreisow, R. Keil, A.V. Korovin, U. Peschel, S. Nolte, A. Tünnermann, Tuning the structural properties of femtosecond-laser-induced nanogratings. Appl. Phys. A Mater. Sci. Process. **100**, 1–6 (2010)
16. S. Richter, M. Heinrich, S. Doering, A. Tünnermann, S. Nolte, Formation of femtosecond laser-induced nanogratings at high repetition rates. Appl. Phys. A Mater. Sci. Process. **104**, 503–507 (2011)
17. Y. Shimotsuma, M. Sakakura, P.G. Kazansky, M. Beresna, J. Qiu, K. Miura, K. Hirao, Ultrafast manipulation of self-assembled form birefringence in glass. Adv. Mater. **22**(36), 4039–4043 (2010)
18. P. Yang, Femtosecond laser-pulse-induced birefringence in optically isotropic glass. J. Appl. Phys. **95**, 5280–5283 (2004)
19. C. Hnatovsky, R.S. Taylor, E. Simova, V.R. Bhardwaj, D.M. Rayner, P.B. Corkum, Polarization-selective etching in femtosecond laser-assisted microfluidic channel fabrication in fused silica. Opt Lett **30**(14), 1867–1869 (2005)
20. C. Hnatovsky, R.S. Taylor, E. Simova, P.P. Rajeev, D.M. Rayner, V.R. Bhardwaj, P.B. Corkum, Fabrication of microchannels in glass using focused femtosecond laser radiation and selective chemical etching. Appl. Phys. A **84**, 47 (2006)

21. M. Lancry, B. Poumellec, K. Cook, J. Canning, Nanogratings and molecular oxygen formation during femtosecond laser irradiation in silica. in *IQEC/CLEO Pacific Rim*, 2011
22. S. Richter, A. Plech, M. Steinert, M. Heinrich, S. Döring, F. Zimmermann, U. Peschel, E.B. Kley, A. Tünnermann, S. Nolte, On the fundamental structure of femtosecond laser-induced nanogratings. Laser Photon. Rev. **6**, 787–792 (2012)
23. R.A.D. Mackenzie, G.D.W. Smith, Focused ion beam technology: a bibliography. Nanotechnology **1**, 163 (1990)
24. A. Guinier, G. Fournet, *Small-Angle Scattering of X-rays* (Wiley, New York, 1955)
25. A. Plech, P. Leiderer, J. Boneberg, Femtosecond laser near field ablation. Laser Photon. Rev. **3**, 435 (2009)
26. M. Sztucki, T. Narayanan, G. Beaucage, In situ study of aggregation of soot particles in an acetylene flame by small-angle X-ray scattering. J. Appl. Phys. **101**, 114304 (2007)
27. G. Beaucage, Approximations leading to a unified exponential/power-law approach to small-angle scattering. J. Appl. Crystallogr. **28**, 717 (1995)
28. A. Plech, V. Kotaidis, M. Lorenc, J. Boneberg, Femtosecond laser near-field ablation from gold nanoparticles. Nat. Phys. **2**, 44 (2006)
29. S. Ibrahimkutty, P. Wagener, A. Menzel, A. Plech, S. Barcikowski, Nanoparticle formation in a cavitation bubble after pulsed laser ablation in liquid studied with high time resolution SAXS. Appl. Phys. Lett. **101**, 103104 (2012)
30. S.M. Eaton, H. Zhang, M.L. Ng, J. Li, W. Chen, S. Ho, P.R. Herman, Transition from thermal diffusion to heat accumulation in high repetition rate femtosecond laser writing of buried optical waveguides. Opt. Express **16**, 9443–9458 (2008)
31. G. Petite, P. Daguzan, S. Guizard, P. Martin, Conduction electrons in wide-bandgap oxides: a subpicosecond time-resolved optical study. Nucl. Instrum. Meth. B **107**, 97–101 (1996)
32. P. Martin, S. Guizard, P. Daguzan, G. Petite, P. D'Olivera, P. Meynadier, M. Perdix, Subpicosecond study of carrier trapping dynamics in wide-band-gap crystals. Phys. Rev. B **55**, 5799–5810 (1997)
33. S. Richter, F. Jia, M. Heinrich, S. Döring, U. Peschel, A. Tünnermann, S. Nolte, The role of self-trapped excitons and defects in the formation of nanogratings in fused silica. Opt. Lett. **37**, 482–484 (2012)
34. D. Wortmann, M. Ramme, J. Gottmann, Refractive index modification using fs-laser double pulses. Opt. Express **15**, 10149–10153 (2007)
35. R.T. William, K.S. Song, The self-trapped exciton. J. Phys. Chem. Solids **51**, 679–716 (1990)
36. J.H. Stathis, M.A. Kastner, Time-resolved photoluminescence in amorphous silicon dioxide. Phys. Rev. B **35**, 2972–2979 (1987)
37. N. Itoh, T. Shimzu-Iwayama, T. Fujita, Excitons in crystaline and amorphous SiO_2: formation, relaxation and conversion to Frenkel pairs. J. Non-Cryst. Solids **179**, 194–201 (1994)
38. T.E. Tsai, D.L. Griscom, E.J. Friebele, Mechanism of intrinisc Si E'-center photogeneration in high-purity silica. Phys. Rev. Lett. **61**, 444–446 (1988)
39. K. Tanimura, C. Itoh, N. Itoh, Transient optical absorption and luminescence induced by band-to-band excitation in amorphous SiO_2. Solid State Phys. **21**, 1869–1876 (1988)
40. J.W. Chan, T. Huser, S. Risbud, D.M. Krol, Structural changes in fused silica after exposure to focused femtosecond laser pulses. Opt. Lett. **26**, 1726–1728 (2001)
41. P.P. Rajeev, M. Gertsvolf, E. Simova, C. Hnatovsky, R.S. Taylor, V.R. Bhardwaj, D.M. Rayner, P.B. Corkum, Memory in nonlinear ionization of transparent solids. Phys. Rev. Lett. **97**, 253001 (2006)
42. L. Skuja, M. Hirano, H. Hosono, K. Kajihira, Defects in oxide glasses. Phys. Status Solidi **2**, 15 (2005)
43. J.W. Chan, T.R. Huser, S.H. Risbud, D.M. Krol, Modification of fused silica glass network associated with waveguide fabrication using femtosecond laser pulses. Appl. Phys. A **76**, 367–372 (2003)
44. H. Nishikawa, E. Watanabe, E. Ito, Decay kinetics of the 4.4 eV photoluminescence associated with the two states of oxygen-deficient-type defect in amorphous SiO_2. Phys. Rev. Lett. **72**, 2101–2104 (1994)

45. K. Kajihara, L. Skuja, M. Hirano, H. Hosono, Formation and decay of nonbridging oxygen hole centers in SiO_2 glasses induced by F_2 laser irradiation: *In situ* observation using a pump and probe technique. Appl. Phys. Lett. **79**, 1757–1759 (2001)
46. D. Grojo, M. Gertsvolf, H. Jean-Ruel, S. Lei, L. Ramunno, D.M. Rayner, P.B. Corkum, Self-controlled formation of microlenses by optical breakdown inside wide-band-gap materials. Appl. Phys. Lett. **93**(24), 243118 (2008)
47. A. Brodeur, S.L. Chin, Ultrafast white-light continuum generation and self-focusing. JOSA B **16**, 637–650 (1999)
48. Z. Bomzon, V. Kleiner, E. Hasman, Formation of radially and azimuthally polarized light using space-variant subwavelength metal stripe gratings. Appl. Phys. Lett. **79**, 1587–1589 (2001)
49. M. Beresna, M. Gecevicius, P.G. Kazansky, T. Gertus, Radially polarized optical vortex converter created by femtosecond laser nanostructuring of glass. Appl. Phys. Lett. **98**, 201101 (2011)
50. C. Hnatovsky, V. Shvedov, W. Krolikowski, A. Rode, Revealing local field structure of focused ultrashort pulses. Phys. Rev. Lett. **106**, 123901 (2011)
51. K. Wicker, R. Heintzmann, Single-shot optical sectioning using polarization coded structured illumination. J. Opt. **12**, 084010 (2010)

Chapter 4
Femtosecond-Laser Induced Nanostructures in TiO_2

Susanta Kumar Das, Hamza Messaoudi, Kiran Dasari, Wolfgang Seeber and Rüdiger Grunwald

Abstract TiO_2 nanostructures are important functional materials with a growing number of applications in fields like medicine, photochemistry or photovoltaics. We demonstrate that highly reproducible nanostructures can be generated on the surface of bulk as well as thin film material by exploiting the phenomenon of laser-induced periodic surface structures (LIPSS). The influence of key parameters like pulse number, laser fluence, wavelength, and surface quality on the formation of such nanoripples is discussed. The time-integrated theory of Drude and Sipe is extended by the nonlinear excitation of transparent materials into a transient metal-like state enabling for the effective generation of surface plasmon polaritons.

4.1 Introduction

Nanostructured surfaces of titanium dioxide (TiO_2) are of increasing interest for various applications like superwetting [1, 2], self cleaning and antifogging [3–5], photovoltaics [6], gas sensors [7], bio-technology [8, 9], or photocatalysis [10–12]. One possible approach to nanoscale patterns is the generation of laser-induced periodic surface structures (LIPSS). As it was shown in the literature, ripple-like LIPSS can be generated in the focal zones of laser beams in many kinds of solid state materials [13–22]. Orientation, periods and depth of the ripple structures can be controlled by the parameters polarization, fluence, wavelength, and the number of pulses interacting with the sample. LIPSS can be classified depending on their spatial frequencies. Typically, two types of ripples are distinguished by comparing

S. Kumar Das · H. Messaoudi · K. Dasari · R. Grunwald (✉)
Max Born Institute for Nonlinear Optics and Short-Pulse Spectroscopy,
Max-Born-Strasse 2a, D-12489 Berlin, Germany
e-mail: grunwald@mbi-berlin.de

W. Seeber
Otto-Schott-Institut für Glaschemie, Friedrich-Schiller-Universität Jena,
Fraunhoferstraße 6, 07743 Jena, Germany

© Springer International Publishing Switzerland 2015

S. Sakabe et al. (eds.), *Progress in Nonlinear Nano-Optics*,
Nano-Optics and Nanophotonics, DOI 10.1007/978-3-319-12217-5_4

their periods to the center wavelength of the exciting laser. Structures with larger periods are referred to as low spatial frequency LIPSS (LSFL) or wavelength ripples, whereas structures with significantly smaller periods are called high spatial frequency LIPSS (HSFL) or sub-wavelength ripples. HSFL are of high practical importance for applications where large structured surface areas are required. They are generally formed with highly intense ultrashort-pulsed (femtosecond or picosecond) lasers. To explain the specific phenomena on this time scale, several hypotheses have been proposed [23–26]. Although the ripple formation was proven to be strongly connected to the excitation of surface plasmon-polaritons (SPP), the full complexity and dynamics of the physical processes is still the subject of controversial discussions. In particular, the role of local and global material transport and self-organized re-arrangement is not clear enough, changes of the polarization dependent ripple orientation are not explained and the detailed mechanisms leading to the smallest ripple periods are widely unknown. Our recent investigations indicate that a model based on multiphoton-induced plasmons can best explain the origin of such structures [27].

In this chapter, we like to present a convenient and efficient method for the generation of nanoscale features in TiO_2 on the basis of ultrashort-pulse LIPSS. The experimental findings are compared to the theoretical description of the excitation processes.

4.2 Methods of LIPSS Generation in Scanning Mode

For large-area nanostructuring, usually the direct laser ablation [28] or photolithography are the methods of choice because of the high possible precision and reproducibility. The necessary positioning accuracies, multi-step procedures or clean-room conditions are time-consuming and cost-effective. Currently, LIPSS methods are studied with respect to their capability to be easy-to-realize, cheap and convenient approaches for a fast structuring of large areas on nanoscale.

Concerning the LIPSS formation procedure, two different approaches are known. In the first case, the sample remains stationary during the exposure by the laser pulses (*fixed focus method*). In the second operation mode, the sample moves stepwise or continuously through the focus (*scanning focus method* [29–32]). In the fixed focus mode, a certain number of subsequently emitted pulses N all hit the same area on the sample. This means that any feedback induced by the ripple structures is steadily increasing from pulse to pulse and a kind of accumulation effect is expected. Furthermore, in fixed focus regime, the intensity profile of the focus (e.g. Gaussian) causes a spatial variation of the LIPSS process which can be nonlinearly transformed in the case of a multiphoton absorption. In the scanning focus mode, the feedback induced by already grown ripples is reduced depending on the ratio between translation speed and pulse repetition frequency. At optimized parameters, the focus envelope perpendicular to the vector of movement determines the ripple contrast only in this direction and extended, high quality ripple structures

can be produced. Besides the uniformity of the line focus, the linearity of the scan and the pointing stability of the laser have to be carefully controlled as well. If the available energy per pulse is sufficiently high, an extended line focus can be used to enhance the simultaneously treated area and thus to enable for a high-speed processing with coherently linked ripples [33].

4.3 Roughness and Initial Stages of fs-LIPSS in TiO_2 Bulk Crystals

A typical SEM image of nanostructures generated in a TiO_2 surface by the fixed focus method is shown in Fig. 4.1. The period of these structures was found to be about 180 nm. The structures were generated with a Ti:sapphire laser emitting pulses with a pulse duration (FWHM) of 150 fs at a center wavelength of 800 nm and a repetition frequency of 1 kHz. The substrate was a rutile-type, single side-polished commercial TiO_2 crystal. The maximum fluence in the center of the laser spot was 0.75 J/cm^2 and the pulse number $N = 40$.

The pulse number was found to be a key parameter for the generation of such structures. In particular, at low numbers of pulses ($N \leq 10$) it was difficult to obtain perfectly ordered, periodic ripple patterns. Instead of this, we mostly found meandering structures under these conditions which can be regarded to be typical for the initial stage of ripple evolution (Fig. 4.2a, [34]). The two-dimensional Fast Fourier Transform (2D-FFT) analysis of the spatial distributions taken from scanning electron microscope (SEM) images suggests the dominance of extremely high spatial frequency components (Fig. 4.2b).

On the other hand, pulse numbers $N \geq 100$ were found to strongly facilitate the appearance of structures with a distinct periodicity (quasi-periodic ripples) [34]. All of these findings were related to smooth surfaces with a rms roughness in the range

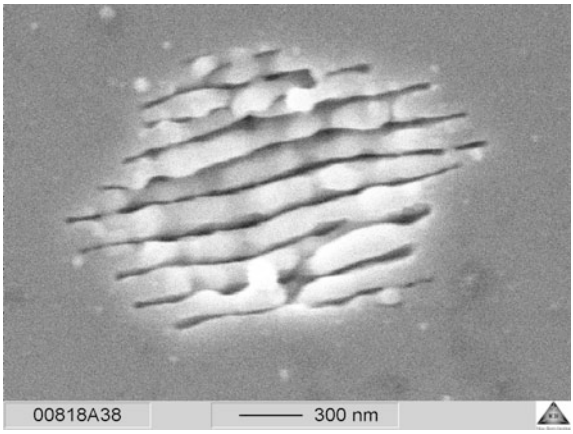

Fig. 4.1 Highly uniform HSFL generated at the surface of a TiO_2 single crystal with Ti:sapphire laser pulses (40 pulses, peak fluence 0.75 J/cm^2, center wavelength 800 nm, repetition frequency 1 kHz)

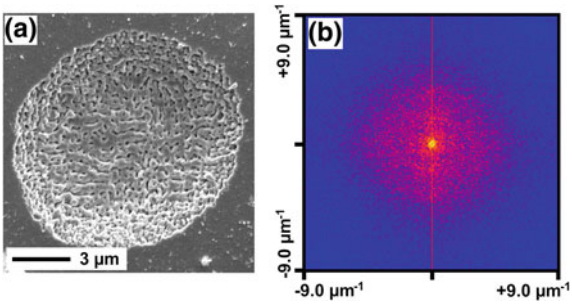

Fig. 4.2 Structure of the laser-irradiated area after a low number of pulses: meander-like laser-induced random structures created in a TiO_2 surface after exposure with $N = 10$ pulses at the fundamental wavelength of a Ti:sapphire laser (pulse duration 150 fs, central wavelength 800 nm, pulse energy 2.3 µJ, fluence 1.46 J/cm^2); **a** SEM image of the ablated area with random nanostructures, **b** corresponding 2D-FFT data (image post-processed by nonlinear amplitude filtering, field of view 4.23 × 4.23 µm^2, *Courtesy* Journal of Applied Physics [34])

of 1 nm. In experiments with TiO_2-surfaces of higher roughness (about 7 nm), however, the enhanced scattering in the very beginning leads to a shift of onset of the structure formation to significantly lower pulse numbers. The minimum required fluence for formation LIPSS in rough surface was even found to be 30 % below that of the polished surface [35]. This observation supports the models based on an SPP-related mechanism of LIPSS because the resonant spatial frequency components are excited with a higher probability in the rough surface [36, 37]. It should be mentioned that, in general, one has to expect the existence of an optimum roughness range because of the losses which counteract the enhancement.

4.4 Experimental Results with Line Focus and Moving Substrate

To exploit the specific advantages of the scanning LIPSS generation with line-shaped focal zones and a linear substrate translation, the process parameters were carefully optimized [33]. The experiments were performed using the second harmonic (center wavelength 400 nm) of the femtosecond laser pulses of a linearly polarized, mode-locked Ti:sapphire laser with chirped-pulse amplification (Spitfire, Spectra Physics; center wavelength 800 nm, repetition frequency 1 kHz). For the second harmonic generation (SHG), a 250 µm thick, type-I cut, beta barium borate (BBO) crystal. The SHG was separated from the fundamental wave by spectrally selective mirrors and filters and varied by a set of calibrated neutral density filters in a range up to a maximum value of 804 µJ.

The corresponding setup is schematically drawn in Fig. 4.3. Nanostructures were induced in a commercially available rutile-type single crystal TiO_2 sample.

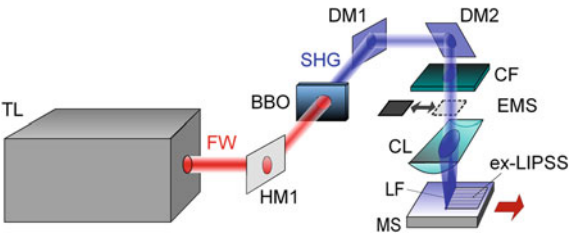

Fig. 4.3 Experimental set-up for extended-area *LIPSS* with line focus and moving substrate; *TL* Ti:sapphire laser, *FW* fundamental wave, *HM1* high reflectance mirror, *BBO* beta barium borate crystal for *SHG*, *DM1* and *DM2* dichroic mirrors (HR @ 400 nm, AR @ 800 nm), *EMS* electromechanical shutter, *CF* colour glass filter (BG39), *CL* cylindrical lens, *LF* line focus, *MS* moving substrate on xyz stage, *ex-LIPSS* extended-area LIPSS with nanoripples, *red arrow* direction of substrate movement (schematically) (*Courtesy* Nanotechnology [33])

It was found that the observed ripple periods strongly depend on pulse energy and fluence. This is illustrated by Figs. 4.4 and 4.5. The SEM pictures show nanostructures of different morphology and scale with average periods of 340 nm (LSFL) and 90 nm (HSFL) obtained at pulse energies of 270 and 153 μJ, respectively. Obviously, higher spatial frequencies were generated at lower fluence and, vice versa, lower spatial frequencies are observed in regions of higher fluence. For fixed Gaussian-shaped spatial intensity distributions (without scanning), this leads to the often reported atoll-like high-frequency structure surrounding a low-frequency core area which represents in many cases a deeper ablation crater.

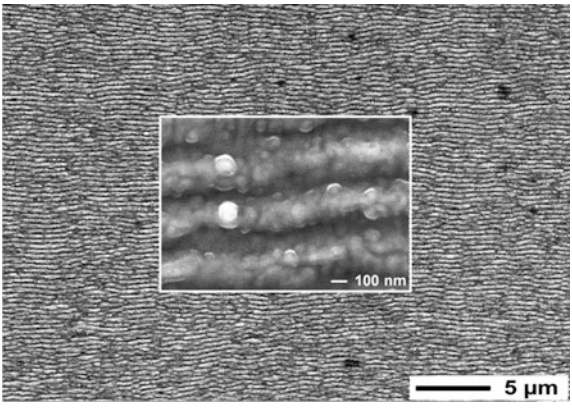

Fig. 4.4 SEM images of LSFL with an average spatial period of 340 nm formed in TiO_2 by a sample movement across a line focus (pulse energy 270 μJ, scan velocity 0.5 mm/s) (*Inset* part at higher resolution) (*Courtesy* Nanotechnology [33])

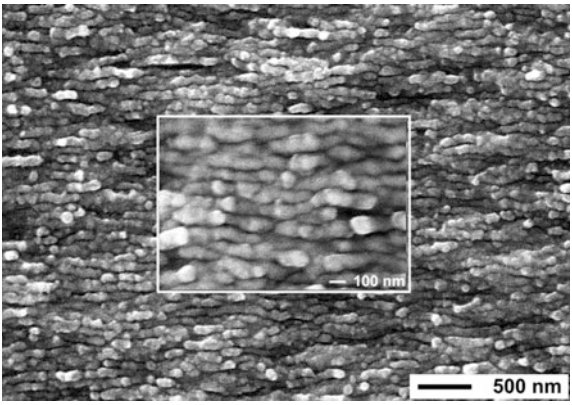

Fig. 4.5 SEM images of sub-100-nm HSFL (average spatial period: 90 nm) formed in TiO_2 by a sample movement across a line focus (pulse energy 270 μJ, scan velocity 0.05 mm/s) (*Inset* part at higher resolution). The patterns show a higher degree of randomness compared to the structures in Fig. 4.4 (*Courtesy* Nanotechnology [33])

4.5 Theoretical Estimation of the Optical Constants

The excitation of SPPs is known to take place at the interface of a metal and a dielectric. If dielectric or semiconducting materials like TiO_2 or similar metal oxides are excited with ultrashort pulses at extremely high intensities, they can also can behave like metals. The excited carrier density of such materials in the damage threshold region can amount to the range of 10^{20} cm^{-3}–10^{23} cm^{-3}. The results of preliminary numerical studies on the basis of the classical Drude model (assuming a time-averaged carrier generation) strongly support the assumption of a metal-like behavior of TiO_2 for realistic parameters. At excited carrier densities above 5×10^{20} cm^{-3}, the material reaches reflectivity values as typical for metals (see Fig. 4.6, [33]).

4.6 Generation of Uniform LIPSS Areas in Thin TiO_2 Films

The scanning method described above was applied to create nanostructures on large areas at high speed. To better understand the basic mechanisms of excitation, however, we studied the generation of LIPSS in thin TiO_2 films with the fixed focus method. In this case, the conditions were not additionally modified by an overlap of interaction zones caused by the sample translation. These well defined conditions were used to determine the dependence of the LIPSS generation on the number of laser pulses and fluence. Samples of different roughness were grown by sputtering at variable pressure [37]. The results of the LIPSS experiments indicate that

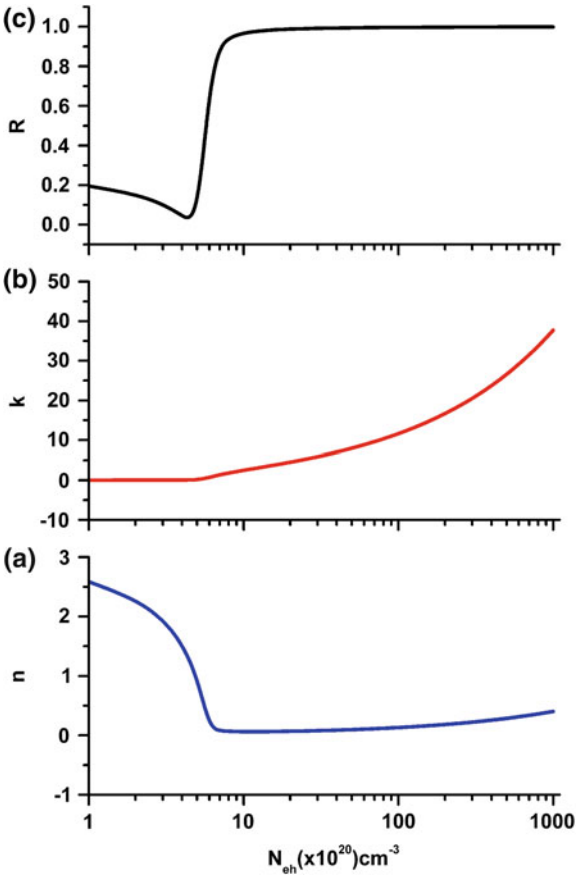

Fig. 4.6 Variation of **a** the real part n, **b** the imaginary part k of the refractive index, and **c** the reflectivity R with the photo-excited carrier density in rutile-type bulk TiO_2 (please notice the logarithmic abscissa). In the model, the reflectivity was chosen to be $R = |(\tilde{n} - 1)/(\tilde{n} + 1)|^2$ with the complex refractive index $\tilde{n} = n + ik$ (*Courtesy* Nanotechnology [33])

material ablation and ripple generation appear as co-existing phenomena. Towards larger numbers of pulses and/or higher fluence, ablation plays an increasing role and causes damaged areas which extend from the center to the rim. Because of the low material thickness, ablation can easily erase the nanostructures in the central part (Fig. 4.7).

Therefore it becomes evident that the creation of highly uniform LIPSS areas with Gaussian beams is highly challenging and requires to carefully balance the critical parameters. The result of such a process optimization is shown in Fig. 4.8. It can be recognized that for the selected parameters a fairly uniform distribution of nanoscale LIPSS was produced in a thin TiO_2 film.

Three cases with a complete, partial and negligible ablation of the layer over the irradiated area are compared in Fig. 4.9. The optimum number of laser pulses corresponding to the conditions related to Fig. 4.8 was found to be in the range between $N = 5$ and $N = 20$ (region III of Fig. 4.9). Here, the fluence was chosen to be close to the damage threshold of the material.

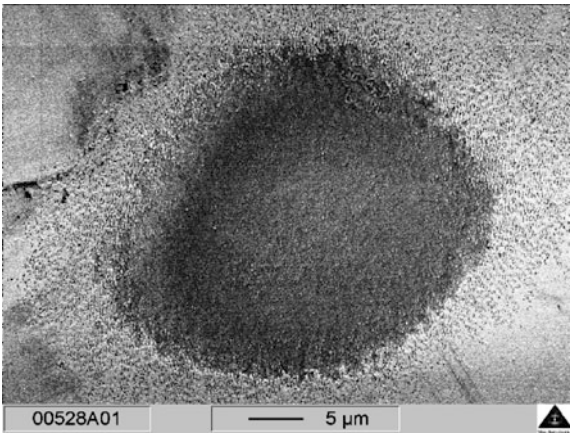

Fig. 4.7 Material ablation in thin films caused by the most intense part of a Gaussian intensity profile restricts the ripple formation to the outer edges (here: maximum fluence 0.6 J/cm^2, $N = 20$, layer thickness about 200 nm)

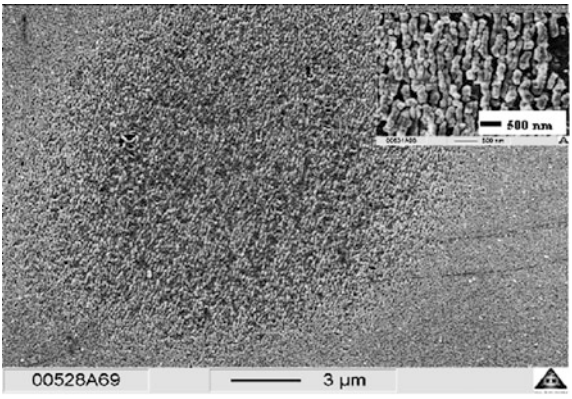

Fig. 4.8 Generation of nanoscale LIPSS of relatively high uniformity over the whole processed area of a thin TiO_2 film (*inset* on top morphology in larger magnification) (Fluence 0.3 J/cm^2, number of pulses $N = 20$)

The observation of LIPSS even at a very low number of pulses in our thin film experiments was attributed to the nano-grains in the sample. As pointed out like in the case of unpolished TiO_2 bulk crystal, these grains enable an efficient coupling of the laser pulse to the SPPs. A typical SEM image of LIPSS generated by applying the line scanning method at a pulse duration of 120 fs and a center wavelength of 800 nm is shown in Fig. 4.10.

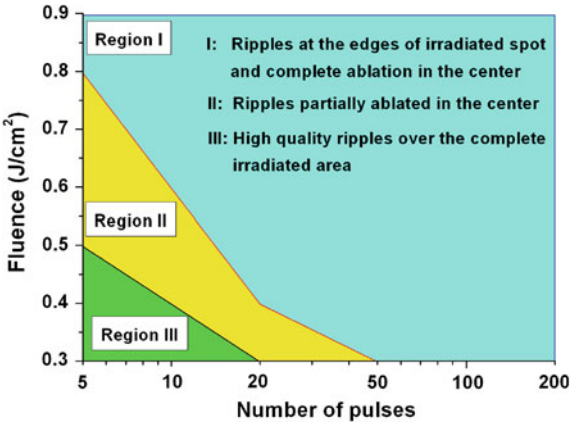

Fig. 4.9 Distinct processing regimes in the parameter map for LIPSS generation in TiO_2 thin films (*Courtesy* Proc. SPIE [37])

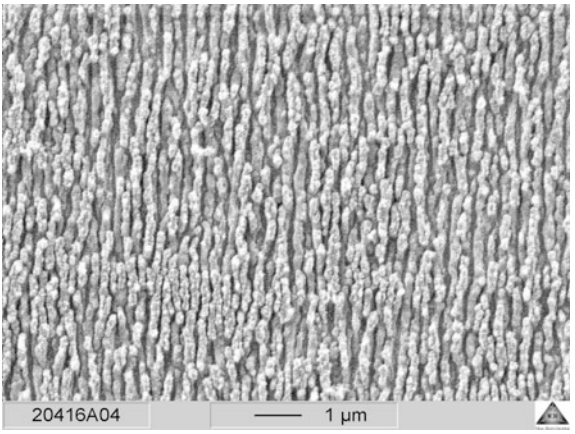

Fig. 4.10 LIPSS in TiO_2 generated by the line scanning method at a center wavelength of 800 nm (pulse duration 120 fs)

The typical periods of these structures were found to be almost similar to what we observed in the TiO_2 bulk material. Similar structures were generated across an area as large as 15×25 mm^2 for potential applications in photocatalysis.

4.7 Conclusions and Outlook

We demonstrated that nanostructures can be generated on the surface of bulk and thin film of TiO_2 by utilizing the phenomenon of a self-organized generation of laser-induced periodic surface structures with intense femtosecond pulses. By carefully optimizing the parameters, it is possible to obtain even uniform structured areas with surface ripples on sub-wavelength scale. Large-area, high-speed structuring is obtained with the method of line focus and moving substrate. The randomness and

coherence of the structures can be influenced by the speed of translation. The initial roughness plays an important role for the evolution of the ripples in the first stage. The correspondence between experimental results and theoretical estimations of the optical constants based on Drude theory indicates the relevance of the excitation of surface plasmon-polaritons and favours local instead of global material transport mechanisms. Future simulations have to also include the time-dependence of the optical constants like reflectivity and refractive index and possible consequences of the non-stationarity.

The reported easy and cost-effective way to generate LIPSS promises to stimulate various applications like superwetting, self-cleaning and antifogging, photovoltaics, surface-enhanced spectroscopy, photoelectron generation, gas sensors, bio-technology, or photocatalysis. Recently, structures with very similar features compared to our results presented here have been successfully applied to demonstrate highly bio-compatible TiO_2 surfaces.

The improvement of the quality of the nanostructures and the identification of the physical limits for extremely small structures are still a challenge for future work.

References

1. W.Y. Gan, S.W. Lam, K. Chiang, R. Amal, H. Zhao, M.P. Brungs, Novel thin film with non-UV activated superwetting and antifogging behaviours. J. Mat. Chem. **17**, 952–954 (2007)
2. S. Song, L. Jing, S.H. Fu, Y. Luan, Superhydrophilic anatase TiO_2 film with the micro- and nanometerscale hierarchical surface structure. Mat. Lett. **62**, 3503–3505 (2008)
3. S.W. Lam, W.Y. Gan, K. Chiang, R. Amal, TiO_2 semiconductor—a smart self-cleaning material. J. Aust. Ceramic Soc. **44**, 6–11 (2008)
4. S. Law, S.W. Lam, W.Y. Gan, J. Scott, R. Amal, Effect of film thickness and agglomerate size on the superwetting and fog-free characteristics of TiO_2 films. Thin Solid Films **517**, 5425–5430 (2009)
5. T. Tölke, A. Kriltz, A. Rechtenbach, The influence of pressure on the structure and the self-cleaning properties of sputter deposited TiO_2 layers. Thin Solid Films **518**, 4242–4246 (2010)
6. B. O'Regan, M. Grätzel, A low-cost, high-efficiency solar cell based on dye-sensitized colloidal TiO_2 films. Nature **353**, 737–739 (1991)
7. H.F. Lu, F. Li, G. Liu, Z.G. Chen, D.W. Wang, H.T. Fang, G.Q. Lu, Z.H. Jiang, H.M. Cheng, Amorphous TiO_2 nanotube arrays for low-temperature oxygen sensors. Nanotechnology **19**, 405504 (2008)
8. R. Karpagavalli, A. Zhou, P. Chellamuthu, K. Nguyen, Corrosion behavior and biocompatibility of nanostructured TiO_2 film on Ti6Al4V. J. Biomed. Mat. Res. **83A**, 1087–1095 (2007)
9. K. Ozasa, S. Nemoto, Y. Li, M. Hara, M. Maeda, K. Mochitate, Contact angle and biocompatibility of sol-gel prepared TiO_2 thin films for their use as semiconductor-based cell-viability sensors. Surf. Interface Anal. **40**, 579–583 (2008)
10. B. Li, J. Zhao, K. Onda, K.D. Jordan, J. Yang, H. Petek, Ultrafast interfacial proton-coupled electron transfer. Science **311**, 1436–1440 (2006)
11. T.J. Whang, H.Y. Huang, M.T. Hsieh, J.J. Chen, Laser-induced silver nanoparticles on titanium oxide for photocatalytic degradation of methylene blue. Int. J. Mol. Sci. **10**, 4707–4718 (2009)

12. Z. Wang, J. Liu, Y. Dai, W. Dong, S. Zhang, J. Chen, Dimethyl sulfide photocatalytic degradation in a light-emitting-diode continuous reactor: kinetic and mechanistic study. Ind. Eng. Chem. Res. **50**, 7977–7984 (2011)
13. M. Shen, J.E. Carey, C.H. Crouch, M. Kandyla, H.A. Stone, E. Mazur, High-density regular arrays of nanometer-scale rods formed on silicon surfaces via femtosecond laser irradiation in water. Nano Letters **8**, 2087–2091 (2008)
14. A.Y. Vorobyev, C. Guo, Effects of nanostructure-covered femtosecond laser-induced periodic surface structures on optical absorptance of metals. Appl. Phys. A **86**, 321–324 (2007)
15. B. Kumar, R.K. Soni, Submicrometre periodic surface structures in InP induced by nanosecond UV laser pulses. J. Phys. D Appl. Phys. **41**, 155303 (2008)
16. R. Taylor, C. Hnatovsky, E. Simova, Applications of femtosecond laser induced self-organized planar nanocracks inside fused silica glass. Laser Photon. Rev. **2**, 26–46 (2008)
17. Y. Shimotsuma, M. Sakakura, K. Miura, J.R. Qiu, P.G. Kazansky, K. Fujita, K. Hirao, Application of femtosecond-laser induced nanostructures in optical memory. J. Nanosci. Nanotech. **7**, 94–104 (2007)
18. J. Bonse, H. Sturm, D. Schmidt, W. Kautek, Chemical, morphological and accumulation phenomena in ultrashort-pulse laser ablation of TiN in air. Appl. Phys. A **71**, 657–667 (2000)
19. H. Hiraoka, W.Y.Y. Wong, T.M. Wong, C.T. Hung, W.C. Loh, F.M. Lee, Pulsed laser processing of polymer and ceramic surfaces. J. Photopolym. Sci. Technol. **10**, 205–210 (1997)
20. S. Baudach, J. Bonse, W. Kautek, Ablation experiments on polyimide with femtosecond laser pulses. Appl. Phys. A **69**, S395 (1999)
21. R. Le Harzic, D. Dörr, D. Sauer, F. Stracke, H. Zimmermann, Generation of high spatial frequency ripples on silicon under ultrashort laser pulses irradiation. Appl. Phys. Lett. **98**, 211905 (2011)
22. M. Zamfirescu, M. Ulmeanu, F. Jipa, O. Cretu, A. Moldovan, G. Epurescu, M. Dinescu, R. Dabu, Femtosecond laser induced periodic surface structures on ZnO thin films. JLMN-J. Laser Micro/Nanoeng. **4**, 7 (2009)
23. J.E. Sipe, J.F. Young, J.S. Preston, H.M. van Driel, Laser-induced periodic surface structure, I. Theory Phys. Rev. B **27**, 1141–1154 (1983)
24. T.Q. Jia, H.X. Chen, M. Huang, F.L. Zhao, J.R. Qiu, R.X. Li, Z.Z. Xu, X.K. He, J. Zhang, H. Kuroda, Formation of nanogratings on the surface of a ZnSe crystal irradiated by femtosecond laser pulses. Phys. Rev. B **72**, 125429 (2005)
25. M.S. Trtica, B.M. Gakovic, B.B. Radak, D. Batani, T. Desai, M. Bussoli, Periodic surface structures on crystalline silicon created by 532 nm picosecond Nd:YAG laser pulses. Appl. Surf. Sci. **254**, 1377–1381 (2007)
26. M. Huang, F. Zhao, Y. Cheng, N. Xu, Z. Xu, Origin of laser-induced near-subwavelength ripples: interference between surface plasmons and incident laser. ACS Nano **3**, 4062–4070 (2009)
27. R. Grunwald, S.K. Das, A. Debroy, E. McGlynn, H. Messaoudi, in *Nonlinear Optical Mechanism of Forming Periodical Nanostructures in Large Bandgap Dielectrics*. IESC Proceedings Series (Institut d'Études Scientifiques de Cargèse, France, in press)
28. M. Huang, F. Zhao, Y. Cheng, N. Xu, Z. Xu, Large area uniform nanostructures fabricated by direct femtosecond laser ablation, Opt. Express **16**, 19354 (2008)
29. R. Wagner, J. Gottmann, A. Horn, E.W. Kreutz, Subwavelength ripple formation induced by tightly focused femtosecond laser radiation, Appl. Surf. Sci. **252**, 8576–8579 (2006)
30. M. Huang, F. Zhao, Y. Feng, Y. Cheng, N. Xu, Z. Xu, Large area uniform nanostructures fabricated by direct femtosecond laser ablation, Opt. Express **16**, 19354–19365 (2008)
31. Q.Z. Zhao, S. Malzer, L.J. Wang, Formation of subwavelength periodic structures on tungsten induced by ultrashort laser pulses, Opt. Lett. **32**, 1932–1934 (2007)
32. J. Gottmann, D. Wortmann, M.H. Jungemann, Fabrication of sub-wavelength surface ripples and in-volume nanostructures by fs-laser induced selective etching, Appl. Surf. Sci. **255**, 5641–5646 (2009)
33. S.K. Das, K. Dasari, A. Rosenfeld, R. Grunwald, Extended-area nanostructuring of TiO_2 with femtosecond laser pulses at 400 nm using a line focus. Nanotechnology **21**, 155302 (2010)

34. S.K. Das, D. Dufft, A. Rosenfeld, J. Bonse, R. Grunwald, Femtosecond-laser induced quasi-periodic nanostructures on TiO_2 surfaces. J. Appl. Phys. **105**, 084912 (2009)
35. S.K. Das, M. Rohloff, S. Höhm, A. Pfuch, W. Seeber, A. Rosenfeld, R. Grunwald, in *Formation of Laser-Induced Periodic Structures in TiO_2 Crystals Depending on the Surface Quality*. CLEO 2011 (Technical Digest, CTuAA2, USA, 2011)
36. H. Raether, *Surface Plasmons on Smooth and Rough Surfaces and on Gratings*. Springer Tracts in Modern Physics, vol. 111 (Springer, New York, 1988)
37. S.K. Das, A. Rosenfeld, M. Bock, A. Pfuch, W. Seeber, R. Grunwald, Scattering-controlled femtosecond-laser induced nanostructuring of TiO_2 thin films. Proc. SPIE **7925**, 7925–7942 (2011)
38. T. Shinonaga, N. Horigutchi, M. Tsukamoto, A. Nagai, K. Yamashita, T. Hanawa, Femtosecond laser induced periodic nanostructures on titanium dioxide film for improving biocompatibility. Proc. SPIE **8609**, 8609–8622 (2013)

Chapter 5
Formation of Laser-Induced Periodic Surface Structures (LIPSS) on Dielectrics and Semiconductors upon Double-Femtosecond Laser Pulse Irradiation Sequences

Sandra Höhm, Marcus Rohloff, Joerg Krüger, Joern Bonse and Arkadi Rosenfeld

Abstract The formation of laser-induced periodic surface structures (LIPSS) on different materials (silicon, fused silica, quartz) with linearly polarized fs-laser irradiation is studied experimentally. In dielectrics, the importance of transient excitation stages in the LIPSS formation is demonstrated by using (multiple) cross-polarized double-fs-laser-pulse irradiation sequences. A characteristic decrease of the spatial LIPSS periods is observed for double-pulse delays of less than 2 ps along with a characteristic 90°-rotation of the LIPSS orientation.

5.1 Introduction

Since its first observation by Birnbaum on semiconductor surfaces [1] LIPSS were observed in nearly all materials. The generation of such ripples by laser irradiation is, therefore, a universal phenomenon [2–4], even if the exact physical mechanisms and their manifestations depend on the irradiated material and the irradiation parameters.

During the interaction of strongly absorbing materials such as metals or semiconductors with linearly polarized radiation at normal incidence in many cases LIPSS with spatial periods close to the irradiation wavelength were observed. It is

S. Höhm (✉) · M. Rohloff · A. Rosenfeld (✉)
Max-Born-Institut für Nichtlineare Optik und Kurzzeitspektroskopie,
Max-Born-Straße 2a, 12489 Berlin, Germany
e-mail: hoehm@mbi-berlin.de

A. Rosenfeld
e-mail: rosenfeld@mbi-berlin.de

J. Krüger · J. Bonse
BAM Bundesanstalt für Materialforschung und -prüfung,
Unter den Eichen 87, 12205 Berlin, Germany

© Springer International Publishing Switzerland 2015

S. Sakabe et al. (eds.), *Progress in Nonlinear Nano-Optics*,
Nano-Optics and Nanophotonics, DOI 10.1007/978-3-319-12217-5_5

now generally accepted that this type of "wavelength ripples" (often termed "LSFL", low-spatial-frequency LIPSS) is created due to interference effects of the incident laser radiation with a "surface electromagnetic wave", which is generated by the rough surface during irradiation [5, 6].

With regard to the irradiation of solids with femtosecond laser pulses, wavelength ripples were already observed for a variety of different materials, e.g., on metals [7], ceramics [8, 9], semiconductors [10–12], polymers [13] and dielectrics [14–16]. Interestingly, in most cases the ripple periods are slightly smaller than the wavelength. Although a clear correlation with the orientation of the linear polarization of the laser radiation was observed, the relative orientation between the electric field vector and the ripples depends on the material. The wavelength ripple type was observed preferably for moderate numbers of pulses per spot ($N < 100$) and for laser energy densities (fluences) just above the single-pulse ablation threshold of the material.

Many studies of the last years on femtosecond laser ablation of different materials reported a new ripple type (sometimes called "HSFL", high-spatial-frequency LIPSS) with spatial periods significantly below the irradiation wavelength [17–20]. This new ripple type occurs exclusively in femtosecond (or sub-ps) laser irradiation. HSFL were observed with periods down to one tenth of the wavelength. These subwavelength ripples are significantly different from the classical wavelength ripples. The reason of the formation of such HSFL is currently discussed controversially in the scientific community. Various explanations have been proposed, such as a self-organized structure formation during the relaxation of highly excited surface away from equilibrium by the explosive ion emission [19], or the frequency-doubling at the irradiated surface [21, 22]. Likewise, the widely recognized ab-initio theory of Sipe et al. [4] was used to explain HSFL for the fs-irradiation of diamond films [16].

In addition to key parameters such as laser fluence, pulse duration and type of material, other irradiation parameters were identified as being important, e.g., the beam polarization, the wavelength, the angle of incidence and the irradiation environment (air, vacuum, liquids). For example, the irradiation in air showed that the HSFL can arise in chemically modified (oxidized) material [8]. Moreover, the irradiation in liquids can result also in the formation of LIPSS with very small spatial periods, as demonstrated in [23] for fs-laser processing of silicon in an aqueous contact. In this case periods of about 100 nm were observed. Similarly, small feature sizes (70–100 nm) were also detected in the irradiation of silicon with 90-MHz femtosecond oscillator radiation through an oil-immersion objective of high numerical aperture [24].

Regarding the dynamics of the emergence of LIPSS, only few experiments have been performed in the past, although this point was already addressed experimentally [25, 26] during the development of the ab-initio theory [4]. However, these early reflection and diffraction experiments with 20-ns laser pulse excitation and cw laser-probing revealed in the regime of LIPSS formation inhomogeneous melting of the surface on the nanosecond timescale. Since the laser-induced phase transitions took place already during the exciting laser pulses, the necessary time-resolution to observe the impact of laser-induced carrier-excitation on the LIPSS

dynamics was missing. In our new experimental approach, we take benefit from the sub-ps pulse durations available from Ti:sapphire laser systems along with the possibilities of temporal pulse shaping and we will demonstrate a new way for the control of LIPSS. This allows us to reveal the impact of temporally distributed energy deposition to wide band gap materials (semiconductors and dielectrics) and to prove the importance of transient fs-laser-induced excitation stages to the formation of fs-LIPSS in these materials.

5.2 Experimental

High-purity double-side polished 20 × 20 × 2 mm^3 samples made either of fused silica [*a*-SiO_2, Suprasil, Heraeus GmbH, Hanau, Germany] or of single-crystalline synthetic quartz [*c*-SiO_2, (0001) crystal cut orientation] were chosen as dielectric sample materials, both supplied by CrysTec GmbH, Berlin, Germany. As semiconducting material, standard single-side polished single-crystalline silicon wafers [*n*-doped, (111)-oriented, 400 µm thick] were selected.

A commercial chirped pulse Ti:sapphire regenerative laser amplifier system (Clark-MXR, TRA-1000) was used to generate linearly polarized laser pulses of $\tau \sim 150$ fs duration at $\lambda = 800$ nm central wavelength and with a pulse repetition frequency of $\nu \sim 150$ Hz. Sequences of multiple (N_{SPS}) single fs-laser pulses were selected by a synchronized electromechanical shutter and then focused normally to the sample surface by a spherical lens ($f = 100$ mm) to Gaussian beam radii $w_0(1/e^2) \sim 18$ µm at the sample surface. The laser pulse energies were controlled by a half-wave-plate-polarizer combination and monitored by a pyroelectric pulse energy detector. The peak fluences (ϕ_0) of the Gaussian-like beam profile in front of the sample were determined according to a method proposed by Liu [27]. The uncertainty in the laser fluences given here is less than 20 %. All irradiations were performed in air environment under normal incidence.

In some experiments, double-fs-pulses were generated from a fs-pulse train (150 fs, 800 nm, 150 Hz) using a Michelson-interferometer (MI). The MI-setup allowed the generation of near-equal energy double-fs-pulse sequences of variable pulse delays Δt between −40 and +40 ps and with a temporal accuracy of ∼0.2 ps. For crossed polarization experiments a phase retarding quarter-wave plate was added to the reference arm (RA) of the MI which rotates the linear polarization state of one of the laser pulses passing through the MI by 90° (see Fig. 5.1). Negative delays indicate the arrival of this pulse (RA) prior to that from the other arm with variable arm (VA) length. The thin-film non-polarizing beam-splitter used in the MI caused a slightly different pulse energy relation in the two arms (0.54•E in the RA and 0.46•E in the VA).

In analogy to the experiments with single-pulse sequences, the desired number of double-fs laser pulses N_{DPS} was selected by an electromechanical shutter. The pulse sequences passing the MI were focused by a spherical 75-mm focal distance lens normally onto the sample surface, where the laser beam exhibits a Gaussian

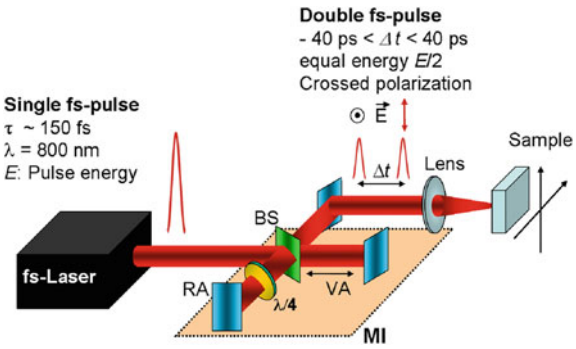

Fig. 5.1 Scheme of the experimental setup used for double-fs-pulse irradiation with crossed-polarized double-fs-beams. For parallel polarization the quarter wave-plate (λ/4) is removed. *BS* thin-film beam splitter (non-polarizing); *E* single laser pulse energy; Δt double-pulse delay; *VA* variable arm; *RA* reference arm

fluence distribution with a ($1/e^2$-)radius $w_0 \sim 13$ µm. For double-pulse irradiation, we refer to the total peak fluence $\phi_{0,\mathrm{tot}}$ accumulated over the peak fluence of both individual fs-laser pulses. The laser-irradiated surface regions were inspected and characterized by optical (OM), scanning electron (SEM) and scanning force microscopy (SFM).

5.3 Results and Discussion

It is well known that the laser fluence and the number of laser pulses per spot are essential parameters for the formation of LIPSS. Therefore, we have studied the influence of both parameters on the fs-LIPSS formation on silica upon irradiation with multiple single-fs-pulse sequences. The corresponding results are discussed in Sect. 5.3.1 (fluence dependence) and in Sect. 5.3.2 (pulse number dependence). Even if the damage threshold of fused silica is lower than that of quartz by ~10 % for pulse numbers less than ten per spot), we have not observed significant differences between both types of silica with respect to the morphology of the LIPSS. Hence, the results presented in the following for one of the materials are also representative for the other polymorph. In Sect. 5.3.3 results of the impact of parallel or cross-polarized double-fs-pulses of varying delays on the fs-LIPSS are presented.

5.3.1 Fluence Dependence of LIPSS

Figure 5.2 shows scanning electron micrographs of a quartz (c-SiO_2) surface after irradiation with $N_{\mathrm{SPS}} = 10$ single fs-laser pulses of different peak fluences between $\phi_0 = 5.4$ J/cm^2 (Fig. 5.2a) and $\phi_0 = 8.3$ J/cm^2 (Fig. 5.2d). At the lowest fluence

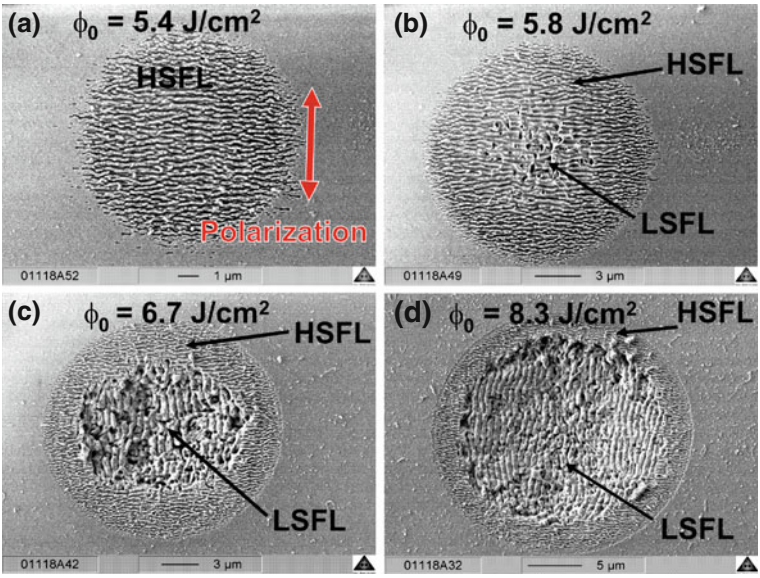

Fig. 5.2 SEM images of a quartz surface after irradiation with N_{SPS} = 10 linearly polarized single laser pulses (λ = 800 nm, τ = 150 fs) of different peak fluences between ϕ_0 = 5.4 J/cm^2 (**a**) and ϕ_0 = 8.3 J/cm^2 (**d**). The direction of the laser beam polarization is indicated in (**a**). Note the individually different *scaling bars* in all images

[ϕ_0 = 5.4 J/cm^2, Fig. 5.2a] solely HSFL were observed having an orientation of the lines perpendicular to the laser beam polarization. At ϕ_0 = 5.8 J/cm^2 the onset of the formation of LSFL can be observed in the center of the irradiated spot (Fig. 5.2b). For higher fluences, they become more pronounced and show an orientation parallel to the polarization (Fig. 5.2c, d). Due to the Gaussian shape of the laser beam profile, the central crater area covered by LSFL is additionally surrounded by an annular region where HSFL are formed (at smaller local fluence values). Obviously, at a fixed number of laser pulses, a transition from HSFL to LSFL occurs when a critical fluence threshold is exceeded. This is illustrated schematically in Fig. 5.3. In the upper part the spatial Gaussian beam shape of the laser is shown with the peak fluence ϕ_0. As the threshold for the HSFL formation is lower than for the LSFL one can see the sub-wavelength ripples for a medium local laser fluence only in the outer part of the modified area. In the inner part, where the local fluence is higher, the formation of LSFL is dominant.

5.3.2 Pulse Number Dependence of LIPSS

Figure 5.4 shows scanning electron micrographs of quartz surfaces after irradiation with sequences consisting of different numbers of single fs-laser pulses [N_{SPS} = 5,

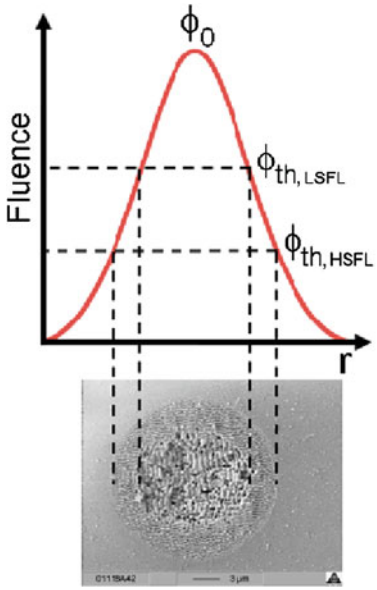

Fig. 5.3 Illustration of fluence regimes (schematic) for the formation of HSFL and LSFL upon irradiation with a spatially Gaussian laser beam profile of medium peak fluence where both types of LIPSS (HSFL and LSFL) can be observed. The *horizontal lines* indicate the two different thresholds for LSFL and HSFL formation ($\phi_{th,\,LSFL} > \phi_{th,\,HSFL}$)

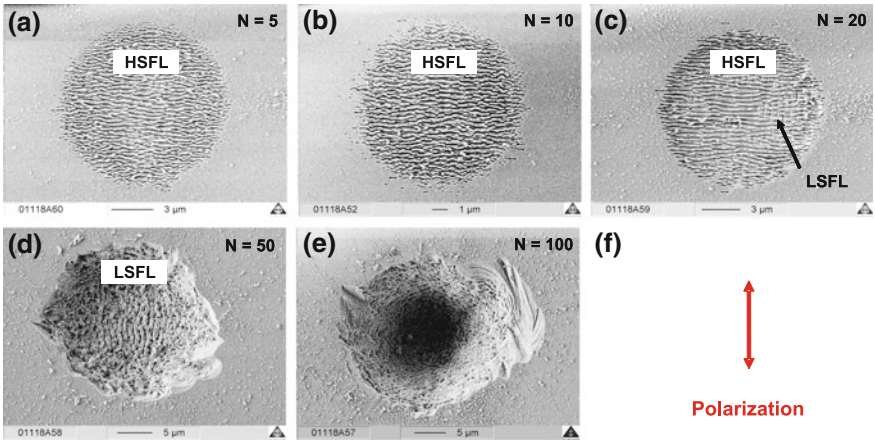

Fig. 5.4 SEM micrographs of a quartz surface after irradiation with a varying number [N_{SPS} = 5 (**a**) to N_{SPS} = 100 (**e**)] of linearly polarized single laser pulses (λ = 800 nm, τ = 150 fs) at a fixed peak fluence of ϕ_0 = 5.4 J/cm^2. The direction of the laser beam polarization is indicated in (**f**). Note the individually different *scaling bars* in all images

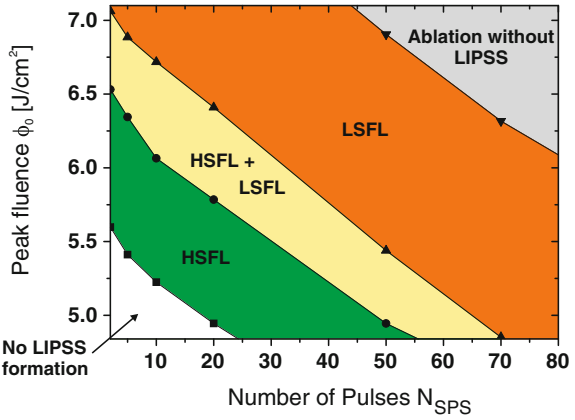

Fig. 5.5 Parameter regimes (peak fluence ϕ_0 vs. number of laser pulses N_{SPS}) for the LIPSS formation on quartz. The *dots* (*triangles*, *circles*, *squares* and *diamonds*) represent measured data points

Fig. 5.4a, up to $N_{SPS} = 100$, Fig. 5.4e] at a fixed peak fluence of $\phi_0 = 5.4$ J/cm^2. At a low number of laser pulses ($N_{SPS} = 5 - 10$) only HSFL are formed in the ablation craters (Fig. 5.4a, b). However, if a critical pulse number is exceeded ($N_{SPS} \sim 20$), LSFL can be observed at the bottom of the crater (see Fig. 5.4c, d). Interestingly, in Fig. 5.4d HSFL are not visible around the LSFL region, confirming that the HSFL are formed at local fluences very close to the ablation threshold in the regions where the crater edges are formed. For $N_{SPS} = 100$ pulses per spot (Fig. 5.4e), a deep and rough crater has been formed without clear indications of LIPSS. Comparing Figs. 5.4d and e suggests that incubation effects significantly increase the ablation rate for larger N_{SPS}. They are typically originating from the laser-induced formation of defect states and color centers which additionally can cause a change of the absorption behaviour of the material [28]. Those interpulse changes of the optical properties of the irradiated silica are supposedly one origin for the change of the LIPSS morphologies from HSFL towards LSFL.

In Fig. 5.5 the parameter regimes (peak fluence versus number of laser pulses per spot) for the LIPSS formation on quartz are shown. At very high peak fluences and pulse numbers ablation can be observed without the formation of any LIPSS. In contrast, at peak fluences only slightly above the ablation threshold, solely HSFL are observed. Incubation effects lower the ablation threshold for an increasing number of laser pulses [28], a trend which can be seen also in all LIPSS regimes of Fig. 5.5. For intermediate peak fluences both LSFL and HSFL can be observed in the same irradiated spot (even if located in different, spatially separated regions).

5.3.3 LIPSS Formation upon Double-fs-Pulse Irradiation

5.3.3.1 Parallel Polarization

In order to gain additional insights into the mechanisms and dynamics of the LSFL formation in fused silica, a double-fs-pulse experiment was performed to reveal

influences of a "temporally distributed" deposition of optical energy into the material. Starting from the knowledge of the regime of LSFL formation upon irradiation with single-pulse sequences (discussed above), the number of double-fs-pulse irradiation sequences was set to N_{DPS} = 15 while the total accumulated peak fluence $\phi_{0,tot}$ (considering both pulses) was chosen between 3.9 and 4.7 J/cm^2 where only the joint action of both fs-pulses leads to the formation of LIPSS at the sample surface, i.e., conditions close to the LSFL threshold.

At fluences slightly above the damage threshold ($\phi_{0,tot}$ = 3.9 J/cm^2 − 4.7 J/cm^2) for fused silica under conditions for HSFL generation (N_{DPS} = 15), the delay between the fs-pulse pair was systematically varied. For the given conditions, the pulses passing through any individual interferometer arm (while blocking the other arm) were not sufficient to damage the sample surface. HSFL were observed for the joint action of both laser pulses only. Figure 5.6 shows an example of SEM images of surface areas in fused silica irradiated with double-fs-pulse sequences of three different delays (Δt < 1.5 ps) at three different total peak fluences. For the highest fluence [$\phi_{0,tot}$ = 4.7 J/cm^2, Fig. 5.6a], the multiple double-pulse laser sequence can

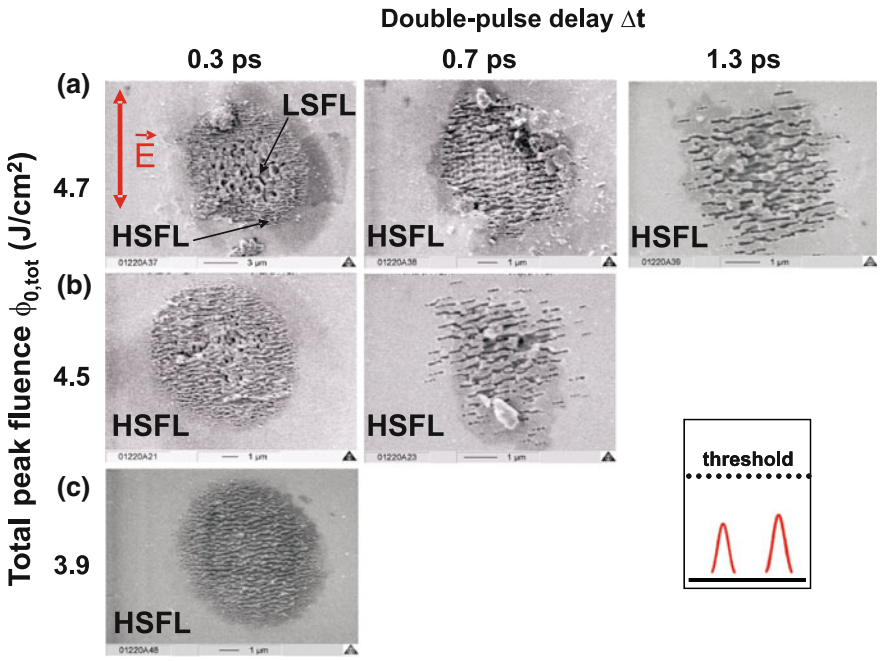

Fig. 5.6 SEM micrographs of a fused silica surface after the exposure to N_{DPS} = 15 parallel polarized double-fs-pulse sequences of varying delays (Δt = 0.3 − 1.3 ps) at three different total peak fluences $\phi_{0,tot}$. **a** 4.7 J/cm^2, **b** 4.5 J/cm^2, **c** 3.9 J/cm^2. At these fluences permanent surface modifications are only visible at the given delays. Note the different magnifications used in the individual micrographs. The direction of the laser beam polarization is indicated in (**a**). The insert visualizes the threshold fluence relation to the peak fluences of the individual pulses in the double-fs-pulse sequence. Data taken from [33]

generate HSFL until a delay of about 1.3 ps. At a lower fluence [$\phi_{0,tot}$ = 4.5 J/cm^2, Fig. 5.6b], the HSFL are formed for delays up to 0.7 ps and for the lowest fluence [$\phi_{0,tot}$ = 3.9 J/cm^2, Fig. 5.6c] the HSFL are observed solely at the shortest delay of 0.3 ps. In all three cases the HSFL are vanishing at delays larger than the maximally chosen ones.

At fluences significantly above the damage threshold ($\phi_{0,tot}$ = 6.7 J/cm^2) and under conditions for LSFL generation (N_{DPS} = 5), the dependence of the surface morphology on the double-pulse delay was analyzed in a similar way. Figure 5.7 shows as an example several SEM images of LIPSS morphologies generated at four different delays Δt between 0.3 and 40 ps. At the shortest delay of Δt = 0.3 ps (Fig. 5.7a), only LSFL are visible within the ablation crater (parallel to the laser beam polarization). For somewhat larger delays of Δt = 1.3 ps, the LSFL area decreases and an annulus is formed around that region in which HSFL can be observed (perpendicular to the polarization, see Fig. 5.7b). At even larger delays of Δt = 6.7 ps both LSFL and HSFL are observed simultaneously while the LSFL area in the central crater region further decreases (Fig. 5.7c). At the longest delay of Δt = 40 ps, the LSFL are vanishing and HSFL are dominating the surface morphology (Fig. 5.7d).

In order to evaluate the impact of the double-pulse delay on the LSFL and HSFL characteristics, SFM measurements were used to quantify (i) the ripple periods of the LSFL and HSFL, (ii) the ripple modulation depth of the LSFL, and (iii) the maximum depth of the ablation craters for the same conditions as previously chosen in Fig. 5.7, i.e., at a total peak fluence of $\phi_{0,tot}$ = 6.7 J/cm^2 and for N_{DPS} = 5. Except the HSFL period all geometrical parameters were determined from cross-sectional

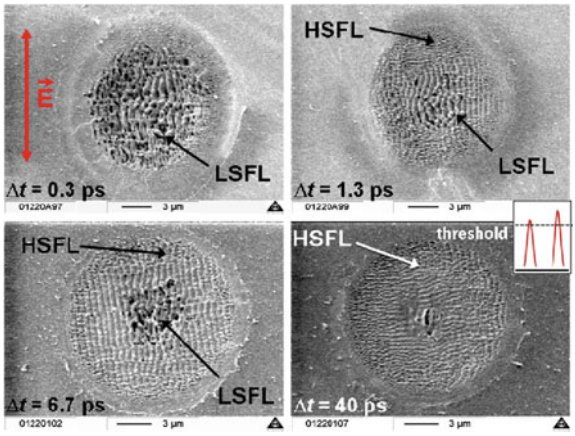

Fig. 5.7 SEM micrographs of a fused silica surface after irradiation with N_{DPS} = 5 parallel polarized double-fs-pulse sequences of varying delays ($\Delta t \leq 40$ ps) at a total peak fluence of $\phi_{0,tot}$ = 6.7 J/cm^2. The direction of the laser beam polarization is indicated in (**a**). The inset illustrates the pulse fluences of the individual pulse in the double-fs-pulse sequence in relation to the threshold fluence. Data taken from [33]

profiles of the SFM-topography close to the center of the laser-irradiated spots with an uncertainty of approx. 10 %. Figure 5.8 shows a compilation of these parameters as a function of the double-fs-pulse delay in a semi-logarithmic representation. At the chosen laser fluence, most characteristic parameters rapidly decrease within less than ∼1.3 ps down to saturation values. The maximum crater depth (full squares) is reduced from ∼1.8 μm close to the zero delay to values between 0.6 and 0.4 μm in the range between 1.3 and 40 ps. Simultaneously, the LSFL modulation depth (full stars) decreases from ∼250 nm down to 50–100 nm. Most strikingly, the LSFL period (full circles) decreases within less than 1 ps from values of ∼750 nm ($\Lambda_{LSFL} \sim \lambda$) down to a saturation value of ∼550 nm ($\Lambda_{LSFL} \approx \lambda/n$, with $n = 1.453$ for fused silica at $\lambda = 800$ nm), as it can be expected from a transition of metallic to dielectric behaviour. In contrast, at the given conditions, the HSFL can be observed only for delays larger than ∼1 ps and their spatial period (open triangles) remains almost constant within the given limit of accuracy at $\Lambda_{HSFL} \approx (375 \pm 25)$ nm up to $\Delta t = 40$ ps delay.

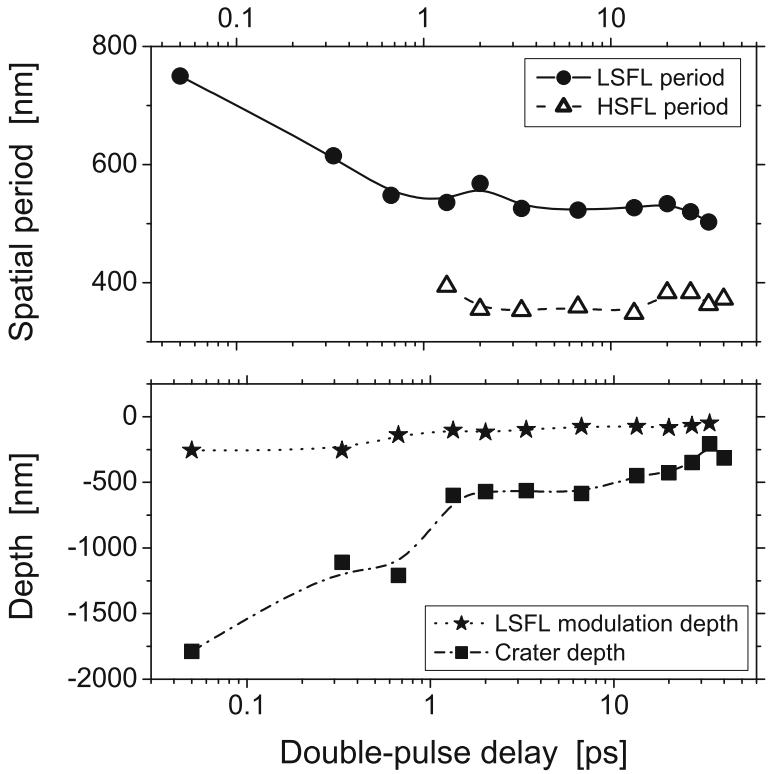

Fig. 5.8 Spatial periods of LSFL and HSFL (*upper graph*), ripple modulation depth, and crater depth (both *lower graph*) in fused silica upon irradiation with $N_{DPS} = 5$ parallel polarized double-fs-pulses at a total peak fluence of $\phi_{0,tot} = 6.7$ J/cm^2 as a function of the pulse delay ($|\Delta t| < 40$ ps). Note the semi-logarithmic scaling. The *lines* guide the eye. Data taken from [33]

5.3.3.2 Crossed Polarization

Upon excitation of fused silica with double-fs-pulse sequences of crossed polarization in which each of the individual fs-pulses has a peak fluence somewhat below the ablation threshold we could observe for the first time a turn over of the LIPSS direction by 90° when the delay changes its sign (and consequently the polarization of the first pulse is oriented perpendicular too) [29]. The LIPSS direction always depends on the polarization direction of the first incident pulse of the sequence, even if its intensity is somewhat less than that of the second one. This applies both for the LSFL and the HSFL and is demonstrated in Fig. 5.9. The rotation of the direction of both ripple types can be seen clearly here. The LSFL are dominant at short delays, however, the HSFL can be observed at longer delays depending on the lifetime of the excited electron plasma in the conduction band of the solid.

For silicon, the effect on crossed polarized fs laser pulses is different. At conditions where the peak fluence of both individual fs-pulse of the double-pulse sequence was below the ablation threshold, the strongest pulse determines the ripple direction (perpendicular to the laser beam polarization, see Fig. 5.10).

The following scenario of LSFL formation upon double-fs-pulse irradiation is proposed here: In fused silica, due to the strong nonlinear interaction of the fs-laser pulses with the material [30], already small variations of the absorbed fluence can lead to strong local changes of the optical material properties, promoting the initially dielectric material locally into a metallic state (associated with a dense electron plasma in the conduction band) [31]. These spatial variations in the absorbed local

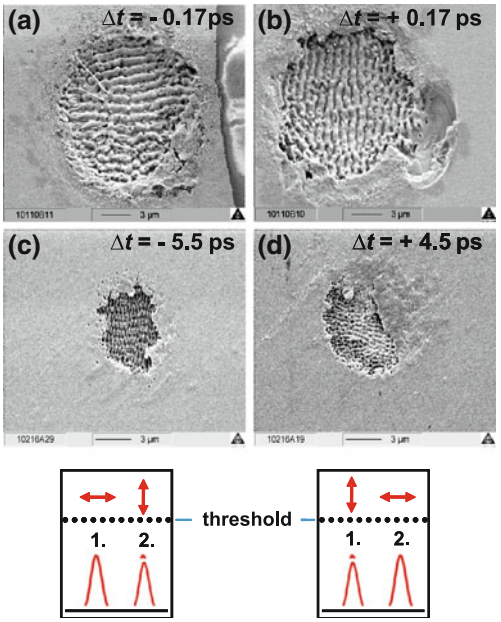

Fig. 5.9 SEM micrographs of a fused silica surface after irradiation with $N_{DPS} = 5$ cross-polarized double-fs-pulse sequences of varying delays ($|\Delta t| < 6$ ps) at a total peak fluence of $\phi_{0,tot} = 5.9$ J/cm^2. LSFL dominate at short delays (**a**, **b**) while HSFL dominate at longer delays (**c**, **d**). The scheme *below* the SEM images illustrates the polarization direction of the first pulse and the pulse fluences in relation to the threshold fluence

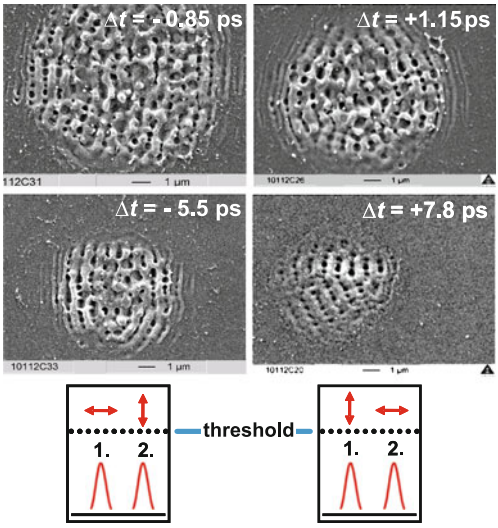

Fig. 5.10 SEM micrographs of a silicon surface after irradiation with $N_{DPS} = 10$ cross-polarized double-fs-pulse sequences of varying delays ($|\Delta t| < 8$ ps) at a total peak fluence of $\phi_{0,tot} = 0.31$ J/cm^2. The scheme *below* the SEM images illustrates the polarization direction of the first pulse and the pulse fluences in relation to the threshold fluence

fluence are caused by interference between the incident laser pulse and a surface scattered electromagnetic wave [4, 32] consequently imprinting an intensity pattern having modulation lengths of the order of the wavelengths. At fluences close to the value required for the generation of LSFL, the first pulse arriving to the sample imprints such a pattern of locally modulated absorptivity (low absorption in dielectric regions, strong absorption in metallic regions) in the central spot area, which is then further "amplified" by the second pulse until the damage threshold of the material is locally exceeded and the surface becomes rippled. Repetitive irradiation by N_{DPS} fs-laser pulse pairs further reinforces the LSFL morphology.

In case of strong laser excitation (high fluences, Figs. 5.7 and 5.8), the metallic state is created within the entire central crater area reducing the local variation of the optical properties and thus discriminating the "amplification effect" by the second pulse. Hence, at small delays Δt, in analogy to metals the formation of LSFL is then favoured which are finally covering almost the entire modified region. At large delays (Figs. 5.7 and 5.8, Δt = 6.7 and 40 ps), significant parts of the energy deposited by the first pulse can relax before the second laser pulse arrives or can be shielded from the sample material by an increased surface reflectivity or by the ablating material both created by the first laser pulse. Hence, the LSFL start to disappear and HSFL become the dominant surface morphology at very large delays.

In silicon, the optical absorption of the laser pulses is rather strong compared to the dielectrics and the formation of LSFL has been already shown to be related to the excitation of surface plasmon polaritons once the initially semiconducting material transiently turns in a metallic state [32]. Since this occurs most efficiently for the strongest fs-pulse in the double-pulse sequence, the orientation of the LIPSS is dominated by that pulse.

5.4 Conclusions

Two different types of fs-LIPSS were observed on silica and quartz surfaces upon irradiation with NIR fs-laser pulse sequences in air environment. In quartz, low-spatial-frequency LIPSS (LSFL) with periods between 500 and 880 nm and an orientation parallel to the laser beam polarization were observed for fluences above ~ 6 J/cm^2 (for ten single pulses). Below that fluence, high-spatial-frequency LIPSS (HSFL) with spatial periods between 170 and 450 nm were found perpendicular to the polarization. Similarly, at a fixed peak fluence a critical number of laser pulses exists above which HSFL transform into LSFL ($N_{SPS} \sim 20$ for $\phi_0 = 5.4$ J/cm^2).

The formation of LSFL and HSFL in fused silica upon irradiation with multiple parallel polarized double-fs-pulses ($\tau = 150$ fs, $\lambda = 800$ nm) was studied experimentally for temporal delays Δt between 0 and 40 ps at different peak fluences. For low fluences close to the damage threshold (where only the joint action of both laser pulses induces LIPSS), predominantly HSFL are observed. The delay range for their appearance is limited to 1–2 ps and significantly shortens with decreasing fluences. In contrast, at high fluences and for sufficiently short delays a transient metallic state is created within the entire central spot area. The second pulse is then interacting with the more metal-like surface favouring the formation of LSFL. The systematic variation of the double-fs-pulse delay revealed a transition of the LSFL spatial period from $\Lambda_{LSFL} \sim 750$ nm $\approx \lambda$ ("metallic behaviour") down to $\Lambda_{LSFL} \sim 550$ nm $\approx \lambda/n$ ("dielectric behaviour") in the sub-ps range, while the HSFL period remains almost constant $\Lambda_{HSFL} \sim (375 \pm 25)$ nm within the entire delay regime up to 40 ps. Our results directly proof the impact of the laser-induced electrons in the conduction band on the LIPSS formation upon fs-laser pulse irradiation of dielectrics and underline the importance of transient changes of the optical properties for the generation of fs-LIPSS.

The formation of LIPSS in fused silica upon irradiation with multiple cross-polarized double-fs-pulses ($\tau = 150$ fs, $\lambda = 800$ nm) was studied experimentally for absolute delays between −20 and +20 ps at different peak fluences. For low fluences (where one pulse only or the joint action of both laser pulses induces LSFL), the polarization of the first laser pulse arriving at the surface determines the orientation of the LSFL even if the energy of this first pulse is smaller than that of the second pulse. In contrast, for silicon the strongest pulse determines the ripple direction even when the fluence of each individual pulse of the double pulse sequence is below the ablation threshold.

Acknowledgments The authors would like to thank M. Tischer (MBI) for taking the SEM images. This work was supported by the German Science Foundation (DFG) under grants no. RO 2074/7-1 and KR 3638/1-1.

References

1. M. Birnbaum, Semiconductor surface damage produced by ruby lasers. J. Appl. Phys. **36**, 3688–3689 (1965)
2. H.M. van Driel, J.E. Sipe, J.F. Young, Laser-induced periodic surface structure on solids: a universal phenomenon. Phys. Rev. Lett. **49**, 1955–1958 (1982)
3. A.E. Siegman, P.M. Fauchet, Stimulated Wood`s anomalies on laser-illuminated surfaces. IEEE J. Quantum Electron. **QE-22**, 1384–1403 (1986) (and references therein)
4. J.E. Sipe, J.F. Young, J.S. Preston, H.M. van Driel, Laser-induced periodic surface structure. I. Theory. Phys. Rev. B **27**, 1141–1154 (1983)
5. D.C. Emmony, R.P. Howson, L.J. Willis, Laser mirror damage in germanium at 10.6 μm. Appl. Phys. Lett. **23**, 598–600 (1973)
6. Z. Guosheng, P.M. Fauchet, A.E. Siegman, Growth of spontaneous periodic surface structures on solids during laser illumination. Phys. Rev. B **26**, 5366–5381 (1982)
7. J. Krüger, Ultrakurze Laserimpulse in der Mikromaterialbearbeitung, Dissertation, BTU Cottbus, 1999
8. J. Bonse, H. Sturm, D. Schmidt, W. Kautek, Chemical, morphological and accumulation phenomena in ultrashort-pulse laser ablation of TiN in air. Appl. Phys. A **71**, 657–665 (2000)
9. G. Dumitru, V. Romano, H.P. Weber, M. Sentis, W. Marine, Ablation of carbide materials with femtosecond pulses. Appl. Surf. Sci. **205**, 80–85 (2003)
10. J. Bonse, S. Baudach, J. Krüger, W. Kautek, M. Lenzner, Femtosecond laser ablation of silicon-modification thresholds and morphology. Appl. Phys. A **74**, 19–25 (2002)
11. J. Bonse, J.M. Wrobel, J. Krüger, W. Kautek, Ultrashort-pulse laser ablation of indium phosphide in air. Appl. Phys. A **72**, 89–94 (2001)
12. A. Borowiec, M. Couillard, G.A. Button, H.K. Haugen, Sub-surface damage in indium phosphide caused by micromachining of grooves with femtosecond and nanosecond laser pulses. Appl. Phys. A **79**, 1887–1890 (2004)
13. S. Baudach, J. Bonse, W. Kautek, Ablation experiments on polyimide with femtosecond laser pulses. Appl. Phys. A **69**(Suppl.), S395–S398 (1999)
14. D. Ashkenasi, A. Rosenfeld, H. Varel, M. Wähmer, E.E.B. Campbell, Laser processing of sapphire with picosecond and sub-picosecond pulses. Appl. Surf. Sci. **120**, 65–80 (1997)
15. M. Lenzner, Femtosecond laser-induced damage of dielectrics. Int. J. Mod. Phys. B **13**, 1559–1578 (1999)
16. Q. Wu, Y. Ma, R. Fang, Y. Liao, Q. Yu, X. Cheng, K. Wang, Femtosecond laser-induced periodic surface structure on diamond film. Appl. Phys. Lett. **82**, 1703–1705 (2003)
17. A. Borowiec, H.K. Haugen, Subwavelength ripple formation on surfaces of compound semiconductors irradiated by femtosecond pulses. Appl. Phys. Lett. **82**, 4462–4464 (2003)
18. T. Crawford, H.K. Haugen, Sub-wavelength surface structures on silicon irradiated by femtosecond laser pulses at 1300 and 2100 nm wavelengths. Appl. Surf. Sci. **253**, 4970–4977 (2007)
19. J. Reif, F. Costache, M. Henyk, M. Pandelov, Ripple revisited: non-classical morphology at the bottom of femtosecond ablation craters in transparent dielectrics. Appl. Surf. Sci. **197–198**, 891–895 (2002)
20. X.J. Wu, T.Q. Jia, F.L. Zhao, M. Huang, N.S. Xu, H. Kuroda, Z.Z. Xu, Formation mechanisms of uniform arrays of periodic nanoparticles and nanoripples on 6H-SiC crystal surface induced by femtosecond laser ablation. Appl. Phys. A **86**, 491–495 (2007)
21. J. Bonse, M. Munz, H. Sturm, Structure formation on the surface of indium phosphide irradiated by femtosecond laser pulses. J. Appl. Phys. **97**, 013583 (2005)
22. T.Q. Jia, H.X. Chen, M. Huang, F.L. Zhao, J.R. Qiu, R.X. Li, Z.Z. Xu, X.K. He, J. Zhang, H. Kuroda, Formation of nanogratings on the surface of a ZnSe crystal irradiated by femtosecond laser pulses. Phys. Rev. B **72**, 125429 (2005)
23. G. Daminelli, J. Krüger, W. Kautek, Femtosecond laser interaction with silicon under water confinement. Thin Solid Films **467**, 334–341 (2004)

24. R. Le Harzic, H. Schuck, D. Sauer, T. Anhut, I. Riemann, K. König, Sub-100 nm nanostructuring of silicon by ultrashort laser pulses. Opt. Express **13**, 6651–6656 (2005)
25. J.F. Young, J.S. Preston, J.E. Sipe, H.M. van Driel, Time-resolved evolution of laser-induced surface structure on germanium. Phys. Rev. B **27**, 1424–1427 (1983)
26. H.M. van Driel, J.E. Sipe, J.F. Young, Laser-induced coherent modulation of solid and liquid surfaces. J. Lumin. **30**, 446–471 (1985)
27. J.M. Liu, Simple technique for measurements of pulsed Gaussian-beam spot sizes. Opt. Lett. **7**, 196–198 (1982)
28. A. Rosenfeld, M. Lorenz, R. Stoian, D. Ashkenasi, Ultrashort-laser-pulse damage threshold of transparent materials and the role of incubation. Appl. Phys. A **69**(Suppl.), S373–S376 (1999)
29. M. Rohloff, S.K. Das, S. Höhm, R. Grunwald, A. Rosenfeld, J. Krüger, J. Bonse, Formation of laser-induced periodic surface structures on fused silica upon multiple cross-polarized double-femtosecond-laser-pulse irradiation sequences. J. Appl. Phys. **110**, 014910 (2011)
30. D. Puerto, J. Siegel, W. Gawelda, M. Galvan-Sosa, L. Ehrentraut, J. Bonse, J. Solis, Dynamics of plasma formation, relaxation, and topography modification induced by femtosecond laser pulses in crystalline and amorphous dielectrics. J. Opt. Soc. Am. B **27**, 1065–1076 (2010)
31. D. Dufft, A. Rosenfeld, S.K. Das, R. Grunwald, J. Bonse, Femtosecond laser-induced periodic surface structures revisited: a comparative study on ZnO. J. Appl. Phys. **105**, 034908 (2009)
32. J. Bonse, A. Rosenfeld, J. Krüger, On the role of surface plasmon polaritons in the formation of laser-induced periodic surface structures upon irradiation of silicon by femtosecond-laser pulses. J. Appl. Phys. **106**, 104910 (2009)
33. A. Rosenfeld, M. Rohloff, S. Höhm, J. Krüger, J. Bonse, Formation of laser-induced periodic surface structures on fused silica upon multiple parallel polarized double-femtosecond-laser-pulse irradiation sequences. Appl. Surf. Sci. **258**, 9233–9236 (2012)

Part III
Laser-Induced Nanostructures: Nanostructures Formation at Metal Surfaces

Chapter 6
Scaling of Grating Spacing with Femtosecond Laser Fluence for Self-organized Periodic Structures on Metal

Shuji Sakabe, Masaki Hashida, Shigeki Tokita, Yasuhiro Miyasaka, Masahiro Shimizu and Shunsuke Inoue

Abstract Periodic structures self-organized on metals irradiated by femtosecond laser pulses were carefully observed, and the spacing of the periodic grating structure is analyzed to determine its dependence on laser fluence. The spacing λ_S is found to be universally $0.5\lambda_L < \lambda_S < 0.85\lambda_L$ for laser wavelength λ_L. Under the hypothesis that the periodic structure corresponds to a surface plasma wave induced by a femtosecond laser pulse, the grating spacing is scaled and formulated in terms of laser fluence so that a simple formula will be available for future study of laser-induced periodic surface structures.

6.1 Introduction

Since the discovery that periodic structures form on mirror surfaces irradiated by laser pulses, the self-organization of periodic structures such as gratings has been actively studied [1]. For picosecond and nanosecond pulses, the formation of the structures is currently attributed to interference between incident light and scattered light. The line spacing of such periodic grating structures is thus given by λ/n $(1 \pm \sin\theta)$, where λ, θ, and n are the laser wavelength, the laser beam incidence angle, and the refractive index of the material, respectively [2–5]. Accordingly, the line spacing is greater than the laser wavelength when the incidence is normal to the surface and $n < 1$ for laser-produced plasma on the surface.

S. Sakabe (✉) · M. Hashida · S. Tokita · Y. Miyasaka · M. Shimizu · S. Inoue
Advanced Research Center for Beam Science, Institute for Chemical Research, Kyoto University, Gokasho, Uji, Kyoto 611-0011, Japan
e-mail: sakabe@laser.kuicr.kyoto-u.ac.jp

S. Sakabe · M. Hashida · S. Tokita · Y. Miyasaka · M. Shimizu · S. Inoue
Division of Physics and Astronomy, Graduate School of Science, Kyoto University, Kitashirakawa, Oiwake-cho, Sakyo, Kyoto-ku 606-8502, Japan

© Springer International Publishing Switzerland 2015

S. Sakabe et al. (eds.), *Progress in Nonlinear Nano-Optics*,
Nano-Optics and Nanophotonics, DOI 10.1007/978-3-319-12217-5_6

Owing to the remarkable advances in intense femtosecond-pulse laser technology, phenomena induced by laser–matter interactions are now observable which are completely inaccessible to picosecond- and nanosecond-pulse lasers. A fundamental phenomenon induced by femtosecond-pulse laser irradiation is the emergence of self-organized periodic grating structures on the surface of a material or inside it. These self-organized structures differ from those mentioned in the introduction in that the line spacing is much shorter than the laser wavelength, which effectively excludes light interference as a possible explanation. Periodic grating structures formed under femtosecond-pulse laser irradiation have been found for metals [6, 7], semiconductors [8, 9], and insulators [10, 11]. Furthermore, the possible applications of such self-organized gratings have been intensively studied and developed for scientific [12, 13] and industrial [14, 15] uses. However, the physical mechanism whereby femtosecond-pulse laser irradiation induces the self-organization of periodic gratings has yet to be explained, with the lone exception of self-organized nano gratings in glass materials. For transparent materials, self-organized grating structures oriented perpendicular to the laser polarization direction have been attributed to the following mechanisms: for glass materials, laser-induced plasma waves in bulk plasma [16, 17]; for diamond-like carbon, the excitation of surface-plasmon polaritons in the surface layer [18]; and for CaF_2, directional atomic surface diffusion anisotropy arising from plasmon-coupled metallic colloid arrays induced by laser pulses [19]. In the reports on those materials, the grating spacings are found to depend on laser fluence and the observed discrete spacings (bifurcation) are discussed. The spacings of grating structures for transparent materials are much shorter than the spacings for metals; therefore, the mechanisms proposed for transparent materials are not applicable to metals.

For metals irradiated with linearly polarized laser light, the grating structures formed on the metal surface are oriented perpendicular to the laser polarization. The line spacing of the grating structures is shorter than the laser wavelength and depends on laser fluence [6, 7, 16–28]. However, the mechanism of self-organization is still under investigation. The characteristics of the structures depend on material properties and laser parameters (fluency, pulse duration, number of pulses, etc.). Even for the same metal, experimental results reported in the literature [6, 7, 16–43] cannot be directly compared if the laser parameters are different. The relation between the type of metal and the line spacing of periodic grating structures has not been investigated, and therefore the amount of systematic experimental data is insufficient for discussing the mechanism at present.

Against this background, our laboratory has systematically investigated the self-organization of periodic grating structures on metals [44]. For interpreting the experimentally observed structures, this chapter presents a laser fluence scaling relation [45] for the line spacing of gratings self-organized on metal surfaces under femtosecond laser pulses. In the literature, the term laser-induced periodic surface structure (LIPSS) has been applied to self-organized grating structures on various surfaces. Therefore, in what follows, we use the phrase “femtosecond LIPSS on metal” to describe the case where the formation of such structures on metal is induced by femtosecond laser pulses.

6.2 Experiments on LIPSS Production and Measurement

Hashida et al. from our laboratory have reported experimentally determined ablation rates [46, 47] and the observation of femtosecond LIPSS on copper (Cu) [7]. That study was the first to show that the LIPSS line spacing depends on laser fluence. We have further refined the experimental techniques to observe the pure phenomena with greater precision [44]. In early work in this area, Hashida et al. scanned the laser pulses along the metal surface, and the laser intensity was not uniform on the metal because of the Gaussian transverse mode of the pulse. Here, a more refined experiment is described. To ablate metals, we used linearly polarized laser pulses (160-fs pulse duration, 800-nm center wavelength, 10-Hz repetition rate) from a Ti:sapphire chirped-pulse amplification laser system (T^6-laser, ICR, Kyoto University). The root-mean-square fluctuation of pulse energy is ±0.3 % [48]. In air, the laser pulses are focused onto the metal by a spherical lens with focal length of 100 mm (*F*/15). The focal spot is 45 μm in diameter. To ensure structural uniformity in the irradiated area on the surface, the spatial distribution of laser intensity is adjusted to be as uniform as a super-Gaussian profile. The laser pulses are directed at normal incidence onto the target surface. The targets are aluminum (Al), gold (Au), Cu, titanium (Ti), platinum (Pt), molybdenum (Mo), and tungsten (W) metals, which were mechanically polished. The roughness, as characterized by the arithmetic mean value, is less than 2 nm for all metals. Through a pair of half-wave plates and two polarizers, the energy is varied in the range of 1.1–34 μJ, corresponding to fluence of 50–2,100 mJ/cm^2. Energy (average of 500 pulses) is measured just before irradiating a target for each laser fluence. The number of irradiating pulses is 50 in all experiments. The irradiated spots are separated by more than 100 μm. Laser-produced surface structures are examined by scanning electron microscopy (SEM; JSM-5560 made in JEOL). The line spacing of a periodic grating is determined by reading the peak value in the frequency domain after taking the Fourier transform for the 20 μm × 15 μm area of the SEM image, which is equivalent to the laser irradiated area on the target. The resolution of the present line spacing measurement is better than 34 nm. The line spacing of the grating structure is determined by analyzing a set of 10 irradiated spots on a metal surface. To evaluate the ablation rate, the crater produced by 200 laser pulses is measured by confocal laser scanning microscopy (HL-150, Lasertec).

Figure 6.1 shows typical SEM images with the map of melting point and thermal diffusion length. Note that an image of lead (Pb) from a preliminary study is also shown, but the Pb specimen was irradiated with a Gaussian transverse mode pulse. For Ti, Pt, Mo, and W LIPSSs are clearly produced, whereas no LIPSS is produced for Cu, Au, Al, or Pb. It can bee seen that metals with a higher melting point are suitable targets for LIPSS production. Al and Mo have almost the same thermal diffusion rate, but only Mo shows clear LIPSS formation.

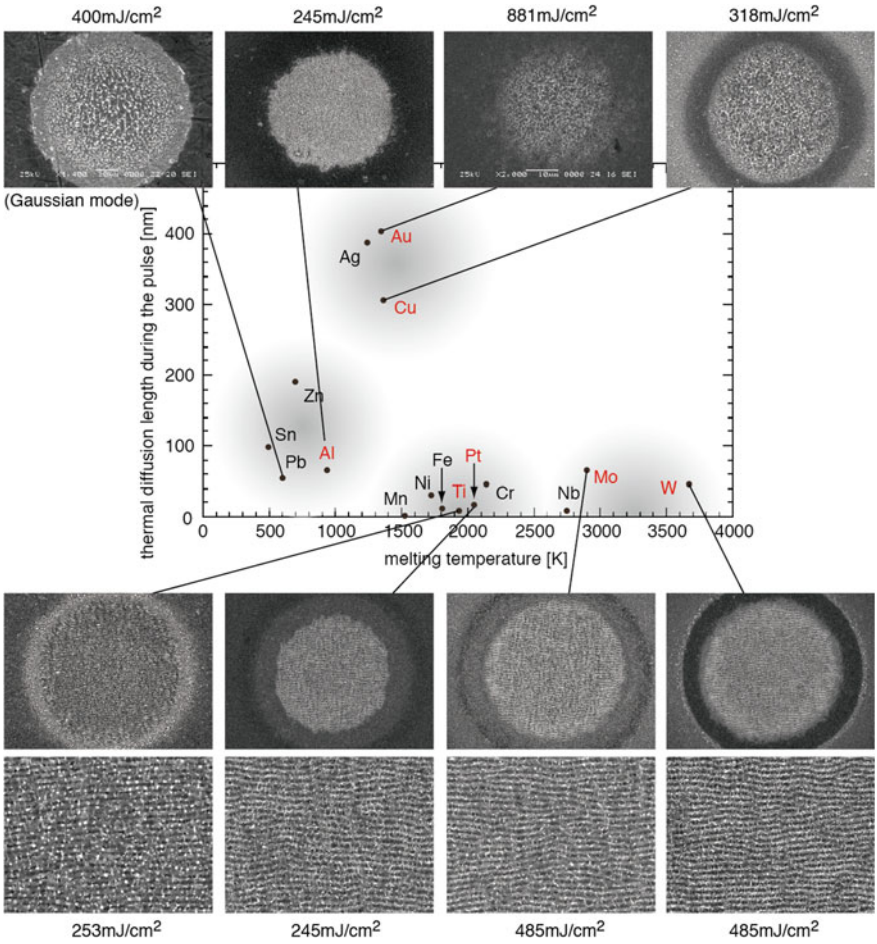

Fig. 6.1 SEM pictures of the metal surface irradiated by super-Gaussian transverse mode femtosecond laser pulses. Metals are mapped on a plot of melting temperature versus thermal diffusion length. Only images in which LIPSS can be seen are magnified. The magnified area is 20 μm × 15 μm

6.3 Features of Femtosecond LIPSS on Metals

Under the present irradiation conditions, LIPSS is not observed on Al, Cu, or Au, but is clearly observed on Ti, Pt, Mo, and W. LIPSSs tend to be produced on metals with a higher melting point. Figure 6.2 shows the relation between laser fluence and LIPSS line spacing on Ti. Femtosecond LIPSS on Ti is characterized by the following features:

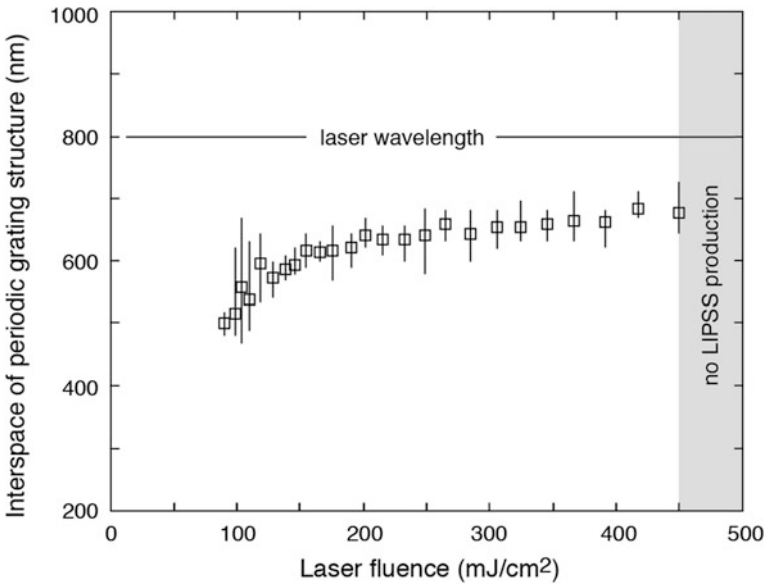

Fig. 6.2 Dependence of LIPSS line spacing on laser fluence for Ti

(1) The gratings are produced perpendicular to the laser polarization plane.
(2) The line spacing depends on laser fluence.
(3) The LIPSS is not formed at >0.45 J/cm^2.
(4) The line spacing is shorter than the laser wavelength (λ = 800 nm) and no LIPSS line spacing of 700–800 nm is observed, that is, the line spacing is shorter than 0.85λ.
(5) The line spacing becomes considerably shorter (about half of the laser wavelength, 0.5λ) near the ablation threshold as the laser fluence is decreased.

None of these features are observed in nanosecond-pulse laser ablation.

6.4 Plasma Waves on Surface

We have proposed an interpretation of the observed LIPSS spacing, where we assume that LIPSS generation occurs through the following process: (1) plasma waves are induced on the surface by the femtosecond laser pulse; (2) spatially localized ion-rich areas Coulomb-exploded into vacuum [49, 50], and consequently the thin layer is ablated and the interspaces of the gratings are printed during the first several pulses (the number of pulses depends on the laser energy fluence, and at certain high fluence values, only a single pulse is involved in this stage and the following one); and (3) the electric field is enhanced near the initially printed

structures by subsequent pulses, and near-field light ablates the surface, thus deepening the grating structures [51–53].

When a plasma wave (electron wave) is driven in a bulk plasma by a laser pulse, the plasma wave dispersion is given by $\omega^2 = \omega_p^2 + 3/2{v_{th}}^2k^2$, where ω and k are the angular frequency and the wavenumber of the plasma wave, v_{th} is the thermal speed of electrons in the plasma, and ω_p is the plasma frequency. From the dispersion, the wavenumber of the plasma wave is $k^2 = (\omega_L^2 - 4\pi n_e e^2/m)m/(3k_B T_e)$, where ω_L is the angular frequency of laser light, k_B is the Boltzmann constant, n_e is the electron density, T_e is the electron temperature, and m is the mass of an electron. Therefore, for a given electron density and temperature, the wavelength of the plasma wave can be any value, shorter or longer than the laser wavelength. The characteristics observed in the experiment thus cannot be explained from this relation.

For nanosecond-pulse laser–matter interactions, the leading edge of a laser pulse heats the solid target, which is converted into plasma. The plasma is heated by the subsequent portion of the pulse and expands at sonic speed. Therefore, the majority of the pulse interacts with the expanding plasma. In laser–bulk plasma interactions, the laser pulse propagates inside the plasma with a dispersion of $\omega^2 = \omega_p^2 + c^2k^2$, where ω and k are the angular frequency and the wavenumber of the electromagnetic wave (laser light), and c is the speed of light in vacuum. The laser pulse cannot propagate to depths beyond the point where $n_e = m\omega^2/(4\pi e^2)$. On the other hand, for femtosecond-pulse laser–matter interactions, even when the peak of a pulse arrives at the surface of the material, the produced plasma is still in close contact with the solid-state matter. The plasma produced by the laser expands at the sonic speed $c_s = (k_B T_e/m)^{1/2}$, and therefore the plasma scale length is of the order of $c_s\underline{\tau}$, where $\underline{\tau}$ is the pulse duration. For instance, the expansion of a 10-eV plasma is only 100 nm during a 100 fs laser pulse. The plasma scale length is sufficiently short for the plasma to form a surface. Therefore, the pulse can interact with the surface formed by the plasma rather than with the bulk plasma.

The dispersion of the surface plasma is given by $ck = \omega\{\varepsilon_1\varepsilon_2/(\varepsilon_1 + \varepsilon_2)\}^{1/2}$ [54, 55], where ε_1 and ε_2 are the respective permittivities of the materials separated by the surface. Here, if we assume that the surface separates plasma from vacuum, then $\varepsilon_1 = 1 - \omega_p^2/\omega^2$ and $\varepsilon_2 = 1$, and a plasma wave (plasmon) can be induced with the following dispersion:

$$ck^2 = \omega^2 \frac{1 - \omega_p^2/\omega^2}{2 - \omega_p^2/\omega^2}.$$

For the case that the laser pulse drives the surface plasma wave directly, the dispersion is schematically shown in Fig. 6.3. Laser light with frequency ω_L cannot be transferred into the plasma wave when $\omega_L > \omega_p/\sqrt{2}$. In order for the condition $\omega_L < \omega_p/\sqrt{2}$ to be fulfilled, the plasma electron density must be greater than 3.5×10^{21} cm^{-3} for 800 nm (375 THz) laser light. If such a high-density plasma is produced on the solid surface, the wavenumber of the plasma wave is larger than that of the laser light, that is, the wavelength of the plasma wave λ_p is $0 < \lambda_p < 800$ nm,

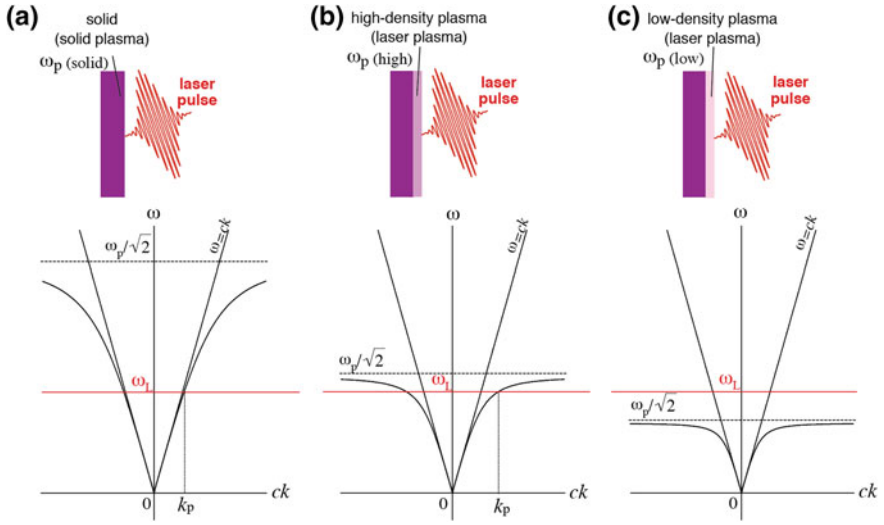

Fig. 6.3 Dispersion of surface plasma waves: **a** solid-state (metal) plasma, **b** high-density laser plasma, and **c** low-density laser plasma. For **a** and **b** the plasma wave can be directly induced, but the wavelengths of the plasma wave are $\lambda_{SP} \sim \lambda_L$ and $0 < \lambda_{SP} < \lambda_L$, respectively. For **c** the plasma wave cannot be directly induced

which is not in agreement with 300 nm $< \lambda_p <$ 700 nm of the experimental result. Even without laser-produced plasma on the metal, surface plasma can be considered when the metal is treated as a solid-state metal plasma. The plasma frequency of metal [56] is on the order of 10^{16} Hz, which is much higher than the frequency of the laser light, and therefore the wavenumber of the plasma wave is comparable with that of the laser light, and then $\lambda_p \approx 800$ nm.

As discussed above, to drive the surface plasma directly by a laser pulse, the plasma density must be high enough to satisfy the condition that $\omega_L < \omega_p/\sqrt{2}$; in that case, the wavelength of the plasma wave will be different from the line spacing of the experimentally observed LIPSS. We have proposed a coupling with low-density plasma. A high-intensity laser pulse can be converted into a surface plasma wave on low-density plasma by a parametric process (Fig. 6.4). The parametric process of photon → photon + plasmon is referred to as stimulated Raman scattering for bulk plasma. The parametric conditions of $\omega_L = \omega_2 + \omega_{SP}$ and $\mathbf{k}_L = \mathbf{k}_2 + \mathbf{k}_{SP}$, where the subscripts L, 2, and SP indicate incident laser light, scattered light, and surface plasma wave, respectively, are reduced to

$$\begin{aligned} \omega_L - \omega_{SP} &= ck_{SP} - ck_L, \\ \omega_L &= ck_L, \\ \omega_{SP}^2 &= c^2 k_{SP}^2 + \frac{1}{2}\omega_p^2 - \left(c^4 k_{SP}^4 + \frac{1}{4}\omega_p^2\right)^{1/2}. \end{aligned}$$

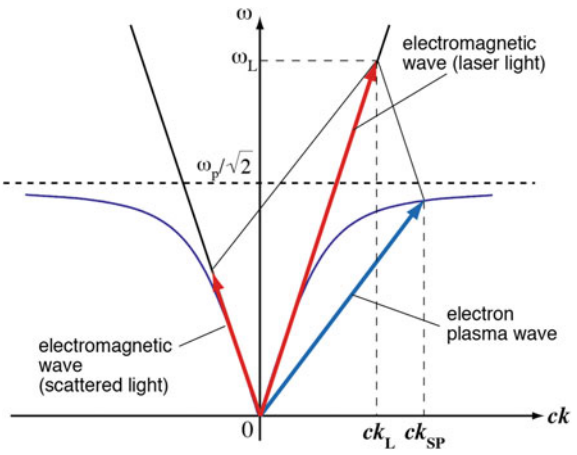

Fig. 6.4 Parametric decay of laser light to a surface plasma wave and scattered electromagnetic wave

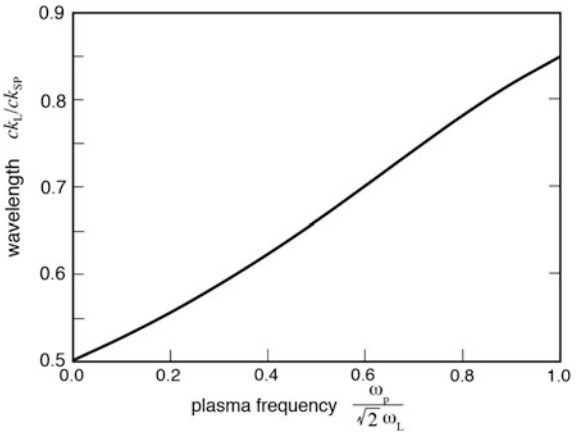

Fig. 6.5 Dependence of the wavelength of plasma wave induced by parametric decay on plasma frequency

The wavenumber of the plasma wave stimulated by the parametric process can be related to the plasma frequency (Fig. 6.5). The k_L/k_{SP} ratio (= λ_{SP}/λ_L, where λ_{SP} and λ_L indicate the wavelengths of surface plasma wave and laser light, respectively) changes from 0.5 to 0.85 for plasma frequencies in the range $0 < \omega_p < \sqrt{2}\omega_L$, where the plasma wavenumber increases as the plasma frequency decreases. The plasma wave travels slowly (Fig. 6.4b), and the group velocity is low. For instance, a plasma wave whose wavelength is 70 % that of the laser light travels at 3×10^{-2} times the speed of light. Even for a laser pulse with duration of 100 fs, the plasma wave moves only 0.9 μm. During this interval, an ion-enriched local area appears, and the ions experience strong Coulomb repulsion until the peak of the next electron wave arrives at that position, which can result in Coulomb explosion [49–52], thus giving rise to the formation of periodic grating structures. The depth of these gratings cannot be estimated in a straightforward manner within this

interpretive framework. Once such structures are formed, an enhancement process might occur. For instance, the grating structures might be enhanced (become deeper) under the influence of localized static electric fields on the surface (near-field effect [53]) during subsequent laser pulses. Furthermore, the parametric excitation of surface plasma waves and the subsequent Coulomb explosion can contribute to the initial printing of periodic grating structures. Here, only the line spacing of the grating structures is discussed.

6.5 Scaling of LIPSS Line Spacing with Laser Fluence

The line spacing of gratings corresponds to the wavelength of the induced plasma wave. As k_L/k_{SP} ($= \lambda_{SP}/\lambda_L$) changes from 0.5 to 0.85, the line spacing changes in the range 400–680 nm. This is in fairly good agreement with the experimental results for laser fluence higher than about 0.08 J/cm^2 (Fig. 6.2), which indicates that when the laser fluence is in the range 0.08–0.45 J/cm^2, the spacings change from 470 to 680 nm. To interpret the scaling of line spacing with laser fluence, the dependence of the surface electron density n_e on the laser fluence F must be known, but this relation has not been established experimentally. The electron density n_e of the plasma bulk produced by the laser on the surface is proportional to the ablation rate, which is usually given by $\ln(F/F_{th})$, where F_{th} is an ablation threshold. The heated plasma bulk with temperature T_e expands at sonic speed $c_s = (k_B T_e/m)^{1/2}$, the surface electron density decreases from the bulk density to n_e/c_s, and the temperature T_e is proportional to the laser fluence F. Therefore, the scaling relation is discussed under the following assumptions.

(1) At the maximum fluence at which LIPSS can be observed (F_M), the plasma (electron) density is $\omega_p = \sqrt{2}\omega_L$.
(2) At the laser ablation threshold (F_{th}), the plasma density is zero ($\omega_p = 0$).
(3) The electron density changes according to $n_e = n_{e0} F^{-1/2} \ln(F/F_{th})$ in the range of $F_{th} < F < F_M$.

Thus,

$$n_e = \frac{m\omega_L^2}{2\pi e^2}\left(\frac{F}{F_M}\right)^{-1/2}\frac{\ln F/F_{th}}{\ln F_M/F_{th}}.$$

For the experimental result shown in Fig. 6.2, the ablation threshold was measured separately and found to be 0.074 J/cm^2. Figure 6.6a shows the scaling under the present interpretation compared with experimental results. Reasonable agreement can be seen.

The orientation of the observed gratings discussed here is perpendicular to the laser polarization plane, and so we may reasonably conclude that the plasma waves are driven by the electric field of the light. The present parametric process model

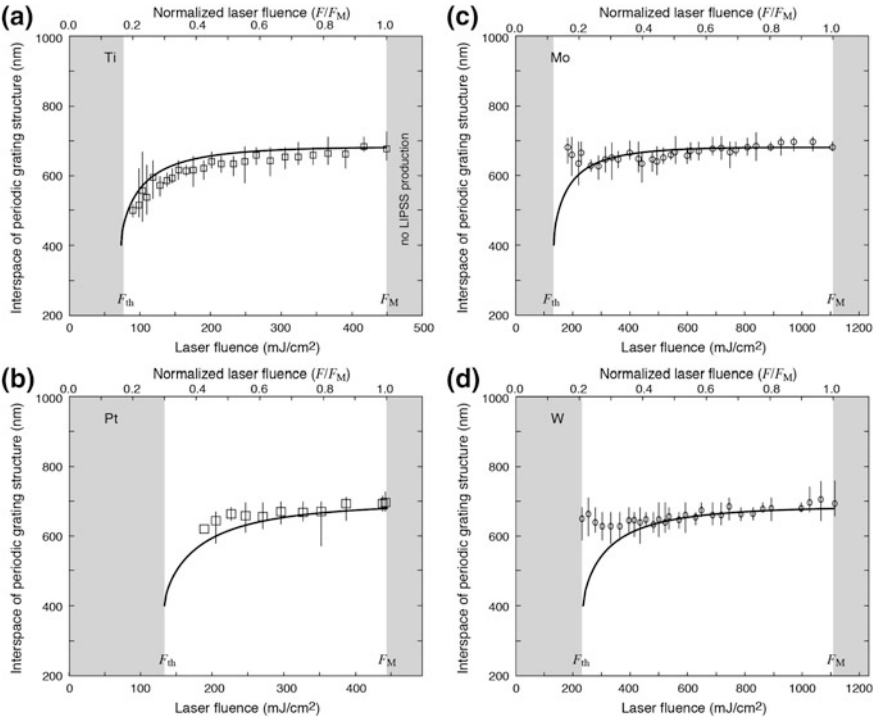

Fig. 6.6 Scaling of LIPSS line spacing with laser fluence: experimental measurement results and calculation results based on the proposed parametric decay model for **a** Ti, **b** Pt, **c** Mo, and **d** W

predicts that the line spacing is 0.5–0.85 times the laser wavelength. Although the line spacing reported for many materials can be explained by this model, ambiguity remains in regard to the plasma (electron) density at the surface. The plasma density depends on the laser fluence, and therefore the dependence of the line spacing on the laser fluence must be established.

6.6 Universal Scaling of LIPSS Line Spacing for Metal

To determine a mechanism that is universally applicable to metals and to obtain a universal scaling relation for LIPSS interspaces, the dependence of line spacing on laser fluence for other metals is examined. Figure 6.6b–d shows the relations for Pt, Mo, and W. The laser fluences that result in LIPSS are different among these metals. However, if the laser fluence is normalized by the maximum fluence F_M and the ablation threshold F_{th} is known, the relations become similar (almost equivalent) to one another and to the relation for Ti (Fig. 6.6a).

From a comparison of Fig. 6.6a, b with Fig. 6.6c, d, differences are seen near the ablation threshold. As laser fluence is decreased, the line spacing does not decrease monotonically; instead, it increases at around 0.25–0.3 F_M. This phenomenon is not yet clearly understood, but here we propose a possible explanation. The surface is defined by the laser-produced plasma and atmosphere, and the laser plasma layer is located on the metal surface. Without laser-produced plasma, the metal surface appears and solid-state plasma forms the surface. With a laser plasma layer on the metal, the laser plasma forms the surface. However, when the plasma layer is thinner than the Debye length, the plasma frequency can no longer be defined by the density of laser plasma layer. For such a case, an effective density must be defined. Then, even near the ablation threshold, the surface plasma density can become as high as that corresponding to $\omega_p = \sqrt{2}\omega_L$. At even high effective plasma density, the wavelength λ_{SP} of the induced plasma wave does not exceed $0.85\lambda_L$, as long as the plasma wave is induced by parametric decay. Figure 6.6c, d show such upper limit near the ablation thresholds. At the moment, for the reason why such increases are not seen for Ti and Pt remains unclear.

6.7 Summary

The formation of femtosecond LIPSSs has been investigated for Al, Au, Cu, Ti, Pt, Mo, and W metals. LIPSSs are formed on only Ti, Pt, Mo, and W, whereas no LIPSS is formed on Al, Au, or Cu. LIPSSs tend to form on metals with a higher melting temperature. To interpret the LIPSS line spacing, we have proposed a mechanism of LIPSS self-organization. The line spacing is determined by the wavelength of the plasma wave induced on the surface (interface between laser plasma and air) by parametric decay of laser light. The wavelength of the plasma wave λ_{SP} scales with the laser fluence F as follows.

$$\lambda_{SP} \cong Ax^3 + Bx^2 + Cx + D$$
$$A = -0.1731, \quad B = 0.316, \quad C = 0.2068, \quad D = 0.5013$$
$$x = \left(\frac{F}{F_M}\right)^{-1/2} \frac{\ln F/F_{th}}{\ln F_M/F_{th}}$$

Here, F_{th} is the fluence at the ablation threshold, and F_M is the maximum fluence at which LIPSS is formed. Near the ablation threshold only, discrepancy is observed for some metals; nonetheless, $0.5 < \lambda_{SP} < 0.85$.

The present scaling has been confirmed even for 400 nm laser wavelength [57].

References

1. D.C. Emmony, R.P. Howson, L.J. Willis, Appl. Phys. Lett. **23**, 598 (1973)
2. A.K. Jain, V.N. Kulkarni, D.K. Sood, J.S. Uppal, J. Appl. Phys. **52**, 4882 (1981)
3. F. Keilmann, Y.H. Bai, Appl. Phys. A Solids Surf. A **29**, 9 (1982)
4. Z. Guosheng, P.M. Fauchet, A.E. Siegman, Phys. Rev. B **26**, 5366 (1982)
5. J.F. Young, J.S. Preston, H.M. van Driel, J.E. Sipe, Phys. Rev. B **27**, 1155 (1983)
6. M. Hashida, M. Fujita, Y. Izawa, A.F. Semerok, in *Laser Precision Microfabrication*, *Proceedings of SPIE*, ed. by I. Miyamoto et al., vol. 4830 (SPIE, Washington, 2002), pp. 452–457
7. M. Hashida, K. Nagashima, M. Fujita, M. Tsukamoto, M. Katto, Y. Izawa, in *Proceedings of the 9th Symposium on Microjoining and Assembly Technology in Electronics*, ed. by K. Atsumi, vol. 9 (Japan Welding Society, Tokyo, 2003), pp. 517–522
8. N. Yasumaru, K. Miyazaki, J. Kiuchi, H. Magara, in *Proceedings of the 3rd Asian Pacific Laser Symposium* (*APLS2002*), ed. by K. Toyoda (Laser Society of Japan, Osaka, 2003), pp. 594–597
9. N. Yasumaru, K. Miyazaki, J. Kiuchi, Appl. Phys. A Mater. Sci. Process. **76**, 983 (2003)
10. J. Reif, F. Costache, M. Henyk, S.V. Pandelov, Appl. Surf. Sci. **197–198**, 891 (2002)
11. F. Costache, M. Henyk, J. Reif, Appl. Surf. Sci. **208–209**, 486 (2003)
12. S. Matsumoto, A. Yane, S. Nakashima, M. Hashida, M. Fujita, Y. Goto, S. Takahashi, J. Am. Chem. Soc. **129**, 3840 (2007)
13. N. Yasumaru, K. Miyazaki, J. Kiuchi, Appl. Surf. Sci. **254**, 2364 (2008)
14. H. Sawada, Rev. Laser Eng. **33**, 525 (2005)
15. T. Katou, N. Abe, M. Yamanaka, K. Matsumoto, Rev. Laser Eng. **36**, 144 (2008)
16. J. Reif, O. Varlamova, F. Costache, Appl. Phys. A Mater. Sci. Process. **92**, 1019 (2008)
17. F. Costache, S. Eckert, J. Reif, Appl. Phys. A Mater. Sci. Process. **92**, 897 (2008)
18. G. Miyaji, K. Miyazaki, Opt. Express **16**, 16265 (2008)
19. Y. Shimotsuma, P.G. Kazansky, J. Qiu, K. Hirao, Phys. Rev. Lett. **91**, 247405 (2003)
20. A.Y. Vorobyev, V.S. Makin, C. Guo, J. Appl. Phys. **101**, 034903 (2007)
21. A.Y. Vorobyev, C. Guo, Appl. Surf. Sci. **253**, 7272 (2007)
22. M. Tsukamoto, K. Asuka, H. Nakano, M. Hashida, M. Katto, N. Abe, M. Fujita, Vacuum **80**, 1346 (2006)
23. V.S. Makin, R.S. Markin, A.Y. Vorobyev, C. Guo, Tech. Phys. Lett. **34**, 387 (2008)
24. A.Y. Vorobyev, C. Guo, J. Appl. Phys. **104**, 063523 (2008)
25. Q.Z. Zhao, S. Malzer, L.J. Wang, Opt. Lett. **32**, 1932 (2007)
26. E.V. Golosov, V.I. Emel'yanov, A.A. Ionin, Yu.R. Kolobov, S.I. Kudryashov, A.E. Ligachev, Yu.N. Novoselov, L.V. Seleznev, D.V. Sinitsyn, JETP Lett. **90**, 107 (2009)
27. J. Wang, C. Guo, J. Appl. Phys. **100**, 023511 (2006)
28. G.A. Shafeev, J. Degert, N. Lascoux, E. Freysz, in *Proceedings of the Conference on Lasers and Electro-Optics* (*CLEO*), Baltimore, Maryland, 2005 (unpublished)
29. A.Y. Vorobyev, C. Guo, J. Appl. Phys. **103**, 043513 (2008)
30. J. Wang, C. Guo, Appl. Phys. Lett. **87**, 251914 (2005)
31. J. Gottmann, D. Wortmann, M. H-Jungemann, Appl. Surf. Sci. **255**, 5641 (2009)
32. A.Y. Vorobyev, C. Guo, Phys. Rev. B **72**, 195422 (2005)
33. J. Kim, S. Na, S. Cho, W. Chang, K. Whang, Opt. Lasers Eng. **46**, 306 (2008)
34. S.E. Kirkwood, A.C. van Popta, Y.Y. Tsui, R. Fedosejevs, Appl. Phys. A Mater. Sci. Process. **81**, 729 (2005)
35. A. Weck, T.H.R. Crawford, D.S. Wilkinson, H.K. Haugen, J.S. Preston, Appl. Phys. A Mater. Sci. Process. **89**, 1001 (2007)
36. A. Weck, T.H.R. Crawford, D.S. Wilkinson, H.K. Haugen, J.S. Preston, Appl. Phys. A Mater. Sci. Process. **90**, 537 (2008)
37. R.V. Volkov, D.M. Golishnikov, V.M. Gordienko, A.B. Savel'ev, JETP Lett. **77**, 473(2003)
38. A.Y. Vorobyev, C. Guo, Appl. Phys. A Mater. Sci. Process. **86**, 321 (2007)

39. B.K. Nayak, M.C. Gupta, K.W. Kolasinski, Appl. Phys. A Mater. Sci. Process. **90**, 399 (2008)
40. V. Oliveira, S. Ausset, R. Vilar, Appl. Surf. Sci. **255**, 7556 (2009)
41. Y. Huang, S. Liu, W. Li, Y. Liu, W. Yang, Opt. Express **17**, 20756 (2009)
42. H. Zhang, M. Tang, J. McCoy, T. Her, Opt. Express **15**, 5937 (2007)
43. Q.Z. Zhao, S. Malzer, L.J. Wang, Opt. Express **15**, 15741 (2007)
44. K. Okamuro, M. Hashida, Y. Miyaaka, Y. Ikuta, S. Tokita, S. Sakabe, Phys. Rev. B **82**, 165417 (2010)
45. S. Sakabe, M. Hashida, S. Tokita, S. Namba, K. Okamuro, Phys. Rev. B **79**, 033409 (2009)
46. M. Hashida, A. Semerok, O. Gobert, G. Petite, J.F. Wagner, in *Nonresonant Laser-Matter Interaction* (*NLMI-10*), *Proceedings of SPIE*, ed. by M.N. Libenson, vol. 4423 (SPIE, Washington, 2000), pp. 178–185
47. M. Hashida, A.F. Semerok, O. Gobert, G. Petite, Y. Izawa, J.F. Wagner, Appl. Surf. Sci. **197–198**, 862 (2002)
48. S. Tokita, M. Hashida, S. Masuno, S. Namba, S. Sakabe, Opt. Express **16**, 14875 (2008)
49. S. Sakabe, K. Shirai, M. Hashida, S. Shimizu, S. Masuno, Phys. Rev. A **74**, 043205 (2006)
50. S. Sakabe, S. Shimizu, M. Hashida, F. Sato, T. Tsuyukushi, K. Nishihara, S. Okihara, T. Kagawa, Y. Izawa, K. Imasakai, T. Iida, Phys. Rev. A **69**, 023203 (2004)
51. M. Hashida, S. Namba, K. Okamuro, S. Tokita, S. Sakabe, Phys. Rev. B **81**, 115442 (2010)
52. Y. Miyasaka, M. Hashida, Y. Ikuta, K. Otani, S. Tokita, S. Sakabe, Phys. Rev. B **86**, 075431 (2012)
53. N. Nedyalkov, T. Miyanishi, M. Obara, Appl. Surf. Sci. **253**, 6558 (2007)
54. V.M. Agranovivh, D.L. Mills (ed.), *Surface Polaritons* (North-Holland, Amsterdam, 1982)
55. A.M. Bonch-Bruevich, M.N. Libenson, V.S. Makin, V.V. Trubaev, Opt. Eng. **31**, 718 (1992)
56. M. Sparks, E. Loh Jr, J. Opt. Soc. Am. **69**, 847 (1979)
57. M. Hashida, Y. Ikuta, Y. Miyasaka, S. Shimizu, S. Tokita, S. Sakabe, Appl. Phys. Lett. **102**, 174106 (2013)

Part IV
Nonlinear Nano-Optics: Plasmonic Nanostructures and Metamaterials

Chapter 7
Interplay Between Strong Coupling and Radiative Damping in Hybrid Excitonic-Plasmonic Nanostructures

Ralf Vogelgesang, Wei Wang, Parinda Vasa, Robert Pomraenke, Ephraim Sommer, Antonietta De Sio and Christoph Lienau

Abstract Surface plasmon polaritons (SPPs), optical excitations at the interface between a metal and a dielectric, carry significant potential for guiding and manipulating light on the nanoscale (Bozhevolnyi et al. Nature 440(7083):508–511, 2006; Lal et al. Nat Photonics 1(11):641–648, 2007; Maier et al. Nat Mater 2 (4):229–232, 2003). Their weak optical nonlinearities, however, hinder active device fabrication, e.g., for all-optical switching (Chang et al. Nat Phys 3(11):807–812, 2007; Dintinger et al. Adv Mater 18(13):1645, 2006; MacDonald et al. Nat Photonics 3(1):55–58, 2009; Vasa et al. ACS Nano 4:7559–7565, 2010) or information processing (Engheta Science 317(5845):1698–1702, 2007; Gonzalez-Tudela et al. Phys Rev Lett 106:020501, 2011). Recently, strong optical dipole coupling between SPPs and nonlinear quantum emitters with normal mode splittings of up to 700 meV has been demonstrated (Aberra Guebrou et al. Phys Rev Lett 108:066401(5p), 2012; Bellessa et al. Phys Rev Lett 93:036404, 2004; Dintinger et al. Phys Rev B 71:035424, 2005; Fofang et al. Nano Lett 8:3481–3487, 2008; Hakala et al. Phys Rev Lett 103(5):053602, 2009; Sonnefraud et al. ACS Nano 4(3):1664–1670, 2010). The predicted ultrafast energy transfer between quantum emitters and SPP fields could be a crucial microscopic mechanism for switching light by light on the nanoscale. Here, we present the first real-time observation of ultrafast Rabi oscillations in a J-aggregate/metal nanostructure, evidencing coherent energy transfer between excitonic quantum emitters and SPP fields. We demonstrate coherent manipulation of the coupling energy by controlling the exciton density on a 10-fs timescale, a step forward towards coherent, all-optical ultrafast plasmonic circuits and devices. We report on the interplay between strong coupling and radiative damping of strongly coupled excitons (Xs) and surface plasmon polaritons (SPPs) in a hybrid system made of J-aggregate and metal nanostructures. The optical response of the system is probed at the field level by angle-resolved spectral interferometry.

R. Vogelgesang (✉) · W. Wang · P. Vasa · R. Pomraenke · E. Sommer
A. De Sio · C. Lienau
Institut für Physik, Carl von Ossietzky Universität, 26111 Oldenburg, Germany
e-mail: ralf.vogelgesang@uni-oldenburg.de

C. Lienau
e-mail: christoph.lienau@uni-oldenburg.de

© Springer International Publishing Switzerland 2015

S. Sakabe et al. (eds.), *Progress in Nonlinear Nano-Optics*,
Nano-Optics and Nanophotonics, DOI 10.1007/978-3-319-12217-5_7

We show that two different energy transfer channels coexist: coherent resonant dipole-dipole interaction and an incoherent exchange due to the spontaneous emissions of a photon by one emitter and subsequent reabsorption by another. The interplay between both pathways results in a pronounced modification of the radiative damping due to formation of super- and sub-radiant polariton states. This is confirmed by probing the nonlinear response of the polariton system and explained within a coupled oscillator model. Such a strong modification of the radiative damping opens up new directions in coherent active plasmonics.

7.1 Introduction

Metallic nanostructures can bind electromagnetic radiation to their surfaces in a phenomenon called surface plasmon polaritons (SPPs) [4, 8, 34, 39]. Recently SPPs have been used in a rapidly expanding array of applications, thanks to their ability to guide light on ultrashort length and time scales. Even further exploitation is looming, once the intrinsic flaws of weak optical nonlinearities and short propagation lengths of SPPs can be overcome [52]. Providing the missing nonlinearity and gain is a key step towards realizing novel active plasmonic devices, which combine the size scalability of electronics with the operational bandwidth of photonics. One promising avenue to this goal is the coupling of SPPs to nonlinear optical resonances such as excitons (Xs) in molecular or semiconducting nanostructures. This approach has been championed for various device classes such as all-optical [1, 15, 40, 50, 56] and plasmonic switches [2, 35, 44, 45, 55] single-photon transistors [10, 24], and nanolasers [7, 14, 30, 33, 41–43, 51, 61]. Hybrid excitations in such systems can blend the favorable light-localization properties of SPPs with the enhanced nonlinearities of active quantum emitters. And the coupling strength between the excitonic optical dipole moment and the vacuum SPP field may even exceed their individual linewidths, resulting in the formation of hybrid X-SPP modes with energy splittings approaching the X resonance energy [5, 13, 19, 26, 50].

From a dynamical perspective, strong X-SPP coupling results not only in a radiative exchange of energy with the environment. Also, the two systems couple to each other radiatively and exchange energy between them [11, 25, 60]. Two distinct types of interactions can contribute [3, 27, 36, 48, 49, 54]: (i) The resonant dipole-dipole interaction induces a *coherent* exchange of photon energy between the two emitters, which preserves the relative phase between their optical polarizations. This exchange leads to the well-known formation of hybridized states [11, 13, 16]. (ii) An *incoherent* exchange of photon energy is possible, when one system emits a photon spontaneously, which is then reabsorbed by the second. Both types exist even in the absence of any external excitations, as they are both mediated by vacuum field fluctuations vacuum field fluctuations [6, 62]. Their interplay alters both the energetics and the dynamics of the system, i.e. energetic mode splitting occurs in conjunction with

in cooperative emission phenomena known as sub- and super-radiance [12]. Such modified damping rates are important in many strongly coupled systems such as trapped ions [11], molecular aggregates [31], excitonic quantum dots [9] and wells [23], and plasmonic excitations in nanostructures [37, 46, 53, 59].

7.2 A Prototype Hybrid System

In recent years the combination of J-aggregate molecular excitons and surface plasmon polaritons has emerged as a convenient sample system for the study of hybrid nanostructures [5, 13, 22, 50, 56, 57]. Their radiative properties exhibit a wide variability as a function of angle of incidence. Coherent coupling energies as large as several hundreds of meV have been demonstrated [5, 13, 50, 56]. In addition, subradiant and super-radiant X-SPP hybrid states are distinctly observable, in particular at zero detuning angle. This points to vacuum-mediated *incoherent* exchange processes, because for *coherent* interactions alone, one would expect equal damping rates at zero detuning. This explanation is corroborated by real-time measurements of ultrashort polariton dynamics. We find Rabi oscillations between the excitons and SPPs, whose period and thus the optical nonlinearity of this hybrid nanostructure is parametrically modulated on an ultrafast 10 fs time scale.

To appreciate these characteristics, we consider first the two individual systems separately. Figure 7.1 shows typical reflectivity spectra of a bare dye film, deposited on a smooth gold surface. A strong molecular resonance manifests itself at a wavelength of $\lambda = 693\,\text{nm}$. Evidently, this spectral feature is independent of the angle of incidence. The molecular ensemble acts in a perfectly satisfactory description as a single two-level system, without any spatial dispersion.

In contrast, a grating structure, carved into a smooth gold surface, exhibits a pronounced spatial dispersion, with strong spectral absorption features whose resonance energies shift considerable with angle of incidence, as can be seen in Fig. 7.2. This dispersion is a manifestation of the inherent dispersion of surface

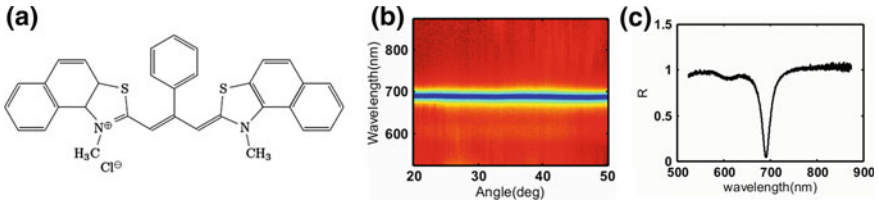

Fig. 7.1 Angle-resolved, p-polarized linear reflectivity spectra of a 50 nm-thick film of J-aggregate molecules in a polymer matrix coated onto a gold surface. **a** Molecular structure of the dye. **b** Spectral reflectivity measurements for wavelengths between 500 and 900 nm as a function of angle of incidence between 20° and 50°, showing essentially no dispersion of the reflectivity with angle of incidence. **c** Typical single reflectivity spectrum, showing the dispersionless feature at $\lambda = 693\,\text{nm}$ (1.789 eV) due to J-aggregate molecules

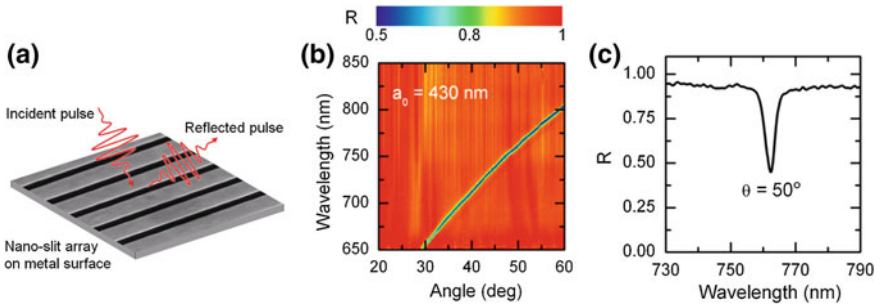

Fig. 7.2 Angle-resolved, p-polarized linear reflectivity spectra of a nano-slit array on gold film. **a** Schematic of the grating structure excited by an ultrashort pulse. **b** Spectral reflectivity measurements of a $a_0 = 430\,\text{nm}$ for wavelengths between 650 and 850 nm as a function of angle of incidence between 20° and 60°, exhibiting a clear dispersion of the reflectivity with angle of incidence due to the grating wavevector matching condition. **c** Typical reflectivity spectrum, taken at $\theta = 50°$, showing a *narrow* absorption feature at $\lambda = 763\,\text{nm}$ due to the excitation of surface plasmon polaritons

plasmons on the one hand, and their coupling to the incident photonic modes being facilitated by the periodic grating structure on the other hand. The grating compensates the wavevector mismatch between these two dispersions, folding back the surface plasmon polariton dispersion into the first Brillouin zone associated with its periodicity.

Another characteristic of the grating slits are their sharp geometric features, which has a significant impact on the distribution of local electromagnetic fields. At corners and edges with deeply sub-wavelength radius of curvature, surface plasmons exhibit a marked tendency to be enhanced. The numerical simulations

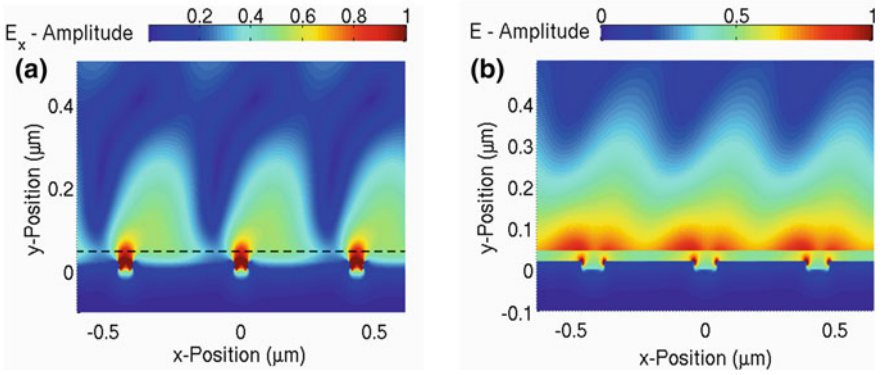

Fig. 7.3 Electric field amplitude inside a gold grating coated with a 25 nm-thick polymer matrix, plotted in the plane of incidence of the exciting radiation. Resonant excitation as in Fig. 7.2c results in strongly localized field amplitudes. **a** The **E**-component along the direction parallel to the solid-air interface is most intense near the edges of the grating slits, dropping rapidly away from them. **b** The total field amplitude $|\mathbf{E}|$ exhibits a similar localization, with somewhat less contrast

illustrated in Fig. 7.3 represent a typical case of this effect. In particular the electric field strength appears strongly enhanced in the rather small region between the two neighboring edges of each slit. In the larger area between slits, a considerably lower field strength is observed. This is already an indication that a homogeneous film of dye molecules might exhibit two different regimes of optical interactions. Molecules situated between slits can be expected to respond to incident photons very much like the films that have been discussed in Fig. 7.1—with essentially no spatial dispersion. In contrast, molecules in volumes near the slit edges may experience rather strong coupling with the grating-enabled surface plasmons polaritons.

Figure 7.4 shows schematically how strong coupling between excitons and surface plasmon polaritons may lead to pronounced effects on their respective dispersions. In the Brillouin zone picture, depicted in Fig. 7.4a, a crossing may occur between the dispersionless exciton resonance and the SPP dispersion. Exactly at this point in the frequency-wavevector map, coupling between the two individual systems leads to an energy level splitting, as shown in Fig. 7.4b. In the vicinity of this so-called "zero detuning" point, the level splitting results in the formation of two anti-crossing exciton-surface-plasmon polariton dispersion branches. The energetically higher branch is called the "upper polariton" (UP) and correspondingly the lower branch "lower polariton" (LP). At zero detuning, the UP and LP branches represent entirely new physical systems with a 50–50 mixture of both surface plasmonic and excitonic character. Far off the anticrossing point the physical nature of the coupled systems may be qualified to as predominantly "SPP-like" or "exciton-like".

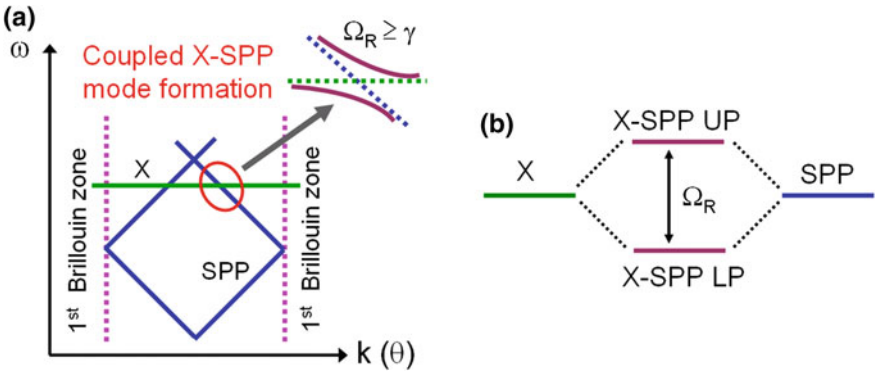

Fig. 7.4 Schematic of the formation of coupled exciton-plasmon-polariton modes. **a** Diagram of the dispersions of an uncoupled dye film and a smooth gold/dielectric interface in frequency (ω) and wavevector (k) space. The periodic grating structure gives rise to a Brillouin zone, into which the surface plasmon polaritons dispersion is back folded (Adapted from Naure Photonics 7,128132 (2013)). **b** Near the crossing of this grating plasmon dispersion and that of the dye, exciton-plasmon coupling leads to the formation of coupled polariton modes. In case of strong coupling, the two branches split into distinctly observable *upper* and *lower* polariton dispersions

7.3 Experimental

7.3.1 Sample Fabrication

We investigated J-aggregate/metal hybrid nanostructures made of gold nanoslit arrays ($150 \times 150\ \mu m^2$) with periods of 400–460 nm fabricated by focused ion beam milling (FEI Helios NanoLab 600(i)). The 50 nm dye film coatings were prepared from the cyanine dye $2,2'$-dimethyl-8-phenyl-5,6,5′,6′-dibenzothiacarbocyanine chloride (Hayashibara Biochemicals Laboratories, Inc.) dissolved in polyvinyl alcohol (PVA 80 % hydrolyzed, Sigma Aldrich, 26 mg), methanol (4 ml) and water (1 ml). The concentration of the dye in dry PVA is typically $0.5\ mol/dm^3$, with an optical density of 0.4 [56]. The J-aggregate exciton resonance is observed at ~ 1.79 eV [46, 56]. A slit-array period is chosen so that its first order polymer-metal plasmon mode coincides in energy with the exciton and the SPP radiative damping rate is minimized, which in the present the case is found for a depth of 30 nm and a width of 45 nm [29, 46].

7.3.2 Spectral Interferometry

The high-resolution, angle-resolved spectral interferometry setup is indicated schematically in Fig. 7.5a [46, 47]. All experiments are performed using an angle-resolved reflectivity setup with an angular resolution of $\delta\theta = 0.2°$. For the linear reflectivity spectra, p-polarized broadband pulses (1.6–2.0 eV) from an ultrafast coherent white-light source (Fianium SC-450-4) with 80 MHz-repetition rate are used. They are split into sample and reference pulses in a balanced and chirp-compensated Mach-Zehnder interferometer. We record the complex sample response, i.e., the reflection coefficient

$$r(\omega) = \sqrt{R_0(\omega)}e^{i\varphi(\omega)} = \frac{E_s(\omega)}{E_r(\omega)}, \tag{7.1}$$

where, $E_s(\omega)$ and $E_r(\omega)$ are the electric field amplitudes of the reflected sample and the reference beam at frequency ω, respectively. $R_0(\omega)$ is the intensity of the reflectivity spectrum, measured non-interferometrically. And the spectral phase $\varphi(\omega)$ can be obtained independently from an interferometric measurement. With the help of an adjustable delay τ between the two interferometer arms a set of interference fringes with deliberate spacing $\omega\tau$ is generated according to

$$\begin{aligned}\left|E_s(\omega) + E_r(\omega)e^{-i\omega\tau}\right|^2 = &\left(1 + |r(\omega)|^2\right)|E_r(\omega)|^2 \\ &+ 2|E_r(\omega)||E_s(\omega)|\cos(\omega\tau + \varphi(\omega)).\end{aligned} \tag{7.2}$$

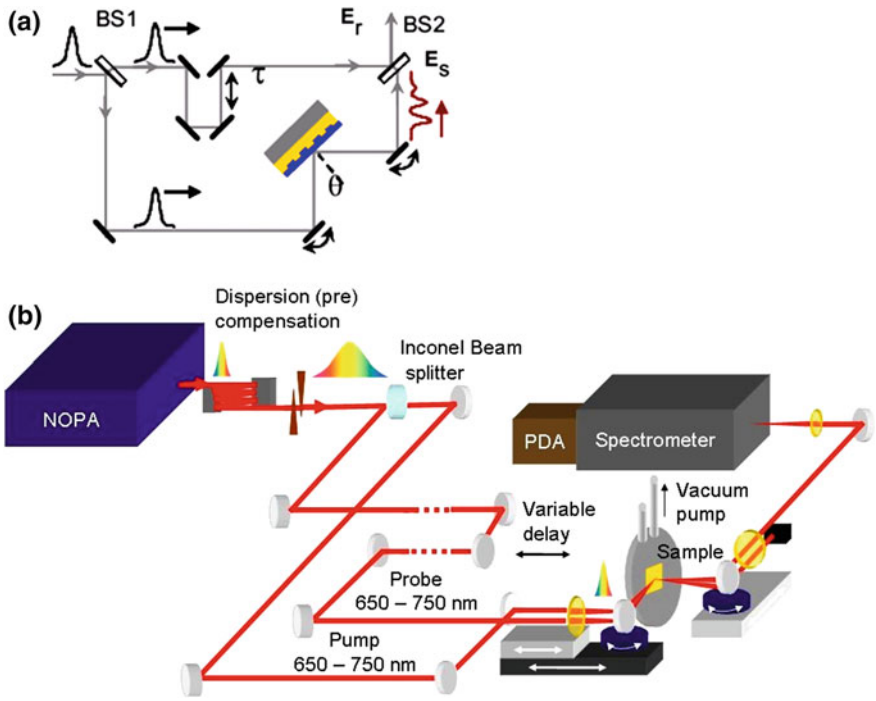

Fig. 7.5 Schematics of the experimental setups. **a** Angle-resolved spectral interferometry setup. *BS* Beam splitter, τ variable delay (Adapted with permission from [60]. Copyright (2013) American Chemical Society). **b** Femtosecond pump-probe spectrometer. Ultrashort pulses with a spectrum extending from 650 nm (1.9 eV) to 750 nm (1.65 eV) are derived from a non-collinear optical parametric amplifier (NOPA) operating at a repetition rate of 1 kHz. The p-polarized pulses are compressed to sub-15 fs duration using chirped mirrors, split into a pair of pump and probe pulses with variable delay τ and are focused nearly collinearly onto the sample at a variable angle of incidence θ. Differential reflectivity spectra $\Delta R/R$ are recorded using a spectrometer equipped with a linear photodiode array (Reprinted from Nature Photonics 7, 128132 (2013))

As the corresponding cosine term indicates, an analysis of the deviations from the imposed spacing yields the spectral phase $\varphi(\omega)$.

Transient $\Delta R/R$ measurements are performed in a femtosecond pump-probe spectrometer, depicted in Fig. 7.5b. The first stage of the light source is a regeneratively amplified, mode-locked Ti:Sapphire laser system (Quantronix Integra C) operating at a repetition rate of 1 kHz and with 1.6 eV photon energy. The emitted pulses have a duration of 150 fs and an energy of 500 μJ. This system drives a non-collinear optical parametric amplifier (NOPA), which generates broadband near-infrared pulses centered at 1.8 eV and with a spectrum extending from 1.65 to 1.9 eV. Before the NOPA pulses are split into a pair of p-polarized pump and probe pulses, the dispersion they suffer along the optical path is pre-compensated by multiple bounces on chirped mirrors (Venteon) so that at the sample they have

sub-15 fs duration. They are slightly displaced vertically, along the axis of the spectrometer entrance slit. At the sample, they coincide in a focus area of ~ 100 μm at an angle of incidence of about 30° with respect to the sample normal. For improved suppression of interference artifacts in the ΔR spectra, one of the pump beam mirrors is vibrated. All experiments are performed at room temperature. To minimize J-aggregate photobleaching, the sample is held under vacuum conditions.

7.4 Theoretical Modelling

7.4.1 Linear Optical Response of Bare Dye Film

The linear optical response of J-aggregates can be described phenomenologically with a susceptibility that features two Lorentzian-type resonances,

$$\chi(\omega) = \sum_{k=1}^{2} \frac{A_k e^{i\phi_k}}{(\omega_{0,k}^2 - \omega^2 - i\omega 2\gamma_k)}. \tag{7.3}$$

One represents the strong and narrow resonance centered around 1.79 eV and the other denotes the broad and weak monomer shoulder at around 2.0 eV. The dielectric function of a dye film prepared as a solution of J-aggregate molecules is given by

$$\varepsilon_m = 1 + f\,\chi(\omega) + (1 - f)\chi_{PVA}. \tag{7.4}$$

Here, the filling factor $f = 0.1$ depends on the concentration of J-aggregates, and the susceptibility of PVA is taken as approximately constant, $\chi_{PVA} = 1.4$, over the relevant frequency range. With this description, both the reflectivity spectrum R_X and spectral phase φ_X of a bare dye film on gold such as the one used in Fig. 7.1 can be analyzed simultaneously. A numerical fit to the normalized complex optical response $r_{norm} = r_{dye}/r_{gold}$ of the air/dye/gold layered system (described in a transfer matrix formalism) yields the unknown parameters $\{A_k, \phi_k, \omega_{0,k}, \gamma_k\}$. Here r_{dye} is the reflection coefficient of the whole layered system and r_{gold} is the reflection coefficient measured on uncoated gold film.

7.4.2 Coherent and Incoherent Coupling Mechanisms

Both the ensemble of exciton modes and that of SPP modes may be considered as a single oscillator. They are described by complex eigenfrequencies ($\tilde{\omega}_X = \omega_X - i\gamma_X$ for the X-system and $\tilde{\omega}_P = \omega_P - i\gamma_P$ for the SPP-system). Their real parts represent

the eigenenergies ($\hbar\omega_X$ and $\hbar\omega_P$) and their imaginary parts the population damping rates ($\gamma_X = \Gamma_X/2$ and $\gamma_P = \Gamma_P/2$) due to radiative or non-radiative processes.

Strong coupling between excitons and plasmons is characterized on the one hand by a Hermitian matrix element $\hbar\Omega_R$ that is large compared to the damping terms $\hbar\gamma_X$ and $\hbar\gamma_P$. In case of mutual resonance, the excitonic and plasmonic subsystems may coherently exchange energy with an oscillation frequency referred to as Rabi frequency Ω_R. On the other hand, an incoherent interaction channel is available, in which the systems amplitudes exhibit no fixed phase relation. This process is the result of spontaneous emission by one system of photons into the vacuum which are reabsorbed by the other. Its characteristic is an anti-Hermitian matrix element $\hbar\gamma_{XP}$, referred to as generalized (or cross-) damping term [3, 32, 38, 49].

It should be noted that both the coherent and incoherent interactions emerge only as a property of the strongly coupled hybrid system [3]. They cannot be attributed to either of the individual X or SPP system alone. As we will see later, both types of interactions play important roles in the present case, resulting in the observed sub- and super-radiance of the hybridized modes. To describe the coherent and incoherent processes algebraically, we employ a coupled oscillator model with a 2×2 matrix [46, 58]

$$H = \hbar\left[\begin{pmatrix} \tilde{\omega}_X & \Omega_R \\ \Omega_R^* & \tilde{\omega}_P \end{pmatrix} - i\begin{pmatrix} 0 & \gamma_{XP} \\ \gamma_{XP} & 0 \end{pmatrix}\right]. \tag{7.5}$$

By diagonalizing this coupling matrix, the hybrid superposition modes of the coupled system are found.

7.4.3 Hybrid X-SPP Modes

The coupled polariton modes that characterize the system of interacting excitons and surface plasmons give rise to the linear and differential reflectivity spectra measured for such systems. They are simulated by solving optical Bloch equations using the density matrix formalism. In these simulations, the exciton system is modeled as an effective two-level-system consisting of ground state $|0\rangle$ and one excited state $|X\rangle$. Any biexcitonic contributions may be neglected. The SPP mode is described as a photon-like harmonic oscillator that is only weakly excited out of its ground state, i.e., only the lowest excited state $|P\rangle$ has to be considered, rendering the SPPs also an effective two-level system. The simulations include the dipole coupling between X and SPP. In addition, the action of the external laser field is considered with a semiclassical coupling to both systems. Radiative damping and pure dephasing of excitons is implemented phenomenologically in a Lindblad formalism [3].

Without delving further into the finer points of the justification for the 2 × 2 model, we discuss here the consequences. The eigenvalues of the matrix (7.5) are directly related to the complex eigenenergies of the hybrid mode energies—and thus, when viewed as a function of angle of incidence, also to their dispersions. We obtain

$$\tilde{\omega}_{UP} = \left(\frac{\tilde{\omega}_X + \tilde{\omega}_P}{2}\right) + \sqrt{\frac{\Delta^2}{4} + \left(|\Omega_R|^2 - \gamma_{XP}^2\right) - 2i\gamma_{XP}\Re(\Omega_R)}, \tag{7.6}$$

$$\tilde{\omega}_{LP} = \left(\frac{\tilde{\omega}_X + \tilde{\omega}_P}{2}\right) - \sqrt{\frac{\Delta^2}{4} + \left(|\Omega_R|^2 - \gamma_{XP}^2\right) - 2i\gamma_{XP}\Re(\Omega_R)}, \tag{7.7}$$

for the upper and lower polariton mode frequency, respectively. $\Delta = \tilde{\omega}_X - \tilde{\omega}_P$ is the difference of the complex exciton and plasmon frequencies. Its real part expresses the detuning.

The significance of the cross-damping term $\hbar\gamma_{XP}$ becomes evident, when we consider the implications of (7.6) and (7.7) for the imaginary parts of the eigenenergies of the polaritons. At zero detuning ($\Re\Delta = 0$) and in the strong coupling regime ($|\Omega_R|^2 > \gamma_{XP}^2$) a difference in the damping rates of the hybrid modes (the imaginary parts of the mode frequencies) can be found only if the last term under the root does not vanish, that is, $\gamma_{XP}\Re(\Omega_R) \neq 0$. Only if the incoherent coupling coefficient γ_{XP} is not zero do the two hybrid modes exhibit different damping rates.

The coherent superposition of X and SPP wavefunctions that form the hybrid X-SPP polariton modes are given by the associated eigenvectors of the coupling matrix (7.5),

$$|UP\rangle = \frac{1}{B_+}\{(\Delta + A)|X\rangle + 2D|P\rangle\}, \tag{7.8}$$

$$|LP\rangle = \frac{1}{B_-}\{(\Delta - A)|X\rangle + 2D|P\rangle\}. \tag{7.9}$$

Here $B_\pm = \sqrt{|\Delta \pm A|^2 + 4|D|^2}$ are normalization constants and A is (twice) the square root term from (7.6) and (7.7), written in the more compact form $A = \sqrt{\Delta^2 + 4CD}$, with $C = \Omega_R - i\gamma_{XP}$ and $D = \Omega_R^* - i\gamma_{XP}$.

7.5 Results

Measured angle-dependent reflectivity amplitude ($R_0(\omega)$) and phase ($\varphi(\omega)$) spectra are shown in Fig. 7.6a, b, respectively. A clear signature of anti-crossing behavior of the X and SPP is observed, corroborating that strong X-SPP coupling results in the formation of hybrid UP and LP polariton modes. In addition, a significant

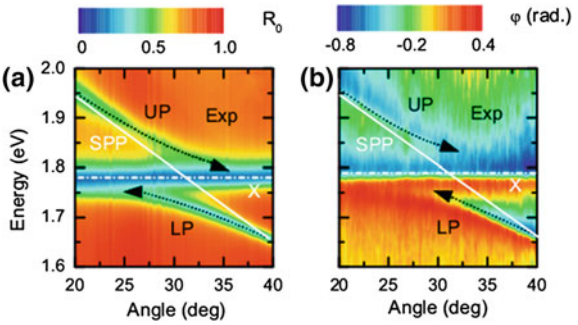

Fig. 7.6 Angle-resolved reflectivity spectra of a hybrid structure consisting of a gold nanoslit array coated with a 50-nm-thick J-aggregate dye film. **a** Observed reflectivity amplitude $R_0(\theta, \omega)$ and **b** corresponding spectral phase $\varphi(\theta, \omega)$. The *black* (*white*) *lines* in (**a**) and (**b**) mark the coupled (uncoupled) mode dispersions (Adapted with permission from [60]. Copyright (2013) American Chemical Society)

absorption band can be noticed at the unperturbed J-aggregate exciton resonance (~ 1.79 eV). As is apparent in Fig. 7.3, in our samples, the SPP fields are strongly confined inside or near the slits and coupling effects are most pronounced for excitons in these locations. Excitons further away from the slits will not exhibit strong Rabi splitting. Evidently, contributions from both strongly interacting ("coupled") and weakly interacting ("uncoupled") dye molecules have to been taken into account. Each of the three resonances is characterized by a clear jump in the spectral phase in Fig. 7.6b.

7.5.1 Phenomenological Description

As the reflectivity measurements represent a coherent superposition of contributions from the X-SPP system and a broadband reflection from the underlying thick gold layer, Fano-like line shapes are to be expected [21, 46, 57]. Without knowledge of the detailed microscopic mechanisms, an accurate description of the optical response of the coupled system is nevertheless feasible by fitting a sum of harmonic oscillator response functions to $R_0(\omega)$ and $\varphi(\omega)$ for each angle of incidence separately (Fig. 7.6a, b), according to

$$\sqrt{R_0(\omega)}e^{i\varphi(\omega)} = \alpha + \sum_m \beta \left[\frac{|\mu_m|^2 \cdot e^{i\phi_m}}{\omega_m - i\gamma_m - \omega} + \frac{|\mu_m|^2 \cdot e^{-i\phi_m}}{\omega_m + i\gamma_m + \omega} \right]. \tag{7.10}$$

Here, α and β are background and scaling amplitudes, respectively, which are assumed to vary slowly over the frequency range of interest. The indices $m = 1, 2, 3, 4$ represent LP, UP, the uncoupled J-aggregate resonance, and an additional

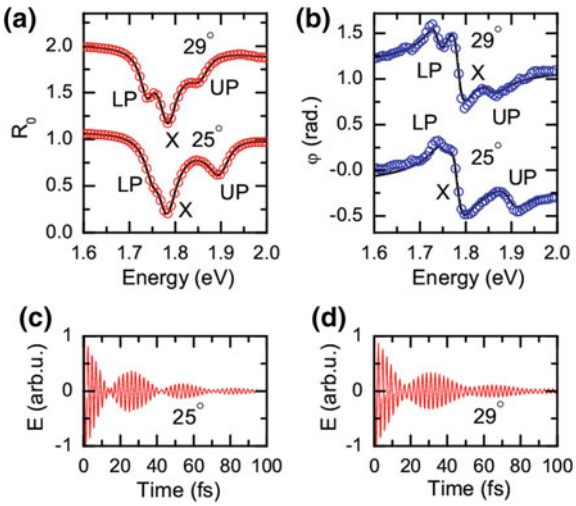

Fig. 7.7 **a**, **b** Experimental (*circles*) and simulated (*solid lines*) reflectivity spectra (**a**) and spectral phases (**b**) at $\theta = 25°$ and 29° (*vertically* shifted). **c**, **d** Time structure of the electric field emitted by the hybrid UP and LP modes at 25° (**c**) and 29° (**d**), showing distinct polarization beats with frequency $\omega_{UP} - \omega_{LP}$ (Adapted with permission from [60]. Copyright (2013) American Chemical Society)

broad shoulder at $\sim$2 eV, attributed to some residual dye monomer. μ_m, ϕ_m, and ω_m denote the effective dipole moment, phase, and resonance frequency of the individual resonances, respectively. γ_m is the spectral half width at half maximum.

In Fig. 7.7a, b a comparison is shown between the measured and fitted spectra for angles of incidence corresponding to large detuning (25°) and small detuning (29°). From (7.10) the temporal structure of the polariton response to a weak impulsive excitation can be extracted. As is evident in Fig. 7.7c, d, even within the short damping time of <100 fs, the reemitted polariton field exhibits polarization oscillations with a beat frequency $\omega_{UP} - \omega_{LP}$. At this point, this is only an indirect hint towards periodic energy transfer between Xs and SPPs. As we will discuss below, time-resolved experiments provide independent direct evidence [58].

7.5.2 Homogeneity of the J-Aggregates Resonance

As we have found, a description based on (7.10) reproduces the measured results faithfully. Remarkably, though, this description does not take into account any inhomogeneous broadening effects. In particular, as the resonance terms represent ensembles of fundamental emitters, the question of possible influences of disorder-broadening needs to be addressed. To show that the J-aggregate resonance is indeed almost homogeneously broadened, we employ here a rather sensitive visual tool: A plot

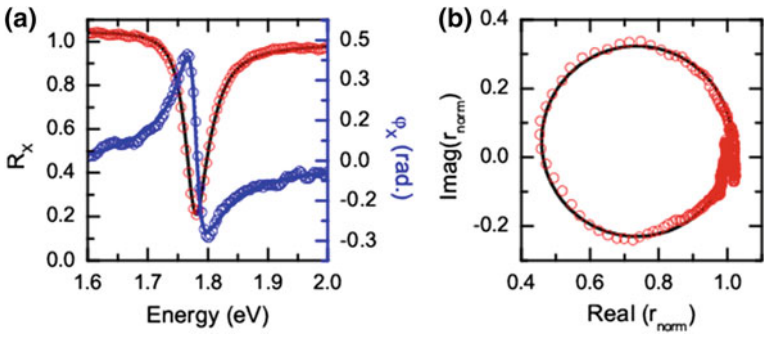

Fig. 7.8 **a** Observed (*red circles*) and fitted (*solid black*) reflectivity spectra $Rx(\omega)$, and corresponding observed (*blue circles*) and fitted (*solid blue*) spectral phase $\phi(\omega)$, measured on a coated planar gold film at the angle of incidence of 20°. **b** The corresponding observed normalized reflection coefficient r_{norm} plotted in the complex plane (*red circles*). The *black circle* is a fitted circular function (Adapted with permission from [60]. Copyright (2013) American Chemical Society)

of the optical response in the complex plane facilitates a comparison with the idealized circular shape of a perfectly homogeneous system.

The complex optical response of J-aggregates at the field level is accessible in spectral interferometry (see also Fig. 7.5). To focus exclusively on the dye system, a planar gold film with a spin-coated a dye layer is used. The reflectivity spectrum R_X and spectral phase φ_X of the coated gold film are shown in Fig. 7.8a for an angle of incidence of 20°.

The clear signature of a homogeneously broadened single resonance is best observed, however, when the spectral response is plotted in the complex plane, as shown in Fig. 7.8b [28]. Evidently, all measured data are found on a nearly perfectly circular trace. If the system's response would be inhomogeneously broadened, that trace would take a more or less severely flattened shape. Broadening widths on the order of a few percent of the homogeneous linewidth are easily noticeable with such plots. Further evidence for the excellent homogeneity of the bare dye film is obtained by using (7.3) to describe the permittivity of the J-aggregate film with purely homogeneous Lorentzians. We fit the complex reflectivity spectrum $\sqrt{R_X}\exp(i\varphi_X)$ within the frame work of the transfer matrix formalism. The comparison of the measured data with the numerically fitted solid line in Fig. 7.8a shows that the main resonance of the dye layer is very well represented by a single Lorentzian line shape, i.e., inhomogeneous broadening is essentially absent.

7.5.3 Coherent Dynamics

In previous investigations, the physical cause of the anti-crossing spectral behavior of strongly coupled systems was found in the periodic transfer of energy due to the

emission and reabsorption of photons [5, 13, 26, 56]. A large value of Ω_R implies rather short time scale of $T_R = \pi/\Omega_R \sim 30$ fs for the associated oscillation period. To investigate the coherent polariton dynamics, we employ ultrafast, angle-resolved pump-probe spectroscopy capable of resolving these Rabi oscillations in time. Nearly collinearly propagating pump and probe pulses with sub-15 fs duration are mildly focused onto the sample at variable angle of incidence θ. Both are p-polarized with a center wavelength in the visible at ~ 1.8 eV, with a spectral band-width that covers both polariton branches. The pump pulse excites impulsively polariton wavepackets whose dynamics are manifested in the differential reflectivity spectrum ($\Delta R/R$).

The recorded map of $\Delta R/R$ as a function of time delay τ between pump and probe pulses and probe frequency ω is shown in Fig. 7.9a for a hybrid nanostructure with $a_0 = 430$ nm and $\theta = 39°$. In this configuration, the SPP mode is shifted to the red of the X resonance (at 1.789 eV) by ~ 75 meV. The data reveal a strong nonlinear signal near 1.789 eV and a weaker signal at the LP resonance (near 1.65 eV). The signal near 1.789 eV does not exhibit oscillatory behavior. It is rather similar to the nonlinear response of a bare dye film deposited on a planar gold mirror, whose behavior is well understood in terms of a cascaded exciton-biexciton model [18, 56].

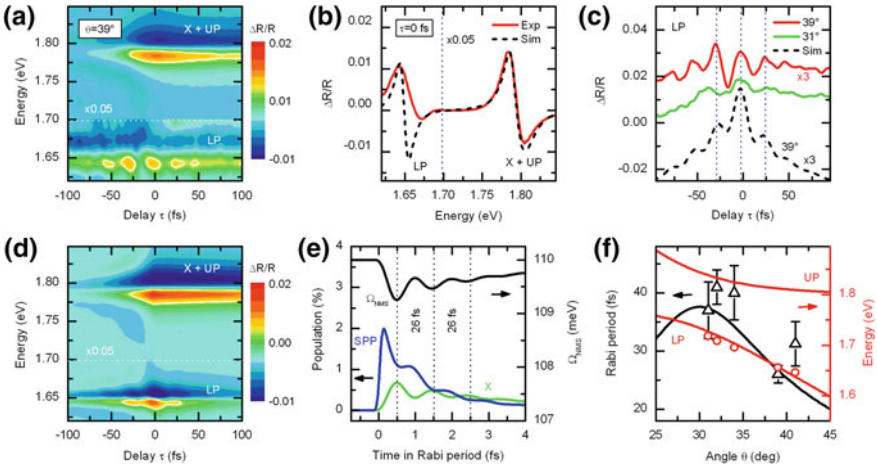

Fig. 7.9 Coherent dynamics of X-SPP Rabi oscillations. **a** Measured differential reflectivity map $(\Delta R/R)(\omega, \tau)$ for a hybrid structure (grating period 430 nm), recorded at an angle of incidence of 39°. Clear temporal Rabi oscillations are seen near the LP resonance at 1.64 eV. **b** Comparison of measured (*solid line*) and simulated (*dashed line*) differential reflectivity spectra at zero delay. **c** Time evolution of the $\Delta R/R$ signal near the LP resonance, measured at θ = 39° and θ = 31°. Pronounced sub-40 fs Rabi oscillations are noticeable. The shorter oscillation period for the larger angle of incidence reflects the increased X-SPP detuning. The dashed line (*vertically* displaced by −0.025) represents simulated dynamics for θ = 39°. **d** Simulated $(\Delta R/R)(\omega, T)$ map. **e** pump-induced SPP and exciton population dynamics at θ = 39°. **f** Comparison of calculated (*solid lines*) and observed (*open symbols*) oscillation periods and LP resonance energies as functions of θ. The simulated dispersion relations are included (Reprinted from Nature Photonics 7, 128132 (2013))

More significant in the present context is the ΔR signal near the LP resonance. This nonlinear response is characterized by a dispersive spectral lineshape (Fig. 7.9b) with $\Delta R > 0$ at lower probe energies. Interestingly, it shows clearly discernable oscillations in time with a period of $T_R = 27$ fs (Fig. 7.9c) both at positive ($\tau > 0$) and negative delays. As these oscillations persist for about ±50 fs, it is likely that the radiative damping of the SPP modes limits the coherence time [29]. Towards zero detuning between X and SPP, signal amplitude and oscillation period increase. Taken together, all these facts point towards coherent X-SPP Rabi oscillations being observed in this hybrid X-SPP system.

The physical mechanisms leading to this observation are briefly: (i) an initial preferential excitation of coherent polariton wavepacket on the SPP side of the system (whose absorption coefficient exceeds that of the participating dye molecules by about two orders of magnitude). (ii) a subsequent oscillatory exchange of energy between the two subsystems. This description is corroborated by simulations, which reproduce the measured reflectivity maps faithfully, as shown in Fig. 7.9d. From the same model we can extract the exciton and SPP population dynamics numerically (see Fig. 7.9e) and find alternating maxima between the X and SPP populations, which are separated by half a Rabi period, as expected for a Rabi exchange.

Curiously, our observations from Fig. 7.9a correlate a dispersive ΔR spectrum with maxima that concur with the maxima in the SPP population, not the X population. This indicates that exciton saturation is not the dominant nonlinearity in this case. As we have shown before [56], the creation of an X population $n_X(t)$ transiently reduces the normal mode splitting according to $\Omega_R(t) = \Omega_R^0\sqrt{1 - 2n_x(t)}$ (see also Fig. 7.9e), resulting in a transient blue shift of the LP resonance to a time-average and consequently the dispersive LP nonlinearity observed in Fig. 7.9b. This interpretation is supported by optical Bloch equation simulations (Fig. 7.9d), which reproduce both the oscillatory LP dynamics (Fig. 7.9c) and the dispersive ΔR lineshape (Fig. 7.9b). Further experiments at different angles of incidence, which provide independent access to the Rabi period for different detunings, also back this interpretation, as reported in Fig. 7.9f.

7.6 Summary

The compound nanostructures composed of J-aggregate films deposited on metal gratings are a model system for the study of strong coupling. In particular, when the excitonic resonance of the dye layer are coupled to localized plasmonic modes at the metal surface, the formation of energy-split polariton modes is easily observed. A distinct advantage is the possibility to tune the interaction by adjusting the parallel momentum of the incident radiation. At zero detuning the upper and lower polariton branches are fully hybridized mixtures of excitons and surface plasmons. These two modes exhibit distinctly different lifetimes, i.e., the upper and lower polariton mode become super- and sub-radiant. Realtime observations of this behavior by ultrafast pump-probe spectroscopy not only confirm the splitting of lifetime, they also reveal

coherent Rabi oscillations. We find that the Rabi periods are temporarily increased during the transient population of the polaritonic levels. This reversible transient reduction of Rabi frequencies is the dominant non-linearity.

References

1. M. Abb, P. Albella, J. Aizpurua, O.L. Muskens, All-optical control of a single plasmonic nanoantenna-ITO hybrid. Nano Letters **11**(6), 2457–2463 (2011)
2. C. Argyropoulos, P.-Y. Chen, F. Monticone, G. D'Aguanno, A. Alu, Nonlinear plasmonic cloaks to realize giant all-optical scattering switching. Phys. Rev. Lett. **108**(26), 263905 (2012)
3. U. Akram, Z. Ficek, S. Swain, Decoherence and coherent population transfer between two coupled systems. Phys. Rev. A **62**, 013413 (2000)
4. S. Aberra Guebrou, C. Symonds, E. Homeyer, J.C. Plenet, Y.N. Gartstein, V.M. Agranovich, J. Bellessa, Coherent emission from a disordered organic semiconductor induced by strong coupling with surface plasmons. Phys. Rev. Lett. **108**, 066401 (5p) (2012)
5. J. Bellessa, C. Bonnand, J.C. Plenet, J. Mugnier, Strong coupling between surface plasmons and excitons in an organic semiconductor. Phys. Rev. Lett. **93**, 036404 (2004)
6. A. Boca, R Miller, K.M. Birnbaum, A.D. Boozer, J. McKeever, H.J. Kimble, Observation of the vacuum Rabi spectrum for one trapped atom. Phys. Rev. Lett. **93**(23), 233603 (2004)
7. D.J. Bergman, M.I. Stockman, Surface plasmon amplification by stimulated emission of radiation: quantum generation of coherent surface plasmons in nanosystems. Phys. Rev. Lett. **90**(2), 027402 (2003)
8. S.I. Bozhevolnyi, V.S. Volkov, E. Devaux, J.Y. Laluet, T.W. Ebbesen, Channel plasmon subwavelength waveguide components including interferometers and ring resonators. Nature **440**(7083), 508–511 (2006)
9. Y.N. Chen, D.S. Chuu, T. Brandes, Current detection of superradiance and induced entanglement of double quantum dot excitons. Phys. Rev. Lett. **90**, 166802 (2003)
10. D.E. Chang, A.S. Sorensen, E.A. Demler, M.D. Lukin, A single-photon transistor using nanoscale surface plasmons. Nat. Phys. **3**(11), 807–812 (2007)
11. R.G. DeVoe, R.G. Brewer, Observation of superradiant and subradiant spontaneous emission of two trapped ions. Phys. Rev. Lett. **76**, 2049–2052 (1996)
12. R.H. Dicke, Coherence in spontaneous radiation processes. Phys. Rev. **93**, 99–110 (1954)
13. J. Dintinger, S. Klein, F. Bustos, W.L. Barnes, T.W. Ebbesen, Strong coupling between surface plasmon-polaritons and organic molecules in subwavelength hole arrays. Phys. Rev. B **71**, 035424 (2005)
14. K. Ding, Z.C. Liu, L.J. Yin, M.T. Hill, M.J.H. Marell, P.J. van Veldhoven, R. Noetzel, C.Z. Ning, Room-temperature continuous wave lasing in deep-subwavelength metallic cavities under electrical injection. Phys. Rev. B **85**(4), 041301 (2012)
15. J. Dintinger, I. Robel, P.V. Kamat, C. Genet, T.W. Ebbesen, Terahertz all-optical molecule-plasmon modulation. Adv. Mater. **18**(13), 1645 (2006)
16. C. Dahmen, B. Schmidt, G. von Plessen, Radiation damping in metal nanoparticle pairs. Nano Lett. **7**(2), 318–322 (2007)
17. N. Engheta, Circuits with light at nanoscales: optical nanocircuits inspired by metamaterials. Science **317**(5845), 1698–1702 (2007)
18. H. Fidder, J. Knoester, D.A. Wiersma, Observation of the one-exciton to two-exciton transition in a J aggregate. J. Chem. Phys. **98**(8), 6564–6566 (1993)
19. N.T. Fofang, T.-H. Park, O. Neumann, N.A. Mirin, P. Nordlander, N.J. Halas, Plexcitonic nanoparticles: plasmon-exciton coupling in nanoshell-J-aggregate complexes. Nano Letters **8**, 3481–3487 (2008)

20. A. Gonzalez-Tudela, D. Martin-Cano, E. Moreno, L. Martin-Moreno, C. Tejedor, F.J. Garcia-Vidal, Entanglement of two qubits mediated by one-dimensional plasmonic waveguides. Phys. Rev. Lett. **106**, 020501 (2011)
21. C. Genet, M.P van Exter, J.P Woerdman, Fano-type interpretation of red shifts and red tails in hole array transmission spectra. Opt. Commun. **225**, 331–336 (2003)
22. D.E. Gomez, K.C. Vernon, P. Mulvaney, T.J. Davis, Surface plasmon mediated strong exciton-photon coupling in semiconductor nanocrystals. Nano Letters **10**(1), 274–278 (2010)
23. M. Hübner, J. Kuhl, T. Stroucken, A. Knorr, S.W. Koch, R. Hey, K. Ploog, Collective effects of excitons in multiple-quantum-well Bragg and anti-Bragg structures. Phys. Rev. Lett. **76**, 4199–4202 (1996)
24. J. Hwang, M. Pototschnig, R. Lettow, G. Zumofen, A. Renn, S. Goetzinger, V. Sandoghdar, A single-molecule optical transistor. Nature **460**(7251), 76–80 (2009)
25. C. Hettich, C. Schmitt, J. Zitzmann, S. Kühn, I. Gerhardt, V. Sandoghdar, Nanometer resolution and coherent optical dipole coupling of two individual molecules. Science **298** (5592), 385–389 (2002)
26. T.K. Hakala, J.J. Toppari, A. Kuzyk, M. Pettersson, H. Tikkanen, H. Kunttu, P. Torma, Vacuum Rabi splitting and strong-coupling dynamics for surface-plasmon polaritons and rhodamine 6G molecules. Phys. Rev. Lett. **103**(5), 053602 (2009)
27. A. Ishizaki, G.R. Fleming, Unified treatment of quantum coherent and incoherent hopping dynamics in electronic energy transfer: reduced hierarchy equation approach. J. Chem. Phys. **130**(23), 234111 (2009)
28. M. Jurna, E.T. Garbacik, J.P. Korterik, J.L. Herek, C. Otto, H.L. Offerhaus, Visualizing resonances in the complex plane with vibrational phase contrast coherent anti-stokes Raman scattering. Anal. Chem. **82**(18), 7656–7659 (2010)
29. D.S. Kim, S.C. Hohng, V. Malyarchuk, Y.C. Yoon, Y.H. Ahn, K.J. Yee, J.W. Park, J. Kim, Q. H. Park, C. Lienau, Microscopic origin of surface-plasmon radiation in plasmonic band-gap nanostructures. Phys. Rev. Lett. **91**, 143901 (2003)
30. M. Khajavikhan, A. Simic, M. Katz, J.H. Lee, B. Slutsky, A. Mizrahi, V. Lomakin, Y. Fainman, Thresholdless nanoscale coaxial lasers. Nature **482**(7384), 204–207 (2012)
31. S.-H. Lim, T.G. Bjorklund, F.C. Spano, C.J. Bardeen, Exciton delocalization and superradiance in tetracene thin films and nanoaggregates. Phys. Rev. Lett. **92**, 107402 (2004)
32. R.H. Lehmberg, Radiation from an *n*-atom system. I. general formalism. Phys. Rev. A **2**, 883–888 (1970)
33. Y.-J. Lu, J. Kim, H.-Y. Chen, C. Wu, N. Dabidian, C.E. Sanders, C.-Y. Wang, M.-Y. Lu, B.-H. Li, X. Qiu, W.-H. Chang, L.-J. Chen, G. Shvets, C.-K. Shih, S. Gwo, Plasmonic nanolaser using epitaxially grown silver film. Science **337**(6093), 450–453 (2012)
34. S. Lal, S. Link, N.J. Halas, Nano-optics from sensing to waveguiding. Nat. Photonics **1**(11), 641–648 (2007)
35. H. Lu, X. Liu, L. Wang, Y. Gong, D. Mao, Ultrafast all-optical switching in nanoplasmonic waveguide with Kerr nonlinear resonator. Opt. Express **19**(4), 2910–2915 (2011)
36. S. Liu, D. Schmitz, S.-S. Jester, N.J. Borys, S. Hoeger, J.M. Lupton, Coherent and incoherent interactions between cofacial H-conjugated oligomer dimers in macrocycle templates. J. Phys. Chem. B **117**(16, SI), 4197–4203 (2013)
37. B. Luk'yanchuk, N.I. Zheludev, S.A. Maier, N.J. Halas, P. Nordlander, H. Giessen, C.T. Chong, The Fano resonance in plasmonic nanostructures and metamaterials. Nat. Mater. **9**(9), 707–715 (2010)
38. P.W. Milonni, P.L. Knight, Retarded interaction of two nonidentical atoms. Phys. Rev. A **11**, 1090–1092 (1975)
39. S.A. Maier, P.G. Kik, H.A. Atwater, S. Meltzer, E. Harel, B.E. Koel, A.A.G. Requicha, Local detection of electromagnetic energy transport below the diffraction limit in metal nanoparticle plasmon waveguides. Nat. Mater. **2**(4), 229–232 (2003)
40. K.F. MacDonald, Z.L. Samson, M.I. Stockman, N.I. Zheludev, Ultrafast active plasmonics. Nat. Photonics **3**(1), 55–58 (2009)

41. M.A. Noginov, G. Zhu, A.M. Belgrave, R. Bakker, V. M. Shalaev, E.E. Narimanov, S. Stout, E. Herz, T. Suteewong, U. Wiesner, Demonstration of a spaser-based nanolaser. Nature **460** (7259), 1110–U68 (2009)
42. M.A. Noginov, G. Zhu, M. Mayy, B.A. Ritzo, N. Noginova, V.A. Podolskiy, Stimulated emission of surface plasmon polaritons. Phys. Rev. Lett. **101**(22), 226806 (2008)
43. R.F. Oulton, V.J. Sorger, T. Zentgraf, R.-M. Ma, C. Gladden, L. Dai, G. Bartal, X. Zhang, Plasmon lasers at deep subwavelength scale. Nature **461**(7264), 629–632 (2009)
44. D. Pacifici, H.J. Lezec, H.A. Atwater, All-optical modulation by plasmonic excitation of CdSe quantum dots. Nat. Photonics **1**(7), 402–406 (2007)
45. R.A. Pala, K.T. Shimizu, N.A. Melosh, M.L. Brongersma, A nonvolatile plasmonic switch employing photochromic molecules. Nano Lett. **8**(5), 1506–1510 (2008)
46. C. Ropers, D.J. Park, G. Stibenz, G. Steinmeyer, J. Kim, D.S. Kim, C. Lienau, Femtosecond light transmission and subradiant damping in plasmonic crystals. Phys. Rev. Lett. **94**, 113901 (2005)
47. F. Reynaud, F. Salin, A. Barthelemy, Measurement of phase-shifts introduced by nonlinear optical phenomena on subpicosecond pulses. Opt. Lett. **14**(5), 275–277 (1989)
48. G.D. Scholes, Long-range resonance energy transfer in molecular systems. Annu. Rev. Phys. Chem. **54**, 57–87 (2003)
49. S.I. Schmid, J. Evers, Interplay of vacuum-mediated inter- and intra-atomic couplings in a pair of atoms. Phys. Rev. A **81**, 063805 (2010)
50. T. Schwartz, J.A. Hutchison, C. Genet, T.W. Ebbesen, Reversible switching of ultrastrong light-molecule coupling. Phys. Rev. Lett. **106**, 196405 (2011)
51. A.K. Sarychev, G. Tartakovsky, Magnetic plasmonic metamaterials in actively pumped host medium and plasmonic nanolaser. Phys. Rev. B **75**(8), 085436 (2007)
52. M.I. Stockman, Nanoplasmonics: past, present, and glimpse into future. Opt. Express **19**(22), 22029–22106 (2011)
53. Y. Sonnefraud, N. Verellen, H. Sobhani, G.A.E. Vandenbosch, V.V. Moshchalkov, P. Van Dorpe, P. Nordlander, S.A. Maier, Experimental realization of subradiant, superradiant, and fano resonances in ring/disk plasmonic nanocavities. ACS Nano **4**(3), 1664–1670 (2010)
54. T. Scholak, T. Wellens, A. Buchleitner, Optimal networks for excitonic energy transport. J. Phys. B-At. Mol. Opt. Phys. **44**(18, SI), 184012 (2011)
55. V.K. Valev, J.J. Baumberg, C. Sibilia, T. Verbiest, Chirality and chiroptical effects in plasmonic nanostructures: fundamentals, recent progress, and outlook. Adv. Mater. **25**(18), 2517–2534 (2013)
56. P. Vasa, R. Pomraenke, G. Cirmi, E. De Re, W. Wang, S. Schwieger, D. Leipold, E. Runge, G. Cerullo, C. Lienau, Ultrafast manipulation of strong coupling in metalmolecular aggregate hybrid nanostructures. ACS Nano **4**, 7559–7565 (2010)
57. P. Vasa, R. Pomraenke, S. Schwieger, Y.I. Mazur, V. Kunets, P. Srinivasan, E. Johnson, J.E. Kihm, D.S. Kim, E. Runge, G. Salamo, C. Lienau, Coherent exciton/surface-plasmon-polariton interaction in hybrid metal-semiconductor nanostructures. Phys. Rev. Lett. **101**, 116801 (2008)
58. P. Vasa, W. Wang, R. Pomraenke, M. Lammers, M. Maiuri, C. Manzoni, G. Cerullo, C. Lienau, Real-time observation of ultrafast Rabi oscillations between excitons and plasmons in J-aggregate/metal hybrid nanostructures. Nat. Photonics **7**, 128 (2013)
59. H. Wang, D.W. Brandl, F. Le, P. Nordlander, N.J. Halas, Nanorice: a hybrid plasmonic nanostructure. Nano Letters **6**(4), 827–832 (2006)
60. W. Wang, P. Vasa, R. Pomraenke, R. Vogelgesang, A. De Sio, E. Sommer, M. Maiuri, C. Manzoni, G. Cerullo, C. Lienau, Interplay between strong coupling and radiative damping of excitons and surface plasmon polaritons in hybrid nanostructures, ACS Nano. **8**(1), 1056–1064 (2014)
61. K. Yu, A. Lakhani, M.C. Wu, Subwavelength metal-optic semiconductor nanopatch lasers. Opt. Express **18**(9), 8790–8799 (2010)
62. T. Yoshie, A. Scherer, J. Hendrickson, G. Khitrova, H.M. Gibbs, G. Rupper, C. Ell, O.B. Shchekin, D.G. Deppe, Vacuum Rabi splitting with a single quantum dot in a photonic crystal nanocavity. Nature **432**(7014), 200–203 (2004)

Chapter 8
Direct fs Laser Writing of 3D Nanostructures

Elmina Kabouraki, Konstantina Terzaki, Vasileia Melissinaki, Maria Manousidaki, Maria Vamvakaki and Maria Farsari

Abstract Recent work in three-dimensional microstructuring of photosensitive materials by femtosecond lasers is reviewed. The applications of nonlinear and quenching phenomena allow one to overcome both surface absorption and the diffraction limit to produce 3D microstructures with sub-diffraction limit resolution. Potential applications in the emerging fields of photonics and microfluidics are discussed.

8.1 Introduction

Direct fs Laser Writing (DLW) based on multi-photon polymerization (MPP) of polymeric mixtures allows the fabrication of three-dimensional (3D) structures of millimeter size with sub-100 nm resolution [1–3]. When the beam of an ultra-fast laser is focused into the volume of a photosensitive, transparent material, the polymerization process can be initiated by non-linear absorption within the focal volume. By moving the laser focus in a three dimensional manner, 3D structures of high resolution can be fabricated inside the material. The technique has been used with a variety of acrylate, hybrid and epoxy materials and several components and devices have been fabricated such as photonic and plasmonic crystals [4–6], micromechanical, microoptical and microfluidic devices [7–10], tissue engineering scaffolds [11–13], and microscopic models (Fig. 8.1). Nowadays, resolution well below 100 nm is routinely achieved.

The unique capability of DLW lies in that it allows the fabrication of computer-designed, fully 3D structures with resolution beyond the diffraction limit. No other competing technology offers these advantages. Classic 3D prototyping techniques such as UV laser stereolithography, 3D inkjet printing and laser sintering can also

E. Kabouraki · K. Terzaki · V. Melissinaki · M. Manousidaki · M. Vamvakaki · M. Farsari (✉)
IESL-FORTH, N. Plastira 100, 70013 Heraklion, Crete, Greece
e-mail: mfarsari@iesl.forth.gr

© Springer International Publishing Switzerland 2015

S. Sakabe et al. (eds.), *Progress in Nonlinear Nano-Optics*,
Nano-Optics and Nanophotonics, DOI 10.1007/978-3-319-12217-5_8

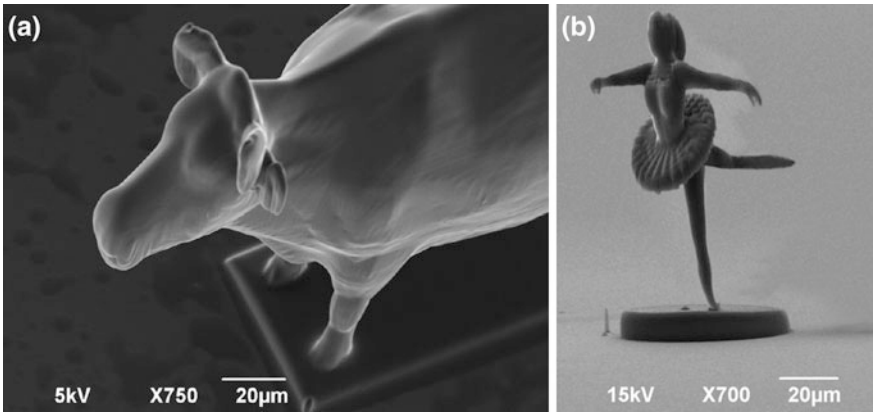

Fig. 8.1 3D model of a cow (**a**) and a dancer (**b**). Made by Areti Mourka and Mary Manousidaki, FORTH

produce fully three-dimensional structures, however, they cannot provide resolution better than a few microns. On the other hand, lithographic techniques with superior resolution, such as e-beam lithography, cannot produce anything more complicated than high-aspect ratio two-dimensional structures.

Here, we first describe the principles of DLW and how it is possible to beat the diffraction limit. Then we describe the most recent developments in high-resolution 3D structures and the materials most commonly used. Finally we describe its use in photonics and microfluidics.

8.2 Theoretical Issues of Multi-photon Polymerization

When it comes to using light for the construction of three dimensional micro-structures with sub-100 nm resolution, there are two obstacles that have to be overcome; surface absorption of the material and the diffraction limit. The first is overcome by employing nonlinear multiphoton absorption; the second by using materials with well-defined polymerization threshold. These are described in detail in the following paragraphs.

8.2.1 The Mechanism of Multi-photon Absorption

Photopolymerization follows the general scheme for any polymerization. However, the use of light, rather than heat, to drive the reaction has certain advantages, such as the elimination of solvent and thermal initiators, the high reaction rates at room temperature and the spatial and temporal control of the polymerization.

Multiphoton polymerization occurs because of nonlinear multi-photon absorption; to date only two- and three-photon polymerizations have been demonstrated. The mechanisms involved in both cases are the same; in two photon absorption, the excited species instead of absorbing one photon of energy *hv*, they absorb two photons of energy *hv*/2, while in three photon absorption, they absorb 3 photons of energy *hv*/3. We will limit our description here to two-photon polymerization.

There are two types of multi-photon absorption: sequential and simultaneous. In sequential, the absorbing species are excited to a real intermediate state, where, a second photon is absorbed. The presence of the intermediate energy state implies that the material is absorbing at this specific wavelength; it will therefore be a surface effect and will follow the Beer-Lambert law. In simultaneous absorption, there is no real intermediate energy state i.e., the material is transparent at that wavelength. Instead, there is a virtual intermediate energy state and two-photon absorption happens only if another photon arrives within the virtual state lifetime. For this to occur high intensities are required, which can be provided by a tightly focused ultrafast laser beam.

The most commonly used lasers for this purpose are Ti:Sapphire fs lasers, fibre lasers emitting in the 800 nm spectral region, and picosecond pulse duration green lasers. These light sources have two main advantages; firstly they have short pulses, picosecond or less, so they do not cause thermal damage. Secondly their wavelengths, in the region 530–800 nm, is twice the wavelength of polymerization of a wide range of photopolymers. In addition, most photopolymers are transparent at those wavelengths, which allows in-volume focusing of the laser beam with minimal scattering.

8.2.2 The Diffraction Limit

It is popularly believed that the highest resolution that can be achieved by a focused light beam is given by Abbe's diffraction limit [14].

$$0.5\frac{\lambda}{N.A.}$$

where λ is the laser wavelength and *N.A.* is the numerical aperture of the focusing objective; this has fuelled the race for ever decreasing wavelengths, such as electron wavelengths and for alternative, non-light patterning techniques such as atomic force microscopy (AFM) and near-field scanning optical microscopy (NSOM); techniques only allow for surface and not in-volume patterning. To produce 3D structures with in-volume patterning, and produce photopolymerized voxels smaller than that defined by the diffraction limit, materials with well defined photopolymerization thresholds need to be used.

To start with, when absorbing the light, the photoinitiator becomes excited and produces radicals; these radicals attack monomer molecules to form macroradicals

of the polymer. Finally, the radicals are terminated to give the polymer. Radical termination can be also induced by oxygen and other molecules in the system, known as scavengers. Quenching competes with photopolymerization and is usually considered detrimental to the process. In multi-photon photopolymerization, however, it can be used to circumvent the diffraction limit and produce structures of very high resolution. This can be done by modifying the light intensity at the focal point so that the light-produced radicals, whose spatial concentration is proportional to the square of the light intensity, exceed the quenchers and initiate polymerization only at the area where the exposure energy is larger than the threshold. In this case, the diffraction limit becomes just a measure of the focal spot size and it does not really determine the polymerization voxel size.

8.2.3 DLW Inspired by Stimulated-Emission-Depletion Fluorescence Microscopy

One recent development which has successfully and substantially increased the resolution not only of single lines but also of structures is DLW inspired by stimulated-emission-depletion (STED) fluorescence microscopy [15, 16]. In STED-DLW, two laser beams are used; one is used to generate the radicals, and the second beam to deactivate them. Several schemes have been proposed including single-photon (rather than multi-photon) excitation [17], a one-colour scheme [18], and multi-photon two-colour scheme [19, 20]. In addition to increasing the resolution, the possibility to shape the de-activating beam allows the very precise control of the voxel shape, and therefore the polymerization shape. Photonic nanostructures with ultra-high resolution have been made using STED-DLW [19]. However, the implementation of DLW-STED is complicated, requiring very fine beam control and specialized photoinitiators which not only have high two-photon cross-section, but also high fluorescence quantum efficiency [19, 21]. To date, only geometrically simple 3D structures like woodpiles and voxels have been fabricated using this technique.

8.2.4 Diffusion-assisted DLW

It has been shown recently that it is possible to increase the resolution of multi-photon polymerization by employing a scheme based on quencher diffusion, in a chemical equivalent of STED [22]. This is based on the combination of a mobile quenching molecule with a slow laser scanning speed, allowing the diffusion of the quencher in the scanned area, the depletion of the generated radicals, and the regeneration of the consumed quencher.

One method for increasing the resolution of DLW is the use of an inhibiting molecule, such as a radical quencher, in the photo-polymerizable material [23].

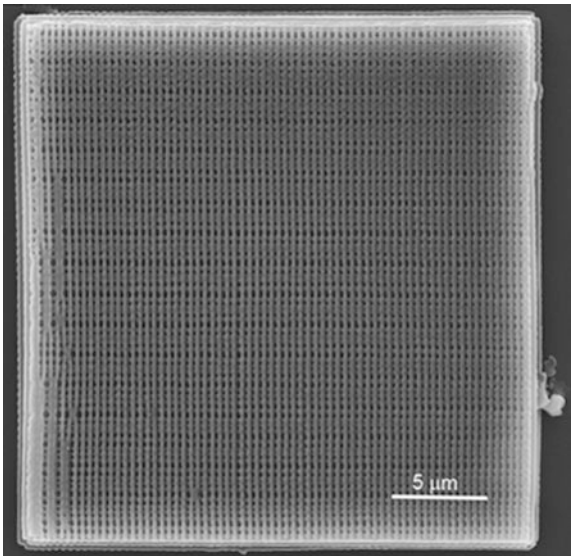

Fig. 8.2 A woodpile structure with period 400 nm, fabricated using diffusion-assisted DLW. *Source* Sakellari et al. [22]

However, quenchers only reduce the absolute number of radicals, achieving a similar effect to simply reducing the laser power. Indeed, efforts to date to improve resolution using quenchers have marginally increased the resolution of single, suspended lines, and they have not produced any high resolution 3D structures. More importantly, they have not reduced the distance between high resolution lines [19]. This can be addressed by using a mobile quencher, which diffuses faster that the laser scanning speed, therefore replenishing the molecules that have consumed radicals. This way the photopolymerization voxel can be made arbitrary small, and the maximum resolution is determined by other factors such as the structure design and the mechanical stability of the polymer. Employing this diffusion-assisted DLW, woodpile photonic crystals with period 400 nm were fabricated, the smallest period achieved to date using a single laser beam (Fig. 8.2). A description of photonic crystals is made later in the applications section.

8.3 Materials for DLW

8.3.1 Introduction

A material or composite suitable for structuring by multi-photon polymerization must contain at least two basic components: a polymerizable material, which will become the polymeric written structure, and a photoinitiator, which will absorb the laser light and provide the active species that will cause this polymerization. To date, a large combination of polymeric materials and photoinitiators have been used for this purpose. These are mostly negative photoresists such as acrylate materials [24, 25],

the epoxy-based photoresist SU-8 [2], and hybrid materials [26, 27]. There are also a few examples of positive resists being used [5, 28]. In the following sections, we will discuss briefly these photoinitiators and negative polymeric materials.

8.3.2 Photoinitiators

During photopolymerization a liquid or gel material bearing polymerizable groups is converted into a solid polymer; this transformation is induced by light. In conventional, one-photon polymerization, a light sensitive molecule, the 'photoinitiator', absorbs the incident radiation and produces active species, which causes the photopolymerization. In two-photon polymerization, however, where the polymerization happens into the volume of the material, there are extra conditions that must be met [1, 24]:

(i) Both the photoinitiator and the monomer material need to be transparent at the employed laser wavelength, so to allow the laser beam transmission and in-volume focusing.
(ii) The monomer needs to be transparent at the two-photon absorption wavelength (λ/2) to avoid thermal damage or ablation.
(iii) The photoinitiator needs not only to absorb at the two photon wavelength, but also to have a high probability to absorb two photons and generate active species; in other words to have a high two-photon absorption cross-section.

There are two main classes of photoinitiators used to date in DLW, depending on the nature of active species they generate: radical photoinitiators and cationic photoinitoators. Radical photoinitiators are more widely used and, upon light irradiation, they generate free radicals which initiate a polymerization process of acrylate or vinyl monomers. Cationic initiators are photo-acid generators that produce cations upon light irradiation and are used for the polymerization of epoxides or vinyl ethers [29–31].

An effective DLW photoinitiator has a high quantum yield in the generation of the active moieties, high thermal stability and stability in darkness and is highly soluble in the polymerization medium. The most commonly used free radical photoinitiator is benzophenone and its derivatives [11, 32].

8.3.3 Organic Photopolymers

The first materials used for two-photon polymerization were acrylate photopolymers [33]. These materials have several properties which make them attractive for multi-photon polymerization applications: a wide variety of their composite or organic monomers are commercially available; they are transparent at visible and

near infrared wavelengths, and can be therefore be processed by IR and green ultrafast lasers; they can be developed in common, non-aggressive solvents such as isopropanol; they can be polymerized fast and with low shrinkage; and, after polymerization they are mechanically and chemically stable.

Due to their versatile chemistry, acrylate photopolymers have been used in their pure form but also doped with other materials to add them functionality. They have been doped with TiO_2 nanoparticles to increase their refractive index for photonic crystal applications [34]; with CdS nanoparticles for the fabrication of light-emitting 3D structures [35, 36]; with metal-binding materials to cover them with metals using electroless plating [37, 38]; with chitosan to make them suitable for bio-applications [39]; with MEH-PPV to make them electroluminescent [40].

8.3.4 SU-8

SU-8 is a negative, epoxy-based photo-resist commonly used for the fabrication of high-aspect ratio structures, using standard contact lithography or LIGA. Its absorption maximum is at 365 nm. When exposed to the right light, SU-8's long molecular chains cross-link, causing the material to become insoluble to most common solvents. For this to happen, the SU-8 films require to be treated with heat after laser writing.

The possibility to structure SU-8 by two-photon polymerization was first demonstrated by Witzall et al., who employed single shots from Ti:Sapphire femtosecond amplifier to fabricate small dots [41]. More complex 2D and 3D structures were built by Belfield et al. and by Kuebler et al., respectively, who worked on the development of novel, efficient photoinitiators for cationic polymerization [42, 43]. Since then, SU-8 has been used by a large number of research teams involved in DLW [44–48].

SU-8 is thermally stable, transparent in the visible and highly resistant to solvents, acids and bases. These properties make it suitable for permanent use application; by itself, SU-8 has been employed for the fabrication of photonic [49] and microfluidic [50–52] structures, while it has also been covered with metal for metamaterials fabrication [53, 54].

8.3.5 Photosensitive Hybrid Materials

Over the last few years, DLW materials research has focused on the development of photosensitive hybrid composites. Especially, silicate-only based photopolymers have proved to be a very popular choice, as they can be commercially available and they combine properties of silicate glasses such as hardness, chemical and thermal stability, and optical transparency with the laser processing at low temperatures of organic polymers; properties impossible to achieve with just inorganic or polymeric

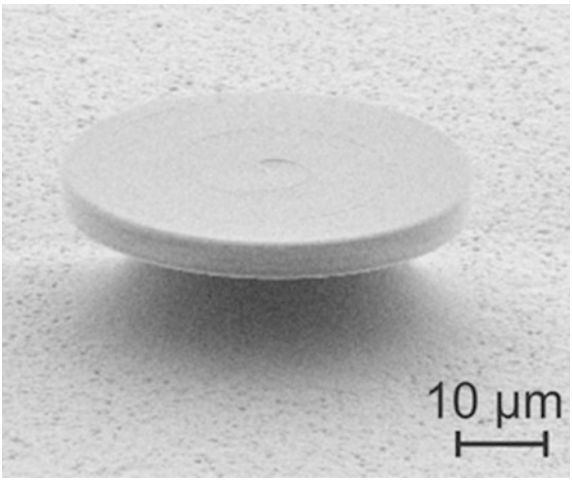

Fig. 8.3 A microdisk fabricated using ORMOCER®. *Source* Grossmann et al. [67]

materials [55–72]. The most widely used and studied silicate material is the photopolymer ORMOCER®, commercially available from Microresist Technologies, Germany, and it has been used for a variety of mostly photonic applications, like the active polymer microdisk of Fig. 8.3.

ORMOCER® and other silicate-only based hybrid materials have provided the possibility to fabricate high resolution 3D structures, they do not allow, however, the optimization and 'fine-tuning' of the materials properties for specific applications. The versatile chemistry of hybrid composites allows the co-polymerization of more than one metal alkoxide; this has been shown to enhance the material's mechanical stability and allow the modification of its optical properties. There are a few examples of composite photosensitive sol-gels used in 2PP applications [26, 32, 73–75]; recently, Ovsianikov et al. showed that under specific fluence conditions, specific material combinations can be structured into complex 3D structures without shrinkage [76, 77]. In addition to metal alkoxides, hybrid materials chemistry provides the possibility of the inclusion of functional groups, such as nonlinear optical molecules [78], quantum dots [79], and metal binding materials [6, 80].

8.4 Biopolymers

One of the applications proposed for DLW is scaffolds for tissue engineering, and drug delivery. To this end, there has been some limited research into the synthesis and structuring of biodegradable polymers, hydrogels and proteins. Seidlits et al. [81] reported the 3D structuring of a hydrogel in 2007. The same team used a picosecond pulse green laser to structure pure protein (bovine serum albumin, BSA) [82]. BSA and also avidin using flavin mononucleotide as the photosensitizer were crosslinked by Turunen et al. [83]. Claeyssens et al., synthesized and structured a

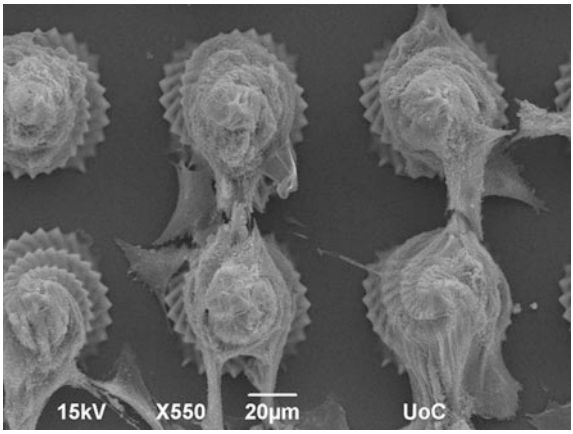

Fig. 8.4 Neural cells on polylactide 3D scaffolds. *Source* Melissinaki et al. [12]

novel, photostructurable copolymer based on polycaprolactone [11], while the same researchers later reported the fabrication of 3D structures, based on a polylactide-based polymer, employed for the alignment of neural cells (Fig. 8.4) [12]. Finally, Ovsianikov et al. made structures using poly(ethylene glycol) diacrylates of different molecular weights and investigated their cytotoxicity properties for biomedical applications [84].

There has also been some research by FORTH on the functionalization of the surface of 3D structures with biomolecules. They made 3D structures using hybrid materials, and functionalized them with biotin [85, 86] and amyloid peptides [66], targeting applications such as sensing and tissue engineering.

8.5 Applications

There have been several applications proposed for multi-photon polymerization technologies; in this work we will describe applications in photonic crystals and micromechanical and microfluidic systems.

8.5.1 Photonic Crystals

Photonic crystals (PhCs) are structures consisting of spatially alternating regions with different dielectric constants [87]. Propagation of light of a certain frequency range, called the photonic bandgap, is forbidden in such structures; when the dielectric constant periodicity occurs in all directions one is talking about 3D photonic crystals. Changing the topology and dielectric constant contrast of photonic crystals, means their optical properties can be tailored in a specific manner. Many fascinating applications of photonic crystals are possible: control of

spontaneous emission, zero-threshold lasing, lossless guiding of light, dispersion management, nonlinear frequency conversion, etc. Future possible applications include all optical signal processing, optical transistors and eventually all-optical computers.

Ever since the concept of the 3D photonic crystal was introduced by E.Yablonovitch [88] and S. John [89], photonic crystals have been the subject of intensive research. Over the last few years, the theory of 3D photonic crystals has been studied extensively; the fabrication, however, of photonic crystals with a full 3D (omnidirectional) bandgap in the visible range is still a challenging task, mainly limited by the resolution and/or flexibility of currently available structuring technologies. For practical applications of photonic crystals, inexpensive and reliable nanofabrication techniques are required.

The ability to create complex 3D structures with sub-100 nm resolution makes DLW technology ideal for the fabrication of 3D photonic crystals; in addition to its high resolution, it also allows the introduction of defects at any desired location, a crucial requirement for the practical applications of photonic crystals [87]. One major disadvantage, however, is that all the materials successfully structured by DLW to date have low refractive indices, in the order of 1.5. In order for a photonic crystal to have full bandgaps the difference between the material and its environment (usually air) has to be larger than 2. This has fuelled the race for making metallic, conducting photonic crystals [54].

There have been three main approaches to fabricate metallic structures: multiphoton reduction of metal ions, DLW into a positive-tone photoresist followed by electrochemical deposition of metal, and DLW of negative photoresists and subsequent metallization of the 3D nanostructures using electroless plating.

The first approach, multiphoton reduction of metal ions, is the only method that can create pure metallic, fully 3D nanostructures; however, it is limited, by the reduced transparency of the metal ion solutions at the laser wavelengths commonly used (500–800 nm). To overcome this problem, dilute metal-ion solutions are used, which result in 3D structures lacking mechanical stability and integrity [90, 91].

The second method, DLW of a positive-tone photoresist followed by electrochemical deposition of metal, has been demonstrated only recently [5]. A positive resist was used to create hollow structures, which were subsequently filled by gold using electrochemical deposition. The structures fabricated were of excellent quality, with a uniform metal deposition and high mechanical stability provided by the hollow frames, resulting in very high resolution gold structures. However, due to the deposition of the gold through the structure holes, this technique can only be used to fabricate a limited range of geometries, and it is fundamentally a 2.5 dimensions fabrication technique.

The third method, DLW of negative photoresists and subsequent metallization of the 3D nanostructures using electroless plating, is the one that has attracted the most attention to date [4, 92]. The term electroless plating was originally adopted to describe a method of plating metallic substrates without the benefit of an external source of electric current. In general it is characterised by the selective reduction of metal ions only at the surface of a catalytic substrate immersed into an aqueous

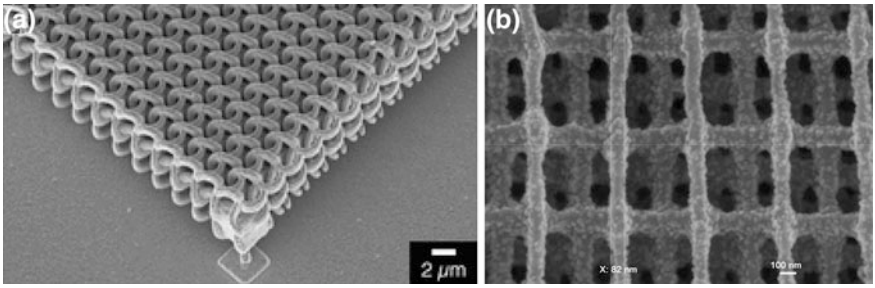

Fig. 8.5 3D metallic photonic crystals made using **a** non selective, **b** selective electroless plating. *Source* Radke et al. [4] and Vasilantonakis et al. [6]

solution of metal ions, with continued deposition on the substrate through the catalytic action of the deposit itself [93, 94]. In this case, again two different approaches have been followed; the first uses lithographic materials such as the negative photoresist SU-8, or acrylate materials to fabricate the 3D structures [4]. However, in order to activate the surface for electroless plating, additional processing for surface functionalization is required and hence the quality, structural integrity and resolution of the structures depend on the photosensitive material and the subsequent surface processing step. The resolution and structure integrity can be very good, however, as the density of the metal binding sites on the structure cannot be controlled, the metallization quality can vary. In addition, there is no selectivity and the substrate as well as the structure is metallized, often requiring the separation of the structure from the substrate (Fig. 8.5a) [4]. These concerns are addressed by the second approach, which uses a photosensitive material doped with the metal binding sites [6, 80]. In this case, the density and distribution of the binding sites can be controlled and high quality metallized structures are obtained, like the one in Fig. 8.5b.

8.5.2 Micromechanical and Microfluidic Systems

Further promising applications of DLW are in the field of rapid prototyping and fabrication of micromechanical and microfluidic systems. In this section, a few examples of structures fabricated by DLW are presented. In Fig. 8.6 a microvalve is shown [95]. This valve is designed to control blood flow and can be made without requiring further assembly. Figure 8.6a shows the microvalve with ¼ of the casing missing, in order to show the interior of the valve, while Fig. 8.6b shows the whole valve. Figure 8.6c, d show the valve in open and closed positions, respectively.

Another example can be seen in Fig. 8.7, where a three-dimensional filter with micrometre-sized pores, in a commercial microfluidic chip is shown [10]. The filter is fabricated inside an already sealed microfluidic channel using DLW, which

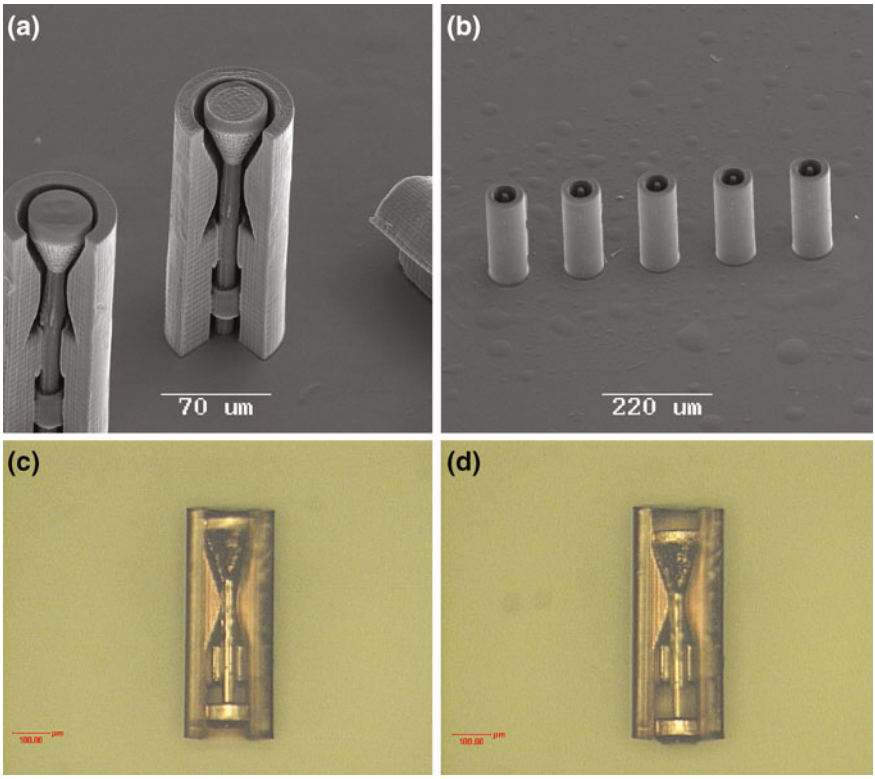

Fig. 8.6 A 3D, readily assembled microvalve designed to control blood flow. **a** Microvalve with ¼ of the casing removed, to allow inspection of the valve interior. **b** The whole microvalve. **c** The valve open. **d** The valve closed. *Source* Schizas et al. [95]

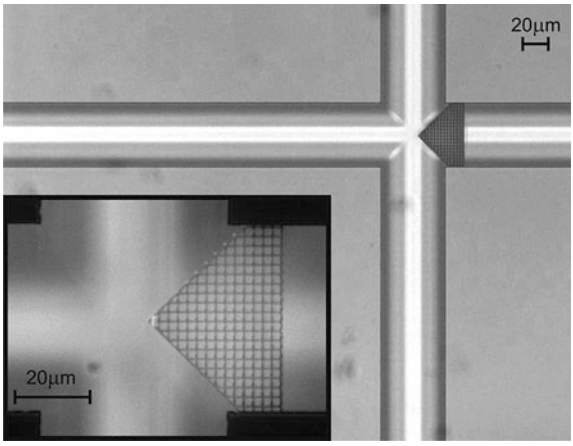

Fig. 8.7 A three-dimensional filter with micrometre-sized pores, in a commercial microfluidic chip. *Source* Amato et al. [10]

enables integration of the filter by post-processing in a chip that has been fabricated by standard technologies. This device is designed for plasma separation from whole blood.

8.6 Conclusions

We reviewed some of the recent work in three-dimensional microstructuring of photosensitive materials by femtosecond lasers. The applications of nonlinear and quenching phenomena allow one to overcome both surface absorption and the diffraction limit to produce 3D microstructures with sub-diffraction limit resolution. We have also described some of the chemistry used and some of the potential applications of this very powerful technology in the fields of photonics and microfluidics.

Acknowledgments This work was partly funded by the EOARD Grant 113090 and by LaserLab Europe (ULF-FORTH001589). K.T was supported by the GSRT grant Herakleitos II.

References

1. H.-B. Sun, S. Kawata, *Two-photon Photopolymerization and 3D Lithographic Microfabrication*, ed. by N. Fatkullin. NMR. 3D Analysis. Photopolymerization, vol. 170 (Springer, Berlin, 2004), pp. 169–273
2. S. Juodkazis, V. Mizeikis, H. Misawa, Three-dimensional microfabrication of materials by femtosecond lasers for photonics applications. J. Appl. Phys. **106**, 051101 (2009)
3. M. Farsari, M. Vamvakaki, B.N. Chichkov, Multiphoton polymerization of hybrid materials. J. Opt. **12**, 124001 (2010)
4. A. Radke, T. Gissibl, T. Klotzbücher, P.V. Braun, H. Giessen, Three-dimensional bichiral plasmonic crystals fabricated by direct laser writing and electroless silver plating. Adv. Mater. **23**, 3018–3021 (2011)
5. J.K. Gansel, M. Thiel, M.S. Rill, M. Decker, K. Bade, V. Saile, G. von Freymann, S. Linden, M. Wegener, Gold helix photonic metamaterial as broadband circular polarizer. Science **325**, 1513–1515 (2009)
6. N. Vasilantonakis, K. Terzaki, I. Sakellari, V. Purlys, D. Gray, C.M. Soukoulis, M. Vamvakaki, M. Kafesaki, M. Farsari, Three-dimensional metallic photonic crystals with optical bandgaps. Adv. Mater. **24**, 1101–1105 (2012)
7. D. Palima, A.R. Bañas, G. Vizsnyiczai, L. Kelemen, P. Ormos, J. Glückstad, Wave-guided optical waveguides. Opt. Express **20**, 2004–2014 (2012)
8. M. Malinauskas, A. Zukauskas, V. Purlys, K. Belazaras, A. Momot, D. Paipulas, R. Gadonas, A. Piskarskas, H. Gilbergs, A. Gaidukeviciute, I. Sakellari, M. Farsari, S. Juodkazis, Femtosecond laser polymerization of hybrid/integrated micro-optical elements and their characterization. J. Opt. **12**, 124010 (2010)
9. M. Malinauskas, A. Gaidukeviciute, V. Purlys, A. Zukauskas, I. Sakellari, E. Kabouraki, A. Candiani, D. Gray, S. Pissadakis, R. Gadonas, A. Piskarskas, C. Fotakis, M. Vamvakaki, M. Farsari, Direct laser writing of microoptical structures using a Ge-containing hybrid material. Metamaterials **5**, 135–140 (2011)

10. L. Amato, Y. Gu, N. Bellini, S.M. Eaton, G. Cerullo, R. Osellame, Integrated three dimensional filter separates nanoscale from microscale elements in a microfluidic chip. Lab Chip **12**, 1135–1142 (2012)
11. F. Claeyssens, E.A. Hasan, A. Gaidukeviciute, D.S. Achilleos, A. Ranella, C. Reinhardt, A. Ovsianikov, S. Xiao, C. Fotakis, M. Vamvakaki, B.N. Chichkov, M. Farsari, Three-dimensional biodegradable structures fabricated by two-photon polymerization. Langmuir **25**, 3219–3223 (2009)
12. V. Melissinaki, A.A. Gill, I. Ortega, M. Vamvakaki, A. Ranella, J.W. Haycock, C. Fotakis, M. Farsari, F. Claeyssens, Direct laser writing of 3D scaffolds for neural tissue engineering applications. Biofabrication **3**, 045005 (2011)
13. F. Klein, B. Richter, T. Striebel, C.M. Franz, G. von Freymann, M. Wegener, M. Bastmeyer, Two-component polymer scaffolds for controlled three-dimensional cell culture. Adv. Mater. **23**, 1341–1345 (2011)
14. E. Abbe, Theorie des Mikroskops und der mikroskopischen Wahrnehmung. Arch. Microskop. Anat. **9**, 413 (1873)
15. S.W. Hell, J. Wichmann, Breaking the diffraction resolution limit by stimulated emission: stimulated-emission-depletion fluorescence microscopy. Opt. Lett. **19**, 780–782 (1994)
16. T.A. Klar, S. Jakobs, M. Dyba, A. Egner, S.W. Hell, Fluorescence microscopy with diffraction resolution barrier broken by stimulated emission. Proc. Natl. Acad. Sci. USA **97**, 8206–8210 (2000)
17. T.F. Scott, B.A. Kowalski, A.C. Sullivan, C.N. Bowman, R.R. McLeod, Two-color single-photon photoinitiation and photoinhibition for subdiffraction photolithography. Science **324**, 913–917 (2009)
18. L.J. Li, R.R. Gattass, E. Gershgoren, H. Hwang, J.T. Fourkas, Achieving lambda/20 resolution by one-color initiation and deactivation of polymerization. Science **324**, 910–913 (2009)
19. J. Fischer, M. Wegener, Three-dimensional direct laser writing inspired by stimulated-emission-depletion microscopy. Opt. Mater. Express **1**, 614–624 (2011)
20. Y. Cao, Z. Gan, B. Jia, R.A. Evans, M. Gu, High-photosensitive resin for super-resolution direct-laser-writing based on photoinhibited polymerization. Opt. Express **19**, 19486–19494 (2011)
21. T.J.A. Wolf, J. Fischer, M. Wegener, A.N. Unterreiner, Pump-probe spectroscopy on photoinitiators for stimulated-emission-depletion optical lithography. Opt. Lett. **36**, 3188–3190 (2011)
22. I. Sakellari, E. Kabouraki, D. Gray, V. Purlys, C. Fotakis, A. Pikulin, N. Bityurin, M. Vamvakaki, M. Farsari, Diffusion-assisted high resolution direct femtosecond laser writing. ACS Nano (2012). doi:10.1021/nn204454c
23. W.-E. Lu, X.-Z. Dong, W.-Q. Chen, Z.-S. Zhao, X.-M. Duan, Novel photoinitiator with a radical quenching moiety for confining radical diffusion in two-photon induced photopolymerization. J. Mater. Chem. **21**, 5650–5659 (2011)
24. C.N. LaFratta, J.T. Fourkas, T. Baldacchini, R.A. Farrer, Multiphoton fabrication. Angew. Chem. Int. Ed. **46**, 6238–6258 (2007)
25. M. Farsari, G. Filippidis, K. Sambani, T.S. Drakakis, C. Fotakis, Two-photon polymerization of an Eosin Y-sensitized acrylate composite. J. Photochem. Photobiol. A **181**, 132–135 (2006)
26. M. Farsari, B.N. Chichkov, Two-photon fabrication. Nat. Photonics **3**, 450–452 (2009)
27. M. Farsari, M. Vamvakaki, B.N. Chichkov, Multiphoton polymerization of hybrid materials. J. Opt. **12**, 124001 (2010, in print)
28. W.H. Zhou, S.M. Kuebler, K.L. Braun, T.Y. Yu, J.K. Cammack, C.K. Ober, J.W. Perry, S.R. Marder, An efficient two-photon-generated photoacid applied to positive-tone 3D microfabrication. Science **296**, 1106–1109 (2002)
29. M.P. Stevens, *Polymer Chemistry: An Introduction*, 3rd edn. (Oxford University Press, New York, 1999)
30. H.R. Allcock, F.W. Lampe, J.E. Mark, *Contemporary Polymer Chemistry*, 3rd edn. (Pearson-Prentice Hall, Upper-Saddle River, 2003)
31. P.C. Hiemenz, T.P. Lodge, *Polymer Chemistry,* 2nd edn. (CRC Press, New York, 2007)

32. B. Bhuian, R.J. Winfield, S. O'Brien, G.M. Crean, Investigation of the two-photon polymerisation of a Zr-based inorganic-organic hybrid material system. Appl. Surf. Sci. **252**, 4845–4849 (2006)
33. S. Maruo, O. Nakamura, S. Kawata, Three-dimensional microfabrication with two-photon-absorbed photopolymerization. Opt. Lett. **22**, 132–134 (1997)
34. X.M. Duan, H.B. Sun, K. Kaneko, S. Kawata, Two-photon polymerization of metal ions doped acrylate monomers and oligomers for three-dimensional structure fabrication. Thin Solid Films **453–454**, 518–521 (2004)
35. Z.B. Sun, X.Z. Dong, W.Q. Chen, S. Nakanishi, X.M. Duan, S. Kawata, Multicolor polymer nanocomposites: in situ synthesis and fabrication of 3D microstructures. Adv. Mater. **20**, 914–919 (2008)
36. Z.B. Sun, X.Z. Dong, W.Q. Chen, S. Shoji, X.M. Duan, S. Kawata, Two- and three-dimensional micro/nanostructure patterning of CdS-polymer nanocomposites with a laser interference technique and in situ synthesis. Nanotechnology **19**, 035611 (2008)
37. F. Formanek, N. Takeyasu, T. Tanaka, K. Chiyoda, A. Ishikawa, S. Kawata, Selective electroless plating to fabricate complex three-dimensional metallic micro/nanostructures. Appl. Phys. Lett. **88**, 3 (2006)
38. N. Takeyasu, T. Tanaka, S. Kawata, Fabrication of 3D metal/polymer microstructures by site-selective metal coating. Appl. Phys. A Mater. Sci. Process. **90**, 205–209 (2008)
39. D.S. Correa, P. Tayalia, G. Cosendey, D.S. dos Santos, R.F. Aroca, E. Mazur, C.R. Mendonca, Two-photon polymerization for fabricating structures containing the biopolymer chitosan. J. Nanosci. Nanotechnol. **9**, 5845–5849 (2009)
40. C.R. Mendonca, D.S. Correa, F. Marlow, T. Voss, P. Tayalia, E. Mazur, Three-dimensional fabrication of optically active microstructures containing an electroluminescent polymer. Appl. Phys. Lett. **95**, 113309 (2009)
41. G. Witzgall, R. Vrijen, E. Yablonovitch, V. Doan, B.J. Schwartz, Single-shot two-photon exposure of commercial photoresist for the production of three-dimensional structures. Opt. Lett. **23**, 1745–1747 (1998)
42. K.D. Belfield, K.J. Schafer, Y.U. Liu, J. Liu, X.B. Ren, E.W. Van Stryland, Multiphoton-absorbing organic materials for microfabrication, emerging optical applications and non-destructive three-dimensional imaging. J. Phys. Org. Chem. **13**, 837–849 (2000)
43. S.M. Kuebler, K.L. Braun, W.H. Zhou, J.K. Cammack, T.Y. Yu, C.K. Ober, S.R. Marder, J. W. Perry, Design and application of high-sensitivity two-photon initiators for three-dimensional microfabrication. J. Photochem. Photobiol. A Chem. **158**, 163–170 (2003)
44. W.H. Teh, U. Durig, G. Salis, R. Harbers, U. Drechsler, R.F. Mahrt, C.G. Smith, H. J. Guntherodt, SU-8 for real three-dimensional subdiffraction-limit two-photon microfabrication. Appl. Phys. Lett. **84**, 4095–4097 (2004)
45. S. Juodkazis, V. Mizeikis, K.K. Seet, M. Miwa, H. Misawa, Two-photon lithography of nanorods in SU-8 photoresist. Nanotechnology **16**, 846–849 (2005)
46. V. Mizeikis, K.K. Seet, S. Juodkazis, H. Misawa, Three-dimensional woodpile photonic crystal templates for the infrared spectral range. Opt. Lett. **29**, 2061–2063 (2004)
47. K.K. Seet, V. Mizeikis, S. Matsuo, S. Juodkazis, H. Misawa, Three-dimensional spiral-architecture photonic crystals obtained by direct laser writing. Adv. Mater. **17**, 541–545 (2005)
48. K.K. Seet, V. Mizeikis, S. Juodkazis, H. Misawa, Three-dimensional circular spiral photonic crystal structures recorded by femtosecond pulses. J. Non-Cryst. Solids **352**, 2390–2394 (2006)
49. M. Deubel, G. Von Freymann, M. Wegener, S. Pereira, K. Busch, C.M. Soukoulis, Direct laser writing of three-dimensional photonic-crystal templates for telecommunications. Nat. Mater. **3**, 444–447 (2004)
50. D. Wu, Q.D. Chen, L.G. Niu, J.N. Wang, J. Wang, R. Wang, H. Xia, H.B. Sun, Femtosecond laser rapid prototyping of nanoshells and suspending components towards microfluidic devices. Lab Chip **9**, 2391–2394 (2009)

51. G. Kumi, C.O. Yanez, K.D. Belfield, J.T. Fourkas, High-speed multiphoton absorption polymerization: fabrication of microfluidic channels with arbitrary cross-sections and high aspect ratios. Lab Chip **10**, 1057–1060 (2010)
52. M. Stoneman, M. Fox, C.Y. Zeng, V. Raicu, Real-time monitoring of two-photon photopolymerization for use in fabrication of microfluidic devices. Lab Chip **9**, 819–827 (2009)
53. Y.S. Chen, A. Tal, D.B. Torrance, S.M. Kuebler, Fabrication and characterization of three-dimensional silver-coated polymeric microstructures. Adv. Funct. Mater. **16**, 1739–1744 (2006)
54. M.S. Rill, C. Plet, M. Thiel, I. Staude, G. Von Freymann, S. Linden, M. Wegener, Photonic metamaterials by direct laser writing and silver chemical vapour deposition. Nat. Mater. **7**, 543–546 (2008)
55. M. Straub, L.H. Nguyen, A. Fazlic, M. Gu, Complex-shaped three-dimensional microstructures and photonic crystals generated in a polysiloxane polymer by two-photon microstereolithography. Opt. Mater. **27**, 359–364 (2004)
56. R. Houbertz, G. Domann, C. Cronauer, A. Schmitt, H. Martin, J.U. Park, L. Frohlich, R. Buestrich, M. Popall, U. Streppel, P. Dannberg, C. Wachter, A. Brauer, Inorganic-organic hybrid materials for application in optical devices. Thin Solid Films **442**, 194–200 (2003)
57. R. Houbertz, L. Frohlich, M. Popall, U. Streppel, P. Dannberg, A. Brauer, J. Serbin, B.N. Chichkov, Inorganic-organic hybrid polymers for information technology: from planar technology to 3D nanostructures. Adv. Eng. Mater. **5**, 551–555 (2003)
58. M. Farsari, G. Filippidis, C. Fotakis, Fabrication of three-dimensional structures by three-photon polymerization. Opt. Lett. **30**, 3180–3182 (2005)
59. Y. Jun, P. Nagpal, D.J. Norris, Thermally stable organic-inorganic hybrid photoresists for fabrication of photonic band gap structures with direct laser writing. Adv. Mater. **20**, 606–610 (2008)
60. J. Serbin, A. Egbert, A. Ostendorf, B.N. Chichkov, R. Houbertz, G. Domann, J. Schulz, C. Cronauer, L. Frohlich, M. Popall, Femtosecond laser-induced two-photon polymerization of inorganic-organic hybrid materials for applications in photonics. Opt. Lett. **28**, 301–303 (2003)
61. J. Serbin, M. Gu, Superprism phenomena in waveguide-coupled woodpile structures fabricated by two-photon polymerization. Opt. Express **14**, 3563–3568 (2006)
62. J. Serbin, M. Gu, Experimental evidence for superprism effects in three-dimensional polymer photonic crystals. Adv. Mater. **18**, 221–224 (2006)
63. J.F. Li, B.H. Jia, G.Y. Zhou, C. Bullen, J. Serbin, M. Gu, Spectral redistribution in spontaneous emission from quantum-dot-infiltrated 3D woodpile photonic crystals for telecommunications. Adv. Mater. **19**, 3276–3280 (2007)
64. J.F. Li, B.H. Jia, M. Gu, Engineering stop gaps of inorganic-organic polymeric 3D woodpile photonic crystals with post-thermal treatment. Opt. Express **16**, 20073–20080 (2008)
65. T. Woggon, T. Kleiner, M. Punke, U. Lemmer, Nanostructuring of organic-inorganic hybrid materials for distributed feedback laser resonators by two-photon polymerization. Opt. Express **17**, 2500–2507 (2009)
66. V. Dinca, E. Kasotakis, J. Catherine, A. Mourka, A. Ranella, A. Ovsianikov, B.N. Chichkov, M. Farsari, A. Mitraki, C. Fotakis, Directed three-dimensional patterning of self-assembled peptide fibrils. Nano Letters **8**, 538–543 (2008)
67. T. Grossmann, S. Schleede, M. Hauser, T. Beck, M. Thiel, G. von Freymann, T. Mappes, H. Kalt, Direct laser writing for active and passive high-Q polymer microdisks on silicon. Opt. Express **19**, 11451–11456 (2011)
68. J. Trull, L. Maigyte, V. Mizeikis, M. Malinauskas, S. Juodkazis, C. Cojocaru, M. Rutkauskas, M. Peckus, V. Sirutkaitis, K. Staliunas, Formation of collimated beams behind the woodpile photonic crystal. Phys. Rev. A **84**, 5 (2011)
69. E. Brasselet, M. Malinauskas, A. Zukauskas, S. Juodkazis, Photopolymerized microscopic vortex beam generators: precise delivery of optical orbital angular momentum. Appl. Phys. Lett. **97**, 211108 (2011)

70. Z.P. Liu, Y. Li, Y.F. Xiao, B.B. Li, X.F. Jiang, Y. Qin, X.B. Feng, H. Yang, Q.H. Gong, Direct laser writing of whispering gallery microcavities by two-photon polymerization. Appl. Phys. Lett. **97**, 211105 (2011)
71. I. Sakellari, A. Gaidukeviciute, A. Giakoumaki, D. Gray, C. Fotakis, M. Farsari, M. Vamvakaki, C. Reinhardt, A. Ovsianikov, B.N. Chichkov, Two-photon polymerization of titanium-containing sol-gel composites for three-dimensional structure fabrication. Appl. Phys. A **100**, 359–364 (2010)
72. Q. Sun, S. Juodkazis, N. Murazawa, V. Mizeikis, H. Misawa, Freestanding and movable photonic microstructures fabricated by photopolymerization with femtosecond laser pulses. J. Micromech. Microeng. **20**, 035004 (2010)
73. R.J. Winfield, B. Bhuian, S. O'Brien, G.M. Crean, Refractive femtosecond laser beam shaping for two-photon polymerization. Appl. Phys. Lett. **90**, 111115 (2007)
74. R.J. Winfield, B. Bhuian, S. O'Brien, G.M. Crean, Fabrication of grating structures by simultaneous multi-spot fs laser writing. Appl. Surf. Sci. **253**, 8086–8090 (2007)
75. C. Schizas, V. Melissinaki, A. Gaidukeviciute, C. Reinhardt, C. Ohrt, V. Dedoussis, B.N. Chichkov, C. Fotakis, M. Farsari, D. Karalekas, On the design and fabrication by two-photon polymerization of a readily assembled micro-valve. Int. J. Adv. Manuf. Technol. (in print). doi:10.1007/s00170-009-2320-4
76. A. Ovsianikov, J. Viertl, B. Chichkov, M. Oubaha, B. MacCraith, L. Sakellari, A. Giakoumaki, D. Gray, M. Vamvakaki, M. Farsari, C. Fotakis, Ultra-low shrinkage hybrid photosensitive material for two-photon polymerization microfabrication. ACS Nano **2**, 2257–2262 (2008)
77. A. Ovsianikov, S.Z. Xiao, M. Farsari, M. Vamvakaki, C. Fotakis, B.N. Chichkov, Shrinkage of microstructures produced by two-photon polymerization of Zr-based hybrid photosensitive materials. Opt. Express **17**, 2143–2148 (2009)
78. M. Farsari, A. Ovsianikov, M. Vamvakaki, I. Sakellari, D. Gray, B.N. Chichkov, C. Fotakis, Fabrication of three-dimensional photonic crystal structures containing an active nonlinear optical chromophore. Appl. Phys. A Mater. Sci. Process. **93**, 11–15 (2008)
79. B. Jia, D. Buso, J.V. Embden, J. Li, M. Gu, Highly non-linear quantum dot doped nanocomposites for functional three-dimensional structures generated by two-photon polymerization. Adv. Mater. **22**, 2463–2467 (2010)
80. K. Terzaki, N. Vasilantonakis, A. Gaidukeviciute, C. Reinhardt, C. Fotakis, M. Vamvakaki, M. Farsari, 3D conducting nanostructures fabricated using direct laser writing. Opt. Mater. Express **1**, 586–597 (2011)
81. S.K. Seidlits, C.E. Schmidt, J.B. Shear, High-resolution patterning of hydrogels in three dimensions using direct-write photofabrication for cell guidance. Adv. Funct. Mater. **19**, 3543–3551 (2009)
82. E.T. Ritschdorff, J.B. Shear, Multiphoton lithography using a high-repetition rate microchip laser. Anal. Chem. **82**, 8733–8737 (2010)
83. S. Turunen, E. Käpylä, K. Terzaki, J. Viitanen, C. Fotakis, M. Kellomäki, M. Farsari, Pico- and femtosecond laser-induced crosslinking of protein microstructures: evaluation of processability and bioactivity. Biofabrication **3**, 045002 (2011)
84. A. Ovsianikov, M. Malinauskas, S. Schlie, B. Chichkov, S. Gittard, R. Narayan, M. Lobler, K. Sternberg, K.P. Schmitz, A. Haverich, Three-dimensional laser micro- and nano-structuring of acrylated poly(ethylene glycol) materials and evaluation of their cytoxicity for tissue engineering applications. Acta Biomater. **7**, 967–974 (2011)
85. T.S. Drakakis, G. Papadakis, K. Sambani, G. Filippidis, S. Georgiou, E. Gizeli, C. Fotakis, M. Farsari, Construction of three-dimensional biomolecule structures employing femtosecond lasers. Appl. Phys. Lett. **89**, 144108 (2006)
86. M. Farsari, G. Filippidis, T.S. Drakakis, K. Sambani, S. Georgiou, G. Papadakis, E. Gizeli, C. Fotakis, Three-dimensional biomolecule patterning. Appl. Surf. Sci. **253**, 8115–8118 (2007)
87. J.D. Joannopoulos, S.G. Johnson, J.N. Winn, R.D. Meade, *Photonic Crystals: Molding the Flow of Light*, 2nd edn. (Princeton University Press, Princeton, 2008)

88. E. Yablonovitch, Inhibited spontaneous emission in solid-state physics and electronics. Phys. Rev. Lett. **58**, 2059–2062 (1987)
89. S. John, Strong localization of photons in certain disordered dielectric superlattices. Phys. Rev. Lett. **58**, 2486–2489 (1987)
90. Y.Y. Cao, X.Z. Dong, N. Takeyasu, T. Tanaka, Z.S. Zhao, X.M. Duan, S. Kawata, Morphology and size dependence of silver microstructures in fatty salts-assisted multiphoton photoreduction microfabrication. Appl. Phys. A **96**, 453–458 (2009)
91. Y.Y. Cao, N. Takeyasu, T. Tanaka, X.M. Duan, S. Kawata, 3D Metallic nanostructure fabrication by surfactant-assisted multiphoton-induced reduction. Small **5**, 1144–1148 (2009)
92. K. Kaneko, K. Yamamoto, S. Kawata, H. Xia, J.F. Song, H.B. Sun, Metal-nanoshelled three-dimensional photonic lattices. Opt. Lett. **33**, 1999–2001 (2008)
93. G.O. Mallory, J.B. Hajdu (eds.), *Electroless Plating: Fundamentals and Applications* (American Electroplaters and Surface Finishers Society, Orlando, 1990)
94. S. Hrapovic, Y.L. Liu, G. Enright, F. Bensebaa, J.H.T. Luong, New strategy for preparing thin gold films on modified glass surfaces by electroless deposition. Langmuir **19**, 3958–3965 (2003)
95. C. Schizas, V. Melissinaki, A. Gaidukeviciute, C. Reinhardt, C. Ohrt, V. Dedoussis, B.N. Chichkov, C. Fotakis, M. Farsari, D. Karalekas, On the design and fabrication by two-photon polymerization of a readily assembled micro-valve. Int. J. Adv. Manufact. Technol. **48**(5–8), 435–441 (2010)

Chapter 9
Nonlinear Plasmon Optics

Mario Hentschel, Tobias Utikal, Bernd Metzger, Harald Giessen and Markus Lippitz

Abstract We study nonlinear optics in plasmonic nanosystems, discuss the role of structural symmetries and the influence of linear optical properties. In particular, we investigate third harmonic generation from dimer nanoantennas and show that the nonlinear optical response, in contrast to common belief, is not governed by gap nonlinearities but fully described by the linear optical properties of the antenna. A simple nonlinear harmonic oscillator model is shown to reproduce all experimental features.

9.1 Introduction

The optical properties of metal nanoparticles are a large subfield of plasmonics. If an external light field impinges on a metal nanoparticle, as sketched in Fig. 9.1, collective oscillations of the quasi-free conduction electron are excited. The charge cloud is displaced with respect to the fixed ionic background and thus causes local electric fields. The main benefit afforded by plasmonics is its ability to concentrate incoming electromagnetic energy into deep subwavelength volumes. On the one hand the metal particles itself are in general smaller or at least comparable to the wavelength of light. Additionally, the so-called hot spots at which the field enhancement occurs are significantly smaller than the particle itself. The local electric field strength can thus significantly surpass the incoming field strength. The process is moreover surprisingly efficient as the plasmonic resonances couple extremely well to an external light field due to the large resonances dipole moment which is fundamentally connected to the large number of free conduction electrons.

M. Hentschel (✉) · T. Utikal · B. Metzger · H. Giessen · M. Lippitz
4th Physics Institute and Research Center SCoPE, University of Stuttgart,
Pfaffenwaldring 57, 70569 Stuttgart, Germany
e-mail: m.hentschel@pi4.uni-stuttgart.de

M. Hentschel · T. Utikal · M. Lippitz
Max Planck Institute for Solid State Research, Heisenbergstrasse 1, 70569 Stuttgart, Germany

© Springer International Publishing Switzerland 2015

S. Sakabe et al. (eds.), *Progress in Nonlinear Nano-Optics*,
Nano-Optics and Nanophotonics, DOI 10.1007/978-3-319-12217-5_9

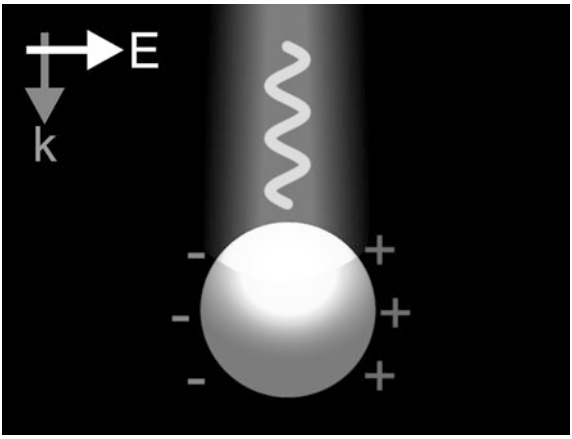

Fig. 9.1 If an external light field with electric field E and wavevector k is incident on a noble metal particle collective oscillations of the quasi-free conduction electrons can be excited. The periodic displacement of the electron cloud with respect to the fixed ionic background of the particle will cause local electric fields in the vicinity of the particle. This confinement of energy into deep subwavelength volumes leads to a significant local field strength which can exceed the incoming one by orders of magnitude

Already early on it was realized that this strong confinement offers a multitude of possible applications. First of all, it enables strong coupling between neighbouring plasmonic particles due to the overlap of the local electric fields. Individual particles can be coupled together to display collective behavior, just as in the case of atoms and molecules [1]. This analogy has led to the development of the plasmon hybridization model [2] which is able to describe plasmonic coupling within the framework of molecular orbital theory known from atomic and molecular physics. This coupling allows for energy transfer and transport below the diffraction limit [3], for the plasmonic analogue of the atomic physics concept of electromagnetically induced transparency (EIT) with even stronger local field enhancements [4–7], for plasmonic molecules and complex systems with tailorable near-field enhancement and confinement [8–10].

What is more, plasmonic resonances are highly sensitive to their dielectric environment. This behavior enables plasmonic sensing due to a spectral shift of the far-field optical response of the structures upon a change in the dielectric surrounding [11–13]. A plethora of sensing applications has been proposed and demonstrated, both in ensembles [14] as well as on the single particle level [15, 16].

From the beginning of plasmonics highly efficient nonlinear optics utilizing plasmonic structures were in the focus of interest. The intensity of, e.g., second harmonic generation (SHG) scales with the fourth power of the fundamental field strength, third harmonic generation (THG) even scales with the sixth power. Keeping in mind that the local electric fields associated with a plasmonic resonance can—at least in theory—exceed the incoming field strength by orders of magnitude, extremely efficient nonlinear conversion efficiencies are to be expected.

The first nonlinear optical experiments on plasmonic systems date back to the early 1980. Wokaun et al. [17] studied second harmonic generation from metal-island films and microstructured silver films and interpreted the enhanced response in terms of localized surface plasma oscillations. Ricard et al. [18] and Hache et al. [19] demonstrated optical phase conjugation from a composite material of gold or silver spheres immersed in water. The value of the optical Kerr coefficient on resonance was found to be about three orders of magnitude larger than off-resonantly. Enhanced second-harmonic generation from rough metallic films was as well investigated in detail [20, 21]. Early on it was realized that plasmon resonances on the surface play an integral role in all the processes, likewise second harmonic generation as well as surface enhanced Raman scattering [22–26]. In fact, in the beginning mostly composite materials with small metal inclusions were studied. Their nonlinear optical properties could be modelled by nonlinear extensions of Maxwell-Garnett [27] and effective-medium theories [28, 29]. Apart from phase conjugation, difference frequency mixing [30], four wave mixing, second harmonic generation, and other nonlinear optical processes were reported.

Conceptually, a number of mechanisms could be responsible for the nonlinear optical response of a metal nanoparticle residing in a dielectric environment:

(1) Surface nonlinearities: When the particle is excited close to its plasmon resonances the quasi free conduction electrons will perform harmonic oscillations. Yet, due to the finite size of the particles and the presence of the surface, anharmonicities will start to play a major role. It has been shown that for very small nanoparticles this anharmonicity can lead to a significant source of third harmonic radiation, showing a fourth order dependence of the TH intensity on the diameter of the particle [31, 32]. In this model the third harmonic contribution can be seen as induced by the surface of the sphere and thus the induced dipole is proportional to the surface area of the sphere. Note that this contribution vanishes as soon as the anharmonicity in the potential vanishes, that is, as soon as the particle becomes too large for the oscillating electrons to see the surface.
(2) Bulk or volume nonlinearities: Another mechanism is linked to the bound electrons of the material itself. The signal could stem from the contribution of the individual constituents of the cluster rather than from its collective properties, thus being a molecular, size-independent property. This contribution would depend on the volume of the nanoparticle as the signal increases linearly with the number of individual “molecules” in the cluster. The nonlinear signal would hence increase with the sixth power of the particle radius. This term is thus considered as the volume contribution to the nonlinear signal.
(3) Field enhancement: The last contribution originates from the enhanced local electric fields associated with the plasmonic resonance. If the particle is surrounded by a dielectric, the strong near-fields can enhance the nonlinear response from this dielectric. Additionally, the near-fields close to the nanoparticle surface can enhance the signal from the bulk nonlinearity of gold itself.

Obviously, the origin of the nonlinearity might vary when changing the studied systems. Additionally, two or more processes might occur simultaneously.

In 2005 Lippitz et al. [33] studied for the first time third harmonic generation from single gold nanoparticles. They attempted to unravel the mechanism responsible for the signals observed, yet, a clear differentiation between surface and bulk contributions was not possible.

In spite of the remaining open questions regarding the nonlinear processes in these comparably simple systems, a multitude of research has been devoted to much more complicated systems. With the advent of well controllable fabrication and synthesis methods, such as electron beam lithography or wet chemical growth methods, complex plasmonic materials became available. One of the first examples is the work by Klein et al., who studied second harmonic generation from arrays of split ring resonators [34]. Split ring resonators are U-shaped nanostructures which basically constitute a nano-scale version of an LC-circuit. Their most intriguing property is the presence of a strong plasmonic resonance which is associated with the excitation of a ring current in the U-shape and thus a magnetic moment at optical frequencies. As such a material property is not present in any naturally occurring material, these composite systems are termed metamaterials. The authors explained the strong second harmonic response in this system by including a nonlinear source term based on the magnetic component of the Lorentz force. For the first time it had been suggested that the tailoring of an artificial material would allow for the tailoring of the nonlinear optical properties beyond the capabilities of naturally occurring materials.

Fuelled by these early experiments nonlinear effects were studied in a plethora of systems, such as—to name a few—SHG on L- and T-shaped nanoparticles [35–39], on chiral [40] and planar chiral systems [41, 42], SHG from 3D nanocups [43] and nano-apertures in metal films [44, 45], SHG from silver triangle arrays [46], THG from individual dimer nanoantennas [47, 48], and from arrays of nanoantennas [49, 50], THG on disk arrays [51], frequency mixing at coupled gold nanoparticles [52, 53], SHG and THG from arrays of split ring resonators [54, 55] and inverse split ring resonators [56]. Moreover, the systems became more complex by incorporating elliptical particles into glasses [57], combination with crystalline substrates [58, 59], coupled systems of plasmonic resonances and waveguide modes [60–63], gaseous media in the vicinity of the nanostructures for enhanced higher harmonics generation [64–66], or metallic shells around highly nonlinear cores [67]. Another degree of complexity was recently introduced by multi-resonant plasmonic systems in the hopes of enhancing the fundamental as well as higher harmonic fields which are involved in the conversion processes [68–71].

However, despite the experiments made, a surprisingly large number of open questions remains. One of the main drawbacks of the conducted experiments—to a surprise—appears to be the complexity of the structures. The motivation behind the complex structures is multifold: Firstly, the structures allow for a nearly arbitrary manipulation of their linear optical properties. Secondly, the geometry of the systems can be manipulated which is believed to be particularly important due to the strong symmetry dependence of nonlinear optical processes. Thirdly, researchers

are driven by the dream of disentangling linear and nonlinear optical properties, that is, strongly different nonlinear optical responses of two systems despite identical linear optical ones.

As already much simpler structures are not yet fully understood the entanglement of a multitude of different factors, such as linear properties, spatial symmetries, changing near-field distributions, the presence of different materials and multiple resonances, makes it nearly impossible to deduce the origin of the nonlinear response and the true influence of the individual subsystems.

Figure 9.2 illustrates an example of such a seemingly straightforward experiment. It has been demonstrated that split ring resonators are comparably efficient sources of second harmonic radiation. As in electric dipole approximation SHG is symmetry forbidden in inversion symmetric systems it is widely believed that symmetry breaking is a key ingredient in this process. Thus, it appears to be straightforward to test this hypothesis by making use of the nearly unlimited structural tunability of plasmonic nanostructures. In reducing the length of the split ring resonator arms the structures can successively been transformed into a bar. In doing so, the symmetry of the system is increased from C_{2v} to D_{2h} [72]. Most importantly, the bar is inversion symmetric and is thus expected to not show any second harmonic response under normal incidence illumination. To first sight, one would thus expect the second harmonic response of the structures to successively decrease from the maximum signal of the "full" split ring resonator to none for the bar, depending on the "degree" of symmetry breaking in the system. Even though there is no real "degree" of asymmetry in geometrical systems such as this, there still needs to be a continuous transition from the one to the other system, i.e., from symmetry allowed SHG to symmetry forbidden SHG (in electric dipole approximation). This experiment should therefore be a convincing test of the symmetry dependence of the second harmonic response.

However, it is imperative to note that the symmetry is not the only property that is changing in the system. Firstly, the linear optical properties will undergo significant changes. The spectral position of the fundamental plasmonic mode basically depends on the overall length of structure. This length decreases as the length of the split ring resonator arms decreases, causing a blue shift of the plasmonic mode. As it

Fig. 9.2 A split ring resonator (SRR) belongs to the C_{2v} symmetry group. As it breaks inversion symmetry the structure allows for second harmonic generation in electric dipole approximation. A *single bar*, being of D_{2h} symmetry, does not allow for SH in electric dipole approximation. Successively reducing the arm length of the SRR should thus allow for the direct observation of the influence of symmetry on the nonlinear optical conversion process

is physically meaningless to compare the response of resonant and off-resonant systems, this spectral shift needs be compensated. This can be done either by increasing the overall size of the structure or by using a tunable laser source to excite the structures. Note that in both cases the amount of gold, which is typically used to fabricate the structures, will significantly change as well. Therefore, if the gold itself is involved in the conversion process, this change in material filling fraction might have significant influence. Furthermore, the overall plasmonic mode will change drastically. The fundamental split ring resonator mode is associated with a magnetic moment, whereas the bar just supports a simple dipolar mode. Thus, the near-field distributions will be dramatically different. Simultaneously, the dipole moment of the resonances will change as well. The reason for this is on the one hand the change in mode character but on the other hand the change in structure volume and hence the change of the number of free electrons participating in the collective oscillations. As a consequence, the spectral linewidth and thus the dephasing time of the different modes in the structures will be strongly different. Yet, already basic nonlinear optical textbooks elaborate on the close connection of a resonance linewidth or damping on the nonlinear optical response [73, 74]. As further direct consequence of the different gold volume, the overall scattering amplitude of the resonance will change, changing the interaction strength of the laser field with the structure. Additionally, when changing the laser wavelength one might probe the spectral dependency of the χ^2 active material from which the signal is fundamentally stemming, which could be the gold or the substrate.

Overall, a change in the second harmonic signal could thus be caused by the changing structural symmetry, the different material filling fractions, the change in resonance linewidth, the change of the scattering amplitude, the change in mode character (disappearance of the magnetic mode), the change in the near-field distribution as well as a spectral dependency of the molecular χ^2 of the substrate or gold. Thus, we have to conclude that such an experiment, despite the fact that it appeared perfectly reasonable in the beginning, is quite difficult to interpret.

In the following, we perform third harmonic generation experiments on a simple prototype system comprising two individual metallic bars or triangles which form nanoscale antennas. The distance between the elements as well as their basic size allows to controllably change the linear optical properties of the system. Additionally, the strong confinement of the local electric fields within the gap of the antennas is expected to generate a strong nonlinear optical response, rendering this system highly interesting.

9.2 Results and Discussion

As already discussed, plasmonic structures such as plasmonic nanoantennas concentrate energy in subwavelength volumes [75–78]. The field enhancement can exceed values of 10^3 [79]. The strongly enhanced local electric fields boost the

nonlinear optical response of nanoantennas and other metallic nanostructures. Similar to the case of metal-dielectric photonic crystals [61], both the optical nonlinearity of the metal [80, 81] and the nonlinearity of the dielectric material [58, 67, 82] in the antenna hot spot can contribute to the signal. Hence, in the case of gap nanonatennas we expect THG from the bare antenna, as well as THG originating from the gap region. The notion of a hot spot suggests that the gap signal exceeds the antenna signal. Yet, it is a priori not possible to disentangle these two contributions without modelling the systems and its response. A full numerical simulation of the local optical field and its interaction with the local nonlinear polarizability is capable to differentiate between these contributions [61]. However, a more intuitive understanding is desirable for a rational design of antennas for nonlinear applications [83]. Many aspects of harmonics generation in nanoantennas are still unclear and not well understood, e.g., the role of resonance strength and width, field enhancement in the hot spot, and the influence of antenna geometries on the overall conversion efficiency. While the nonlinear response of metal nanostructures was optimized in recent publications [33, 47–49, 52, 84], only little attention was paid to the simultaneously modified linear response. However, already nonlinear optics textbooks elaborate on the close connection between linear and nonlinear properties of matter [73].

In order to investigate some of the aforementioned aspects, we study dimer nanoantennas which consist of two equally sized plasmonic nanoparticles separated by a gap. In close proximity to one another the plasmonic resonances in the particles mix and hybridize, giving rise to two new collective modes, as shown in the plasmon hybridization scheme [2] depicted in Fig. 9.3a. For light polarized along the long axis of the antenna, the symmetric dipole allowed mode is decreased in resonance energy, whereas the antisymmetric mode is increased in energy. The latter mode cannot be excited for normal light incidence because of its zero net dipole moment. Hence, the gap size as well as the size of the triangles will determine the spectral position of the dipole allowed mode. This behavior is visible in the experimental linear extinction spectra of a series of bowtie nanoantennas, shown in Fig. 9.3b. For decreasing gap size we observe a strong resonance redshift. Upon ohmic contact the resonance shifts outside the observable wavelength region [85–87]. Thus, we have a system at hand that allows for an independent spectral tunability either by the size of the individual element or by the gap distance. Furthermore, a change of the particle size and thus its volume will allow to tailor the dipole moment or oscillator strength of the plasmonic resonance. Note that we perform all experiments on arrays ($100 \times 100\ \mu m^2$) of nominally identical, noninteracting antennas (Fig. 9.3c) so that a loosely focused laser beam can be used which does not damage the structures during the experiment.

The structures are defined in double layer PMMA using electron beam lithography (Raith e_Line) on a bare Suprasil quartz glass substrate (Heraeus) followed by thermal evaporation of a 2 nm Cr adhesion and a 40 nm Au layer and a subsequent lift-off procedure. Scanning electron microscope images are obtained using a Hitachi S-4800 electron microscope.

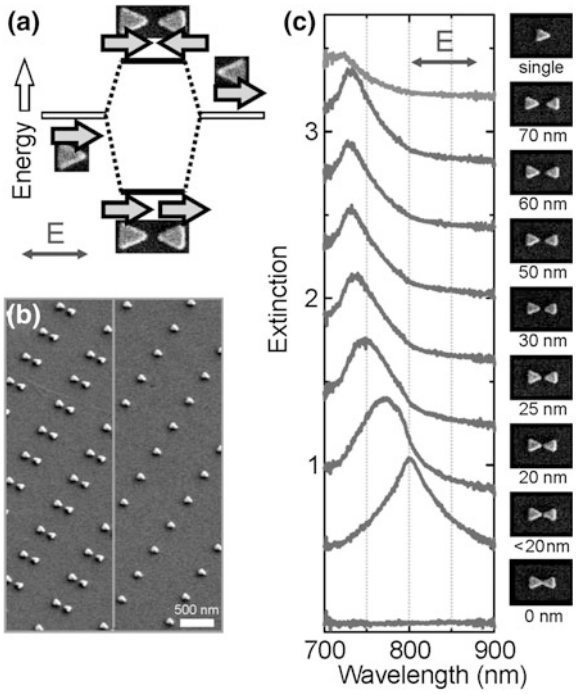

Fig. 9.3 **a** A bowtie nanoantenna constitutes a plasmonic dimer which can be described within the framework of plasmon hybridization. Two collective modes are formed, namely a symmetric dipole-allowed one with a lower resonance energy and an antisymmetric dark mode with higher resonance energy. The dipole-allowed mode can be tuned in resonance energy by the size of the *triangles* and the gap size. The *arrows* depict the electric dipole orientations in a quasistatic picture. **b** Exemplary tilted overview SEM images of the studied antenna arrays. **c** Experimental linear extinction spectra for a series of equally sized *triangles* but decreasing gap size. The spectra have been offset *vertically* for clarity. One observes the predicted resonance red-shift upon closing of the gap. Adapted with permission from [50]. Copyright 2012 American Chemical Society

For the excitation of the nanostructures 8 fs laser pulses centered around 817 nm with a spectral bandwidth extending from 690–930 nm are utilized (VENTEON, pumped by a Coherent Verdi V10). The incoming radiation is focused onto the sample and recollected using spherical mirrors (f = 100 mm). For TH measurements a quartz glass prism sequence is used to filter out the fundamental light. The spectrally resolved detection is performed by a grating monochromator and an attached LN_2 cooled UV-enhanced CCD camera sensitive to the fundamental as well as the TH light in the UV region at around 270 nm (Roper Scientific).

Our setup allows measuring the third-harmonic (TH) radiated by the antennas and simultaneously their linear optical properties using the broadband laser as white light source. This in situ measurement ensures identical excitation conditions of the plasmonic resonances as in the nonlinear optical measurements.

Figure 9.4 depicts the performed linear and nonlinear measurements for an exemplary bowtie antenna array. The left column shows the linear optical properties: Panel (a) shows the spectrum of the driving laser source. The linear spectral response of the antenna array is depicted in panel (b). The interaction strength of the laser source and the nanostructure is basically determined by two quantities: The first is by the spectral detuning between the peak intensity of the laser and the resonance maximum of the plasmonic resonance. In order to excite the plasmonic resonance efficiently it is important to drive it resonantly. Secondly, it is determined by the overall interaction strength of the resonance with an external light field. This interaction strength is given by the resonance dipole moment which is linked to the number of free electrons participating in the collective plasmonic oscillation and thus to the volume of the nanostructure. The resonance dipole moment manifests itself as the area of the extinction peak. In order to quantify the interaction strength between the laser source and the nanostructure we define the so-called linear spectral overlap spectrum, which inherently includes both quantities. It is obtained as the product spectrum of the laser and extinction spectra, as shown in panel (c). It is important to note that the laser spectrum together with the linear extinction spectrum of the nanostructure determines the spectral position of highest interaction. It is hence crucial to measure the linear response carefully.

The right column of Fig. 9.4 depicts the performed linear and nonlinear measurements of the array: In panel (e) the third harmonic (TH) spectrum of the array and in (f) the third harmonic spectrum of the bare glass substrate are shown. Two observations are immediately apparent: The TH signal originating from the antenna array is significantly stronger than the substrate TH. Additionally, the two spectra exhibit their maxima at different spectral positions. The signal from the bare substrate is roughly centred on 272 nm, one third of the wavelength of the peak intensity of the fundamental laser spectrum, whereas the other peaks at $\sim$264 nm. Not only does the presence of the plasmonic resonance seem to boost the TH signal, it is as well spectrally shifting the TH emission maximum.

It is commonly expected that the TH response of a gap nanoantenna is dominated by the contribution arising from the strongly enhanced fields inside the nanoscale gap. If the TH from the hot spot would indeed dominate the TH from the antenna itself, then the nonlinear conversion efficiency of a dimer nanoantenna should drastically increase when the gap size decreases as the near-field localization is particularly strong for small gap sizes. In order to check this intuitive picture, Fig. 9.5 depicts the TH spectra for two different sized bowties upon decreasing gap size. The left column depicts the TH spectra for triangles of $\sim(125 \times 150)$ nm^2 basic size, the right column for a size of $\sim(170 \times 190)$ nm^2. In both cases the gap sizes are varied, starting from single triangles over gap sizes of 70, 60 and 50 nm (from top to bottom). For the smaller antennas we observe a significant increase in the TH signal strength upon decreasing gap size, seemingly consistent with our intuitive expectation. In striking contrast, we observe a strong decrease in TH signal strength upon decreasing gap size for the larger antennas. Furthermore, the larger antennas produce significantly stronger signals for all gap sizes. Additionally, we observe for all antennas a small red-shift of the TH emission maximum under

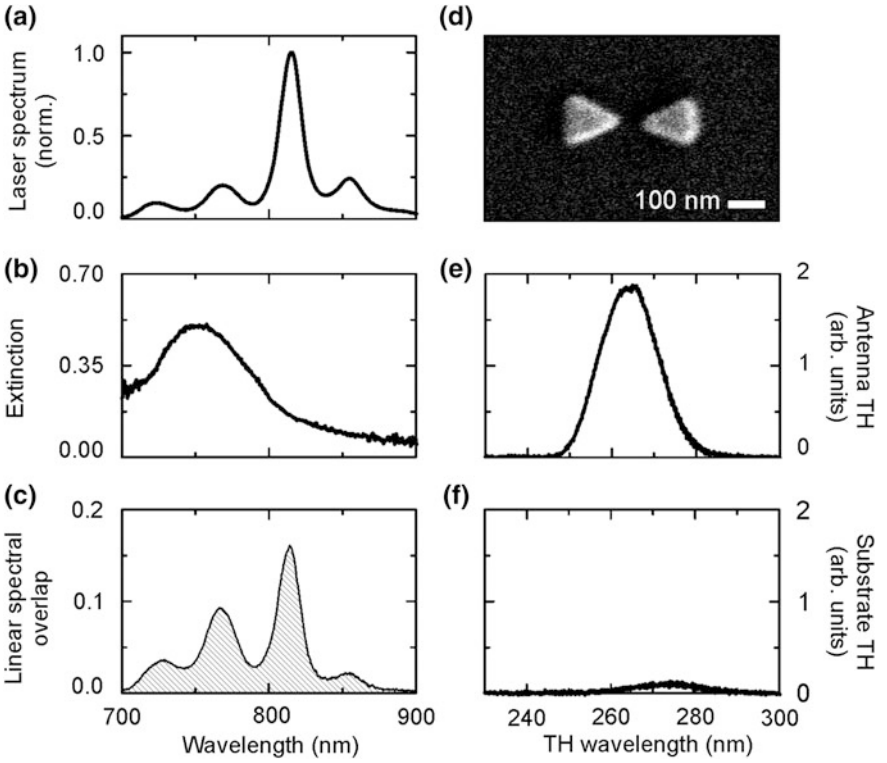

Fig. 9.4 Linear and nonlinear optical properties of a bowtie antenna array, basic *triangle* size (135 × 160) nm^2, gap size 70 nm. **a** Spectrum of the laser source. **b** Linear extinction spectrum of the antenna array. **c** Linear spectral overlap spectrum defined as the product spectrum of the laser and extinction spectra. **d** SEM micrograph of one antenna from the array, periodicity 800 nm × 500 nm. **e** Third harmonic spectrum of the antenna array. **f** Third harmonic spectrum of the bare substrate

closing gap. For the smaller antennas the emission maximum is below 272 nm (indicated by the grey arrow) and approaches this value, whereas the emission maximum is at longer wavelength for the bigger antennas and shifts even further away from it when decreasing the gap size.

These findings are a strong indication that the depicted experiments are dominated by the linear optical response of the antennas and not by gap nonlinearity. We have already shown in Fig. 9.3 that the linear extinction spectrum undergoes a significant red-shift when decreasing the gap size. Additionally, Fig. 9.4 illustrates that the TH emission maximum is below 272 nm for a plasmonic resonance below the maximum laser intensity as the spectral position of maximum interaction strength, as given by the linear overlap spectrum, is below the laser center wavelength. This proves that the plasmon resonance is significantly shifting the maximum TH signal from the intuitively expected one third of the maximum laser intensity.

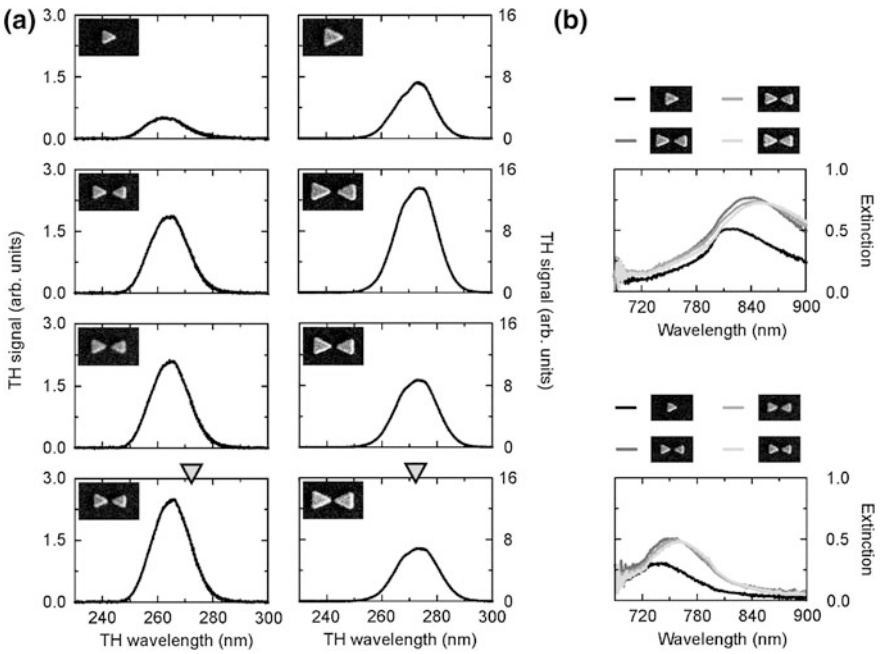

Fig. 9.5 **a** Third harmonic spectra of antenna arrays as a function of decreasing gap size. The *left column* depicts the TH spectra for *triangles* of $\sim(125 \times 150)$ nm^2 basic size, the *right column* for a size of $\sim(170 \times 190)$ nm^2. The gap sizes are varied in both cases from single *triangles*, 70, 60 and 50 nm gap size (from *top* to *bottom*). **b** Linear extinction spectra of the structures in (**a**)

Thus, already from the nonlinear optical behavior we can deduce that the smaller antennas are blue-detuned form the laser center wavelength, whereas the bigger ones are red-detuned. This as well explains the direction of the shift for the two antenna geometries: For decreasing gap size the plasmon resonance red-shifts, as does the spectral position of maximum interaction strength. Therefore, the TH center wavelength is shifting towards the laser center wavelength for the smaller antennas and shifting away from it for the bigger antennas. The measured linear optical spectra which are shown in Fig. 9.5b confirm our interpretation.

To further substantiate this explanation and to deepen our understanding of the underlying processes, we have fabricated a series of samples and studied their TH response. We varied the triangle size and gap size of the bowtie antennas, resulting in 99 different combinations. To modify the field distribution even further, we changed the index of refraction of the environment by covering an identical sample with 100 nm SiO_2. Thirdly, we changed the shape of the antennas from a bowtie antenna (consisting of triangles) to a gap antenna (consisting of rectangles), again varying size of the rectangle and the gap between the rectangles. In total we thus examined 297 antenna fields. Figure 9.6 depicts exemplary SEM micrographs as well as the geometrical dimensions of the structures.

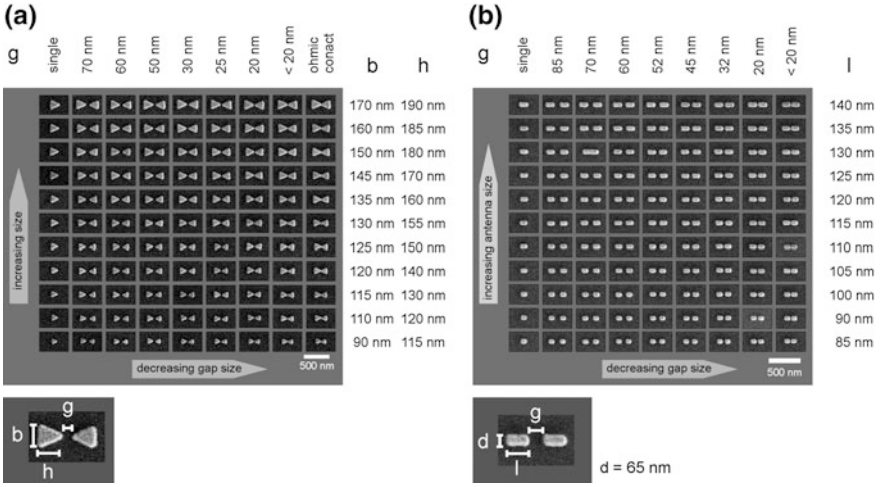

Fig. 9.6 Geometric parameters of the fabricated antenna arrays. **a** Bowtie nanoantennas, each antenna represents an entire 100 × 100 μm^2 array, periodicity 800 nm × 500 nm, gold thickness 40 nm. An identical sample of 99 arrays has been covered with 100 nm SiO_2. **b** Gap nanoantennas consisting of two *rod shaped* nanoparticles. As before, each antenna represents an entire 100 × 100 μm^2 array, periodicity 800 nm × 500 nm, gold thickness 40 nm

The obtained results have shown us the crucial importance of the linear optical properties for the nonlinear optical ones. Hence, it is imperative to know and quantify the linear optical response as only this will render a comparison of the TH conversion efficiencies possible. So far we are not capable to disentangle the influence of the changing linear optical properties under manipulation of the geometrical parameters from any possible influence of gap nonlinearities or possible further unknown contributions.

In Fig. 9.4 we have already introduced the linear spectral overlap spectrum. This spectrum describes how efficient the laser source interacts with the plasmonic nanoantennas. If one integrates this spectrum one obtains a scalar value that quantifies the interaction strength between the external light source and the nanoantenna. In Fig. 9.7a we plot the integrated measured TH signal versus the linear spectral overlap for all 297 antenna arrays. Remarkably, we find a distinct correlation between the two quantities. It is important to note that in this plot we can not distinguish the different antenna arrays. Independent of gap size or basic size all antenna arrays obey the same correlation between the spectral overlap and the TH signal strength. *This is a clear indication that not the actual gap size itself is the key parameter determining the TH signal strength, but rather the linear optical properties, which are the spectral detuning of the plasmonic resonance from the laser source, the amplitude of the resonance, as well as its linewidth being a measure of the quality factor of the resonance.* All these parameters determine the amount of the linear spectral overlap.

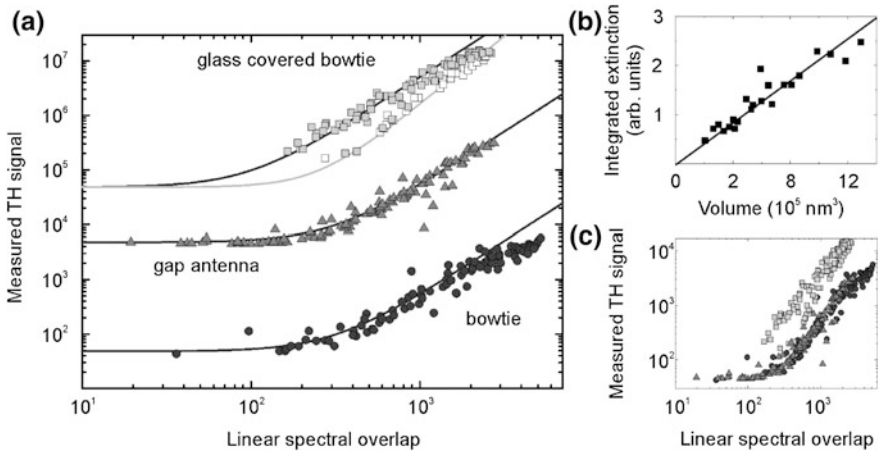

Fig. 9.7 **a** Integrated measured third harmonic signal versus the integrated linear spectral overlap spectrum for the bowtie antenna, gap antenna, and glass covered bowtie antenna arrays. The data points are shifted *upwards* for clarity. **b** Integrated linear extinction versus the nominal volume for a selection of antenna arrays. **c** Comparison of the conversion efficiencies for the different antenna geometries. The data of **a** is plotted without the *vertical* shift for direct comparability

To further underline this strong correlation we have fitted the data points using a function of the form $I_o + A*x^n$. For off-resonant antenna arrays, i.e., antenna arrays with a vanishing spectral overlap, the TH signal approaches a constant value. This behavior is particular visible for the gap antenna arrays. Quite a number of gap antenna arrays are in fact significantly blue-shifted as compared to the laser spectrum. Interestingly, the TH signal strength for the off-resonant case is very similar for the bowtie antennas, gap antennas, and glass covered bowtie antennas. This finding already points to the origin of the signal: The constant background I_o basically describes the TH signal originating from the bare substrate in the absence of any resonant plasmonic object.

The data points for the bowtie and gap antennas follow a quadratic (n = 2) dependence in the linear spectral overlap and no subgroups seem to form here. In contrast, the glass covered bowtie antenna arrays form two distinct subgroups: One follows the same quadratic behavior, the other one is nearly perfectly parameterised by n = 2.5. As the glass covered bowties have the same geometrical dimensions as the uncovered bowties, yet reside in a higher effective refractive index environment due to the SiO_2 overcoating, the resonances are significantly red-shifted. Hence, one possibly explanation for the observed deviations is linked to the spectral position of the plasmonic resonance, meaning whether it is blue- or red-detuned from the laser center wavelength. Therefore, in Fig. 9.7a the red-detuned covered bowtie antenna arrays are depicted with open symbols, the blue-detuned with closed ones. It can be seen that most of the data points of the second subgroup are actually red-detuned structures. Such strongly red-detuned arrays are not present in the bowtie and gap antennas arrays sets. This is why we only observe the first subgroup. We can thus

deduce that the positive or negative detuning between the resonance and the laser source seems to be of crucial influence. Yet, the reason for this behavior remains unclear at this point.

Overall, the question arises why the TH signal strength appears to be quadratic in the spectral overlap and whether or not there is causation. To further elucidate this point, we plot for a selection of arrays in Fig. 9.7b the integrated linear extinction against the nominal volumes of the nanostructures. The integrated extinction depends linearly on the volume of the nanostructure. This behavior is actually not surprising as the overall oscillator strength depends on the number of free electrons and thus on the gold volume. As the extinction enters linearly in the spectral overlap we can thus deduce that the TH signal actually scales quadratically with the volume of the nanostructure.

Figure 9.7c depicts the same data points as Fig. 9.7a, yet without the vertical displacement. In this plot it is apparent that the different antenna geometries do not exhibit the same conversion efficiencies. The bowtie and gap antennas show very similar TH signal strength for the same spectral overlap. In contrast, the glass covered bowtie antennas radiate a significantly stronger TH signal for similar spectral overlap. In order to unravel the reason for the different conversion efficiencies we examine the linear optical response of bowtie and glass covered bowtie antenna arrays in Fig. 9.8 as most of our findings so far could be explained by considering the linear optical properties of the structure.

Figure 9.8a compares the linear extinction spectra for bowtie antenna arrays with and without a SiO_2 overcoating. The geometrical dimensions are identical (triangle size (125 × 150) nm^2, single triangle and 70 nm gap, respectively). The solid lines depict the spectra of the uncovered structures, the dotted ones the covered ones. Two distinct changes are apparent: Due to the higher effective refractive index of

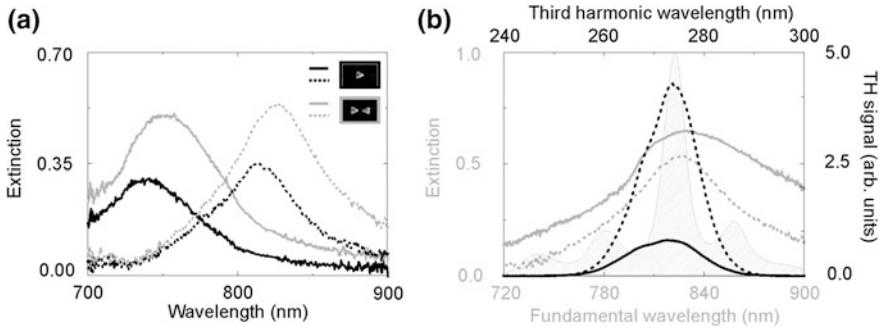

Fig. 9.8 **a** Linear extinction spectra of uncovered (*solid*) and SiO_2 covered (*dotted*) bowtie antenna arrays. The overcoating leads to a resonance red-shift as well as to a narrowing of the linewidth and thus an increase of the quality factor. **b** Linear (*grey*) and nonlinear (*black*) spectra of covered (*dotted*) and uncovered (*solid*) bowtie antenna arrays. In order for the structures to be resonant at about the same wavelength, the covered structures are smaller in size. Despite the larger linear spectral overlap of the uncovered antenna we find that the TH signal from the covered antenna array is significantly stronger. The reason is the higher quality factor of the resonance

the environment the resonances undergo a spectral red-shift. Additionally, the linewidth of the resonances decreases and the amplitude increases. The amplitude increase upon decrease of the width is a direct consequence of the unchanged volume of the nanostructure. The resonance dipole strength, which is linked to the number of free electrons and thus to the volume, manifests itself as the area content of the extinction spectrum. A narrowing of the resonance hence necessarily leads to an increased amplitude. The decreased linewidth implies an increased dephasing time dephasing time of the plasmonic resonance as the spectral width of a resonance is directly linked to the dephasing time of the collective electron oscillation [36]. Plasmonic resonances are radiation damped systems, meaning that the main dephasing channel is caused by radiative losses, i.e., the re-emission of photons. Intrinsic losses such as ohmic losses can be mostly neglected. The increased dephasing time of the resonance is most likely caused by so-called dielectric screening. The homogenous environment of the antenna will respond to the strong electric near-fields of the antenna with an induced electric polarization of opposite sign (yet much smaller than the antenna polarization). This will alter the far-field response as it effectively reduces the dipole moment of the resonance and thus prolongs the dephasing time due to reduced radiation efficiency. Hence, the glass covered bowtie antennas are expected to produce a stronger TH signal. The antennas are basically cavities which store energy and convert part of this energy in TH radiation. An increased dephasing time will increase the interaction time of the near-field with the structures and will thus boost the nonlinear signal strength. Therefore, on first sight, it would be beneficial to increase the quality factor of the resonance as strongly as possible. Yet, it is important to note that an external light field will not be able to efficiently couple energy into a high quality factor cavity. The in- and outcoupling efficiency of a cavity are linked to one another due to reciprocity.

In the above reported experiments it became apparent that the resonant excitation of an antenna is of crucial importance. Thus, we can not directly compare the TH response of the antenna arrays shown in Fig. 9.8a. The uncovered antenna arrays are blue-shifted with respect to the laser spectrum. Therefore a comparison is not meaningful. Figure 9.8b depicts the linear and nonlinear spectra of an uncovered (solid) and a covered (dotted) bowtie antenna array with nearly identical resonance frequencies. In choosing different basic sizes of the triangles we can compensate the resonance red-shift due to the glass overcoating. The linear resonances show a very good overlap with the spectrum of the driving laser source. Very different linewidths of the resonances can be observed, partially caused by dielectric screening. Additionally, as the covered structures are smaller, the overall dipole moment is smaller than for the uncovered, bigger one. Just considering the maximized spectral overlap argument one would expect the uncovered antenna to be the more efficient TH emitter. In contrast one observes a much stronger TH emission from the covered antenna. The reason for this behavior is the significantly higher quality factor of the covered structure. The prolonged interaction time boosts the TH signal, as the local field enhancement is proportional to the dephasing time [36].

9.3 The Nonlinear Harmonic Oscillator Model

The above discussion is a qualitative one. A number of questions remain unanswered. In particular, we have still not convincingly determined the role of the nanoscale gap. The reported findings suggest that the TH signal actually originates from the antenna material itself rather than from the dielectric environment. This is the only explanation why the strongly enhanced near-fields inside the gap do not lead to an additional TH signal from the SiO_2 below or within the gap (in case of the overcoated structures). Indeed, recent reports point to the fact that the nonlinearity of gold exceeds the one of SiO_2 by about three orders of magnitude [81]. Therefore, the actual gap size and the strength of the enhanced field within this gap would be of minor influence. Only very small gaps below or close to the experimentally achievable structure sizes of $\sim$20 nm would lead to noticeable TH from the SiO_2 or from an enhanced confinement of the field to the gold itself.

Another drawback of the linear spectral overlap model and the quality factor argumentation are their inability for any a priori predictions for, e.g., TH signal strengths.

In order to truly unravel different contributions one needs to be able to model one of these contributions and check for experiment-model deviations which would prove the existence of an additional signal contribution. In the following we will perform such a comparison on the basis of a simple harmonic oscillator model.

The left column of Fig. 9.9 depicts in black the linear extinction spectra of bowtie antennas for four different gap sizes but unchanged triangle size in relation to the spectrum of the exciting laser source. Depending on the exact gap size the plasmonic resonances show distinctly different spectral overlap with the driving laser, indicating that the resonances are excited with very unequal efficiency. The right column of Fig. 9.9 depicts the nonlinear optical response of the same structures. The measured TH emission spectra (show in black) point up to two distinct features: First, the overall TH signal strength increases with decreasing gap size. Second, the center wavelength of the TH spectrum is shifting to longer wavelength. As both the overlap of the laser spectrum with the linear plasmon response and the gap size vary simultaneously, it is not a priori clear which parameter causes the increased THG efficiency.

We now demonstrate that all observed features of the nonlinear response are a direct consequence of the *linear* response of the antenna. We model the plasmon resonance of the antenna as a harmonic oscillator, with resonance frequency ω_0, mass m, intrinsic damping constant γ_0, and charge e. To allow for a nonlinear response, we add a cubic perturbation term b to the differential equation [73] of the extension x

$$\ddot{x} + \gamma_0 \dot{x} + \omega_0^2 x - bx^3 = -\frac{e}{m} E_0 e^{-i\omega t}.$$

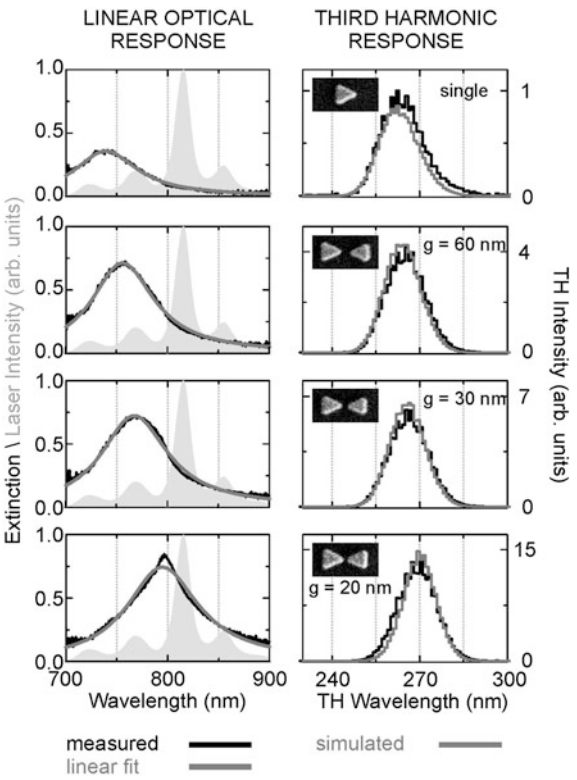

Fig. 9.9 Linear (*left column*) and nonlinear (*right column*) optical response of bowtie antenna patches of four different gap sizes but unchanged *triangle* size. The plasmonic resonance of the bowtie antenna arrays is gradually red-shifting into the regions of higher laser intensity (*grey*) with decreasing gap size. Simultaneously one observes an increase in TH signal strength and a spectral shift of its center wavelength. A damped nonlinear oscillator model catches all experimentally found features directly from the linear optical properties of the bowtie antennas, which enter the model via a fit to the extinction spectra (*green*). Adapted with permission from [50]. Copyright 2012 American Chemical Society

The oscillator is driven by an optical field (frequency ω, amplitude E_0). A medium consisting of such oscillators at a number density N can be described by a linear polarizability $\chi^{(1)}(\omega)$

$$\chi^{(1)}(\omega) = \frac{Ne^2}{\varepsilon_0 m} \cdot \frac{1}{\omega_0^2 - \omega^2 - i\omega\gamma_0} = \frac{Ne^2}{\varepsilon_0 m} \cdot \frac{1}{D(\omega)}.$$

The linear extinction spectrum $\alpha(\omega)$ is given as

$$\alpha(\omega) = \frac{\omega}{c} \cdot \mathrm{Im}\left(\chi^{(1)}(\omega)\right).$$

First, we note that despite the complex shape of the plasmonic nanoantenna, its linear extinction spectrum is well fitted using these relations (see green curves in the left column of Fig. 9.9). This finding indicates that the bowtie antenna behaves like a single harmonic oscillator despite the fact that the excited mode is a hybridized mode of two nanoparticles. The spectral position of this mode is tuned by the gap size. From the fit we extract the resonance frequency ω_0, the damping constant γ_0, and an overall amplitude describing the strength of the resonance.

In this model, the third order polarizability is given as [73]

$$\chi^{(3)}\left(\omega_i, \omega_j, \omega_k, \omega_{THG} = \omega_i + \omega_j + \omega_k\right) = \frac{Ne^4}{\varepsilon_0 m^3} \frac{b}{D(\omega_i) \cdot D\left(\omega_j\right) \cdot D(\omega_k) \cdot D(\omega_{THG})}.$$

Taking the broad coherent laser spectrum $E(\omega) = E_0(\omega) \cdot e^{i\omega t}$ into account, we calculate the TH emission spectrum as

$$I_{THG}\left(\omega_{THG} = \omega_i + \omega_j + \omega_k\right) \propto \omega_{THG}^2 \left| \int_{\omega_i} \int_{\omega_j} \int_{\omega_k} \chi^{(3)}\left(\omega_i, \omega_j, \omega_k, \omega_{THG}\right) \cdot E_0(\omega_i) E_0\left(\omega_j\right) E_0(\omega_k) d\omega_i d\omega_j d\omega_k \right|^2$$

The contribution of the substrate is modelled as spectrally constant $\chi^{(3)}_{sub}$ and added coherently. The nonlinearity parameter b is adjusted such that one value describes all spectra simultaneously. We compare measured and simulated TH spectra for a series of equal bowtie triangle size but different gap sizes in Fig. 9.9. Overall we find excellent agreement between the measurement and the simulation showing that the model is able *to predict* the entire TH spectrum in position, shape, and relative amplitude *solely from the linear optical properties* (Fig. 9.10).

Our nonlinear oscillator model summarizes all the details of the local field distribution in and around the nanoantenna and the corresponding values of the third order polarizability $\chi^{(3)}$ into the nonlinearity parameter b. In a microscopic picture, the plasmon resonance enhances the local field which leads to locally enhanced third-harmonic generation. In such a microscopic picture, one would then integrate coherently over all sources of THG, as done in previous work [61]. The excellent agreement of data and simulations in the right column of Fig. 9.9 demonstrates that already the much simpler macroscopic nonlinear oscillator model contains the essence. At the same time, we expect the model to fail when the local field distribution changes drastically.

In order to test the limits of the nonlinear oscillator model, we varied triangle size and gap size of the bowtie antennas, resulting in 99 different combinations. To modify the field distribution even further, we changed the index of refraction of the environment by covering an identical sample with 100 nm SiO_2. Thirdly, we changed the shape of the antennas from a bowtie antenna (consisting of triangles) to

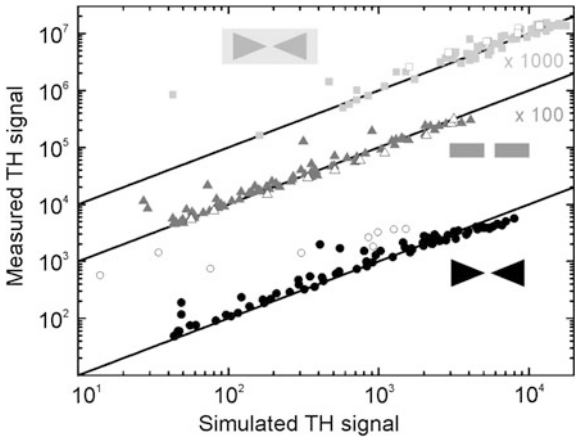

Fig. 9.10 Measured spectrally integrated TH signal versus simulated integrated TH signal based on a single nonlinear oscillator model. The data for the gap antennas (*red*) and the glass covered bowties (*blue*) are shifted vertically for clarity with respect to the bowties (*black*). The *green lines* represent a one-to-one ratio. The experimental data and the model show a very good overall agreement. The antennas behave like single nonlinear oscillators, independently of the antenna gap. *Open symbols* represent antennas with the smallest gap sizes ($\sim$20 nm). All those data points are not included for which the linear spectrum could not be fitted reliably, as the peak position is outside the spectral window of the laser source. Adapted with permission from [50]. Copyright 2012 American Chemical Society

a gap antenna (consisting of rectangles), again varying size of the rectangle and the gap between the rectangles. In total we thus examined 297 antenna fields.

To allow for a direct comparison of experiment and simulation for all fields, Fig. 9.8 compares the integrated TH intensity for bowtie antennas (in black), gap antennas (in red), and glass-covered bowtie antennas (in blue). The data points for the gap antennas and the covered bowtie antennas are displaced vertically for clarity; the green lines each depict a one-to-one relation. Each of the three sets of antennas is described by one constant nonlinearity parameter b, which relate as $b^2_{bowtie} : b^2_{gap_antenna} : b^2_{covered_bowtie} = 1 : 2 : 3$. This reflects the variation in local field distribution between the three sets. Overall we find excellent *quantitative* agreement between the measurement and our model for all three different antenna varieties. Despite the fact that the antennas consist of two independent, yet strongly near-field coupled nanoparticles, they behave as a single oscillator whose nonlinear third harmonic response is excellently modelled by a constant cubic perturbation. We observe a maximum enhancement of the TH signal compared to the TH signal of the bare substrate of about 62 for the gap antennas, 115 for the bowtie antennas, and 311 for the covered bowtie antennas. In each case the antenna geometry that exhibits the maximum enhancement is the one that shows the best and hence highest excitation efficiency of the antenna. For the bowtie antennas this geometry is actually the biggest triangle size with the biggest gap.

If the TH from the hot spot dominated the TH from the antenna itself, then the nonlinear conversion efficiency of a dimer nanoantenna should drastically increase when the gap size decreases as the near-field localization is particularly strong for small gap sizes [48, 79, 88, 89]. In order to check this intuitive picture, the antennas with the smallest gap sizes are depicted with open symbols in Fig. 9.8. For the gap antennas and the glass-covered bowtie antennas they are equally distributed among the data points, indicating that they do not form a sub-group of higher conversion efficiency. In contrast, for the bowtie antennas the data points are consistently above the one-to-one relation line. This finding is an indication that these antennas seem to deviate from the single nonlinear oscillator assumption, showing slightly higher conversion efficiency. SEM inspection of the structures seems to indicate that the gaps of these antennas are slightly smaller than the smallest ones of the covered bowties and the gap antennas. Here, the very small gap modified the local field distribution, leading to a deviation from the nonlinear oscillator model. Apparently only gap sizes below about 20 nm lead to hot spot THG that can dominate antenna THG. Overall we thus find that the nonlinear signal strength of a plasmonic nanoantenna depends on the oscillator strength of the plasmon and its efficient resonant excitation. The only free and designable properties for TH enhancement are the linear properties of the oscillator, which are quality factor (linewidth), resonance frequency, and amplitude. The magnitude of the nonlinearity parameter b can not be manipulated much by simple geometrical variations of the nanoantenna. Our experimentally achieved gaps are not small enough in order to cause an additional nonlinear contribution. Hence, for gaps ≥20 nm the gap merely acts as tuning element.

The integrated TH intensity contains only part of the information in our measured and simulated spectra. To go more into detail, we now turn our attention to the spectral center of mass of the nonlinear spectra. In a naïve picture this position should be solely determined by the laser spectrum, hence it should be identical for all antenna variations. Strikingly, we have seen already in Fig. 9.9 that the TH spectra undergo spectral shifts when changing the plasmon resonance wavelength. This indicates that the linear plasmon spectrum plays a crucial role for the center of mass of the TH spectrum. We find that the nonlinear oscillator model catches the essence of the physics behind this spectral shift. This is demonstrated in Fig. 9.11, which compares the spectral center of mass of the simulated TH spectra to the measured data. The plasmon spectrum causes a shift of the TH center wavelength, as it determines together with the spectrum of the laser source the spectral position of highest interaction and hence the strongest TH signal. Yet, we still find small deviations from the expected 1:1 wavelength relation (shown as grey line in Fig. 9.11). A spectral phase of the laser source, i.e., a temporal chirp between the different wavelength components of the broadband laser pulse, is the likely explanation for these deviations.

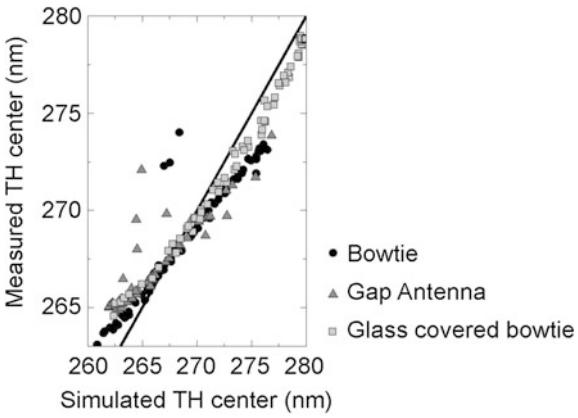

Fig. 9.11 Measured center TH wavelength versus the simulated TH center wavelength. The very good agreement demonstrates that the TH spectrum is not only defined by the laser spectrum but also by the plasmon. Without plasmon resonance, the TH center would be expected at one third of the laser spectral center, indicated by the *grey arrow*. Hence, within a certain wavelength regime, it is possible to shift the center of the TH spectrum by manipulating the plasmon alone. In this figure only patches are included that produce at least three times the background THG, as the latter is independent of the plasmon resonance wavelength. Adapted with permission from [50]. Copyright 2012 American Chemical Society

9.4 Resonantly Enhanced Optical Nonlinearities

We have seen that the nonlinear optical properties of plasmonic structures are governed by their resonant behavior. Hence, it is straightforward and intriguing to view this process in the framework of resonant nonlinearities.

Nonlinear optical processes have become of the utmost importance in basic research as well as in industrial and commercial applications [90]. Mostly, they rely on bulk materials exhibiting off-resonant nonlinearities which are weak and only deliver large signals when employing phase matching techniques [91–93]. Commonly used nonlinear optical materials, such as beta barium borate (BBO) or lithium niobate ($LiNbO_3$), have no resonant optical transitions in their respective operational regime, hence being nearly perfectly transparent. In contrast, optical materials with a resonant transition can enhance nonlinear optical processes when the incident light is tuned to this resonance. Often, these transitions are narrow, weak, and fixed in wavelength as they depend on material parameters, e.g., for second harmonic generation in solids [94, 95] as well as sum-frequency generation [96] and second harmonic generation in molecules [97, 98].

The nonlinear optical polarization for third harmonic generation can be written as

$$P_i(3\omega) \propto \chi^{(3)}_{ijkl} E_j(\omega) E_k(\omega) E_l(\omega)$$

where $E_j(\omega)$ (with $i,j,k,l = x,y,z$) are the electric field components of the incident light field and $\chi^{(3)}_{ijkl}$ is the susceptibility tensor.

The absolute value of the susceptibility tensor components are determined by the linear optical properties of the system. In order for a third harmonic photon to be emitted three photons of the fundamental light field have to be absorbed simultaneously. This process is sketched in Fig. 9.12a. The value of the tensor component is directly proportional to the sum over all transition matrix elements for the three photon absorption process [73]. If there are no absorptive optical transitions in the material all sketched intermediate states are virtual or strongly off-resonant states. As a consequence the tensor component will take a small value, thus the process will be very inefficient. There is, however, one benefit afforded: As there are no resonant transitions involved the tensor component will be nearly independent of the energy of the incoming photons. The process is thus nearly equally inefficient for all energies. Therefore one has an inefficient yet spectrally flat process which is highly desirable for many applications. The conversion process can be made highly efficient by employing, e.g., phase matching techniques in bulk materials. This type of process is therefore termed off-resonant nonlinearity.

Figure 9.12b sketches two possibilities for a resonant nonlinear optical process: If one of the intermediate or the final state is an absorptive material transition the corresponding term in the sum of the transition matrix elements will become resonant. As a consequence the susceptibility tensor component will take a large value. Intuitively, this process is straightforward to understand: If an absorptive transition

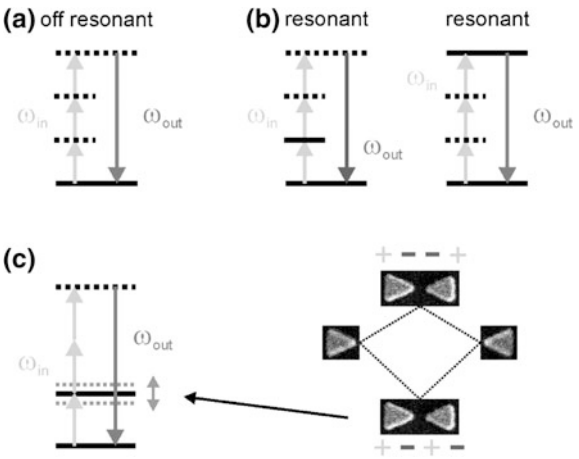

Fig. 9.12 **a** Energy level diagram for off-resonant third harmonic generation. **b** The resonant excitation of a resonant energy level, either an intermediate (*left*) or the final (*right*) state, leads to an increased excitation probability and hence to a resonantly enhanced third harmonic signal. **c** Plasmon hybridization scheme for a bowtie nanoantenna. Two collective modes are formed, namely a symmetric dipole-allowed one with a lower resonance energy and an antisymmetric dark mode with higher resonance energy. The dipole-allowed mode serves as the resonant energy level which can be tuned in resonance energy by the size of the triangles and the gap size

is present a photon can be efficiently absorbed and the energy will be stored, thus increasing the probability of another photon to be absorbed by the material during the lifetime of the excited state and thus increasing the overall conversion efficiency. The drawback, however, is obvious: the process is only efficient for a very limited energy range as it intrinsically relies on a resonance.

In this context, we can view nonlinear plasmonics as an elegant and universal method to strongly enhance an otherwise nonresonant and flat spectral response of the bare gold material. Figure 9.12c depicts a sketch of the working principle. In close proximity to one another the plasmonic resonances in the individual particles of the gap nanoantenna mix and hybridize giving rise to two new collective modes, as shown in the plasmon hybridization scheme [2] depicted in Fig. 9.12c. For light polarized along the long axis of the antenna, the symmetric dipole allowed mode is decreased in resonance energy, whereas the antisymmetric mode is increased in energy. The latter mode cannot be excited for normal light incidence due to its antisymmetric mode pattern. Hence, the gap size as well as the size of the triangles will determine the spectral position of the dipole allowed mode, giving convenient parameters for shifting and tuning the resonant energy level depicted in the energy level diagram.

The proposed scheme of plasmon resonance enhanced nonlinearity offers a multitude of scaling opportunities and extensions. Designing a plasmonic system with simultaneous resonances at the fundamental as well as the harmonic wavelength will allow for resonant enhancement of both levels, rendering even higher conversion efficiencies possible. Additionally, it should be feasible to favour a certain nonlinear process, e.g., difference frequency generation or four wave mixing, over the dominant second and third order processes, respectively, by designing the resonant enhancement of the plasmonic system accordingly.

9.5 Summary and Conclusion

In conclusion, we have demonstrated that nonlinearities in plasmonic nanoantennas are governed by the linear response of the nanoantenna for a large range of geometries. The plasmon resonance energies and the oscillator strength are the key properties that determine the TH signal strength. Not only the spectral detuning between the center wavelength of the laser source and the plasmonic resonance needs to be minimized in order to drive the resonance most efficiently, but also the overall coupling strength of the plasmonic resonance to the external light field needs to be maximized. This coupling strength is characterized by the oscillator strength of the resonance which is fundamentally stemming from the number of electrons involved and hence the volume of the nanostructure. The crucial importance of the plasmonic resonance and the associated enhanced near-fields is underlined by shape and position variations of the TH spectrum. The TH center wavelength can to a large extent be predicted from the laser spectrum and the plasmon resonance.

An additional contribution by the strongly enhanced near-fields concentrated in the gap region is only found for gap sizes below 20 nm. For larger gap sizes the microscopic field distribution does not change any more. The gap size primarily manifests itself in the linear optical properties that influence the efficiency of the laser to drive the plasmon.

References

1. H. Haken, H.C. Wolf, *Molecular Physics and Elements of Quantum Chemistry* (Springer, Berlin, 2003)
2. E. Prodan, C. Radloff, N.J. Halas, P. Nordlander, A hybridization model for the plasmon response of complex nanostructures. Science **302**, 419–422 (2003)
3. S.A. Maier et al., Local detection of electromagnetic energy transport below the diffraction limit in metal nanoparticle plasmon waveguides. Nat. Mater. **2**, 229–232 (2003)
4. N. Liu et al., Plasmonic analogue of electromagnetically induced transparency at the Drude damping limit. Nat. Mater. **8**, 758–762 (2009)
5. S. Zhang, D.A. Genov, Y. Wang, M. Liu, X. Zhang, Plasmon-induced transparency in metamaterials. Phys. Rev. Lett. **101**, 047401 (2008)
6. N. Verellen et al., Fano resonances in individual coherent plasmonic nanocavities. Nano Letters **9**, 1663–1667 (2009)
7. B. Luk'yanchuk et al., The Fano resonance in plasmonic nanostructures and metamaterials. Nat. Mater. **9**, 707–715 (2010)
8. N.J. Halas, S. Lal, W.-S. Chang, S. Link, P. Nordlander, Plasmons in strongly coupled metallic nanostructures. Chem. Rev. **111**, 3913–3961 (2011)
9. N.A. Mirin, K. Bao, P. Nordlander, Fano resonances in plasmonic nanoparticle aggregates. J. Phys. Chem. A **113**, 4028–4034 (2009)
10. J.A. Fan et al., Self-assembled plasmonic nanoparticle clusters. Science **328**, 1135–1138 (2010)
11. J.L. West, N.J. Halas, Engineered nanomaterials for biophotonics applications: improving sensing, imaging, and therapeutics. Annu. Rev. Biomed. Eng. **5**, 285–292 (2003)
12. K.-S. Lee, M.A. El-Sayed, Gold and silver nanoparticles in sensing and imaging: sensitivity of plasmon response to size, shape, and metal composition. J. Phys. Chem. B **110**, 19220–19225 (2006)
13. K.A. Willets, R.P. Van Duyne, Localized surface plasmon resonance spectroscopy and sensing. Annu. Rev. Phys. Chem. **58**, 267–297 (2007)
14. P. Englebienne, Use of colloidal gold surface plasmon resonance peak shift to infer affinity constants from the interactions between protein antigens and antibodies specific for single or multiple epitopes. Analyst **123**, 1599–1603 (1998)
15. G. Raschke et al., Biomolecular recognition based on single gold nanoparticle light scattering. Nano Letters **3**, 935–938 (2003)
16. A.D. McFarland, R.P. Van Duyne, Single silver nanoparticles as real-time optical sensors with zeptomole sensitivity. Nano Letters **3**, 1057–1062 (2003)
17. A. Wokaun et al., Surface second-harmonic generation from metal island films and microlithographic structures. Phys. Rev. B **24**, 849–856 (1981)
18. D. Ricard, P. Roussignol, C. Flytzanis, Surface-mediated enhancement of optical phase conjugation in metal colloids. Opt. Lett. **10**, 511–513 (1985)
19. F. Hache, D. Ricard, C. Flytzanis, Optical nonlinearities of small metal particles: surface-mediated resonance and quantum size effects. J. Opt. Soc. Am. B **3**, 1647 (1986)
20. C.K. Chen, T.F. Heinz, D. Ricard, Y.R. Shen, Surface-enhanced second-harmonic generation and Raman scattering. Phys. Rev. B **27**, 1965–1979 (1983)

21. G.T. Boyd, T. Rasing, J.R.R. Leite, Y.R. Shen, Local-field enhancement on rough surfaces of metals, semimetals, and semiconductors with the use of optical second-harmonic generation. Phys. Rev. B **30**, 519–526 (1984)
22. M. Moskovits, Surface roughness and the enhanced intensity of Raman scattering by molecules adsorbed on metals. J. Chem. Phys. **69**, 4159–4161 (1978)
23. S.L. McCall, P.M. Platzman, P.A. Wolff, Surface enhanced Raman scattering. Phys. Lett. A **77**, 381–383 (1980)
24. J. Gersten, A. Nitzan, Electromagnetic theory of enhanced Raman scattering by molecules adsorbed on rough surfaces. J. Chem. Phys. **73**, 3023 (1980)
25. M. Kerker, D.S. Wang, H. Chew, Surface enhanced Raman scattering (SERS) by molecules adsorbed at spherical particles: errata. Appl. Opt. **19**, 4159–4174 (1980)
26. M. Fleischmann, Raman spectra of pyridine absorbed at silver electrode. Chem. Phys. Lett. **26**, 163–166 (1974)
27. J.E. Sipe, R.W. Boyd, Nonlinear susceptibility of composite optical materials in the Maxwell Garnett model. Phys. Rev. A **46**, 1614–1629 (1992)
28. V.M. Shalaev, E.Y. Poliakov, V.A. Markel, Small-particle composites. II. Nonlinear optical properties. Phys. Rev. B: Condens. Matter **53**, 2437–2449 (1996)
29. V.M. Shalaev, Electromagnetic properties of small-particle composites. Phys. Rep. **272**, 61–137 (1996)
30. A.V. Butenko et al., Nonlinear optics of metal fractal clusters. Z. Phys. D: At. Mol. Clusters **17**, 283–289 (1990)
31. S.V. Fomichev, S.V. Popruzhenko, D.F. Zaretsky, W. Becker, Laser-induced nonlinear excitation of collective electron motion in a cluster. J. Phys. B: At. Mol. Opt. Phys. **4075**, 3817–3834 (2003)
32. S. Fomichev, S. Popruzhenko, D. Zaretsky, W. Becker, Nonlinear excitation of the Mie resonance in a laser-irradiated cluster. Opt. Express **11**, 2433–2439 (2003)
33. M. Lippitz, M.A. van Dijk, M. Orrit, Third-harmonic generation from single gold nanoparticles. Nano Letters **5**, 799–802 (2005)
34. M.W. Klein, C. Enkrich, M. Wegener, S. Linden, Second-harmonic generation from magnetic metamaterials. Science **313**, 502–504 (2006)
35. B.K. Canfield et al., Local field asymmetry drives second-harmonic generation in non-centrosymmetric nanodimers. Nano Letters **7**, 1251–1255 (2007)
36. T. Zentgraf, A. Christ, J. Kuhl, H. Giessen, Tailoring the ultrafast dephasing of quasiparticles in metallic photonic crystals. Phys. Rev. Lett. **93**, 243901 (2004)
37. B. Lamprecht, A. Leitner, F.R. Aussenegg, SHG studies of plasmon dephasing in nanoparticles. Appl. Phys. B **423**, 419–423 (1999)
38. B.K. Canfield, S. Kujala, K. Jefimovs, M. Kauranen, Linear and nonlinear optical responses influenced by broken symmetry in an array of gold nanoparticles. Opt. Express **12**, 419–423 (2004)
39. B.K. Canfield et al., A macroscopic formalism to describe the second-order nonlinear optical response of nanostructures. J. Opt. A: Pure Appl. Opt. **8**, S278–S284 (2006)
40. M.J. Huttunen et al., Nonlinear chiral imaging of subwavelength-sized twisted-cross gold nanodimers. Opt. Mater. Express **1**, 2501–2503 (2011)
41. V.K. Valev et al., Asymmetric optical second-harmonic generation from chiral G-shaped gold nanostructures. Phys. Rev. Lett. **104**, 2–5 (2010)
42. V.K. Valev et al., The origin of second harmonic generation hotspots in chiral optical metamaterials. Opt. Mater. Express **1**, 6233–6241 (2011)
43. Y. Zhang, N.K. Grady, C. Ayala-Orozco, N.J. Halas, Three-dimensional nanostructures as highly efficient generators of second harmonic light. Nano Letters **11**, 5519–5523 (2011)
44. T. Xu, X. Jiao, G.P. Zhang, S. Blair, Second-harmonic emission from sub-wavelength apertures: effects of aperture symmetry and lattice arrangement. Opt. Express **15**, 13894–13906 (2007)
45. A. Lesuffleur, L.K.S. Kumar, R. Gordon, Enhanced second harmonic generation from nanoscale double-hole arrays in a gold film. Appl. Phys. Lett. **88**, 261104 (2006)

46. A.M. Moran, J. Sung, E.M. Hicks, R.P. Van Duyne, K.G. Spears, Second harmonic excitation spectroscopy of silver nanoparticle arrays. J. Phys. Chem. B **109**, 4501–4506 (2005)
47. T. Hanke et al., Efficient nonlinear light emission of single gold optical antennas driven by few-cycle near-infrared pulses. Phys. Rev. Lett. **103**, 257404 (2009)
48. T. Hanke et al., Tailoring spatiotemporal light confinement in single plasmonic nanoantennas. Nano Letters **12**, 992–996 (2012)
49. K.D. Ko et al., Nonlinear optical response from arrays of Au bowtie nanoantennas. Nano Letters **11**, 61–65 (2011)
50. M. Hentschel, T. Utikal, H. Giessen, M. Lippitz, Quantitative modeling of the third harmonic emission spectrum of plasmonic nanoantennas. Nano Letters **12**, 3778–3782 (2012)
51. B. Lamprecht, J.R. Krenn, A. Leitner, F.R. Aussenegg, Resonant and off-resonant light-driven plasmons in metal nanoparticles studied by femtosecond-resolution third-harmonic generation. Phys. Rev. Lett. **83**, 4421–4424 (1999)
52. M. Danckwerts, L. Novotny, Optical frequency mixing at coupled gold nanoparticles. Phys. Rev. Lett. **98**, 026104 (2007)
53. S. Palomba, M. Danckwerts, L. Novotny, Nonlinear plasmonics with gold nanoparticle antennas. J. Opt. A: Pure Appl. Opt. **11**, 114030 (2009)
54. M.W. Klein, M. Wegener, N. Feth, S. Linden, Experiments on second- and third-harmonic generation from magnetic metamaterials. Opt. Express **15**, 5238–5247 (2007)
55. S. Linden et al., Collective effects in second-harmonic generation from split-ring-resonator arrays. Phys. Rev. Lett. **109**, 1–5 (2012)
56. N. Feth et al., Second-harmonic generation from complementary split-ring resonators. Opt. Lett. **33**, 1975–1977 (2008)
57. A. Podlipensky, J. Lange, G. Seifert, H. Graener, I. Cravetchi, Second-harmonic generation from ellipsoidal silver nanoparticles embedded in silica glass. Opt. Lett. **28**, 716–718 (2003)
58. F.B.P. Niesler et al., Second-harmonic generation from split-ring resonators on a GaAs substrate. Opt. Lett. **34**, 1997–1999 (2009)
59. M. Gentile et al., Investigation of the nonlinear optical properties of metamaterials by second harmonic generation. Appl. Phys. B **105**, 149–162 (2011)
60. M. Klein, T. Tritschler, M. Wegener, S. Linden, Lineshape of harmonic generation by metallic nanoparticles and metallic photonic crystal slabs. Phys. Rev. B **72**, 115113 (2005)
61. T. Utikal et al., Towards the origin of the nonlinear response in hybrid plasmonic systems. Phys. Rev. Lett. **106**, 133901 (2011)
62. T. Utikal, M. Hentschel, H. Giessen, Nonlinear photonics with metallic nanostructures on top of dielectrics and waveguides. Appl. Phys. B **105**, 51–65 (2011)
63. T. Utikal, M.I. Stockman, A.P. Heberle, M. Lippitz, H. Giessen, All-optical control of the ultrafast dynamics of a hybrid plasmonic system. Phys. Rev. Lett. **104**, 113903 (2010)
64. S. Kim et al., High-harmonic generation by resonant plasmon field enhancement. Nature **453**, 757–760 (2008)
65. I. Park et al., Plasmonic generation of ultrashort extreme-ultraviolet light pulses. Nat. Photonics **5**, 677–681 (2011)
66. M. Sivis, M. Duwe, B. Abel, C. Ropers, Nanostructure-enhanced atomic line emission. Nature **485**, E1–E3 (2012)
67. Y. Pu, R. Grange, C.-L. Hsieh, D. Psaltis, Nonlinear optical properties of core-shell nanocavities for enhanced second-harmonic generation. Phys. Rev. Lett. **104**, 207402 (2010)
68. K. Thyagarajan, S. Rivier, A. Lovera, O.J.F. Martin, Enhanced second-harmonic generation from double resonant plasmonic antennae. Opt. Express **20**, 12860 (2012)
69. H. Harutyunyan, G. Volpe, R. Quidant, L. Novotny, Enhancing the nonlinear optical response using multifrequency gold-nanowire antennas. Phys. Rev. Lett. **108**, 1–4 (2012)
70. H. Aouani et al., Multiresonant broadband optical antennas as efficient tunable nanosources of second harmonic light. Nano Letters (2012). doi:10.1021/nl302665m
71. M. Navarro-Cia, S.A. Maier, Broadband near-infrared plasmonic nanoantennas for higher harmonic generation. ACS Nano **6**, 3537–3544 (2012)

72. R.R. Birss, *Symmetry and Magnetism* (North-Holland Publishing Company, Amsterdam, 1966)
73. R.W. Boyd, *Nonlinear Optics* (Elsevier, Amsterdam, 2008)
74. Y.R. Shen, *The Principles of Nonlinear Optics* (Wiley-Interscience, Hoboken, 2002)
75. P. Mühlschlegel, H.-J. Eisler, O.J.F. Martin, B. Hecht, D.W. Pohl, Resonant optical antennas. Science **308**, 1607–1609 (2005)
76. L. Novotny, N. van Hulst, Antennas for light. Nat. Photonics **5**, 83–90 (2011)
77. P.J. Schuck, D.P. Fromm, A. Sundaramurthy, G.S. Kino, W.E. Moerner, Improving the mismatch between light and nanoscale objects with gold bowtie nanoantennas. Phys. Rev. Lett. **94**, 017402 (2005)
78. P. Biagioni, J.-S. Huang, B. Hecht, Nanoantennas for visible and infrared radiation. Rep. Prog. Phys. **75**, 024402 (2012)
79. H. Fischer, O.J.F. Martin, Engineering the optical response of plasmonic nanoantennas. Opt. Express **16**, 9144–9154 (2008)
80. J. Renger, R. Quidant, N. van Hulst, L. Novotny, Surface-enhanced nonlinear four-wave mixing. Phys. Rev. Lett. **104**, 046803 (2010)
81. J. Renger, R. Quidant, L. Novotny, Enhanced nonlinear response from metal surfaces. Opt. Express **19**, 1777–1785 (2011)
82. P.-Y. Chen, A. Alù, Optical nanoantenna arrays loaded with nonlinear materials. Phys. Rev. B **82**, 235405 (2010)
83. D.K. Polyushkin, E. Hendry, E.K. Stone, W.L. Barnes, THz generation from plasmonic nanoparticle arrays. Nano Letters **11**, 4718–4724 (2011)
84. H. Husu et al., Metamaterials with tailored nonlinear optical response. Nano Letters **12**, 673–677 (2012)
85. J.B. Lassiter et al., Close encounters between two nanoshells. Nano Letters **8**, 1212–1218 (2008)
86. J. Zuloaga, E. Prodan, P. Nordlander, Quantum description of the plasmon resonances of a nanoparticle dimer. Nano Letters **9**, 887–891 (2009)
87. O. Pérez-González et al., Optical spectroscopy of conductive junctions in plasmonic cavities. Nano Letters **10**, 3090–3095 (2010)
88. V. Giannini, A.I. Fernández-Domínguez, S.C. Heck, S.A. Maier, Plasmonic nanoantennas: fundamentals and their use in controlling the radiative properties of nanoemitters. Chem. Rev. **111**, 3888–3912 (2011)
89. A. Sundaramurthy et al., Field enhancement and gap-dependent resonance in a system of two opposing tip-to-tip Au nanotriangles. Phys. Rev. B **72**, 165409 (2005)
90. Y.S. Kivshar, Nonlinear optics: the next decade. Opt. Express **16**, 22126–22128 (2008)
91. T. Sasaki, Y. Mori, M. Yoshimura, Y.K. Yap, T. Kamimura, Recent development of nonlinear optical borate crystals: key materials for generation of visible and UV light. Mater. Sci. Eng. R: Rep. **30**, 1–54 (2000)
92. R.S. Weis, T.K. Gaylord, Lithium niobate: summary of physical properties and crystal structure. Appl. Phys. A **37**, 191–203 (1985)
93. M.M. Fejer, G.A. Magel, D.H. Jundt, R.L. Byer, Quasi-phase-matched second harmonic generation: tuning and tolerances. IEEE J. Quantum Electron. **28**, 2631–2654 (1992)
94. M. Fiebig et al., Second harmonic generation in the centrosymmetric antiferromagnet NiO. Phys. Rev. Lett. **87**, 1–4 (2001)
95. M. Fiebig, V.V. Pavlov, R.V. Pisarev, Second-harmonic generation for studying electronic and magnetic structures of crystals: review. J. Opt. Soc. Am. B **22**, 96–118 (2005)
96. M. Belkin, S. Han, X. Wei, Y. Shen, Sum-frequency generation in chiral liquids near electronic resonance. Phys. Rev. Lett. **87**, 1–4 (2001)
97. T.F. Heinz, C.K. Chen, D. Ricard, Y.R. Shen, Spectroscopy of molecular monolayers by resonant second-harmonic generation. Phys. Rev. Lett. **48**, 478–481 (1982)
98. D.A. Higgins, M.B. Abrams, S.K. Byerly, R.M. Corn, Resonant second harmonic generation studies of p-nitrophenol adsorption at condensed-phase interfaces. Langmuir **8**, 1994–2000 (1992)

Part V
Nonlinear Nano-Optics: Photoemission and Nonlinear Spectroscopy

Chapter 10
Strong-Field Photoemission from Metallic Nanotips

Georg Herink, Daniel R. Solli, Max Gulde, Reiner Bormann and Claus Ropers

Abstract Nonlinear photoemission from single nanostructures is investigated over a broad wavelength range in the near- and mid-infrared. The field enhancement at a nanotip apex and mid-infrared excitation enable sub-cycle dynamics, where electrons are ejected from the near-field within a fraction of the optical half-cycle. The implications of this field-driven acceleration are studied via photoemission spectrocopy and numerical simulations.

10.1 Introduction

The linear and nonlinear optical properties of nanostructures of nanostructures provide fascinating means to tailor optical light fields—including field enhancements, sub-wavelength confinement and the control of light propagation.

The intensity-enhancement finds widespread applications in spectroscopy [1] and nonlinear light conversion [1], and it allows for access to highly nonlinear optics with relatively low pulse energies directly from non-amplified ultrafast oscillators [2, 3].

In the strong-field regime—an extreme limit of light-matter interaction—photoionization and electron acceleration is directly governed by the optical electric field rather than the intensity. Experiments with atoms and molecules illustrate unprecedented control over light-electron interactions, aspects recently termed *light-wave electronics* [4], including the generation of attosecond pulses and coherent extreme ultraviolet radiation [5].

At metallic nanotips which offer substantial local field enhancement, the strong-field regime is reached at relatively low incident intensities. It has been shown that nanostructures not only ease the way to the strong-field regime, but that their optical

G. Herink (✉) · D.R. Solli · M. Gulde · R. Bormann · C. Ropers
IV. Institute of Physics, University of Göttingen, 37077 Göttingen, Germany
e-mail: gherink@gwdg.de

© Springer International Publishing Switzerland 2015

S. Sakabe et al. (eds.), *Progress in Nonlinear Nano-Optics*,
Nano-Optics and Nanophotonics, DOI 10.1007/978-3-319-12217-5_10

properties, namely the field-enhancement and the field-localization, lead to light-electron interactions that are unique to nanostructures [6, 7]. This contribution presents recent results from the authors in this field.

10.2 Strong-Field Physics at Metallic Nanotips

The field-enhancement at the apex of a metallic nanotip allows for strongly localized and ultrafast photoemission. The emission process can be studied in a highly controlled geometry at a single nanostructure and has been the subject of a variety of ultrafast spectroscopic investigations focusing on different aspects and physical conditions [7–15].

To overcome the metal work function of several electron volts with an 800 nm excitation wavelength, multiphoton-photoemission (MPP) has been identified as the quasi-instantaneous emission process for moderately biased tips [9]. Due to the nonlinearity of this emission process, the emission site is confined to the apex of the nanotip, resulting in an ultrafast electron point-source with unmatched brightness.

For increasing laser intensities, a transition from multiphoton to strong-field photoemission was shown by measuring the photocurrent as a function of laser pulse energy, see Fig. 10.1c [11]. The reduction of the slope is attributed to the increasing ponderomotive (quiver) energy of photoelectrons, which must be supplied by the laser field. As successive channels of increasing photon number begin to close rapidly with larger fields, the slope of the intensity dependence decreases in the transition region. Simultaneously, the angular electron emission cone narrows as

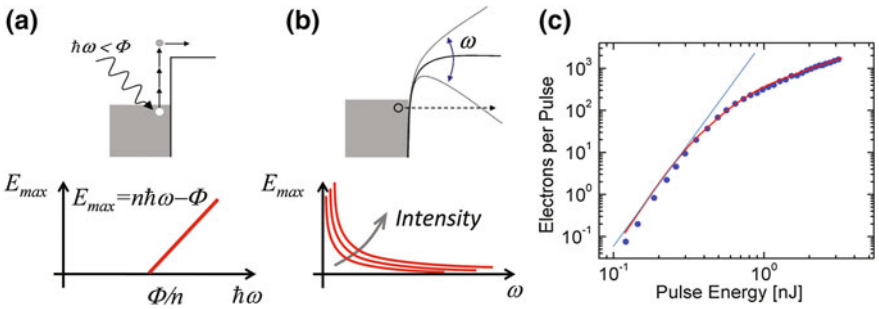

Fig. 10.1 **a** In the multiphoton-photoemission limit, multiple photons with photon energy $\hbar\omega < \phi$ contribute to overcoming the work function Φ. The frequency dependence of the maximum kinetic energy is given by Einstein's photoelectric law modified by the photon number n. **b** In the strong-field regime, the atomic potential is distorted by the strong electric field resulting in tunnel emission through the barrier. Here, the kinetic energy depends on the laser intensity and increases for low frequencies. **c** The transition from multiphoton to strong-field photoemission at gold nanotips is experimentally observed in the behavior of electron yield versus excitation pulse energy: at the transition the slope is reduced from that of the multiphoton process due to channel-closing, which marks the beginning of strong-field interaction. Adapted from [11]

a result of the increasing forward momentum of the liberated electrons due to the light field. A theoretical treatment of the underlying emission mechanisms employing analytical and numerical approaches is given in [16]. Channel-closing in the intermediate intensity regime was also observed in the form of above-threshold photoemission features in the electron kinetic energy distributions [13].

Channel-closing marks the onset of strong-field photoemission, where the ponderomotive energy—and not the work function—dominates the particle dynamics. Here, the classical electric field rather than the photon number is a more appropriate concept to describe the emission process. As a result, carrier-envelope-phase effects on the emission can be observed [14]. At high intensities, the emission process merges into field-induced tunneling or optical field emission (OFE) in the strong field regime. The transition from multi-photon photoemission to optical field emission is well-known in the area of atomic ionization and is characterized by the Keldysh-parameter γ [17], which forms a ratio between the ionization potential and the ponderomotive energy $U_P = e^2F^2/4m\omega^2$, where U_P equals the time-averaged quiver energy of an electron in the laser field, F is the local electric field, ω is the frequency, and e and m are the electron charge and mass, respectively. Keldysh-parameters $\gamma < 1$ indicate the strong-field regime. In the context of photoemission from a metallic surface, the ionization potential is replaced with the work function, and the Keldysh-parameter is commonly expressed as:

$$\gamma = \sqrt{\frac{\phi}{2U_P}}$$

At near-infrared frequencies, access to the strong-field regime at nanostructures is limited by the material damage threshold. However, the exploration of strong-field dynamics benefits from the quadratic wavelength scaling of the ponderomotive energy [18]: tuning the excitation wavelength, for instance, from 0.8 to 8 μm results in a 100-fold increase of the ponderomotive energy at a given intensity. The nanostructure also further enhances the field while spatially confining it to the tip apex. Here, the oscillation amplitude of emitted electrons can exceed the near-field dimensions; this unique property limits the electron-light interactions to a fraction of the optical half-cycle, with *field*-driven rather than intensity-driven dynamics.

10.3 Photoemission from Metallic Nanotips in the Mid-Infrared

In a recent experiment, ultrashort near- and mid-infrared pulses were focused onto an electrochemically etched gold nanotip in an ultrahigh vacuum, as sketched in Fig. 10.2a. The pulses were produced by difference frequency generation of the signal and idler waves from an optical parametric amplifier pumped by a titanium-sapphire

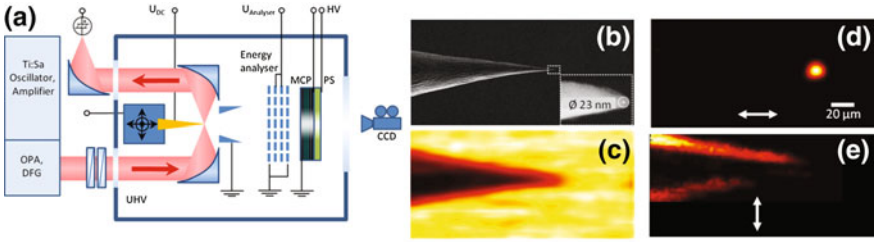

Fig. 10.2 **a** In the experiment, mid-IR pulses are generated by optical parametric amplification (OPA) and difference-frequency generation (DFG) from a titanium-sapphire (Ti:Sa) amplifier system at 1 kHz repetition rate and 30 fs pump pulse duration. The pulses are attenuated and focused onto a gold tip in an ultrahigh vacuum chamber. Photoelectrons are detected by a microchannel plate (MCP) and phosphorus-screen (PS) detector. Spectra are obtained with a retarding field energy analyzer. **b** Scanning electron micrograph of a tip used in the experiment. **c** Scanned raster image of the same tip, obtained by scanning the tip through the focal plane and recording the transmitted intensity. **d** Simultaneously recorded electron yield for polarization parallel to the tip axis showing the localized emission at the tip apex due to the field enhancement. **e** Normalized electron yield for a similar tip with polarization perpendicular to the tip apex. Adapted from [6]

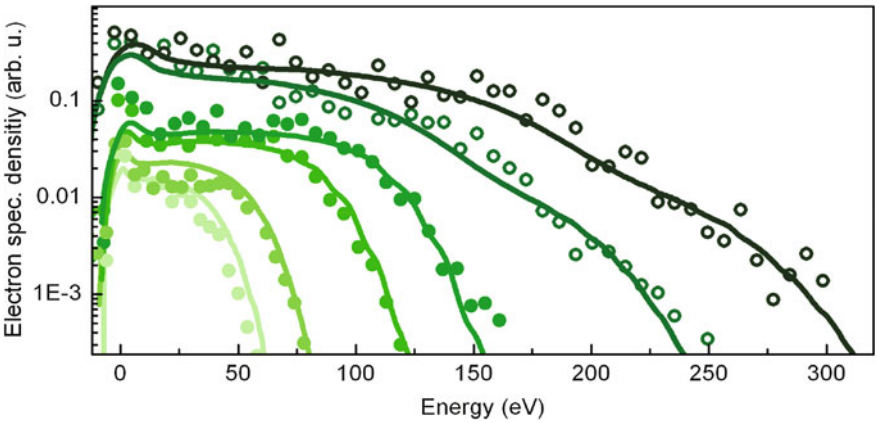

Fig. 10.3 Experimental photoelectron spectra recorded at 3.8 µm wavelength for increasing laser intensity (from *lighter* to *darker green*) and two tips with different radii (*tip radii* 12 nm (*solid circles*) and 22 nm (*open circles*)). The spectra exhibit a broad plateau region extending to cutoff energies that increase with intensity. Calculation results based on the simple man model adapted for near-fields are shown as *solid lines*. From [6]

amplifier system. The electron yield was detected with a double-stage micro-channel-plate phosphor screen detector and a CCD camera.

Kinetic energy distributions were measured by a retarding-field energy analyzer for varying laser intensities, cf. Fig. 10.3. As a hallmark of the strong-field photoelectric effect, the maximum kinetic energy grows with light intensity. Kinetic energies of the photoelectrons of up to 1,000 times the photon energy were detected

at a wavelength of 3.8 µm. The spectra exhibit a broad plateau that is understood and reproduced within the framework of an adapted simple-man description [19]. In a first step, classical electron trajectories are calculated in the time-varying electric laser field, enhanced and spatially localized to the apex region. In a second step, the resulting final kinetic energies for various emission phases are weighed with regard to the momentary current $j(t)$ that adiabatically follows the laser electric field obtained by a Fowler-Nordheim tunneling model [20]:

$$j(t) \propto \Theta(-F_{z=0}(t))\,|F_{z=0}(t)|^2 \exp\left(\frac{-4\sqrt{2m}\Phi^{3/2}}{3\hbar e|F_{z=0}(t)|}\right).$$

From the classical ponderomotive behaviour, a quadratic scaling of the cutoff energy with wavelength is expected. The wavelength-dependence at nanostructures is experimentally investigated by recording electron spectra over a wavelength range spanning from 800 nm to 8 µm. To permit a direct comparison of the spectra, the local field is fixed throughout the measurements by acquiring the spectra with constant total electron yield. This step ensures that variability in the local field due to wavelength-dependent field enhancement and space charge effects are not significant. For the characterization of pulse lengths across the full wavelength range, the ultra-broadband nonlinearity of the photoemission is utilized. By overlapping a pulse with a delayed copy on the nanotip and recording the photoelectron current, interferometric autocorrelation traces (IACs) are acquired (cf. Fig. 10.4). Fitting to the nonlinear tunneling characteristics then provides the pulse lengths. The experimentally determined pulse lengths are approximately 80, 95, 65, 60 and 75 fs for wavelengths of 0.8, 2.6, 4, 6.3 and 8 µm, respectively.

The cutoff energies of photoemission spectra acquired at fixed total current are shown in Fig. 10.5a. In contrast to the well-known classical scalings of direct and

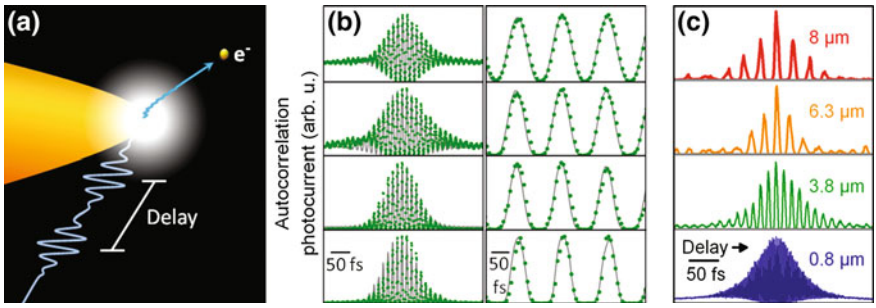

Fig. 10.4 **a** Interferometric autocorrelations (IAC) are taken by overlapping a pulse with a delayed copy on the apex of the tip and recording the electron current as a function of the delay. **b** The nonlinearity, and thus the relative baseline height, is dependent on the incident intensity. Fitting the tunneling characteristics provides a measure of the pulse lengths. The insets on the right show the varying nonlinearity in the center of the IAC traces. **c** Exemplary IAC traces for different wavelengths used in this study. From [6] and its Supplementary Information

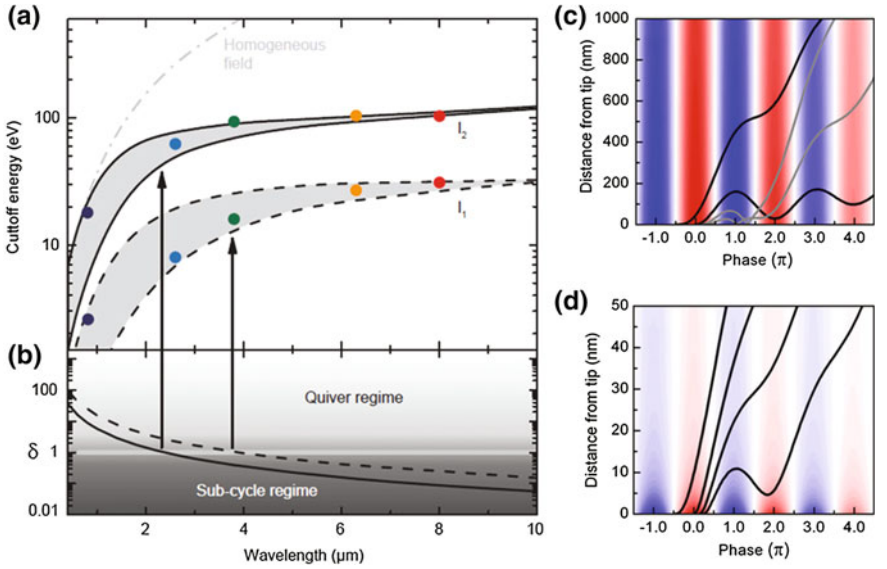

Fig. 10.5 **a** Measured cutoff energies (defined as a maximum energy that includes 99 % of all electrons) for different wavelengths and at two different local intensities, I_1 = 5.4 TW/cm^2 and I_2 = 40 TW/cm^2 (*colored dots*). The cutoff energy saturates for long wavelengths, highlighted by the comparison with the scaling of the ponderomotive energy (*dash-dot line*). The *grey-shaded* corridors indicate calculations with (*upper line*) and without (*lower line*) rescattering. **b** The unity-crossing of the spatial-adiabaticity parameter marks the saturation and the transition to the sub-cycle regime. **c** Exemplary trajectories in a nearly-homogeneous laser fields in contrast to trajectories in spatially-confined fields. **d** The *color code* represents the temporally- and spatially-varying field. The comparison at fixed emission phases shows the reduction of quiver motion and backscattered phases in the spatially-confined field. Adapted from [6]

scattered electrons as $2U_p$ and $10U_p$, respectively, we observe a saturation of the cutoff energies for long wavelengths. This difference can be understood by considering that the excursion amplitude of an electron trajectory at the present local intensities can easily exceed the extension of the tip-enhanced near-fields. Electrons that are accelerated in a positive optical half-cycle can escape the near-field during a fraction of the half-cycle. Thus, the interaction time between the electron and the electric field is reduced, resulting in dynamics determined by the instantaneous electric field rather than the vector potential or the cycle-averaged ponderomotive energy. As a direct result, the wavelength loses its significance for the acceleration process and the kinetic energy becomes wavelength-independent. The transition to this sub-cycle regime is characterized by the ratio of the (1/e)-decay length of the enhanced near-field to the quiver amplitude $l_q = \frac{eF}{m\omega^2}$:

$$\delta = \frac{l_F}{l_q} = \frac{l_F \omega^2}{F}.$$

For δ-parameters below unity, the quiver amplitude exceeds the field decay length, leading to a quenching of the quiver motion [6]. This transition is observed by the saturation in the wavelength-dependent increase of the cutoff energy as seen in Fig. 10.5a for two different local intensities. Alongside the quenching of the quiver motion, rescattering at the surface is strongly reduced. The cutoff energy of rescattered electrons in photoionization experiments with diffraction-limited foci is typically five times larger than that of the direct electrons. In the case of sub-wavelength field localization (low delta), the direct and rescattered maximum kinetic energies converge. Moreover, the contribution of rescattered electrons is continuously reduced in the sub-cycle regime, since rescattered trajectories require persistence in the high field region for back acceleration to occur when the field reverses sign. To illustrate the different dynamics between quasi-homogeneous laser fields and enhanced near-fields, exemplary trajectories are shown in Fig. 10.5b, c for identical emission phases and peak field strengths. As shown in these figures, most emission phases experience nearly linear acceleration, and those resulting in rescattering are strongly suppressed. A quantum mechanical treatment of the strong-field photoemission regime confirms the applicability of simple-man calculations and the reduction of scattering efficiency in highly localized fields [21].

In conclusion, the presented sub-cycle regime exemplifies the unique dynamics emerging from the combination of strong and frequency-tuned ultrafast light fields with nanostructures. These dynamics are non-destructively generated using few-cycle mid-infrared pulses, and the sub-cycle regime enables the direct probing of the electric near-field. These experimental conditions allow for the direct control by the optical electric field and are an example of light-wave electronics at solid surfaces. Combined with appropriate energy filtering schemes and electron-optics, this sub-cycle regime can be exploited for the generation of fast electron packets for ultrafast electron imaging and diffraction experiments.

References

1. T. Hanke et al., Efficient nonlinear light emission of single gold optical antennas driven by few-cycle near-infrared pulses. Phys. Rev. Lett. **103**, 257404 (2009)
2. S. Kim et al., High-harmonic generation by resonant plasmon field enhancement. Nature **453** (7196), 757–760 (2008)
3. M. Sivis, M. Duwe, B. Abel, C. Ropers, Nanostructure-enhanced atomic line emission. Nature **485**, E1 (2012)
4. E. Goulielmakis et al., Attosecond control and measurement: lightwave electronics. Science **317**(5839), 769–775 (2007)
5. T. Brabec, F. Krausz, Intense few-cycle laser fields: frontiers of nonlinear optics. Rev. Mod. Phys. **72**, 545–591 (2000)
6. G. Herink, D.R. Solli, M. Gulde, C. Ropers, Field-driven photoemission from nanostructures quenches the quiver motion, Nature **483**, 190 (2012)
7. D.J. Park et al., Strong field acceleration and steering of ultrafast electron pulses from a sharp metallic nanotip. Phys. Rev. Lett. **109**, 244803 (2012)

8. P. Hommelhoff, Y. Sortais, A. Aghajani-Talesh, M.A. Kasevich, Field emission tip as a nanometer source of free electron femtosecond pulses. Phys. Rev. Lett. **96**(7), 077401 (2006)
9. C. Ropers, D.R. Solli, C.P. Schulz, C. Lienau, T. Elsaesser, Localized multiphoton emission of femtosecond electron pulses from metal nanotips. Phys. Rev. Lett. **98**(4), 043907 (2007)
10. H. Yanagisawa et al., Optical control of field-emission sites by femtosecond laser pulses. Phys. Rev. Lett. **103**, 257603 (2009)
11. R. Bormann, M. Gulde, A. Weismann, S.V. Yalunin, C. Ropers, Tip-enhanced strong-field photoemission. Phys. Rev. Lett. **105**(14), 147601 (2010)
12. P. Hommelhoff, C. Kealhofer, M. Kasevich, Reaching the resolved tunnel regime for a femtosecond oscillator driven field emission electron source. Laser Phys. **19**, 736–738 (2009)
13. M. Schenk, M. Krüger, P. Hommelhoff, Strong-field above-threshold photoemission from sharp metal tips. Phys. Rev. Lett. **105**(25), 257601 (2010)
14. M. Krüger, M. Schenk, P. Hommelhoff, Attosecond control of electrons emitted from a nanoscale metal tip. Nature **475**(7354), 78–81 (2011)
15. H. Yanagisawa et al., Energy distribution curves of ultrafast laser-induced field emission and their implications for electron dynamics. Phys. Rev. Lett. **107**, 087601 (2011)
16. S. Yalunin, M. Gulde, C. Ropers, Strong-field photoemission from surfaces: theoretical approaches. Phys. Rev. B. **84**, 195426 (2011)
17. L.V. Keldysh, Ionization in the field of a strong electromagnetic wave. Sov. Phys. JETP **20**, 1307–1314 (1965)
18. P. Colosimo et al., Scaling strong-field interactions towards the classical limit. Nat. Phys. **4**(5), 386–389 (2008)
19. P.B. Corkum, Plasma perspective on strong-field ionization. Phys. Rev. Lett. **71**, 1994 (1993)
20. R.H. Fowler, L. Nordheim, Electron emission in intense electric fields. R. Soc. Lond. Proc. Ser. A **119**, 173–181 (1928)
21. S. Yalunin et al., Field localization and rescattering in tip-enhanced photoemission. Ann. Phys. **525**, L12 (2013)

Chapter 11
Comparison of Linear and Nonlinear Optical Properties of ZnO Nanorods

Susanta Kumar Das, Frank Güell, Ciarán Gray, Daragh Byrne, Prasanta Kumar Das, Rüdiger Grunwald, Günter Steinmeyer and Enda McGlynn

Abstract Photoluminescence emission from, and third harmonic generation by, ZnO nanorod samples grown using both low and high temperature methods are reported. Our results clearly show that PL emission at cryogenic temperatures from low temperature grown samples is both significantly weaker in intensity and spectrally broader than that from high temperature grown samples. The third harmonic generation efficiency of samples grown by both the low temperature and high temperature methods are however comparable to one another, and much larger than third harmonic generation at a bare quartz surface. Intensity dependence and interferometric frequency resolved optical gating measurements are used to study the third harmonic generation from both sample types. Laser pulse parameters are extracted for pulses subjected to both high and low chirp and our results indicate that ZnO nanostructures grown by low temperature methods allow excellent characterization of ultrafast pulses and are efficient for third harmonic generation and thus are excellent candidate materials for a variety of technological applications.

S. Kumar Das · R. Grunwald · G. Steinmeyer
Max Born Institute for Nonlinear Optics and Short-Pulse Spectroscopy,
Max-Born-Strasse 2a, D-12489 Berlin, Germany

F. Güell
Departament d'Electrònica, Universitat de Barcelona, C/Martí i Franquès 1, E-08028 Barcelona, Catalunya, Spain

C. Gray · D. Byrne · E. McGlynn (✉)
School of Physical Sciences, National Centre for Plasma Science and Technology,
Dublin City University, Glasnevin, Dublin 9, Ireland
e-mail: enda.mcglynn@dcu.ie

S. Kumar Das · P. Kumar Das
School of Applied Sciences, KIIT University,
Bhubaneswar 751024, Odisha, India

© Springer International Publishing Switzerland 2015

S. Sakabe et al. (eds.), *Progress in Nonlinear Nano-Optics*,
Nano-Optics and Nanophotonics, DOI 10.1007/978-3-319-12217-5_11

11.1 Introduction

ZnO nanostructures display an exceptional range of nanomorphologies and can be synthesised by a wide range of growth methods. Materials grown in various morphologies by different growth methods have differing advantages and disadvantages from the point of view of applications [1]. As one example, ZnO synthesised at higher temperatures using vapour phase transport (VPT) results in deposited material with excellent optical emission, but deposition is generally over limited areas, whereas ZnO synthesised at lower temperatures using chemical bath deposition (CBD) results in material with characteristically poor optical properties such as photoluminescence (PL) emission but the growth method allows uniform deposition over large areas [2, 3].

Furthermore, the many promising qualities of ZnO mean that researchers wish to utilise a diverse range of substrates, including flexible plastic substrates. It is generally unfeasible to employ growth temperatures >400 °C with plastic substrates without causing significant substrate damage or destruction. This issue has further spurred the interest of researchers in terms of the development of low temperature (<400 °C and even in some cases <100 °C) CBD methods [4]. ZnO nanostructures grown by such CBD methods show a range of morphologies but in many cases they yield well-aligned arrays of close-packed nanorods with diameters ∼50–300 nm, regardless of the substrate type, dominated by crystal facet energetics and proximity effects [4–6].

In all cases known to the authors, while the structural properties of both VPT- and CBD-grown ZnO nanorods are comparably good and single crystal nanostructures are reported, the linear optical properties, specifically PL emission, are significantly worse for CBD-grown nanostructures compared to VPT-grown material. This is evidenced in a variety of ways in the PL such as (i) generally strong defect band to the bandedge emission ratio, (ii) generally far weaker PL emissions, and, very importantly (iii) very large low temperature PL bound exciton linewidths (∼10 meV) [7]. While the linear optical properties such as PL emission intensity can be somewhat improved by annealing, the linewidths do not improve to anything close to the values (<1 meV) seen in PL from nanostructures grown by VPT [8]. Trade-offs of this nature between linear optical properties and deposition area and scalability are generally found in the different growth methods of ZnO nanostructures, and their origins seem fundamentally linked to the key advantage of the CBD methods, low temperature synthesis. Thus it is difficult to envisage solutions to this problem for linear optical properties, since techniques such as annealing (which is at best only partially successful in improving the PL emission properties) themselves will lead to problems similar to those observed for high temperature growth methods due to the high temperatures involved.

By contrast, the nonlinear properties of these nanomaterials, including third order nonlinearities, and the variation of these properties as a consequence of different growth methods, are less widely reported. For example, there is a limited number of reports of third harmonic generation (THG) from ZnO nanomaterials, whereas a greater number of publications deal with second harmonic generation

(SHG) from ZnO and ZnO nanostructures [9–12]. Frequency conversion and other nonlinear phenomena in ZnO nanostructures are of importance because many application areas might benefit from UV generation via THG. For example ultrashort fs laser pulse characterization is rendered challenging due to the broadband pulse spectrum (>100 nm) which means that dispersive effects can dominate, and this in turn typically requires a sub-20 μm material path for sufficiently broadband phase matching. Thus, one requires very thin nonlinear crystals for this type of application [13]. There have been recent reports of thin nanocrystalline TiO_2 films used for pulses down to 20 fs, which effectively demonstrates the proof of principle that for nano length scale deposits the normal phase-matching constraints associated with traditional bulk nonlinear materials are relaxed [14]. In terms of an application in a very different technology space, efficient UV delivery to sites inside the human body, either by coupling NIR radiation via the "optical tissue window" wavelengths (0.7–1.1 μm) or using waveguides to couple NIR radiation, to nanostructures embedded in tissue in the body, and upconverting to UV, may allow the advancement of new methods of spatially localised UV photodynamic therapy, down to the size of single cells [15–19]. Indeed CBD-grown ZnO nanorods have been used to make measurements within a cell [19]. However these types of applications all rely on high UV conversion efficiencies.

In this chapter PL emission and THG by both CBD-grown and VPT-grown ZnO nanorod samples are reported. These studies clearly show that the low temperature PL emission from CBD-grown samples is both weaker in intensity and broader in terms of key feature linewidths than that from VPT-grown samples. By contrast the THG efficiency of samples grown by both the high temperature and low temperature methods are comparable to one another, and both are much larger than THG generated at a bare quartz surface. Intensity dependence measurement and interferometric frequency resolved optical gating (iFROG) measurements are used to study the THG from both sample types [20, 21]. The laser pulse parameters are extracted when the pulses are subjected to both high and low chirp and our studies indicate that ZnO nanostructures grown by low temperature methods allow excellent characterization of ultrafast pulses (originally <10 fs) and can efficiently generate UV light via THG. Consequently ZnO nanostructures grown by low temperature methods are excellent candidate materials for the technology applications discussed above.

11.2 Experimental Details

11.2.1 ZnO Nanostructure Growth and Structural Characterization

ZnO nanostructures were grown by both CBD (on fused silica substrates and Si (111) or Si (100) substrates) and by VPT (on (11–20) sapphire substrates and Si (111) or Si (100) substrates).

11.2.1.1 CBD Growth

The details of the growth method employed for CBD have been given elsewhere [2, 22, 23]. In summary, substrates cleaned by sonication in acetone and ethanol were dried in a nitrogen stream and then coated with a ZnO seed layer via drop coating. Typically the drop coated seed layer was prepared by applying 3.75 μl per cm^2 of substrate of a 5 mM zinc acetate in absolute ethanol solution for 20 s before rinsing with absolute ethanol and drying the sample with a nitrogen stream. Drop coating was normally repeated four more times and samples were annealed at 350 °C in air for 30 min. ZnO nanorods were deposited on the seeded substrates using a 0.02 M zinc nitrate solution added slowly to an equal volume of 0.8 M NaOH solution with vigorous stirring. This solution was heated to 70 °C and the substrates were then immersed in it, maintaining the temperature for 25 min, with gentle stirring. The substrates were then removed from the solution, washed with DI-H_2O, and dried in a nitrogen stream. This leads to a deposit of densely packed ZnO nanorods, with a thickness of ~1 μm and an average nanorod diameter of ~75 nm. The nanorods are well-aligned perpendicular to the substrate surface.

11.2.1.2 VPT Growth

The details of the VPT growth methods are as follows (more detail may be found in selected references) [2, 24, 25]. Two methods of VPT growth were employed, one involving the seeded layers mentioned above, on Si substrates, and the other using an Au catalyzed vapour-liquid-solid (VLS) process to grow ZnO nanorods on sapphire substrates. For the case of VPT on seeded Si substrates, we have used two methods. Firstly, nanorods were grown by VPT directly through a hexagonal silica template onto CBD ZnO films (prepared using a slightly different method to that described above, based on forced hydrolysis of zinc acetate). The second method used an intermediate zinc acetate CBD stage through a hexagonal silica template to initiate nanorod growth, followed by VPT. Equal masses of graphite and ZnO (0.06 g) were thoroughly mixed and placed in an alumina boat. Substrates were placed over this mixture with the seeded side facing the source powder. The boat was heated to 900 °C in a single zone horizontal tube furnace, with a 90 sccm Ar flow for 1 h, and then cooled to room temperature. More detail on this VPT growth on seeded Si substrates is given in the [2]. For the case of Au catalysed VLS-VPT three differently oriented sapphire substrates were utilised [c-plane (0001), a-plane (11–20) and r-plane (1–102)]. Results below are shown only for samples on a-plane (11–20) substrates with a dense coverage of well-aligned nanorods of mean length ~0.6 μm and mean diameter ~70 nm. Au catalyst was deposited on the substrates by sputtering to yield a 3 nm thick layer. ZnO powder was mixed with graphite powder and growth took place in a CVD furnace with a horizontal quartz tube. Ar was the inert carrier gas and the furnace was heated to 900 °C and the growths took 30 min. More detail on this VLS-VPT growth on sapphire substrates is given [24, 25].

The fact that the morphologies and dimensions of the nanostructures grown by both CBD and VPT are similar allows us to compare their optical behaviour without concerns that effects associated with different morphologies and/or dimensions would strongly affect the conclusions of our work.

The samples were structurally characterized by field emission SEM (FESEM; JEOL JSM-6400F and Hitachi H-4100FE) and X-ray diffraction (XRD; Bruker AXS D8 Advance Texture Diffractometer).

11.2.2 Linear and Nonlinear Optical Characterisation

PL spectra were acquired using the 325 nm line of He-Cd laser with a Bomem Hartmann and Braun DA8 FT spectrometer with the samples in a closed cycle cryostat (Janis Research Co. Inc.). THG studies were carried with a Ti:sapphire laser (Venteon Femtosecond Laser Technologies), pumped by a frequency doubled Nd:YAG. The temporal width, repetition rate and energy of the original pulses from the laser were $\sim$7 fs, 80 MHz and $\sim$5.25 nJ, respectively. The central wavelength is $\sim$810 nm and the spectral bandwidth, as determined by the full width at half maximum (FWHM), is >300 nm. The laser was focussed for THG studies with a beam waist of $\sim$4 μm, giving a peak intensity of $\sim 1.5 \times 10^{12}$ Wcm^{-2} in the case of the direct beam. iFROG measurements were made with a home-built system, using a Michelson interferometer configuration where one mirror is controlled by a piezoelectric controller (step size = 35 nm). Pulses from the two arms of the interferometer are recombined with varying delays and are focussed on the samples, as described above. The THG signal is separated, and residual pump radiation removed, by a THG reflecting mirror and an interference filter. The THG signal is analysed with an EMCCD-based spectrometer (Newton, Andor Technology, the EMCCD was cooled to −75 °C by a Peltier cooler). All THG experiments were carried out at room temperature. The interferometer mirror motion and the spectral data capture were synchronized using in-house LabView-based software. Further analysis of the iFROG data was performed using Femtosoft software (Femtosoft Technologies, FROG 3.0) following Fourier filtering which is used to extract normal frequency resolved optical gating (FROG) data [20].

11.3 Experimental Results and Discussion

11.3.1 ZnO Nanostructure Growth and Structural Characterization

Figure 11.1a shows 45° tilted-view FESEM data of the CBD grown deposit on fused silica, showing a densely packed ZnO nanorod film with a thickness of $\sim$1 μm (and the inset shows a cross-sectional view) with an average nanorod

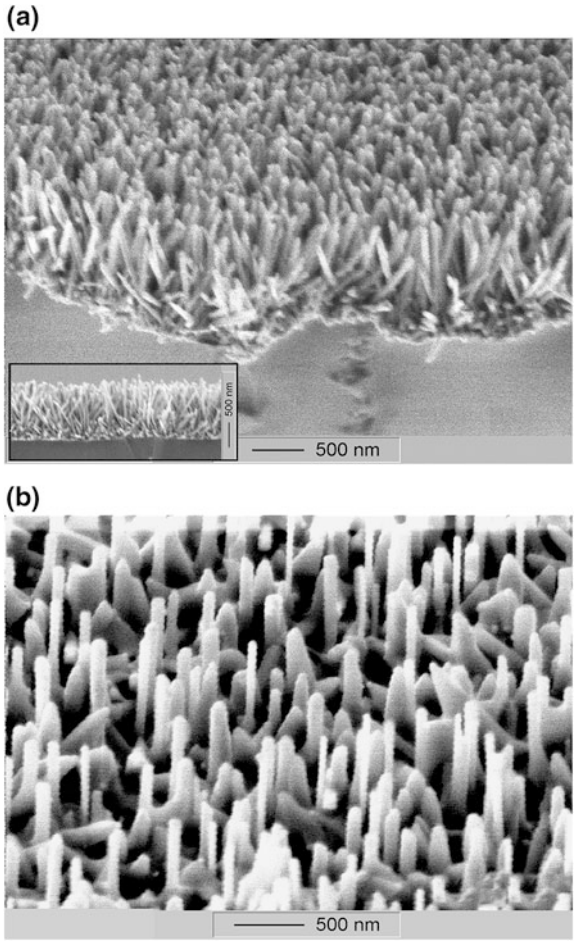

Fig. 11.1 **a** 45° tilted-view FESEM image of CBD-grown ZnO nanorod sample on fused silica (*inset* shows a cross-sectional view); **b** 45° tilted-view FESEM image of VPT-grown ZnO nanorod sample on a-plane sapphire

diameter of ~75 nm. The nanorods are well-aligned normal to the substrate. Figure 11.1b shows FESEM data for the VPT-grown ZnO nanorod sample on sapphire. XRD data (not shown) confirm the crystalline ZnO phase in all cases.

11.3.2 ZnO Nanostructure Linear and Nonlinear Optical Characterisation

Figure 11.2 shows low temperature PL spectra for the CBD-grown (using forced hydrolysis of zinc acetate; samples grown by CBD using the NaOH method showed very weak and in some cases undetectable PL emission at low temperatures) and VPT-grown samples on Si substrates. Figure 11.2a, b show data for different

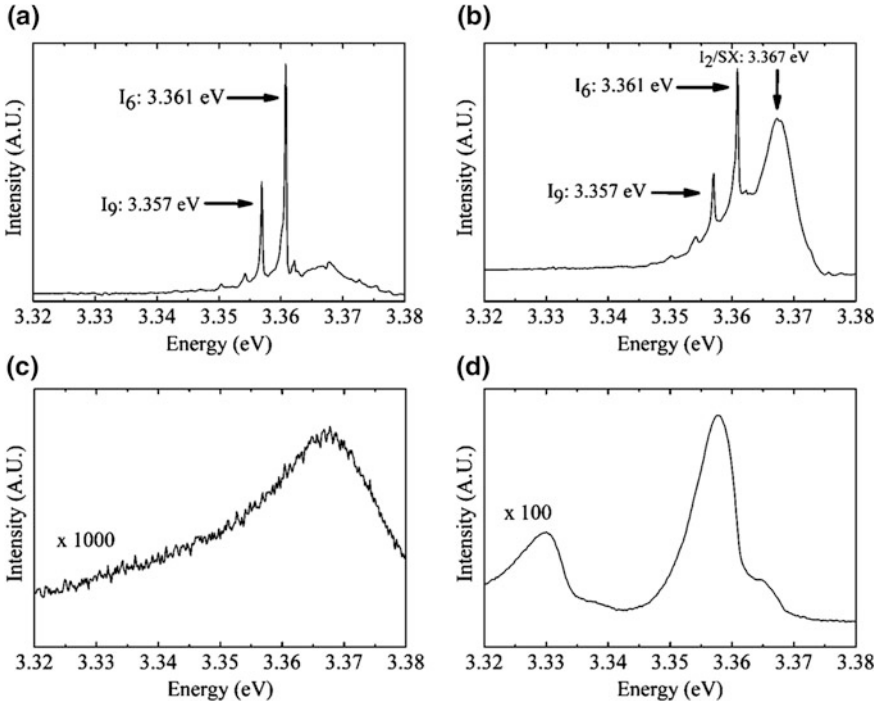

Fig. 11.2 PL emission at low temperature (~18–20 K) from **a** and **b** VPT-grown ZnO nanorod samples on Si; **c** CBD-grown ZnO nanorod sample on Si without anneal; **d** CBD-grown ZnO nanorod sample on Si following 900 °C anneal. The y-axis intensities are comparable in all parts of the figure

VPT-grown samples which both display strong emission and very narrow bound exciton linewidths. Various spectral features can be clearly resolved, including the I_2/SX, I_6 and I_9 lines (following the usual labelling) [26]. The I_6 line at ~3.361 eV is present in all our VPT-grown samples due to Al impurities because the substrate and reaction mixture is placed in an alumina boat during deposition [26]. The FWHM of this peak is ~0.5 meV indicating material of high quality. The I_9 line is found in the majority of samples and is ascribed to indium; the precise origin of indium is uncertain, but it is a common impurity in ZnO and may originate in the source powder or from growth system contamination [27]. An emission at ~3.367 eV is also observed in some samples, corresponding to the surface exciton (SX), assigned to surface adsorbed impurities [28, 29]. The PL emission from CBD-grown material has also been measured, both with and without a final annealing step at 900 °C. The PL emission from the unannealed CBD-grown layer, shown in Fig. 11.2c, is extremely weak. After annealing, some improvement in the PL intensity was observed as shown in Fig. 11.2d. However the signal intensity is still ~100 times weaker than that from VPT-grown samples and the PL peak widths are far broader. Thus it is clear that the PL signal quality, in terms of intensity and spectral linewidth,

is far poorer for the CBD-grown samples, compared to the VPT-grown samples. Before annealing the sole peak detected in the CBD-grown samples is a broad emission at ~3.368 eV, but after annealing this is replaced by a peak close to the I_9 position, supporting the assignment of the I_9 peak in VPT-grown samples to contamination of furnace equipment, as mentioned earlier.

Figure 11.3a displays THG spectra for the CBD-grown sample on fused silica and the VPT-grown sample on a-plane sapphire under focused illumination by Ti: sapphire laser, with conditions as described earlier (the beam splitter in the iFROG set-up has fixed and unequal path lengths, leading to a pulse width of ~11 fs). Figure 11.3a also shows surface enhanced THG (STHG) from a bare quartz surface, recorded under identical conditions. A signal is seen at ~272 nm with bandwidth of ~20 nm from all samples, and this matches the expected spectral position for THG of the 810 nm fundamental laser very well [30]. The identification of this

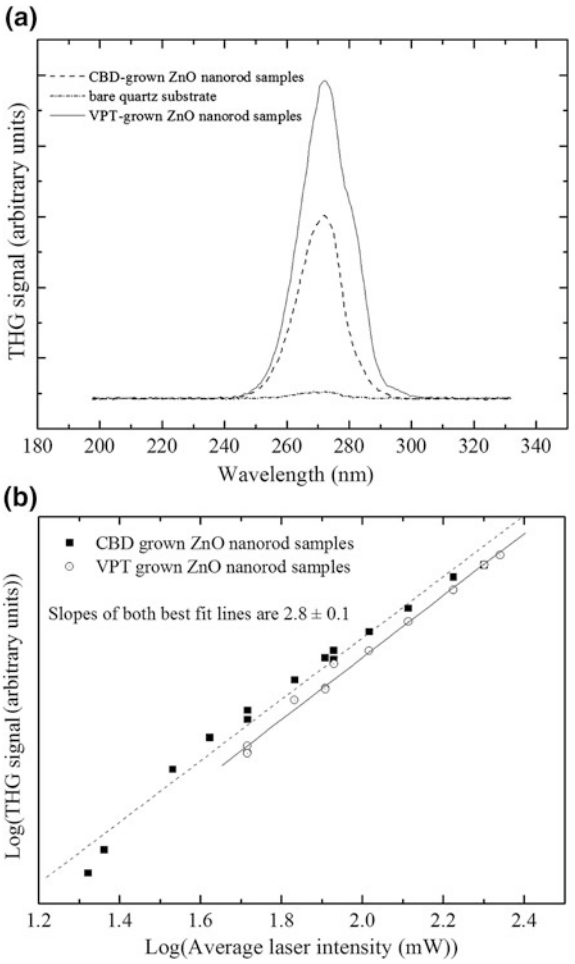

Fig. 11.3 **a** THG spectra for the CBD-grown (on fused silica) and VPT-grown (on a-plane sapphire) ZnO nanorod samples and for a bare quartz substrate, under focused laser excitation; **b** THG intensity variation as a function of exciting laser intensity for both the CBD- and VPT-grown ZnO nanorod samples

signal at 272 nm with THG is further evidenced by the dependence of its intensity on the exciting laser intensity, which is shown in Fig. 11.3b.

The exciting laser intensity was controlled using neutral density (ND) filters which cause temporal broadening of the pulse to ~42 fs (as well as chirp), and this causes a decrease in the peak intensity of the pulse. The broadening does not vary with the different ND filters used and the same laser pulse width was measured for beams which traversed different ND filter combinations, as shown in Fig. 11.5 for a number of different combinations. The THG signal intensity from the CBD-grown and VPT-grown ZnO nanorod samples are comparable. In terms of the spectral details, the VPT-grown sample shows a small long wavelength shoulder, a feature also evident in iFROG data in Fig. 11.4, most likely due to different alignment and/or faceting of the ZnO nanostructures grown by CBD and VPT. It is known that nonlinear processes in nanostructures are often sensitive to the specific crystal termination [31].

In Fig. 11.3b the integrated 272 nm signal intensity (after baseline correction of THG intensity) is plotted versus laser intensity using log–log axes. The order of the nonlinear process should be given by the slope of this graph. For the case of both the CBD- and VPT-grown ZnO samples the slope is 2.8 ± 0.1, almost equal to the value of 3 expected for third order processes. The discrepancy from an exponent of 3 may be due to a variety of physical mechanisms, and understanding its origins more precisely remains an objective as part of our future investigations.

Clearly the THG efficiency of ZnO nanorod samples grown by both CBD and VPT is very similar, and in both cases is much greater than that associated with STHG at a bare quartz sample surface (at least one order of magnitude greater for the ZnO nanorod samples). The results from the characterisation of the nonlinear optical properties of the ZnO nanorod samples grown by both CBD and VPT thus differs very greatly from the characterisation results of the linear optical properties

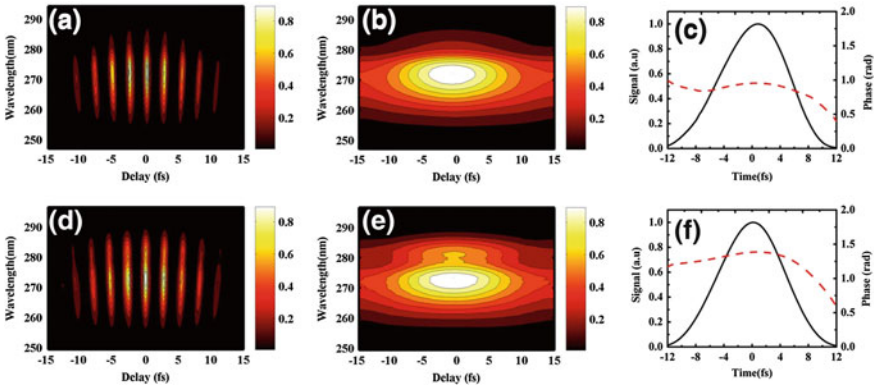

Fig. 11.4 **a** iFROG trace, **b** FROG and **c** temporal pulse profile of THG from ZnO CBD-grown nanorods; **d** iFROG trace, **e** FROG and **f** temporal pulse profile of THG from ZnO VPT-grown nanorods (no ND filter in beam path for any of these measurements)

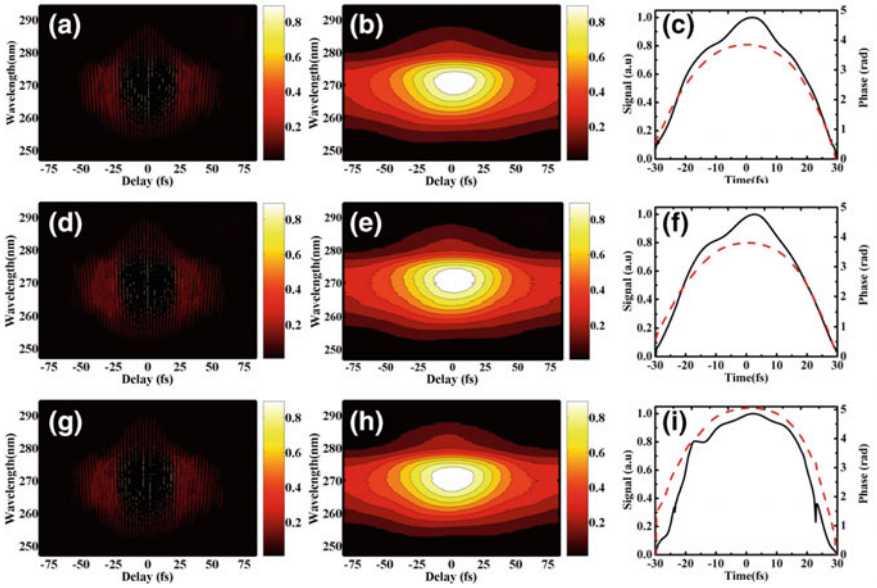

Fig. 11.5 iFROG trace, FROG and temporal pulse profile, respectively, for CBD-grown ZnO nanorods with ND filter optical density 0.04 + 0.04, (**a**–**c**); with ND filter in path with with ND filter optical density 0.04 + 0.2, (**d**–**f**); with ND filter in path with ND filter optical density 0.04 + 0.4, (**g**–**i**)

of ZnO nanorods grown by these two methods, as shown by the PL emission data in Fig. 11.2. The data in Fig. 11.2 show that PL from CBD-grown ZnO nanorods is always much weaker (and far broader spectrally) at low temperatures than that from VPT-grown ZnO nanorods [2, 3].

11.3.3 ZnO Nanorods as Frequency Converters for Third Order Pulse Characterization with iFROG

iFROG data from CBD-grown and VPT-grown ZnO nanorod samples is shown in Fig. 11.4 and the data from both sample types are very similar (noting the shoulder at longer wavelengths for the VPT-grown sample, mentioned earlier). Unprocessed THG iFROG data from the CBD- and VPT-grown samples is shown in Fig. 11.4a and d, respectively. Fourier analysis of these data yields the various order frequency components; the DC and first order components are used to retrieve pulse shape using two independent approaches and thus iFROG allows an internal check on consistency, especially for delay axis calibration [20, 21, 32]. Our analysis concentrates on DC part of the data extracted by Fourier filtering and the resultant data are shown in Fig. 11.4b, e (CBD- and VPT-grown ZnO nanorod samples, respectively). This data is the same as an ordinary FROG trace and can thus be processed

directly by standard software for pulse retrieval. Here we have used commercial software (specified in the Experimental Details section) and the resultant spectral signal and spectral phase are given in Fig. 11.4c, f (CBD- and VPT-grown ZnO nanorod samples, respectively). The pulse duration is estimated at ~11 fs for the case of both CBD- and VPT-grown ZnO nanorod samples.

The remaining nonlinear optical studies presented here are for the CBD-grown nanorod sample because data for VPT-grown samples are identical in all important respects. The time-bandwidth product from FROG analysis was 0.55. An unchirped Gaussian pulse has a time-bandwidth product of 0.44 and the larger product in the present case implies the presence of quadratic chirp; the curved phase profile in Fig. 11.4c also clearly demonstrates this chirp which we attribute to the beam splitter of the iFROG system. This beam splitter has a quartz substrate of thickness 0.7 mm (from Venteon). The group delay dispersion (GDD) of this substrate is ~36 fs^2/mm and thus the net GDD (β_2) due to this beam splitter is 24 fs^2 (i.e. 36 fs^2/mm × 0.7 mm) [33, 34]. The pulse duration (τ) as a function of GDD is described by (11.1) below:

$$\tau = \tau_0 \sqrt{1 + \left(4 \cdot \ln(2) \cdot \left(\frac{\beta_2}{\tau_0^2}\right)\right)^2} \tag{11.1}$$

In (11.1) τ_o = is the unchirped pulse duration (i.e. coming directly from the laser) [33–35]. Inserting values for τ of 11 fs and for β_2 of 24 fs^2 into (11.1) yields a value for the unchirped pulse duration of τ_o = 7 fs, and this value is very close to the value measured by a commercial Few Cycle-Spectral Phase Interferometry for Direct Electric-field Reconstruction (FC-SPIDER; Applied Physics and Electronics—APE Ltd., Berlin, Germany) system of 6.7 fs. This excellent agreement shows the capability of CBD-grown ZnO nanorod samples to accurately recover values for initial pulse durations less than 10 fs.

In order to examine the pulse diagnostics capability of the ZnO nanorod sample under conditions of higher chirp we have measured the pulse parameters after the pulses have traversed highly dispersive (HD) optical materials. The HD optical materials employed are metal coated ND filters (New Focus, 2 filter wheel system), i.e. those previously employed for intensity variation studies shown in Fig. 11.2. We have used three different filtering conditions with quite different transmissions (i.e. ND values of 0.04 + 0.04, 0.04 + 0.2, 0.04 + 0.4; the two values are the ND optical densities of the two filters in the tandem set-up). Typical iFROG and DC component of iFROG (i.e. FROG) traces as well as pulse temporal profiles after traversing the ND filter combination are shown in Fig. 11.5a–i, again for the CBD-grown nanorod sample. The duration of the pulse for all filtering combinations is essentially constant at ~42 fs. This increase in duration is caused by the very large chirp created by the ND filters. We have again used Femtosoft software to extract the spectral phase profile of the pulse (data not shown). Employing a standard Taylor series expansion of this phase profile gives a value for the GDD, β_2, of ~90 fs^2. By using this value in conjunction with the value for τ_o deduced from the

analysis above (7 fs), we can compute the broadened pulse duration, using (11.1) again, to be ~38 fs, a value which is in excellent agreement with the experimentally observed pulse width of 42 fs [33–35]. The residual discrepancy between the computed and experimental values of ~4 fs is because (11.1) only includes second order chirp (GDD, which is normally the most important term), but neglects third order dispersion (TOD) and higher order terms.

11.4 Conclusions

This chapter has compared the linear and nonlinear optical properties of ZnO grown by CBD and VPT. Our data show that the linear optical properties of VPT-grown nanorods are vastly better, and PL emission from VPT-grown nanorods is significantly more intense, as well as displaying much narrower excitonic linewidths at low temperatures. By contrast the nonlinear optical properties, such as THG, of the nanorods grown by the two methods are very similar and nanorods grown by both methods are efficient sources for third harmonic UV generation. The THG signal has been studied using intensity dependence measurements which clearly confirm the third order nonlinear nature of the spectral signal at ~272 nm. ZnO nanorod deposits give THG signals more than a factor of ten larger than STHG generated at a quartz sample surface. This demonstrates the material's suitability as an efficient UV generator using nonlinear up-conversion of red/near IR laser pulses, for ZnO nanorod deposits grown by both CBD and VPT. We have also reported iFROG studies of these ZnO nanorod samples, and have measured laser pulse parameters, as well as effects such as pulse broadening and chirping caused by ND filters utilised in certain configurations. This work clearly shows that ZnO nanorod deposits of this type can efficiently characterize laser pulses (of original durations <10 fs) [36, 37].

The efficiency of both CBD-grown and VPT-grown ZnO nanorods as third harmonic UV generation sources means that a number of growth methods, compatible with various substrates and with differing coverage and scalability capabilities, can be confidently used in future work to drive forward potential applications in iFROG characterization of ultrafast, few cycle, fs pulses, as well as in biophysical studies of single cell UV irradiation.

Acknowledgments EMcG, FG and RG acknowledge LaserLab Europe funding under project MBI001954 enabling travel by EMcG and FG to MBI for extended research visits. RG also acknowledges partial funding of the work by DFG grants (numbers GR1782-12-1 and GR1782-12-2). CG and EMcG acknowledge the Irish Research Council (IRC; formerly the Irish Research Council for Science, Engineering and Technology, IRCSET) for a postgraduate scholarship under the EMBARK initiative. DB and EMcG acknowledge support from Science Foundation Ireland via the Strategic Research Cluster grant entitled "Functional Oxides and Related Materials for Electronics" (FORME). Finally, we gratefully acknowledge T. Elsaesser and M. Tischer (both MBI) for essential support and stimulating discussions.

References

1. A.B. Djurisic, Y.H. Leung, Optical properties of ZnO nanostructures. Small **2**, 944–961 (2006)
2. D. Byrne, E. McGlynn, J. Cullen, M.O. Henry, A catalyst-free and facile route to periodically ordered and c-axis aligned ZnO nanorod arrays on diverse substrates. Nanoscale **3**, 1675–1682 (2011)
3. E. McGlynn, M.O. Henry, J.-P. Mosnier, ZnO wide bandgap semiconductor nanostructures: growth, characterisation and applications, in *Handbook of Nanoscience and Technology*, vol. II ed. by A.V. Narlikar, Y.Y. Fu (Oxford University Press, Oxford, 2009), pp. 575–624
4. L.E. Greene, M. Law, D.H. Tan, M. Montano, J. Goldberger, G. Somorjai, P. Yang, General route to vertical ZnO nanowire arrays using textured seeds. Nano Letters **5**, 1231–1236 (2005)
5. B. Postels, M. Kreye, H.H. Wehmann, A. Bakin, N. Boukos, A. Travlos, A. Waag, Selective growth of ZnO nanorods in aqueous solution. Superlattices Microstruct. **42**, 425–430 (2007)
6. W. Bai, K. Yu, Q.X. Zhang, X. Zhu, D.Y. Peng, Z.Q. Zhu, N. Dai, Y. Sun, Large-scale synthesis of zinc oxide rose-like structures and their optical properties. Phys. E-Low-Dimens. Syst. Nanostruct. **40**, 822–827 (2008)
7. C. Bekeny, T. Voss, H. Gafsi, J. Gutowski, B. Postels, M. Kreye, A. Waag, Origin of the near-band-edge photoluminescence emission in aqueous chemically grown ZnO nanorods. J. Appl. Phys. **100**, 104317 (2006)
8. J. Grabowska, A. Meaney, K. Nanda, J.-P. Mosnier, M. Henry, J.-R. Duclère, E. McGlynn, Surface excitonic emission and quenching effects in ZnO nanowire/nanowall systems: limiting effects on device potential. Phys. Rev. B **71**, 115439 (2005)
9. G.I. Petrov, V. Shcheslavskiy, V.V. Yakovlev, I. Ozerov, E. Chelnokov, W. Marine, Efficient third-harmonic generation in a thin nanocrystalline film of ZnO. Appl. Phys. Lett. **83**, 3993–3995 (2003)
10. K. Wang, J. Zhou, L. Yuan, Y. Tao, J. Chen, P. Lu, Z.L. Wang, Anisotropic third-order optical nonlinearity of a single micro/nanowire. Nano Letters **12**, 833–838 (2012)
11. S.K. Das, M. Bock, C. O'Neill, R. Grunwald, K.M. Lee, H.W. Lee, S. Lee, F. Rotermund, Efficient second harmonic generation in ZnO nanorod arrays with broadband ultrashort pulses. Appl. Phys. Lett. **93**, 181112 (2008)
12. K. Pedersen, C. Fisker, T.G. Pedersen, Second-harmonic generation from ZnO nanowires. Phys. Stat. Sol. **5**, 2671–2674 (2008)
13. Y. Kobayashi, D. Yoshitomi, K. Iwata, H. Takada, K. Torizuka, Ultrashort pulse characterization by ultra-thin ZnO, GaN, and AlN crystals. Opt. Express **15**, 9748–9754 (2007)
14. S.K. Das, C. Schwanke, A. Pfuch, W. Seeber, M. Bock, G. Steinmeyer, T. Elsaesser, R. Grunwald, Highly efficient THG in TiO_2 nanolayers for third-order pulse characterization. Opt. Express **19**, 16985–16995 (2011)
15. C. Zhang, F. Zhang, S. Qian, N. Kumar, J. Hahm, J. Xu, Multiphoton absorption induced amplified spontaneous emission from biocatalyst-synthesized ZnO nanorods. Appl. Phys. Lett. **92**, 233116 (2008)
16. D. Sridhar, J.N. Xie, J.K. Abraham, V.K. Varadan, Synthesis arid photonic property study of ZnO nanowires for a real time photodynamic therapy monitoring probe. Nanosens. Microsens. Biosens. Syst. **6528** L5281–L5281 510 (2007)
17. C. Baratto, E. Comini, G. Faglia, G. Sberveglieri, M. Zha, A. Zappettini, Metal oxide nanocrystals for gas sensing. Sens. Actuators B Chem. **109**, 2–6 (2005)
18. J. Li, D. Guo, X. Wang, H. Wang, H. Jiang, B. Chen, The photodynamic effect of different size ZnO nanoparticles on cancer cell proliferation in vitro. Nanoscale Res. Lett. **5**, 1063–1071 (2010)
19. S.M. Al-Hilli, M. Willander, A. Öst, P. Strålfors, ZnO nanorods as an intracellular sensor for pH measurements. J. Appl. Phys. **102**, 084304 (2007)

20. G. Stibenz, G. Steinmeyer, Interferometric frequency-resolved optical gating. Opt. Express **13**, 2617–2626 (2005)
21. G. Stibenz, G. Steinmeyer, Structures of interferometric frequency-resolved optical gating. IEEE J. Sel. Top. Quantum Electron. **12**, 286–296 (2006)
22. D. Byrne, E. McGlynn, K. Kumar, M. Biswas, M.O. Henry, G. Hughes, A study of drop-coated and chemical bath-deposited buffer layers for vapor phase deposition of large area, aligned, zinc oxide nanorod arrays. Cryst. Growth Des. **10**, 2400–2408 (2010)
23. D. Byrne, E. McGlynn, M.O. Henry, K. Kumar, G. Hughes, A novel, substrate independent three-step process for the growth of uniform ZnO nanorod arrays. Thin Solid Films **518**, 4489–4492 (2010)
24. F. Güell, J.O. Ossó, A.R. Goñi, A. Cornet, J.R. Morante, Synthesis and optical spectroscopy of ZnO nanowires. Superlattices Microstruct. **45**, 271–276 (2009)
25. F. Güell, J.O. Ossó, A.R. Goñi, A. Cornet, J.R. Morante, Direct imaging of the visible emission bands from individual ZnO nanowires by near-field optical spectroscopy. Nanotechnology **20**, 315701 (2009)
26. B.K. Meyer, H. Alves, D.M. Hofmann, W. Kriegseis, D. Forster, F. Bertram, J. Christen, A. Hoffmann, M. Straßburg, M. Dworzak, U. Haboeck, A.V. Rodina, Bound exciton and donor–acceptor pair recombinations in ZnO. Phys. Stat. Solid **241**, 231–260 (2004)
27. M. Strassburg, A. Rodina, M. Dworzak, U. Haboeck, I.L. Krestnikov, A. Hoffmann, O. Gelhausen, M.R. Phillips, H.R. Alves, A. Zeuner, D.M. Hofmann, B.K. Meyer, Identification of bound complexes in ZnO. Phys. Status Sol. **241**, 607–611 (2004)
28. M. Biswas, Growth and characterisation of ZnO nanostructures: excitonic properties and morphology. Ph.D. thesis, Dublin City University, School of Physical Sciences, 2010
29. M. Biswas, Y.S. Jung, H.K. Kim, K. Kumar, G.J. Hughes, S. Newcomb, M.O. Henry, E. McGlynn, Microscopic origins of the surface exciton photoluminescence peak in nanostructures. Phys. Rev. B **83**, 235320 (2011)
30. T. Tsang, Optical third-harmonic generation at interfaces. Phys. Rev. A **52**, 4116–4125 (1995)
31. U. Neumann, R. Grunwald, U. Griebner, G. Steinmeyer, M. Schmidbauer, W. Seeber, Second-harmonic performance of a-axis-oriented ZnO nanolayers on sapphire substrates. Appl. Phys. Lett. **87**, 171108 (2005)
32. A. Anderson, K.S. Deryckx, X.G. Xu, G. Steinmeyer, M.B. Raschke, Few-femtosecond plasmon dephasing of a single metallic nanostructure from optical response function reconstruction by interferometric frequency resolved optical gating. Nano Letters **10**, 2519–2524 (2010)
33. D. Marcuse, distortion in single-mode fibers. Appl. Opt. **19**, 1653–1660 (1980)
34. I. Walmsley, L. Waxer, C. Dorrer, The role of dispersion in ultrafast optics. Rev. Sci. Instrum. **72**, 1–29 (2001)
35. RP Photonics Webpages, chromatic dispersion. http://www.rp-photonics.com/chromatic_dispersion.html
36. S.K. Das, F. Güell, C. Gray, P.K. Das, R. Grunwald, E. McGlynn, ZnO nanorods for efficient third harmonic UV generation. Opt. Mater. Express **4**.701–709 (2014)
37. S.K. Das, F. Güell, C. Gray, P.K. Das, R. Grunwald, E. McGlynn, ZnO nanorods for efficient third harmonic UV generation: erratum. Opt. Mater. Express **4**, 1243 (2014)

Chapter 12
Femtosecond-Laser Induced Periodic Surface Structures for Surface Enhanced Raman Spectroscopy of Biomolecules

Hamza Messaoudi, Susanta Kumar Das, Janine Lange, Friedhelm Heinrich, Sigurd Schrader, Marcus Frohme and Rüdiger Grunwald

Abstract Nanostructured metal surfaces can be used as high-efficiency substrates for surface-enhanced Raman spectroscopy (SERS). For this purpose, laser induced periodic surface structures (LIPSS) were generated by illuminating silver and copper substrates with pulses of a 1-kHz Ti:sapphire femtosecond laser and second harmonic generation (SHG). We report on the details of the structuring experiments and the application of the metallic nanogratings to the SERS of selected types of biomolecules like DNA (herring sperm) and protein molecules (egg albumen) (Messaoudi et al. Proc. SPIE 8972: 8972-17, 2014). Maximum enhancement was detected for Ag substrates processed with at the SHG wavelength of 400 nm and structure periods at a comparable scale. In contrast to that, long-period ripples induced at the fundamental wavelength of 800 nm were found to show the highest enhancement for copper substrates. As a possible explanation we assume an additional significant influence of nanoparticles deposited on the surface. A structuring speed in the range of 0.125 mm^2/s was obtained. The surface quality was characterized by field emission scanning electron microscopy and Raman spectroscopy. As a probably significant factor for the functionality, the chemical modifications of the metal structures were studied as well. The analysis of the vibration spectra indicates that the generation of LIPSS in air leads to thin oxidation layers which may improve the biocompatibility of the nanostructures. The better insight into the complex

H. Messaoudi · S. Kumar Das · R. Grunwald (✉)
Max Born Institute for Nonlinear Optics and Short-Pulse Spectroscopy,
Max-Born-Strasse 2a, D-12489 Berlin, Germany
e-mail: grunwald@mbi-berlin.de

H. Messaoudi · J. Lange · F. Heinrich · S. Schrader · M. Frohme
Engineering Department, University of Applied Sciences Wildau,
Bahnhofstrasse, 15745 Wildau, Germany

H. Messaoudi
Bremen Institute of Applied Beam Technology, Klagenfurter Strasse 2, Bremen, Germany

S. Kumar Das
School of Applied Sciences, KIIT University, Bhubaneswar 751024, Odisha, India

© Springer International Publishing Switzerland 2015

S. Sakabe et al. (eds.), *Progress in Nonlinear Nano-Optics*,
Nano-Optics and Nanophotonics, DOI 10.1007/978-3-319-12217-5_12

mechanisms of laser-induced nanostructure formation is expected to further stimulate neighboring fields of applications of functionalized surfaces like photocatalysis, photovoltaics or biomedicine.

12.1 Introduction

Surface enhanced Raman spectroscopy (SERS) exploits the coupling of optical transitions to vibrational modes for a highly efficient detection of molecules with the ability to even operate with single molecule sensitivity [2–7]. The efficiency enhancement is obtained by different specific mechanisms which are not fully understood because of their complexity. In particular, field enhancement effects appear at nanoscale features on metal surfaces, whereas an alternative path referred to as chemical enhancement is opened by a charge transfer (CT) between metal and molecule.

Apart of the high sensitivity, further advantages of the SERS technique are the label free performance, the capability for real-time application and the corrosion resistance. Moreover, typical substrate materials like Au or Ag (if Ag is coated with a thin oxygen layer) are of particular interest for the SERS of biological and medical objects because of their biocompatibility. This makes it an important tool in such fields, e.g. for the identification and classification of pathogenic microorganisms and bio-molecules [8–14] and enables a reliable indication of various diseases.

The SERS effect was demonstrated for metal substrates with many different types of substructures which are fabricated either by top-down or bottom-up methods. Substrates with metal island films, aggregated metal colloids, electrochemically roughened electrodes, or gold [15] and silver colloidal monolayers are rather complex and irregular. In general, it is difficult to perform reproducible SERS measurements with random, non-uniform or unstable substrates because of the high sensitivity of SERS against shape, size, depth and density of the nanoscale features. Therefore, a systematic study of the basic mechanisms is challenging and reliable specifications can hardly be derived for such kinds of structures.

To better meet the demanding standards of bio-medical applications, deterministic patterning strategies such as electron beam lithography, nano-imprint lithography, or soft lithography have been proposed as alternative approaches with sufficient spatial resolution, uniformity and reproducibility [16, 17]. Most of these technologies, however, are time consuming and expensive because of the need for complex multiple-step clean-room procedures with continuous high-precision chemical and thermal process control.

Here we report on a more simple, convenient and cost-effective top-down process for the fabrication of nanopatterns of relatively good uniformity and regularity which exploits the generation of laser-induced periodic surface structures (LIPSS) [18]. The basics of this nano-technology will be described in the following paragraph. Later on, experimental results concerning the generation of grating-like nanostructures in Ag and Cu by means of a mode-locked Ti:sapphire laser are

presented. The structuring was obtained at the fundamental as well as the second harmonic (SH) wavelengths at 800 and 400 nm, respectively. The capability of the formed LIPSS to serve as efficient substrates for the detection of biological matter with SERS is demonstrated for two selected standard molecules (herring sperm [19] and egg albumen protein [20]). The analysis of spectroscopic data reveals that the substrate surfaces undergo certain chemical modifications during the LIPSS generation in air by oxidation. Possible advantages of substrates covered by thin metal oxide layers because of an enhanced biocompatibility are addressed.

12.2 Laser-Induced Nanostructuring of Metal Substrates with Ultrashort Pulses

As it was previously reported in the literature, metal gratings with periods in the range of a few hundred nanometers can be used to realize an efficient SERS procedure [21–23]. The formation of LIPSS in metals is known from laser experiments, e.g. with noble metals [21, 23, 24, 27], steel [25, 26], Ni [25], Cu [27, 28] or Mo [29].

Although not all details of the LIPSS mechanism are fully understood there is a wide consensus that the formation of nanoripples is initiated by the generation and interference of surface plasmon-polaritons (SPPs) at the surface [27]. The efficiency of LIPSS depends on the material and the pulse duration of the laser. Highly intense femtosecond pulses enable to dynamically alter the optical constants of the material significantly and open new nonlinear excitation channels. A spatially periodical deposition of light energy [30] in the surface leads, on different time scales, to nonthermal ablation as well as self-organized rearrangement processes under contribution of accumulation effects like thermal load [31]. In noble metals, the femtosecond leaser heating of the material is followed by electron-phonon coupling which dominates over the hot electron diffusion [24, 27].

The application of intense, ultrashort-pulsed lasers, in particular femtosecond Ti: sapphire lasers, enables to work in a distinct non-thermal ablation regime which is difficult to realize at longer pulse durations where thermal diffusion and melting dominate. For the creation of highly uniform structured areas, however, a precise control of the laser parameters is necessary [29]. The excitation with ultrashort pulses induces transient carrier oscillations or surface plasmon-polaritons (SPPs) which interfere with the laser field thus forming periodical peaks of carrier density. In the high field of these peaks, a subsequent photo-induced avalanche ionization followed by a Coulomb explosion of the positive charged metal atoms. These steps are considered to be the basic mechanism of nanostructuring under these conditions [32, 33].

The initial phase plays a decisive role in this complex scenario. The coupling of photons to the conduction band starts randomly during the first few laser pulses and is supported by scatterers which favor all spatial frequencies as allowed by the k-vector selection rule. The directional selection is caused by the polarization of the field. The feedback by spatial and polarization selectivity leads to an evolution from random to more regular structures towards higher pulse numbers. Similar physical

mechanisms are also known for large-bandgap dielectric materials and semiconductors where a transient metallic state can be induced by a multiphoton absorption. One important difference between metals and dielectrics is the permanent availability of free carriers in the metal (but hindering the insertion of energy in the surface by high reflectivity) whereas the dielectrics reach the reflective metallic state only temporarily. Another point of relevance is the chemical stability of surfaces. In the case of dielectric metal oxides (TiO_2, ZnO) it is possible to start with a dielectric material and to end up with metallic regions after photoreduction. Nanostructuring of metals in air, on the other hand, can lead to an oxidation of the surfaces. So it turns out that such effects have to be carefully taken into consideration.

By a proper choice of the laser parameters (wavelength, polarization, duration and number of pulses and/or fluence) and material parameters (kind of metal, roughness of the surface), the shape, period and orientation of the LIPSS can be controlled with relatively high precision [34]. This makes the formation of LIPSS attractive as an alternative technology not only for the fabrication of SERS substrates but also for various other applications, e.g. for solar cells [35], light emitting diodes [36], optical memories [37] or hydrophobic surfaces [38]. Many of the previous SERS activities with LIPSS were performed with non-biological molecules, like Rhodamin 6G or benzenethiol. In contrast to other types of nanostructures (e.g. nanoparticles, nanowires), metal substrates with LIPSS [39, 40] exhibit a higher robustness and reach enhancement factors of 10^9 [41]. Furthermore, LIPSS can directly be written in integrated microsystems for SERS [42] or micro-fluidics [43].

12.3 Experimental Techniques

12.3.1 Femtosecond-Laser Preparation of Metallic Substrates for SERS

In the LIPSS experiments, an amplified, linearly polarized Ti:sapphire laser (Spitfire, Spectra Physics) with a FWHM pulse duration of 120 fs and a repetition frequency of 1 kHz was used to generate the LIPSS. Nanoripples were generated by a single-step scanning method with cylindrical focusing optics (cylinder lens) and moving substrate which enables for a high-speed and large-area processing. The technique is capable for the fabrication of coherently linked LIPSS with a higher degree of order compared to conventional scanning methods and was first applied to texturize extended areas of TiO_2 surfaces [44]. Limiting factors are the pulse energy (determining the maximum extension of the line focus) and the homogeneity of the intensity profile along the focus (determining the uniformity with respect to the LIPSS periods).

Apart of the fundamental wavelength at 800 nm, samples were also irradiated at the wavelength of second harmonic generation (SHG) at 400 nm provided by a beta-barium-borate (BBO) crystal. The metal substrates (Ag, Cu) were mounted on a computer controlled x-y-translation stage (MT 65, Newport, velocity range

0.001–2.5 mm/s) and moved in the focal plane of a cylindrical lens (focal length f = 100 mm), perpendicular to the focal line. The Ag substrates (Goodfellow Cambridge Ltd.) had a thickness of 0.5 mm and a purity of 99.95 % and were irradiated in normal incidence. The pulse energy was varied from 75 to 260 µJ at λ_{exc} = 800 nm and from 30 to 368 µJ at λ_{exc} = 400 nm, while the translation speed was stepwise changed (0.005, 0.05 and 0.5 mm/s). The LIPSS were characterized with a field-emission scanning electron microscope (FE-SEM, JEOL JSM-6400F). The spatial frequency spectra of the nanostructures were determined by two-dimensional Fast Fourier Transform (FFT) of the SEM images.

12.3.2 Surface Enhanced Raman Spectroscopy

The SERS studies to be reported here were performed with two types of biomedical standard samples on fs-laser generated metallic LIPSS substrates. The biological reference objects were DNA in herring sperm and protein in egg-albumen. The enhancement of the spectroscopic signal-to-noise ratio was evaluated by comparing the SERS intensities to Raman signals obtained with unprocessed Si and glass bulk substrates. The influence of the processing parameters on the SERS activity was studied as well. Both reference substances were obtained from a commercial source (Sigma-Aldrich Co. LLC). 22.8 mg *herring sperm DNA* were dissolved in a reaction vessel with 1.5 ml of distilled water. Then, 8 µl of this solution were pipetted onto the SERS substrates and dried in vacuum for about 5 min. In a similar manner, 51.2 mg *egg albumen* were dissolved in 500 µl of distilled water. Subsequently, the suspension was briefly stirred with a vortex mixer and set in an ultrasonic bath for another 5 min. Eventually, the solution was tipped on the surface of the substrates and dried for 5 min in vacuum.

For micro-SERS studies, a confocal Raman microscope (WITec alpha 300) was applied. A 488 nm diode-pumped solid-state laser served as the light source. The beam was coupled into the microscope via a single-mode optical fiber, providing a maximum power of about 35 mW at the surface area of interest. A ×10 magnifying objective delivered an optical signal averaging over a small, but sufficiently extended section of the structured surface to ensure the statistical significance. The spectral analysis was performed by a lens-based spectrograph of 300 mm focal length (WITec) equipped with a 3-stage Peltier cooled EMCCD detector (DU970N-BV, Andor Technology). The Raman signal from the focal plane was imaged onto the end-face of a multimode fiber of 100 µm diameter and transmitted to the spectrometer entrance. Thus, the confocal resolution of the microscope as well as the spectral resolution were determined by the fiber geometries in both parts of the setup. In order to access the complete Raman relevant spectral range, the 600 g/mm grating of the spectrometer was employed, resulting in a spectral resolution of approximately 7 cm^{-1}. The laser power was varied from 1 up to 5 mW and the acquisition time of the detection system was fixed to a value of 5 s.

12.4 Experimental Results

12.4.1 Femtosecond-Laser-Induced Periodic Nanostructures in Ag

In the LIPSS experiments, a strong dependence of the nanoripple generation on the scanning velocity was found. At the fastest scanning velocity of 0.5 mm/s, no distinct periodical nanostructures appeared. Therefore, it was not surprising to detect SERS signals from the irradiated regions which were comparable to the signals from unprocessed regions. A significant enhancement of the Raman peaks, however, was found for areas processed at velocities of 0.05 and 0.005 mm/s (i.e. 1 and 2 orders of magnitude slower substrate movement). For this reason, the further experiments were exclusively performed at these both velocities. Within the limits set by the laser parameters and focusing geometry in our arrangement, the line focus method enables to write LIPSS a few mm^2 even in a single scan so that the necessary conditions for a reliable spot-to-spot reproducible SERS detection can be realized.

The structuring capability will be demonstrated by the following result. At a wavelength of 400 nm (SHG) and pulse energies between 210 and 360 μJ, the central part of the LIPSS zone was found to have a lateral dimension of >2.5 mm. In a complete processing cycle, the substrates were linearly moved over a total distance of 500 μm at scanning velocity of 0.05 mm/s during a time interval of 10 s. Thus, the resulting nanostructured area was about 500 × 2500 μm^2 after each particular scanning procedure (i.e. on a scale of an assumed LIPSS period of 500 nm, this area would correspond to 5,000 × 1,000 periods).

It is important to notice that, beside the ripple-like nanostructures, the formation of distributed nanoparticles with characteristic diameters of some 10 nm was also observed at a scanning velocity of 0.005 mm/s and/or at the SHG wavelength of 400 nm. Characteristic parameters of the generated LIPSS and micrometer-size random structures in Ag in dependence on the processing parameters are summarized in Table 12.1.

Table 12.1 Overview on the characteristic parameters of the laser-induced nano- and microstructures on an Ag surface depending on the wavelength and scanning speed

Excitation wavelength (nm)	Scan velocity (mm/s)	Type of structures and feature size
800	0.05	LIPSS, 530(±25) nm
	0.005	Random microstructures, 1–3 μm
		LIPSS, 530(±25) nm
400	0.05	253(±15) nm
	0.005	Random microstructures, 1–3 μm
		LIPSS 253(±15) nm

(Amplified Ti:sapphire laser, pulse duration 120 fs, center wavelength 800 nm, repetition rate 1 kHz)

At a scanning velocity of 0.05 mm/s, low spatial frequency LIPSS dominate within pulse energy windows of 150–250 and 210–360 μJ at excitation wavelengths of 800 and 400 nm, respectively. SEM images of typical corresponding LIPSS at pulse energies of 180 μJ (fundamental wavelength at 800 nm) and 330 μJ (SHG at 400 nm) are shown in Fig. 12.1.

The two-dimensional (directional-selective) Fast Fourier Transform (FFT) plots in the insets of Fig. 12.1a, b contain information about the degree of periodicity of the structures. The analysis yields average values of LIPSS periods of p = 530 nm and p = 255 nm for fundamental and SHG, respectively. The orientation of the

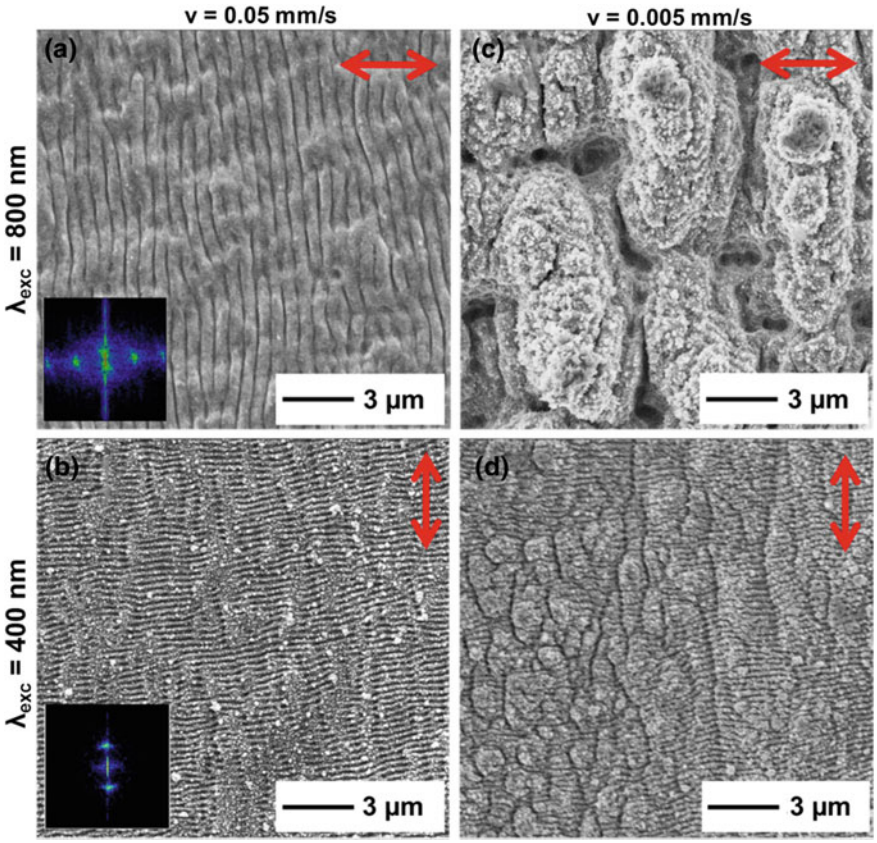

Fig. 12.1 Scanning electron microscope images of laser-induced periodic surface structures (*LIPSS*) on bulk Ag substrates [1]. The structures were obtained by moving substrates through a *line* focus of a Ti:sapphire laser at different excitation wavelengths and scan velocities according to a method described in [44]. The nanoripples in **a** and **b** have periods of 520 (±20) and 255 (±30) nm, respectively (*insets* FFT plots) and result from plasmon interference and nonthermal ablation in the maxima. The pictures in **c** and **d** show larger random structures on few-micrometer scale indicating an additional influence, or even the dominance of material transport processes, chemical changes and/or local explosive ablation processes

LIPSS was found to be perpendicular to the polarization vector of the input radiation at both fundamental or SHG wavelengths.

In similar experiments, LIPSS generation in Cu surfaces was studied [1]. A systematic report on the results will be published elsewhere.

12.4.2 SERS Measurements at Selected Biomolecules

The detected SERS signals from herring sperm DNA on Ag LIPSS at fundamental and SHG wavelengths are plotted in Fig. 12.2. The spectral distributions contain several distinct peaks. A number of characteristic bands between 600 and 1,800 cm^{-1} can be allocated according to [45]. The two distinct peaks at ~1,160 and 1,455 cm^{-1} can be attributed to deoxyribose-phosphate and the peaks at 1,232, 1,369 and 1,509 cm^{-1} are believed to belong to adenine, while the band around 800 cm^{-1} can likely be assigned to stretching vibrations in the main chain of an A-Type DNA. The band at 1,014 cm^{-1}—observed only with the 400 nm LIPSS—can be related to C–O stretching vibrations. Moreover, there is a strong evidence for a cytosine band at 623 cm^{-1} and another deformation mode band of NH_2-group in the adenine-guanine-cytosine molecules at 1,600 cm^{-1}. The bands indicated at 2,900 and 2,945 cm^{-1} can be attributed to some C–H stretching vibrations in the CH_2-groups [4].

If one compares the SERS spectra of detected for egg albumen on the Ag substrate with the SERS signals from unstructured Si and glass surfaces one recognizes that the Ag-substrate with LIPSS enables to reliably detect the protein bands (Fig. 12.3). Distinct spectral peaks were found at 524, 675, 984, 1,355, 1,425 and 1,614 cm^{-1}. According to the paper of Ngarize et al. [20], the band at 524 cm^{-1} corresponds to a disulphide bond of ovalbumen, which accounts already up to a

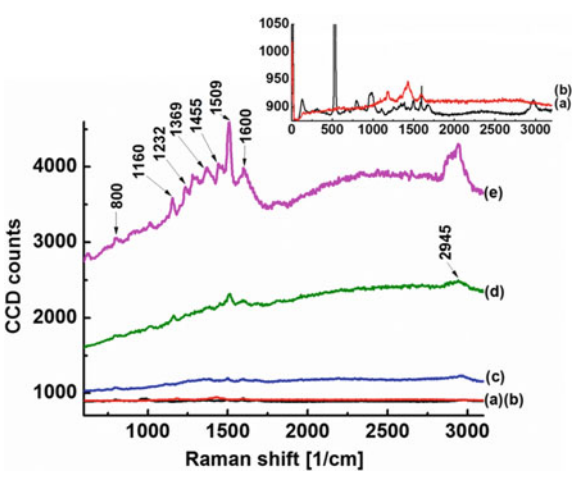

Fig. 12.2 SERS signals from *herring sperm* on Ag substrate in comparison to unstructured standard substrates [1]: *a* unstructured Si, *b* unstructured glass, *c* unstructured Ag, *d* Ag with LIPSS (average period 530 nm), *e* Ag with LIPSS (average period 255 nm)

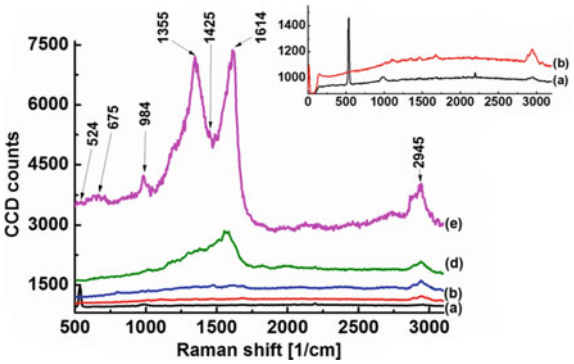

Fig. 12.3 Detected SERS signals from *egg albumen* on Ag substrate in comparison to unstructured standard substrates [1]: *a* unstructured Si, *b* unstructured glass, *c* unstructured Ag, *d* Ag with LIPSS (period 530 nm). *e* Ag with LIPSS (period 255 nm)

share of 54 % of the egg white. The peaks at 1,355 and 1,613 cm^{-1} are believed to be related to the helical structure and to the Amide1 band in egg albumen [21]. For structures generated at the lowest scan velocity of v = 0.005 mm/s, the SERS signals were found to be strongly dependent on the position on the surface. Relevant SERS signals were only detectable when the probe beam was directly focused into the area containing LIPSS.

The characteristic SERS spectra appear to be almost similar from all LIPSS regions independently on the generation wavelength (400 or 800 nm), i.e. the periods are not a critical issue for the molecular excitation paths in the range of chosen parameters. The enhancement of the SERS signals, however, was by a factor >2 higher within LIPSS regions structured at 400 nm compared to the substrates structured at 800 nm. This observation confirms the results of Kahl et al. [22] who demonstrated that a systematical step-down variation of the period of Ag-coated Si gratings between 800 and 400 nm enables a scaling of the SERS enhancement factor up to a factor of 2.

It should be emphasized that the determination of the exact enhancement factors for SERS on biomedical samples is nontrivial because of their strong dependence on the homogeneity of both the samples and the substrates. On the basis of a number of 10 spots per sample, well detectable Raman signals of DNA and protein were obtained with LIPSS on Ag substrates in >70 % of the cases. On the contrary, Raman signals on Si and glass substrates taken under identical conditions were found to be either undetectable or very weak as it can clearly be recognized in the insets of Figs. 12.2 and 12.3. These results agree with the findings of the group of Chang et al. for Rhodamine 6G [21]. Compared to the unstructured Ag, our experiments show an enhancement factor of up to 20 as the result of the femtosecond laser structuring. The maximum enhancement factor for DNA and protein with respect to Si and glass reference substrates was found to be about 200 (Fig. 12.4).

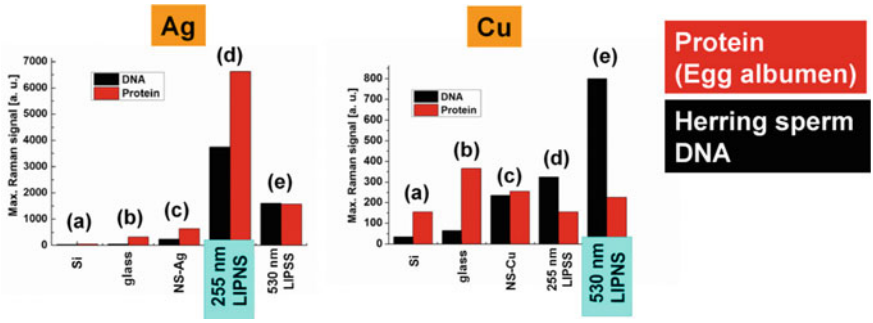

Fig. 12.4 Comparison of the results of SERS experiments with egg albumin and herring sperm for Ag (*left*) and Cu (*right*) substrates for the cases of unstructured and structured surfaces [1]: *a* unstructured Si, *b* unstructured glass, *c* unstructured metal, *d* metal with LIPSS (period 255 nm), *e* metal with LIPSS (period 530 nm)

12.5 Conclusions and Outlook

To conclude, the formation of nanoscale laser-induced periodic surface structures (LIPSS) on metals (in particular Ag and Cu) and their application as SERS substrates in biomedicine was demonstrated. Extended areas were structured in scanning mode by translating the substrates through a line focus of an amplified femtosecond Ti:sapphire laser. The treatment was performed at the fundamental wavelength of 800 nm and at the SHG wavelength of 400 nm. The line scan technique makes the fabrication simple, cost-effective and significantly faster compared to conventional scanning systems with circular focal spots and meandering movement. To optimize the processing conditions, the plasmon-based mechanisms of nanostructure formation in bulk metal samples were studied in detail. Moreover, the chemical modification of the surfaces was found to be a significant part of the chain of coupled partial processes. It was shown that LIPSS on Ag substrates can be obtained in areas larger than 1.25 mm^2 within a processing time of only 10 s. The capability of the LIPSS substrates for the sensitive detection of bio-molecules with surface enhanced Raman spectroscopy (SERS) was verified by proof-of-principle experiments with *egg albumen protein* and *herring sperm DNA*. In case of Ag substrates, the SERS signals for a grating period of 255 nm exceed the signals for a period of 530 nm by a factor >2. An inverse behavior was found for the Cu substrates which is not fully understood up to now. A possible explanation is the appearance of nanoparticles from ablated metal collecting in the grooves of the LIPSS, thus additionally enhancing the signals. The effect has to be studied in more detail.

The SERS results were compared to Raman measurements with reference Si and glass substrates under identical conditions. For both reference surfaces, the SERS signals were very weak. in comparison to smooth Ag surfaces, the SERS signals from structured surfaces with LIPSS were found to be enhanced by factors up to 200.

Future activities have to include a post-processing of the metal surfaces, the combination of nanoripple generation with the insertion of smaller nanoparticles and time dependent studies of charge transfer processes on few-femtosecond scale at nanostructured surfaces. As a cheap and easy way to realize metallic nanostructures for SERS might be to first generate LIPSS in dielectric materials and to finally cover these templates with thin metallic layers. A similar approach has been demonstrated in the literature with silver capped polystyrene nanotube arrays [46]. A further advantage of such a transfer of nanostructures is the free choice of the kind of metal to be deposited independently on particular LIPSS mechanisms.

Acknowledgments The authors wish to thank T. Elsaesser (MBI, Berlin) and W. Seeber (Otto Schott Institute, Jena). The work was financially supported by DFG (project GR 1782/12-2). Figures are presented with permission of the SPIE—international society for optics and photonics.

References

1. H. Messaoudi, S.K. Das, J. Lange, F.Heinrich, S. Schrader, M. Frohme, R. Grunwald, Femtosecond-laser induced nanostructuring for surface enhanced Raman spectroscopy. Proc. SPIE **8972**, 8972-17 (2014)
2. M.J. Natan, Surface enhanced Raman scattering. Faraday Discuss. **132**, 321–328 (2006)
3. A. Barhoumi, D. Zhang, F. Tam, N.J. Halas, Surface-enhanced Raman spectroscopy of DNA. J. Am. Chem. Soc. **130**, 5523–5529 (2008)
4. C.E. Taylor, S.D. Garvey, J.E. Pemberton, Carbon contamination at silver surfaces: surface preparation procedures evaluated by Raman spectroscopy and X-ray photoelectron spectroscopy. Anal. Chem. **68**, 2401–2408 (1996)
5. S. Pahlow, A. März, B. Seise, K. Hartmann, I. Freitag, E. Kämmer, R. Böhme, V. Deckert, K. Weber, D. Cialla, J. Popp, Bioanalytical application of surface- and tip-enhanced Raman spectroscopy. Eng. Life Sci. **12**, 131–143 (2012)
6. B. Küstner, M. Gellner, M. Schutz, F. Schoppler, A. Marx, P. Ströbel, P. Adam, C. Schmuck, S. Schlücker, SERS labels for red laser excitation: silica-encapsulated SAMS on tunable gold/silver nanoshells. Angew. Chem. Int. Ed. **48**, 1950–1953 (2009)
7. M. Culha, B. Cullum, N. Lavrik, C.K. Klutse, Surface-enhanced Raman scattering as an emerging characterization and detection technique. J. Nanotechnol. **2012**, 971380 (2012)
8. J.D. Driskell, Y. Zhu, C.D. Kirkwood, Y. Zhao, Y. Dluhy, R.A. Tripp, Rapid and sensitive detection of rotavirus molecular signatures using surface enhanced Raman spectroscopy. PLoS ONE **5**, e10222 (2010)
9. S.Y. Feng, J.Q. Lin, M. Cheng, Y.Z. Li, G.N. Chen, Z.F. Huang, Y. Yu, R. Chen, H.S. Zeng, Gold nanoparticle based surface-enhanced Raman scattering spectroscopy of cancerous and normal nasopharyngeal tissues under near-infrared laser excitation. Appl. Spectrosc. **63**, 1089–1094 (2009)
10. Y. He, S. Su, T. Xu, Y. Zhong, A. Zapien, J. Li, C. Fan, S.-T. Lee, Silicon nanowires-based highly-efficient SERS-active platform for ultrasensitive DNA detection. Nano Today **6**, 122–130 (2011)
11. S.L. Hennigan, J.D. Driskell, R.A. Dluhy, Y. Zhao, R.A. Tripp, K.B. Waites, D.C. Krause, Detection of mycoplasma pneumoniae in simulated and true clinical throat swab specimens by nanorod array-surface-enhanced Raman spectroscopy. PLoS ONE **5**, e13633 (2010)
12. P. Chen, A.G. Shen, W. Zhao, S.J. Baek, H. Yuan, J.M. Hu, Raman signature from brain hippocampus could aid Alzheimer's disease diagnosis. Appl. Opt. **48**, 4743 (2009)

13. J. Shen, L. Fan, J. Yang, A.G. Shen, J.M. Hu, A longitudinal Raman microspectroscopic study of osteoporosis induced by spinal cord injury. Osteoporos. Int. **21**, 81–87 (2010)
14. C. David, N. Guillot, H. Shen, T. Toury, M.L. de la Chapelle, SERS detection of biomolecules using lithographed nanoparticles towards a reproducible SERS biosensor. Nanotechnology **21**, 475501–475506 (2010)
15. Ö.F. Karatas, E. Sezgin, Ö. Aydin, M. Culha, Interaction of gold nanoparticles with mitochondria. Colloids Surf. B **71**, 315–318 (2009)
16. W. Zheng, H.C. Chiamori, G.L. Liu, L. Lin, F.F. Chen, Nanofabricated plasmonic nano-bio hybrid structures in biomedical detection. Nanotechnol. Rev. **1**, 213–233 (2012)
17. W. Xie, C. Mao, Bio-imaging, detection and analysis by using nanostructures as SERS substrates. J. Mater. Chem. **21**, 5190–5202 (2011)
18. J. Bonse, A. Rosenfeld, J. Krüger, On the role of surface plasmon polaritons in the formation of laser-induced periodic surface structures upon irradiation of silicon by femtosecond-laser pulses. J. Appl. Phys. **106**, 104910 (2009)
19. W. Ke, D. Yu, J. Wu, Raman spectroscopic study of the influence on herring sperm DNA of heat treatment and ultraviolet radiation. Spectrochim. Acta Part A **55**, 1081–1090 (1999)
20. S. Ngarize, A. Adams, N.K. Howell, Studies on egg albumen and whey protein interactions by FT-Raman spectroscopy and rheology. Food Hydrocolloids **18**, 49–59 (2004)
21. H.W. Chang, Y.C. Tsai, C.W. Cheng, C.Y. Lin, Y.W. Lin, T.M. Wu, Nanostructured Ag surface fabricated by femtosecond laser for surface-enhanced Raman scattering. J. Colloid Interface Sci. **360**, 305–308 (2011)
22. M. Kahl, E. Voges, S. Kostrewa, C. Viets, W. Hill, Periodically structured metallic substrates for SERS. Sens. Actuators B **51**, 285–291 (1998)
23. Y. Dai, M. He, B. Lu, X. Yan, G. Ma, Surface-enhanced Raman scattering in femtosecond laser-nanostructured Ag substrate. J. Phys.: Conf. Ser. **276**, 012015 (2011)
24. J. Wang, C. Guo, Numerical study of ultrafast dynamics of femtosecond laser-induced periodic surface structure formation on noble metals. J. Appl. Phys. **102**, 053522 (2007)
25. J.-W. Yao, C.-Y. Zhang, H.-Y. Liu, Q.-F. Dai, L.-J. Wu, S. Lan, A.V. Gopal, V.A. Trofimov, T.M. Lysak, High spatial frequency periodic structures induced on metal surface by femtosecond laser pulses. Opt. Express **20**, 905–911 (2012)
26. Y. Huo, T. Jia, D. Feng, S. Zhang, J. Liu, J. Pan, K. Zhou, Z. Sun, Formation of high spatial frequency ripples in stainless steel irradiated by femtosecond laser pulses in water. Laser Phys. **23**, 056101 (2013)
27. J. Wang, C. Guo, Formation of extraordinarily uniform periodic structures on metals induced by femtosecond laser pulses. J. Appl. Phys. **100**, 023511 (2006)
28. M. Hashida, Y. Miyasaka, Y. Ikuta, S. Tokita, S. Sakabe, Crystal structures on a copper thin film with a surface of periodic self-organized nanostructures induced by femtosecond laser pulses. Phys. Rev. B **83**, 235413 (2011)
29. D. Scorticati, G.-W. Römer, D.F. de Lange, B. Huis in't Veld, Ultra-short-pulsed laser-machined nanogratings of laser-induced periodic surface structures on thin molybdenum layers. J. Nanophotonics **6**, 063528 (2012)
30. J.E. Sipe, J.F. Young, J.S. Preston, H.M. van Driel, Laser induced periodic surface structure. I. Theory. Phys. Rev. B **27**, 1141 (1983)
31. J. Reif, O. Varlamova, M. Ratzke, M. Schade, H.S. Leipner, T. Arguirov, Multipulse feedback in self- organized ripples formation upon femtosecond laser ablation from silicon. Appl. Phys. A **101**, 361–365 (2010)
32. A.Y. Vorobyev, C. Guo, Effects of nanostructure-covered femtosecond laser induced periodic surface structures on optical absorptance of metals. Appl. Phys. A **86**, 321–324 (2007)
33. M. Shen, J.E. Carey, C.H. Crouch, M. Kandyla, H.A. Stone, E. Mazur, High-density regular arrays of nanometer-scale rods formed on silicon surfaces via femtosecond laser irradiation in water. Nano Letters **8**, 2087–2091 (2008)
34. R. Taylor, C. Hnatovsky, E. Simova, Applications of femtosecond laser induced self-organized planar nanocracks inside fused silica glass. Laser Photonics Rev. **2**, 26–46 (2008)

35. R. Torres, T.E. Itina, V. Vervisch, M. Halbwax, T. Derrien, T. Sarnet, M. Sentis, J. Ferreira, F. Torregrosa, L. Roux, Study on laser induced periodic structures and photovoltaic application. AIP Conf. Proc. **1278**, 576–581 (2010)
36. J.T. Chen, W.C. Lai, Y.J. Kao, Y.Y. Yang, J.K. Sheu, Laser-induced periodic structures for light extraction efficiency enhancement of GaN-based light emitting diodes. Opt. Express **20**, 5689–5695 (2012)
37. Y. Shimotsuma, M. Sakakura, K. Miura, J.R Qiu, P. G. Kazansky, K. Fujita, K. Hirao, Application of femtosecond-laser induced nanostructures in optical menory. J. Nanosci. Nanotech. **71**, 94104, 2078–0338 (2007)
38. T. Baldacchini, J.E. Carey, M. Zhou, E. Mazur, Superhydrophobic surfaces prepared by microstructuring of silicon using a femtosecond laser. Langmuir **22**, 4917–4919 (2006)
39. E.D. Diebold, N.H. Mack, S.K. Doorn, E. Mazur, Femtosecond laser-nanostructured substrates for surface-enhanced Raman scattering. Langmuir **25**, 1790–1794 (2009)
40. R. Buividas, P.R. Stoddart, S. Juodkazis, Laser fabricated ripple substrates for surface-enhanced Raman scattering. Ann. Phys. **524**, L5–L10 (2012)
41. C.H. Lin, L. Jiang, Y.H. Chai, H. Xiao, S.J. Chen, H.L. Tsai, One-step fabrication of nanostructures by femtosecond laser for surface-enhanced Raman scattering. Opt. Express **17**, 21581–21589 (2009)
42. C.H. Lin, L. Jiang, H. Xiao, S.J. Chen, H.L. Tsai, Surface-enhanced Raman scattering microchip fabricated by femtosecond laser. Opt. Lett. **35**, 2937–2939 (2010)
43. G.L. Liu, L.P. Lee, Nanowell surface enhanced Raman scattering arrays fabricated by soft-lithography for label-free biomolecular detections in integrated microfluidics. Appl. Phys. Lett. **87**, 074101 (2005)
44. S.K. Das, K. Dasari, A. Rosenfeld, R. Grunwald, Extended-area nanostructuring of TiO_2 with femtosecond laser pulses at 400 nm using a line focus. Nanotechnology **21**, 155302 (2010)
45. W. Ke, D. Yu, J. Wu, Raman spectroscopic study of the influence on herring sperm DNA of heat tratment and ultraviolet radiation. Spectrochim. Acta Part A **55**, 1081–1090 (1999)
46. P. Lovera, N. Creedon, H. Alatawi, M. Mitchell, M. Burke, A.J. Quinn, A. O'Riordan, Low-cost silver capped polystyrene nanotube arrays as super-hydrophobic substrates for SERS applications. Nanotechnology **25**, 175502 (2014)

Part VI
Advanced Theoretical Studies: Linear Simulations

Chapter 13
Design Principles for Plasmonic Nanoparticle Devices

Phillip Manley, Sven Burger, Frank Schmidt and Martina Schmid

Abstract For all applications of plasmonics to technology it is required to tailor the resonance to the optical system in question. This chapter gives an understanding of the design considerations for nanoparticles needed to tune the resonance. First the basic concepts of plasmonics are reviewed with a focus on the physics of nanoparticles. An introduction to the finite element method is given with emphasis on the suitability of the method to nanoplasmonic device simulation. The effects of nanoparticle shape on the spectral position and lineshape of the plasmonic resonance are discussed including retardation and surface curvature effects. The most technologically important plasmonic materials are assessed for device applicability and the importance of substrates in light scattering is explained. Finally the application of plasmonic nanoparticles to photovoltaic devices is discussed.

13.1 Plasmonic Principles

The most interesting properties of metal nanoparticles can be observed in the example of the Lycurgus cup. This is a piece of late antique art currently held by the British Museum. The cup is made of metal artwork interconnected with glass, as shown in Fig. 13.1. This special glass, when illuminated from the outside i.e. viewed in reflection, has a jade coloring, however when illuminated from inside, i.e. in transmission, the glass has a crimson color. This most curious effect is due to the glass containing an extremely dilute distribution of metal nanoparticles, roughly 300 parts per million [36]. On the basis of this fact alone, what properties of metal

P. Manley (✉) · M. Schmid
Helmholtz Zentrum Berlin für Materialien und Energie GmbH, Hahn-Meitner-Platz 1, 14109 Berlin, Germany

P. Manley · S. Burger · F. Schmidt
Zuse Institute Berlin, Takustrasse 7, 14195 Berlin, Germany

M. Schmid
Freie Universität Berlin, Arnimallee 14, 14195 Berlin, Germany

© Springer International Publishing Switzerland 2015

S. Sakabe et al. (eds.), *Progress in Nonlinear Nano-Optics*,
Nano-Optics and Nanophotonics, DOI 10.1007/978-3-319-12217-5_13

Fig. 13.1 The Lycurgus cup has colloidal metal nanoparticles suspended in glass. Due to plasmonic effects the glass appears *green* when viewed in reflection and *red* in transmission. © Trustees of the British Museum

nanoparticles can we infer? The particles must have a strong response when illuminated with light, otherwise such a dilute distribution of particles would not have such a visible effect. Additionally the effect must be wavelength dependent to generate different colors in reflection and transmission. The rest of this section will introduce plasmonics with the aim in mind of explaining the processes occurring when light shines on the Lycurgus cup.

13.1.1 Bulk Plasmons

A plasma is a kind of fluid consisting of positively and negatively charged particles. A plasmon is a collective oscillation of the charge density of a plasma. The free electrons and ion cores in a metal constitute a plasma with a net neutral charge. Local deviations in electron density will cause restoring forces from the fixed ionic cores leading to simple harmonic motion. The frequency of these oscillations can be easily derived [14] and is given by the bulk plasma frequency,

$$\omega_{BP} = \sqrt{\frac{ne^2}{m\epsilon_0}}. \tag{13.1}$$

Where n is the free electron density in the solid, e is the electronic charge, m is the effective mass of the free electrons and ϵ_0 is the permittivity of free space. The electromagnetic field distribution corresponding to a plasmonic excitation corresponds to a solution of the linear Maxwell's equations. The equations allow for both longitudinal and transverse solutions. The longitudinal solutions are associated with charge density oscillations. The transverse solutions are associated with the propagation of radiation in the medium. In the absence of an external magnetic field the two solutions are not coupled together meaning that light cannot excite charge density oscillations. Figure 13.2b shows a sketch of the electronic density oscillations. In the upper part of Fig. 13.2a, ω_{BP} is marked by a grey horizontal line, this

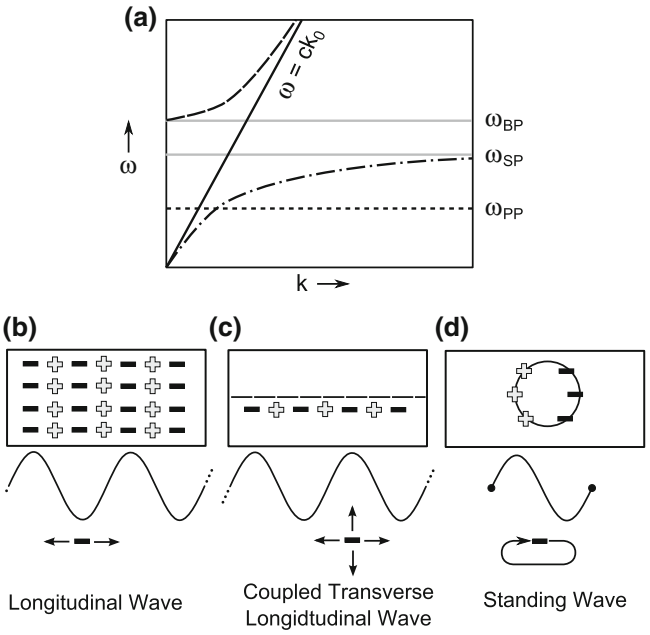

Fig. 13.2 **a** The dispersion for light in vacuum (*solid line*), light in a bulk metal (*dashed line*), surface plasmon polariton at a metal vacuum interface (*dashed dotted line*) and particle plasmon (*dotted line*). The three kinds of plasmonic resonance: **b** the bulk plasmon resonance occurs at ω_{BP} and is a longitudinal wave. **c** The surface plasmon polariton is a coupled transverse longitudinal wave bound to a metal/dielectric interface. **d** The particle plasmon which is a transverse standing wave

is merely a guide to the eye and does not represent a dispersion curve. The bulk plasma frequency for most metals is higher than the frequency of visible light. When light is incident at frequencies lower than the plasma frequency, the incident light causes the electrons to move in such a way that they emit an electric field which cancels out the incident wave and creates a reflected wave. Above ω_{BP} the electrons cannot keep up with light oscillations and light will be transmitted through the sample. In the upper part of Fig. 13.2a there are two lines, the solid black line shows the dispersion of light in vacuum where $\omega = ck_0$, the dashed line shows the dispersion of the propagation of light inside the metal which is given by [14],

$$\omega^2 = \omega_{BP}^2 + c^2k^2, \tag{13.2}$$

where c is the speed of light in vacuum. For $ck \gg \omega_p$ this converges to the free space solution. Due to light not being coupled to this kind of plasmon, it is not of technological importance for photonic devices.

13.1.2 Surface Plasmon Polaritons

There is a second kind of electron density wave which will have coupled transverse and longitudinal components along the surface of a metal. This is schematically shown in Fig. 13.2c [3, 38]. This happens at a lower frequency than ω_{BP}, the upper limit is shown in Fig. 13.2a as grey horizontal line at ω_{SP}. Since this type of wave has coupled longitudinal and transverse parts we call it a surface plasmon polariton (SPP). The dispersion relation for a SPP can be derived using Maxwell's equations [18] and is given by,

$$k = \frac{\omega}{c}\sqrt{\frac{\epsilon_m \epsilon_d}{\epsilon_m + \epsilon_d}}, \tag{13.3}$$

where ϵ_m and ϵ_d are the permittivities of the metal and dielectric either side of the surface. In the limit of large k and assuming the dielectric is vacuum and a lossless Drude model for the metallic permittivity we obtain,

$$\omega_{SP} = \frac{\omega_{BP}}{\sqrt{2}}. \tag{13.4}$$

The well known difficulty in exciting a SPP is that there is a momentum mismatch between light and surface plasmons in the same medium which means they will not be excited by light under normal circumstances. This is demonstrated in Fig. 13.2a, again we note that the solid line shows the dispersion of light in a vacuum, whilst the dash dotted line gives the dispersion of a SPP at a vacuum metal interface. The SPP dispersion is close to the light line in vacuum dispersion for long wavelengths. We say that the SPP is lightlike and in this regime the transverse components will dominate. For shorter wavelengths the SPP dispersion deviates significantly from the light dispersion. Here the longitudinal modes dominate and the SPP is named plasmon like [38]. As we can see the SPP line has a higher momentum (larger k) than the light line for all frequencies. Thus we cannot conserve momentum and energy to convert light into a surface plasmon polariton. This can be circumvented by the use of a prism to increase the light momentum and evanescently couple to the surface [15, 26], or by creating a periodic structure in the metallic surface which gives momentum to the light [29].

13.1.3 Particle Plasmons

The third kind of plasma oscillation shown in Fig. 13.2d is the particle plasmon also called the localised surface plasmon resonance. This is a standing wave of the electron density inside the particle, with surface charge acting as the restoring force. Due to the restoring force being the surface charge and not simply the entire fixed

ion lattice as with the bulk plasmon, the particle plasmon is a transverse standing wave and can therefore be excited by incident light. There are no momentum matching conditions as with the surface plasmon polariton because particle plasmons are standing waves with a net momentum of zero. We might think that the light now has too much momentum, however when the light is absorbed by a conduction band electron and momentum is transferred to the electron, it can be easily dissipated by phonons. In other words the radiation pressure of the incoming light does not push all the electrons out of the nanoparticle because they are held inside the particle by the much stronger force of the lattice. The particle plasmon resonance frequency depends on the polarization (α) in the particle, which for a sphere is given by [35],

$$\alpha = 4\pi\epsilon_0 r^3 \left(\frac{\epsilon_m - \epsilon_d}{\epsilon_m + 2\epsilon_d} \right). \tag{13.5}$$

where r is the sphere radius and ϵ_m and ϵ_d are the permittivities of the metal and dielectric respectively. When the denominator of this equation is equal to zero there will be a resonance. If we assume a simple Drude form for the metallic permittivity and that the surrounding dielectric is vacuum, then we reach the result,

$$\omega_{PP} = \frac{\omega_{BP}}{\sqrt{3}}, \tag{13.6}$$

which has been used to sketch out the position of ω_{PP} in Fig. 13.2a. In this case the dotted horizontal line shows the dispersion for a particle plasmon, this line will always be crossed by the light line (solid line) at a particular frequency k, this means there is no momentum matching condition for particle plasmons.

It is important to know when these results can be applied and for that we need to have a firm concept of what is meant by particle. Particles are objects in which all of the dimensions are small compared to the wavelength of light. For particles of sizes the same order as the wavelength, the previous results can still be applied, however we need to take into account effects like retardation which will be covered in Sect. 13.3. An object with dimensions much larger than the wavelength is for our purposes a bulk object. We should shortly mention that we only consider particles larger than 10 nm in diameter, this is because for particles smaller than this strong quantum effects come into play and classical descriptions for the material dependent parameters in Maxwell's equations are no longer valid.

When the particle is small compared to the wavelength the phase of the electric field will not change considerably over the nanoparticle. This means that all the free electrons in the particle feel the same driving force, causing them to act coherently. This coherence is what causes the large optical response. The approximation which can be made to consider such a small particle is that the electric field is (spatially) constant over the whole nanoparticle. This is often called the dipole approximation as only dipolar modes will be supported by the particle if the electric field is truly constant.

It will simplify our discussion later to consider the particle plasmon system as a damped driven harmonic oscillator. The driving force (F_0) is the incident electric field, the restoring force is the surface polarization charge, which we can imagine as a spring of constant k pulling the electrons back to equilibrium. The damping term γ is equivalent to the three possible decay channels of the plasmon. Firstly it can decay radiatively, emitting a photon of the same frequency as the incoming light. Secondly it can decay due to processes inside the particle, such as phonon scattering, surface scattering or defect scattering. Thirdly, if the particle is surrounded by an absorbing medium, the plasmon can directly excite an electron hole pair in the medium. The equation of motion and its solution are given by [9],

$$\frac{d^2x(t)}{dt^2} = -\omega_0^2 x(\omega) - 2\gamma\frac{dx(t)}{dt} + \frac{F_0}{m}e^{i\omega t}, \tag{13.7}$$

$$x(\omega) = \frac{F_0}{2m\omega_0}\frac{1}{\sqrt{(\omega_0-\omega)^2+(\gamma)^2}}, \tag{13.8}$$

$$\omega_0 = \sqrt{\frac{k}{m}}. \tag{13.9}$$

In going from (13.7) to (13.8) we have assumed $\omega_0 \gg \gamma$. The term ω_0 is the natural resonance frequency which according to (13.5) will be the frequency at which $\epsilon_m = -2\epsilon_d$. However for our toy model we can consider ω_0 to be determined by the spring constant k of the restoring force in (13.9). There will be a peak in x when the denominator of (13.8) becomes small, i.e. when $\omega = \omega_0$, and the height of this peak will be determined by the value of ω_0 and γ. Since $\omega_0 \propto \sqrt{k}$ a weaker restoring force leads to a lower frequency of oscillation (redshift).

Now it is clear why the optical response of metallic nanoparticles is spectrally responsive. The resonance frequency of the metallic alloy in the Lycurgus cup was at the blue end of the spectrum. This means that when the nanoparticles were irradiated with white light, the blue light was scattered more strongly. This causes a blue dominated reflection (perceived as green by the human eye) because the only light we see is the backscattered light. It also causes the red dominated transmission because although the scattered in all directions, the ratio of red to blue light becomes red dominated in the forward direction.

13.1.4 Far Field Effects

In the example of the Lycurgus cup we discussed the effects of metal nanoparticles as viewed from a large distance (compared to the wavelength). These are called far field effects and can be utilized in many optoelectronic devices such as the increase of photocurrent in photodetectors [33], improved outcoupling in silicon LEDs [16], anti-reflection coatings [21] and increased absorption of light in photovoltaics [2, 7].

All these applications rely on the unique light scattering properties of nanoparticles, therefore we now discuss the quantitative measures we can use to evaluate this light scattering. The most fundamental optical measurement of interest is to shine light at the particles and measure how much is transmitted. This results in the measurement of the spectrum of the extinction cross section C_{ext}. The light can be hindered from reaching its original destination via two different processes, it can either be absorbed in the particle or scattered by the particle into a different angle. To understand these two processes quantitatively, the total scattered (C_{sca}) or absorbed (C_{abs}) flux can be calculated using e.g. the finite element method (FEM). For some special cases, such as a single sphere, these can also be calculated with the analytical Mie theory [20] and a comparison in Fig. 13.3 shows that the two methods are in complete agreement for this case. The quantity plotted is the *normalized* extinction cross section (Q_{ext}), sometimes called extinction efficiency although the evocation of the word efficiency is in this case somewhat misleading as Q_{ext} can be greater than one.

The reason we normalize C is that it is important to evaluate the relative scattering strength of differently sized particles fairly. The normalization is given by [5],

$$Q = \frac{C_{Rad}}{C_{Geom}}, C_{Rad} = \frac{\Phi}{\Phi_{Inc}}, C_{Geom} = \frac{A_{Nanop.}}{A_{Comp.Dom.}} \tag{13.10}$$

Q is essentially the ratio of two terms: first the fraction of energy scattered or absorbed, which is given by the total flux scattered or absorbed Φ divided by the total flux incident to the computational domain Φ_{Inc}; this is the cross section we have already discussed, here referred to for clarity as C_{Rad}. The second term is the fraction of light which would be scattered in the ray optics regime and is given by the cross sectional area of the nanoparticle $A_{Nanop.}$ divided by the cross sectional area of the

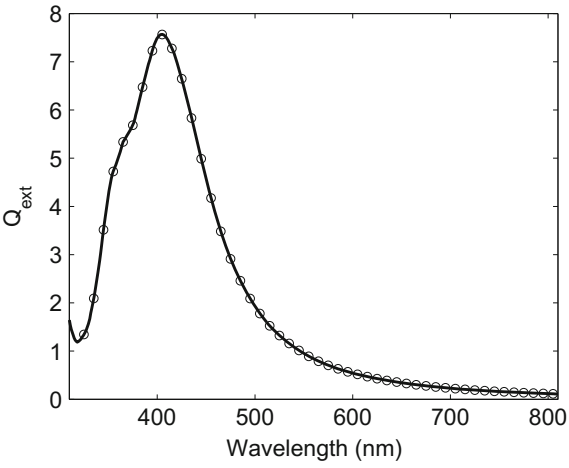

Fig. 13.3 The extinction cross section for a radius 50 nm Ag nanoparticle in vacuum. (*Circles*) are FEM simulation, (*solid line*) is Mie theory simulation

computational domain $A_{Comp.Dom.}$. Concerning far field effects, in addition to the total scattering cross section we can also look at the angular distribution formed which can be crucial for certain devices designs, this topic will be explored further in Sect. 13.4.

13.1.5 Near Field Effects

The other way in which nanoparticles can be used in devices is to harness the strong near fields generated by the plasmon before it decays. There is an algebraicly decreasing electric field extending out from the surface of the nanoparticle. The peak value of this electric field can be extremely high which opens the door to different device capabilities. The possible device applications for this strong localized electric field are numerous, therefore the following list is not exhaustive. Increasing the signal of surface enhanced Raman spectroscopy is possibly the most well known application, as the signal depends on the fourth power of the electric field, enhancement factors of 10^{15} have been reported [24, 25] for molecules in the vicinity of specially designed metal nanoparticles. Other applications include optical waveguides of sizes below the diffraction limit [19, 28], increased absorption in organic solar cells [13, 23], biosensing [1], delivery of dyes for medical applications [10] and separation of chiral molecules [30].

The strength of the electric field in the vicinity of the particle can also be calculated via the FEM and examples are shown in Figs. 13.4 and 13.10. In all the figures the field enhancement can be seen to decay away from the nanoparticle surface. Figure 13.4 shows the near field distribution of a large Ag nanoparticle with radius 150 nm at four different wavelengths of incident light. For incident light of 2,000 nm the dipole approximation is valid and the near field shows a dipole pattern around the center of the nanoparticle. For the shorter wavelength of 850 nm which is approximately where the far field dipole resonance is, we still see dipole dominated radiation. However due to the electric field of the incident light not being constant over the nanoparticle volume, there is some mixing of the dipole and higher order modes. This causes the dipole mode to shift away from the center of the nanoparticle, causing the asymmetrical resonance. At 525 nm the transition to quadrupole dominated resonance has completed with two more resonance lobes forming on the left side of the nanoparticle. For yet shorter wavelengths the quadrupole transitions into the octupole resonance. A more detailed description of effects that different particle shapes can have on the near field resonance will be given in Sect. 13.3.

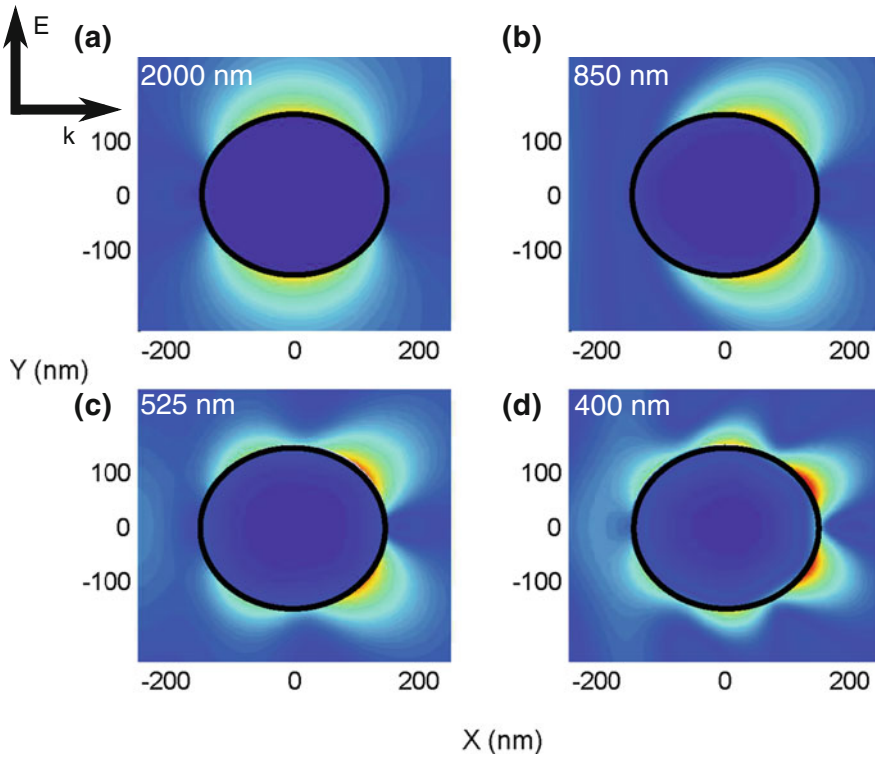

Fig. 13.4 The electric field intensity around a radius 150 nm Ag nanoparticle at different wavelengths of incident light. The wavelengths are shown in the *upper left corner* of each box. For a wavelength of 2,000 nm the field is constant over the whole nanoparticle and the dipole field is placed at the center of the particle. At 850 nm there will be a non negligible variation in the field over the nanoparticle leading to the dipole radiation to be asymmetrically distributed. For even shorter wavelengths the quadrupole and octupole mode become dominant

13.2 Finite Element Method

Having already discussed physical characteristics of plasmonic nanoparticles and what observable quantities we wish to simulate, it is necessary to review the numerical method which will be used during this chapter. The finite element method is a procedure for solving partial differential equations by minimizing an expression made from trial solutions with variable parameters [22, 32]. This is true of all variational problems, the innovations of the finite element method are primarily in the choice of trial functions.

Generally with variational solutions as in the case of Fourier decomposition, we require many trial functions to approximate the solution correctly which can be computationally costly. The finite element method uses higher order polynomial basis functions. In the simulations presented here the order is typically between one

(linear) and six, such simple functions are relatively easy to handle computationally. At first glance these functions would be assumed to give a very poor approximation to the solution; the other key to this problem is the introduction of elements. The computational domain is split up into smaller elements. In each element the solution is assumed to vary slowly enough that simple polynomial functions do provide a good approximation to the solution. The solutions over each element are then reassembled with appropriate boundary conditions to provide the whole solution.

For optical problems we must solve Maxwell's equations [11]. By employing the time harmonic ansatz $\mathbf{E}(t) = \mathbf{E}_0 e^{-i\omega t}$ and assuming no external charges or currents $\rho = \mathbf{J} = 0$ we can obtain two equations for the electric field [27],

$$\nabla \times \mu^{-1} \nabla \times \mathbf{E} - \omega^2 \epsilon \mathbf{E} = 0, \tag{13.11}$$

$$\nabla \cdot \epsilon \mathbf{E} = 0, \tag{13.12}$$

where ϵ and μ are the permittivity and permeability of the element in question respectively.

There are two principle ways to increase the accuracy of our discrete solution with respect to the real solution. Either the mesh upon which we are solving the equation can be refined, e.g. divide the length of every edge in the mesh by two, or the order of approximating polynomial can be increased. We would like to use the input parameters requiring the lowest amount of computational resources. Therefore it is crucial to understand how varying these two parameters affects the precision of the solutions. Furthermore when designing devices one generally requires an optimization procedure. For such a procedure to work we must be able to compare the outcomes of different simulations with only small differences in input parameters. This will lead to a correspondingly small change in the figure of merit. To compare which set of input parameters maximizes the figure of merit it is essential to know the precision to which the simulated quantities are valid.

Due to the method focusing on finding local solutions and then combining said solutions, we can define local error estimates. This allows for the computational algorithm to automatically determine where the solution is least converged and locally refine the mesh there. Figure 13.5 shows the convergence of Q_{ext} in the case of an oblate Ag spheroid in vacuum with axes lengths of 200, 100 and 100 nm. The computation was performed by exploiting the cylindrical symmetry of the problem. This means only a 2D representation of the particle (as seen in Fig. 13.6) needs to be calculated, then the complete 3D solution can be reconstructed [6]. The mesh was refined using two different techniques; global refinement and adaptive local refinement. Plotted in Fig. 13.5 is the absolute difference between the solution with $n = 0, 1, \ldots, N$ refinement steps and the solution with $N + 1$ refinement steps, the x axis shows the amount of unknowns (i.e. the computational effort required) in each case. As expected, refining the mesh increases the computational cost but also increases the precision of the solution. The method of adaptive refinement produces solutions of equal convergence for many fewer unknowns compared to the global refinement strategy.

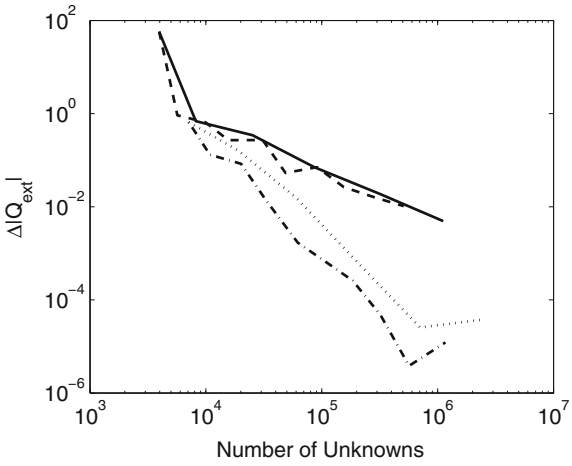

Fig. 13.5 The convergence of Q_{ext} with respect to grid refinements. The (*solid line*) and (*dotted line*) show global grid refinement for finite element degree 2 and 3 respectively. (*Dashed line*) and (*dash dot line*) show adaptive convergence for finite element degree 2 and 3 respectively; the grid is only refined in those places with a higher error until the error is equal everywhere

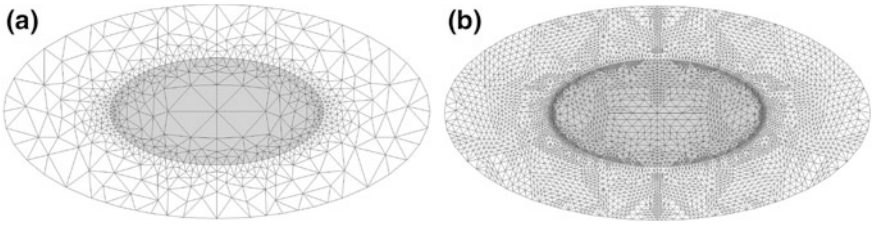

Fig. 13.6 A cross section of the mesh grid used for a typical FEM calculation. The ellipsoidal nanoparticle had been shaded for clarity. **a** is an unrefined grid and **b** shows the same grid after three adaptive refinement steps

Figure 13.6 shows a cross section of a typical mesh grid used for FEM simulations. The grid has been preferentially refined near the boundary between the nanoparticle and the surrounding medium, especially where the curvature is highest. In the later sections we will see that these correspond to areas of large electric field gradient necessitating a high local precision.

By taking the time harmonic ansatz for (13.11) we have converted the problem to a frequency domain problem. This means each computation gives information for a single frequency, cf. time domain methods which can provide an entire frequency spectrum with one computation provided the time step is short enough. However each frequency domain computation is much less demanding than a time domain computation. This can be advantageous for plasmonics as the whole spectrum may not need to be sampled but just a specific subset where the plasmon resonance is located. This can be relatively cheaply computed with frequency domain methods.

Sometimes periodic arrays of nanoparticles are the object of study, in which case the choice of boundary conditions at the computational domain boundary can be naturally fulfilled by periodic boundary conditions. For the case of isolated nanoparticles we need a different kind of boundary condition. If we were to stipulate that the field should discontinuously drop to zero outside of the computational domain it would be equivalent to placing a mirror around the computational domain boundary causing reflections that have nothing to do with the physics of the problem. To eliminate these reflections we require a so called transparent boundary condition. These are realised by an adaptive perfectly matched layer (PML) method. PML is a boundary condition intended to remove these unphysical reflections [8]. It achieves this by firstly creating an extra layer outside the computational domain with the same optical constants as inside. The field in this new layer decays to zero without changing the optical constants. This is achieved by allowing the position variable outside the computational domain to become a complex variable with a steadily increasing imaginary part. The equations for traveling waves contain factors like $exp[i(\mathbf{k}\cdot\mathbf{r} - \omega t)]$. If $\mathbf{r}$ is allowed to become complex then we will have factors proportional to, $exp[i(\mathbf{k}\cdot\Re\{\mathbf{r}\} - \omega t)]exp(-\mathbf{k}\cdot\Im\{\mathbf{r}\})$, which will give an exponential decay. This complexification of the real distance is an exact extension, hence no artificial reflections will be introduced. Residual reflections are due to the discretization and get smaller with finer meshes and larger thicknesses of the PML layer. This type of boundary condition was implemented in all the simulations presented in this chapter.

13.3 Shape Effects

In this section we will detail how the different nanoparticle shapes affect the kind of resonance observed. We begin by considering a single spherical silver particle in vacuum. The fundamental parameter is the radius of the particle, which we wish to vary and simulate the effect this has on the spectrum of Q_{sca} and Q_{abs}. Figure 13.7 shows a contour plot of Q_{ext} with respect to the particle radius and the wavelength. Starting from the low radius end there is almost no response to the scattering for very small particles (10 nm radius). A peak develops in the short wavelength regime upon increasing the radius until at 40 nm the spectrum looks like a strong sharp peak. Upon further increasing the radius this peak redshifts, broadens and reduces in intensity. This peak is associated with the dipole mode of the nanoparticle, this can be deduced from our previous reasoning that the small particles feel a spatially constant electric field which only permits a dipole mode. It can also be seen by looking at the near field as shown earlier in Fig. 13.4a. For radii larger than 75 nm we observe another peak forming at lower wavelengths than the dipole peak. This peak corresponds to the quadrupole resonance which has become significant because our particle has become so large that we can no longer consider the electric field to be spatially constant. Again by observing the near field in Fig. 13.4 we can confirm what physical intuition would suggest; that this mode is quadrupolar. This resonance

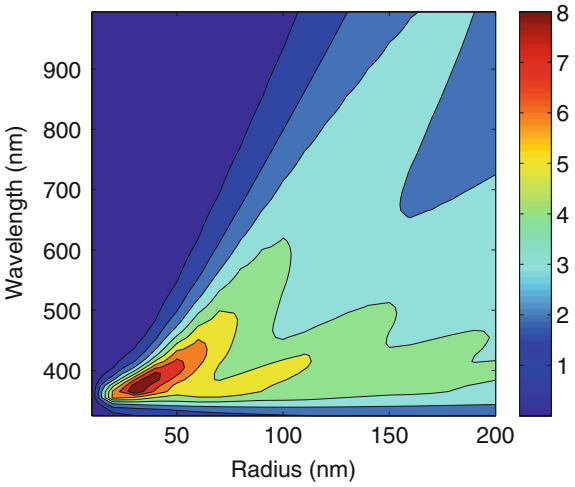

Fig. 13.7 Contour plot of the normalized extinction cross section for a spherical Ag nanoparticle in vacuum. Separated peaks refer to different multipole orders. Reasons for redshifting with increasing radius are discussed in the text

naturally occurs at a lower wavelength than the corresponding dipolar mode for a given radius. The wavelength of light required to excite the quadrupolar mode should be less than that required to excite the dipolar mode. This is because more oscillations need to fit into the same volume of nanoparticle. This mode also shows a redshifting, broadening and reduced peak intensity for increasing radius, the explanation of which is discussed below. The beginning of the octupole mode is also visible between radius 175–200 nm. The same logic for describing the quadrupolar mode can be used here, and indeed any higher order modes which would appear at even larger radii.

All three of the orders show redshifting with increasing particle radius. When increasing the radius, one essentially changes four separate parameters. The first three are the lengths along the three principle axes, these are shown in the inset of Fig. 13.8. They are the **E** direction (direction of polarization), the **k** direction (direction of the wave propagation) and the **H** direction which is perpendicular to both the others. The fourth parameter is the radius of curvature of the object. To determine the relative importance of these factors we start with a sphere of radius 50 nm, then elongate the sphere along one of the three axes whilst keeping the surface curvature constant. A sketch of the different orientations is shown in the inset of Fig. 13.8. Although the volume is changing in each case, the only factor contributing to the volume change is the one which we intend to investigate.

13.3.1 Nanoparticle Length || to E

We first discuss the most dominant effect which is increasing the length parallel to **E**. This will cause redshifting of the resonance due to retardation of the Coulomb force over the particle as can be seen in Fig. 13.8. If we were to apply a constant

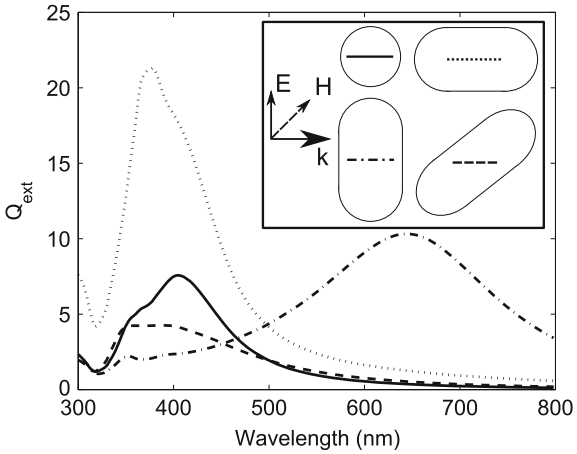

Fig. 13.8 The normalized extinction cross section for a radius 50 nm Ag sphere in vacuum and three orientations of a 200 nm long Ag cylinder in vacuum with ends having the same curvature as the sphere. The *line* style within each shape in the *inset* links the spectra to the different simulation setups

electric field to the nanoparticle, the clouds of electrons and ions will be shifted in opposite directions. Due to the much greater mass of the ions we can consider the acceleration felt due to the electric field to be negligible, therefore we assume the ions are static. This will give rise to a negative and positive surface charge building up causing a restoring Coulomb force to propagate from the positive charge towards the negative charge. This takes a finite time to traverse the entire nanoparticle. Now if the applied field is constant with time the difference is immaterial. However if the driving force is an electric field oscillating in time with a high enough frequency (for our discussion visible light is high enough) we have our harmonic oscillator situation. If we just consider one cycle, as in Fig. 13.9, then as the driving force is applied the electrons start to move away from the ions. In the absence of retardation the restoring force at a given time t_0 will be of a certain strength, then at the later time t_1 the electrons have moved further away and the restoring force has become even larger, just like a spring being stretched out. This is shown in the left panel of Fig. 13.9. Now when we consider the effect of retardation, at our first position where we measured the restoring force, we must now evaluate at the retarded time. This time, let us call it t_{-1} will be in the past with respect to t_0. Thus in the non retarded case, the electron's position at t_{-1} was closer to the equilibrium position, meaning the restoring force was lessened. The same holds true for the electron in the retarded restoring force at time t_1 feeling the same force as in the unretarded case at time t_0. We can now see why retardation of the Coulomb force means a weaker restoring force on the electron, which will lead to a redshift in the resonance. Quantum mechanical calculations have confirmed that this is the case [34]. To see that it must cause a redshift and not a blueshift take the limit of an infinitely

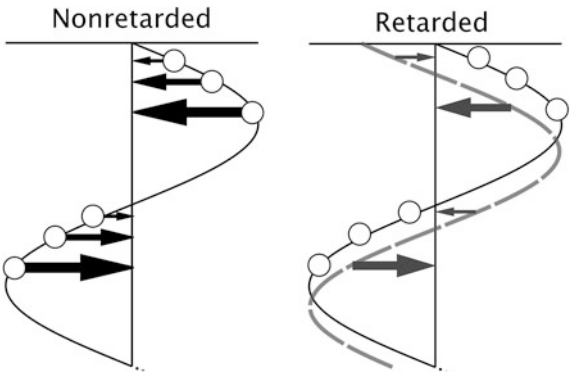

Fig. 13.9 Schematic view of the retarded restoring force. (*Left*) In the non retarded case the restoring force is proportional to the distance of the electron from equilibrium. (*Right*) In the retarded case the restoring force (*dotted curve*) lags behind the electron's position (*solid curve*) due to having to travel across the nanoparticle. This leads to a reduced restoring force compared to the non retarded case

retarded force i.e. zero restoring force. In this case the period of oscillation must be infinite i.e. no oscillation which corresponds to an infinitely large wavelength.

The spectrum is also significantly broadened as well as redshifted. This is because for longer wavelengths the radiative damping increases significantly [31]. This also partly explains why in Fig. 13.7 the different multipoles reduce in intensity for longer wavelengths. The other reason being related to the reduced surface curvature for large spheres which will be elaborated upon in Sect. 13.3.4.

13.3.2 Nanoparticle Length || to k

Next we discuss the effect of changing the length of the particle in the direction of wave propagation. As shown in Fig. 13.8 this causes a slight blueshift and a large increase in intensity. The slight blueshift is due to the small reduction in surface curvature in the direction of polarization, which will be dealt with in more detail in Sect. 13.3.4. If the surface curvature would not have changed then there would be no blueshift. The increase in intensity comes from our normalization condition, we normalized to the area of the particle as seen by the incoming light. When the light is parallel to the long axis this area does not change even though the volume increases. There has also been a change in the lineshape of the resonance. The sphere shows a peak with a shoulder on the short wavelength side signifying a smaller peak there that is not well resolved due to the larger peak. For the cylinder the case is reversed with the main peak being at the lower wavelength side with a shoulder at the longer wavelength side. This is due to the change from a dipole dominated resonance to a quadrupole dominated resonance. This effect is visible in the near field shown in

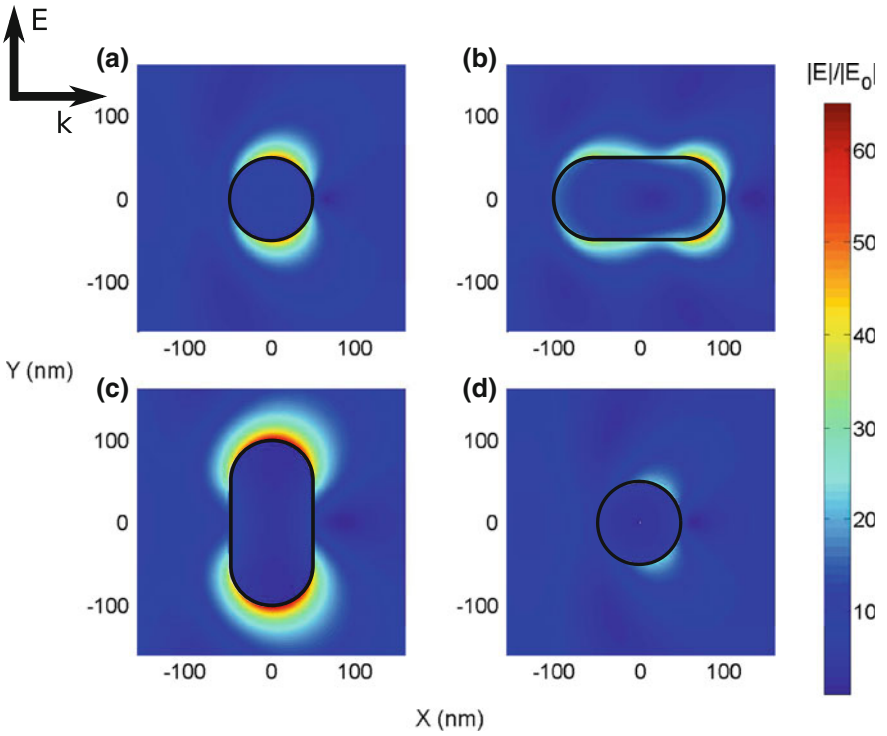

Fig. 13.10 The electric field intensity around differently shaped nanoparticles normalized to the incident field intensity. The direction and polarization of the incident light is shown in the *top left corner*. *Black lines* have been annotated to show the particle outline. **a** A spherical Ag particle of radius 50 nm in vacuum, **b**, **c** and **d** a Ag cylinder of length 200 nm in vacuum, with radius of curvature equal to the sphere. The orientations of the nanoparticles are the same as the *inset* in Fig. 13.8. The wavelength in each case is the peak wavelength of the spectrum in Fig. 13.8. The viewing plane is cut through the center of the nanoparticle

Fig. 13.10b which has four nodes at the nanoparticle boundary for the cylindrical case. When only half a wavelength or less can fit inside the nanoparticle the dipole mode will dominate, whereas for particles larger than half a wavelength of light, the multipole orders begin to dominate. Therefore it is important to keep the length of the particle in the direction of wave propagation short if one wishes to avoid multipolar modes.

13.3.3 Nanoparticle Length || to H

Furthermore we look into changing the particle length parallel to **H**. Here we can see essentially no redshifting or blueshifting but simply a reduction in intensity of the resonance. The near field representation of this resonance in Fig. 13.10d shows

a reduced intensity in the electric field enhancement around the nanoparticle in the plane of polarization. This reduction in intensity of the resonance is due to the particle loosing coherency of oscillations, i.e. the electrons in the center of the particle are not oscillating in phase with those at the edges.

13.3.4 Surface Curvature

Finally we come to the effect of surface curvature. We start with a 60 nm radius sphere and shorten two of the axes equally, thus creating a prolate ellipsoid with increased surface curvature along one axis, along which we choose to direct the polarization. Notice that in this configuration we have kept the length || to **E** constant between the two cases. This is because changing this length had the dominant effect on the spectral position of the resonance as we have seen in Fig. 13.8, thus any changes to the spectrum in this case can be attributed to the effect of surface curvature alone. Figure 13.11 shows the spectra for the original 60 nm radius sphere and for an ellipsoid with polarization along the 60 nm axis. When the polarization of the incident light is along the axis which has been elongated there is a redshifting of the resonance and also an increase in intensity.

As we have already seen, redshift effects are associated with a reduced restoring force in the harmonic oscillator equations. The reduction in restoring force is due to the higher surface to volume ratio in the ellipsoid. In the case we have considered the volume of the sphere is four times that of the ellipsoid, whereas the surface area of the sphere is only ≈2.5 times larger than the ellipsoid. This means that the fixed amount of volume charge is spread more thinly over the surface in the case of the ellipsoid leading to a reduced restoring force. This will naturally lead to an increased intensity of oscillation. However there is another factor which contributes to an increased near field intensity for high surface curvatures. The electric fields

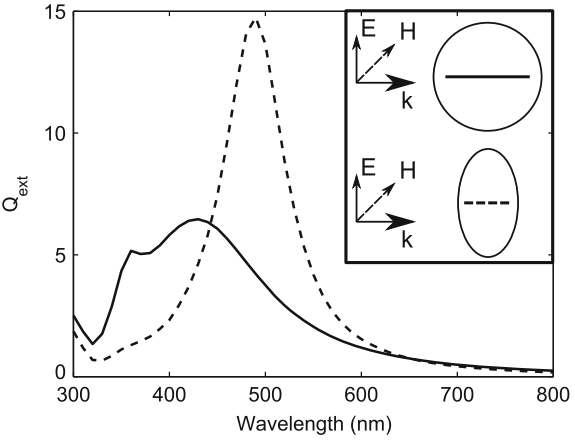

Fig. 13.11 The normalized extinction cross section for (*solid line*) a radius 60 nm Ag sphere in air and (*dashed line*) an ellipsoid with the same radius as the sphere in the direction of polarization, but with 30 nm radii in the other directions

around sharp metallic points are stronger for all wavelengths, not just those at which plasmonic effects are present. This is due to the boundary condition that electric fields must exit a metal normal to the surface, therefore at curved surfaces there is a bunching of the field lines. This effect is commonly referred to as the "lightning rod effect" and is not specific to plasmonics [17].

13.4 Material Effects

13.4.1 Nanoparticle Material

The optical properties of metal nanoparticles depend strongly on the metal in question. Figure 13.12 shows Q_{ext} for aluminium, silver and gold. Q_{ext} is decomposed into the absorption and scattering. The inset shows Q_{sca}/Q_{ext} for each case which we will refer to as scattering efficiency, note that in some literature Q_{sca} is called the scattering efficiency. Each case has a spherical nanoparticle in vacuum with radius chosen to maximise Q_{ext}, i.e. 30, 50 and 80 nm respectively. The Al plasma resonance forms two distinct peaks as the quadrupole mode has already started to become prominent at a nanoparticle radius of 30 nm. The resonance shows a high scattering efficiency that quickly falls off with increasing wavelength. The minimum in scattering efficiency occurs at 800 nm and is due to an absorption from an interband transition. This could prove problematic for usage of Al at optical wavelengths, nevertheless Al has a strong scattering response, comparable to Ag, and could provide a lower cost alternative. Ag has a strong scattering response and a high scattering efficiency over the whole optical region due to interband transitions starting below 300 nm. Au has a weaker response but also a high scattering efficiency. Due to the interband transitions starting below 500 nm, Au cannot be used over the whole optical range but is a strong candidate for IR applications.

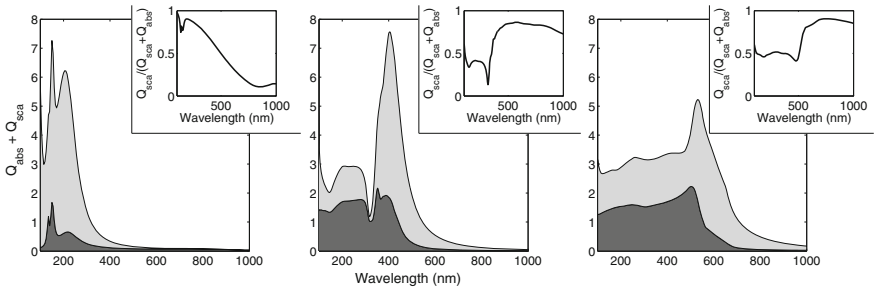

Fig. 13.12 Stacked area plot of normalized extinction cross section (*decomposed into absorption —dark grey* and *scattering—light grey*) for (*left*) aluminium, (*center*) silver and (*right*) gold. *Inset* shows the fraction of light scattered in each case. Each case shows a nanoparticle in vacuum with a radius chosen to maximise the extinction cross section, radii are Al—30 nm, Ag—50 nm and Au —80 nm

The general principles for choosing plasmonic materials for optical or IR devices are $RE\epsilon$ negative and $Im\epsilon$ as close to zero as possible in the frequency range of interest [37]. The first condition is equivalent to having the bulk plasma frequency higher than the frequency range of interest. For the optical region this condition is met by the noble metals. For the IR region this condition can be met by alkali metals, highly doped semiconductors and graphene [4]. In the case of semiconductors it is also necessary for the band gap frequency to be higher than the frequency range of interest to keep the loses low.

For realistic device design more factors than just the optical properties must be taken into account. The chemical properties will also be crucial; copper and aluminium both easily form oxides which can hinder their plasmonic capabilities. Likewise alkali metals are extremely reactive therefore their use in real devices would be problematic.

13.4.2 Homogeneous Medium

Another factor which can be used to control the plasma resonance is the nanoparticle's surrounding medium. In situations where the particles are suspended in a colloid or embedded totally in another material or have a shell structure, the outer medium can be taken as homogeneous. In Fig. 13.13 the extinction cross section of a radius 50 nm Ag sphere is shown for different values of refractive index. The absorption in the surrounding medium is zero. The extinction cross section is redshifted with increasing index of the medium. This is because the surface charge density of the nanoparticle will be partially compensated by the surrounding dielectric atoms causing a weakened restoring force [18]. As we have seen a weaker restoring force (spring constant k) will lead to lower resonance frequency ω_0 for a damped driven harmonic oscillator. Different multipole modes are redshifted at different rates, thus we are able to see in Fig. 13.13 the separation of distinct peaks

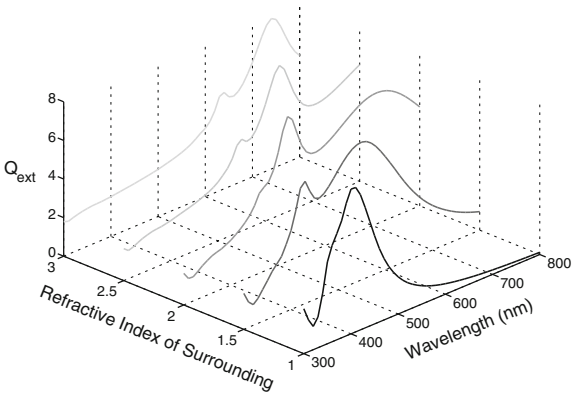

Fig. 13.13 The normalized extinction cross section for a spherical Ag particle of radius 50 nm in media with different refractive indices

which previously were one combined peak. The dipole peak is redshifted the strongest and also undergoes significant broadening until for $n > 2.0$ it is shifted out of the wavelength range shown. The quadrupole peak is also strongly shifted and a third peak corresponding to octupole modes starts to emerge.

In our harmonic oscillator example (13.8) example we saw that the amount of damping in the system will affect both the broadening of the resonance and the amplitude. Therefore a broader resonance will naturally have a lower amplitude. The resonance amplitude will also increase when the resonant frequency ω_0 is redshifted. However if the damping increases at a larger rate then the net effect will be a redshift with no increase in amplitude. Here the dipole mode is significantly broadened, so much that the amplitude decreases whilst redshifting. Conversely the quadrupole resonance is redshifted and increases in amplitude because there is no significant broadening.

13.4.3 Substrate

The more interesting case is that of a particle on a substrate or at a layer interface. Although we see, broadly speaking, similar redshifting behavior to the homogeneous medium case there are some notable exceptions. Resonances can couple to just one particle-medium interface, for example we take the upper half space as vacuum and only change the refractive index of the lower half space, i.e. a particle on a substrate. Then resonances coupled to the air-particle interface will not be redshifted at all by the changing substrate. Through controlling the amount of surface contact of the particle to each layer at a layered interface, different resonances can be shifted at different rates. Perhaps more importantly for optoelectronic applications is the effect on the near field and far field radiation. Both of these radiation types will become more localized to the material with a higher refractive index, due to the higher density of optical states there. This means it is possible to have directional radiation from the particles. Figure 13.14 shows the angular distribution of the far field radiation for silver hemispherical particles at a vacuum/substrate interface for different substrate refractive index values, light is incident from above and the images are in the plane of polarization. In Fig. 13.14a there is no real interface as the lower half space is also vacuum, appropriately we see the classic dipole radiation with equal forward and backscattering. The dotted lines show the angle of total internal reflection inside the substrate assuming transmission into vacuum. In this case the dotted lines extend horizontally out to infinity. This is because for light to be trapped inside a "substrate" which is the same as the surrounding medium, it would have to propagate horizontally as it cannot be totally internally reflected. In the case of (b) and (c) these lines are not horizontal and indicate the direction in which light will be totally internally reflected, i.e. trapped inside the substrate. Additionally we can see that the forward scattering becomes increasingly preferential over the back scattering. The forward scattering is divided into the part which lies inside the cone made by the dotted lines of total internal

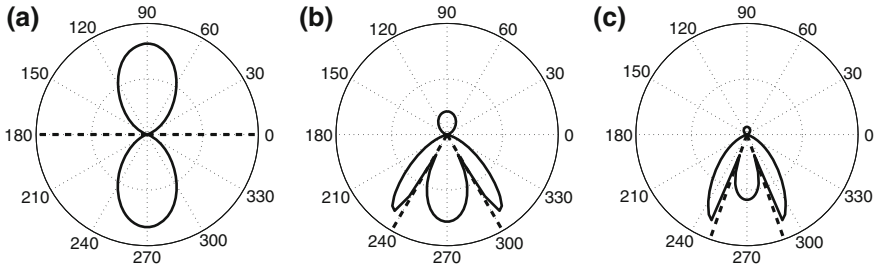

Fig. 13.14 The angular scattered power (*solid lines*) from hemispherical Ag nanoparticles at a vacuum/substrate interface for different substrate refractive indices. The lines subtending the angle of total internal reflection inside the substrate (*dashed lines*). The substrate indices are **a** $n = 1.0$, **b** $n = 2.0$, **c** $n = 3.0$, all substrates are non absorbing. The light is incident from above and images are in the plane of polarization

reflection and those which lie outside. The scattered light inside this cone will not be totally internally reflected and will be transmitted out of the substrate again if the substrate is non absorbing. The two lobes either side, which lie outside the cone, will be reflected upon attempting to leave the substrate, thus providing light trapping within the substrate. As we can see, the fraction of light which is trapped in this way will increase as the substrate index increases.

13.5 Designing Plasmonic Solar Cells

In the previous two sections we have seen how we can manipulate the plasmonic resonance to change the lineshape and peak resonance position. For all applications of plasmonics to technology it is required to tailor the resonance to the optical system in question. As an example we can take the case of nanoparticles integrated into photovoltaics.

Photovoltaic solar cells are required to become thinner to meet cost pressures from other energy sources. Upon making the cells thinner the absorption in the cells will reduce because the light path through the solar cell has become shorter, this can be seen in Fig. 13.15. This will particularly affect light at the red end of the spectrum, at energies slightly above the band gap of the semiconductor absorbing layer, where the absorbance of the semiconductor is low. The first step to increasing the efficiency of solar cells is to change the absorbing material to one with a higher absorption coefficient. The search for better semiconducting materials for photovoltaics still continues today. However this search has already been fruitful, semiconductors such as copper indium gallium diselenide (CIGSe) offer similar absorption to crystalline silicon for a fraction of the material thickness [12]. But there is increasing interest in making the thickness of even thin film cells even lower. In this case we are back to the same problem of insufficient absorption.

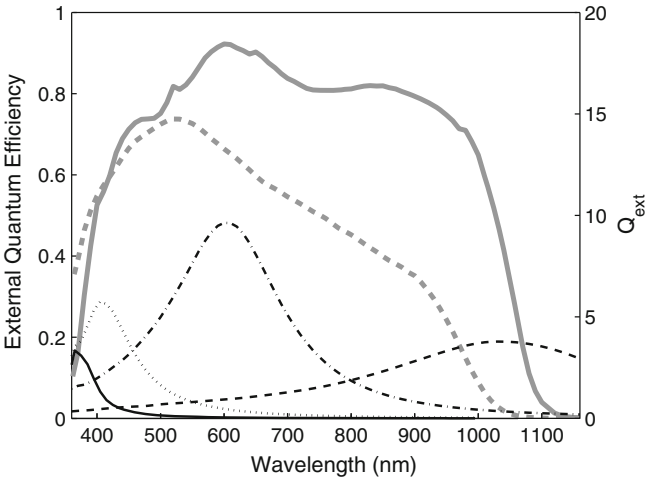

Fig. 13.15 External quantum efficiency for two different thicknesses of CIGS type solar cells. (*Grey thick solid line*) is for a standard 2 μm thick absorbing layer whereas (*grey thick dashed line*) is for a 450 nm thick layer, consequently the absorption is reduced particularly near the band gap. *Black thin lines* represent the normalized scattering cross section for different nanoparticles. (*Solid line*) is a 30 nm radius sphere in vacuum, (*dotted line*) is a 50 nm radius sphere in vacuum, (*dot dashed line*) is a short axis 100 nm long axis 200 nm prolate ellipsoid in vacuum and the (*dashed line*) is a short axis 100 nm long axis 200 nm oblate ellipsoid on an aluminium doped zinc oxide surface

For light incident perpendicular to the plane of the solar cell, we can increase the path length inside the solar cell by scattering the light into high angles. As we have seen, this can be achieved by placing nanoparticles at an interface between two media with different refractive indices. To minimize the absorption losses in the metal we would like to select a plasmonic material with low losses in the optical region, Sect. 13.4 showed that Ag was a good choice based on this criterion. The other materials used in a photovoltaic device cannot be chosen so easily without compromising the original device design, therefore generally one seeks to place the particles at a preexisting interface within the layered system compromising the photovoltaic. For simplicity we choose the top interface between air and aluminium doped zinc oxide.

As previously discussed we require an absorption enhancement at energies close to the semiconductor band gap. For a CIGSe cell that would be at energies just above 1.1 eV or wavelengths shorter than 1,100 nm. Therefore we would like to have a strong scattering response from our nanoparticles in this region. For small spherical silver particles the resonance will typically be at much shorter wavelengths. To achieve device functionality it is necessary to change the size and shape of the particles, using the principles developed in Sect. 13.3. We wish to redshift the spectrum to the correct position, broaden it to cover a large part of the region of absorption loss (here 500–1,100 nm) and have a strong scattering response. Starting from the small nanoparticles we can increase the radius until the dipole scattering response, Q_{sca}, is maximised.

Table 13.1 Table summarizing the different shape and material parameters for metallic nanoparticles and how they affect observable quantities

	Normalized extinction cross section	Scattering efficiency	Angular distribution
Length $\|\|$ to **E**	Increase causes redshift and increased intensity	Increase correlates with increase in scattering efficiency	Remains dipolar
Length $\|\|$ to $\boldsymbol{k}$	No redshift, increase in intensity, multipolar modes emerge	No effect	Increased transmission due to multipolar scattering
Length $\|\|$ to **H**	No redshift, decrease in intensity due to coherence loss	Increase correlates with increase scattering efficiency	Remains dipolar
Surface curvature	Higher curvature causes redshift and increased intensity	No change	Remains dipolar
Material	Low loss metals will have a higher intensity	Lower absorption loss increases scattering efficiency	Each material will show multipolar modes for different wavelengths
Medium refractive index	Increases will redshift the resonance whilst broadening due to radiative damping	No effect	Multipole orders will become spectrally separated due to redshifting at different rates
Substrate	Redshifts will only occur to resonances localized to the side with an increasing refractive index	No effect	Increasing substrate index causes strong forward total scattering and increased high angle scattering

Then we elongate the particle to redshift and broaden the resonance. Finally taking into account the effect of the substrate gives us the resonance position shown. The scattering will have a significant high angle component allowing for a light path enhancement inside the absorbing layer. Due to the extreme broadening the resonance is much less pronounced. To determine the most beneficial amount of broadening is an optimization problem for which we need a fast, accurate and precise method to evaluate the gain in absorption from the nanoparticles. This is why the finite element method has been employed in this chapter. Table 13.1 provides a summary of the different effects discussed in this chapter.

Acknowledgments The authors would like to thank G. Yin for the experimental data shown in Fig. 13.15 and P. Andrä for the Mie theory results shown in Fig. 13.3. The authors would like to acknowledge funding by the DFG (German Research Foundation) in the DFG research center MATHEON and the funding from the Helmholtz-Association for Young Invesitgator group VH-NG-928 within the Initiative and Networking fund.

References

1. J.N. Anker, W. Paige Hall, O. Lyandres, N.C. Shah, J. Zhao, R.P. Van Duyne, Biosensing with plasmonic nanosensors. Nat. Mater. **7**(6), 442–453 (2008)
2. H.A. Atwater, A. Polman, Plasmonics for improved photovoltaic devices. Nat. Mater. **9**(3), 205–213 (2010)
3. W.L. Barnes, A. Dereux, T.W. Ebbesen, Surface plasmon subwavelength optics. Nature **424** (6950), 824–830 (2003)
4. M.G. Blaber, M.D. Arnold, M.J. Ford, A review of the optical properties of alloys and intermetallics for plasmonics. J. Phys. Condens. Matter **22**(14), 143201 (2010)
5. C.F. Bohren, D.R. Huffman, *Absorption and Scattering of Light by Small Particles* (Wiley, New York, 2008)
6. S. Burger, B.H. Kleemann, L. Zschiedrich, F. Schmidt, 3d finite-element simulations of light propagation through circular subwavelength apertures. In *Microtechnologies for the New Millenium*, vol. 7366. Proceedings of SPIE (2009) p. 736621
7. K.R. Catchpole, A. Polman, Design principles for particle plasmon enhanced solar cells. Appl. Phys. Lett. **93**, 191113 (2008)
8. W.C. Chew, W.H. Weedon, A 3d perfectly matched medium from modified maxwell's equations with stretched coordinates. Microwave Opt. Technol. Lett. **7**(13), 599–604 (1994)
9. R.P. Feynman, *The Feynman Lectures on Physics* (3 Volume Set) (Addison Wesley Longman, Boston, 1970)
10. R. Hong, G. Han, J.M. Fernández, B.J Kim, N.S. Forbes, V.M. Rotello, Glutathione-mediated delivery and release using monolayer protected nanoparticle carriers. J. Am. Chem. Soc. **128** (4), 1078–1079 (2006)
11. J.D. Jackson, *Classical Electrodynamics*, 3rd edn. (Wiley, New York, 1998)
12. P. Jackson, D. Hariskos, E. Lotter, S. Paetel, R. Wuerz, R. Menner, W. Wischmann, M. Powalla, New world record efficiency for cu(in, ga)se2 thin-film solar cells beyond 20 %. Prog. Photovoltaics Res. Appl. **19**(7), 894–897 (2011)
13. S.S. Kim, S.I. Na, J. Jo, D.Y. Kim, Y.C. Nah, Plasmon enhanced performance of organic solar cells using electrodeposited Ag nanoparticles. Appl. Phys. Lett. **93**(7), 073307–073307–3 (2008)
14. C. Kittel, *Introduction to Solid State Physics*, 8th edn. (Wiley, New York, 2004)
15. E. Kretschmann, Radiative decay of nonradiative surface plasmon excited by light. Z. Naturf. **23A**, 2135–2136 (1968)
16. K.Q. Le, P. Bienstman, Optical modeling of plasmonic nanoparticles enhanced light emission of silicon light-emitting diodes. Plasmonics **6**(1), 53–57 (2011)
17. P.F. Liao, A. Wokaun, Lightning rod effect in surface enhanced raman scattering. J. Chem. Phys. **76**(1), 751–752 (1982)
18. S.A. Maier, H.A. Atwater, Plasmonics: localization and guiding of electromagnetic energy in metal/dielectric structures. J. Appl. Phys. **98**(1), 011101 (2005)
19. S.A. Maier, P.G. Kik, H.A. Atwater, S. Meltzer, E. Harel, B.E. Koel, Ari A.G. Requicha, Local detection of electromagnetic energy transport below the diffraction limit in metal nanoparticle plasmon waveguides. Nat. Mater. **2**(4), 229–232 (2003)
20. G. Mie, Beiträge zur Optik Trüber Medien, speziell kolloidaler Metallösungen. Ann. Phys. **303**(3), 377–445 (1908)
21. S.G. Moiseev, S.V. Vinogradov, Design of antireflection composite coating based on metal nanoparticles. Phys. Wave Phenom. **19**, 47–51 (2011)
22. P. Monk, *Finite Element Methods for Maxwell's Equations* (Oxford University Press, New York, 2003)
23. A.J. Morfa, K.L. Rowlen, T.H. Reilly, M.J. Romero, J. van de Lagemaat, Plasmon-enhanced solar energy conversion in organic bulk heterojunction photovoltaics. Appl. Phys. Lett. **92**(1), 013504–013504–3 (2008)
24. M. Moskovits, Surface-enhanced spectroscopy. Rev. Mod. Phys. **57**, 783–826 (1985)

25. S. Nie, S.R. Emory, Probing single molecules and single nanoparticles by surface-enhanced raman scattering. Science **275**(5303), 1102–1106 (1997)
26. A. Otto, Excitation of nonradiative surface plasma waves in silver by the method of frustrated total reflection. Z. Phys. **216**, 398–410 (1968)
27. J. Pomplun, S. Burger, L. Zschiedrich, F. Schmidt, Adaptive finite element method for simulation of optical nano structures. Phys. Status Solidi B **244**(10), 3419–3434 (2007)
28. M. Quinten, A. Leitner, J.R. Krenn, F.R. Aussenegg, Electromagnetic energy transport via linear chains of silver nanoparticles. Opt. Lett. **23**(17), 1331–1333 (1998)
29. R.H. Ritchie, E.T. Arakawa, J.J. Cowan, R.N. Hamm, Surface-plasmon resonance effect in grating diffraction. Phys. Rev. Lett. **21**, 1530–1533 (1968)
30. N Shukla, M.A. Bartel, A.J. Gellman, Enantioselective separation on chiral au nanoparticles. J. Am. Chem. Soc. **132**(25), 8575–8580 (2010) (PMID: 20521789)
31. C. Sönnichsen, T. Franzl, T. Wilk, G. von Plessen, J. Feldmann, O. Wilson, P. Mulvaney, Drastic reduction of plasmon damping in gold nanorods. Phys. Rev. Lett. **88**, 077402 (2002)
32. G. Strang, G. Fix, *An Analysis of the Finite Element Method*, 2nd edn. (Wellesley, Cambridge, 2008)
33. H.R. Stuart, D.G. Hall, Island size effects in nanoparticle-enhanced photodetectors. Appl. Phys. Lett. **73**(26), 3815–3817 (1998)
34. M.D. Turner, Md M. Hossain, M. Gu, The effects of retardation on plasmon hybridization within metallic nanostructures. New J. Phys. **12**(8), 083062 (2010)
35. H.C. Van De Hulst, *Light Scattering by Small Particles* (*Dover Books on Physics*) (Dover Publications, New York, 1981)
36. G. Walters, I.P. Parkin, The incorporation of noble metal nanoparticles into host matrix thin films: synthesis, characterisation and applications. J. Mater. Chem. **19**, 574–590 (2008)
37. P.R. West, S. Ishii, G.V. Naik, N.K. Emani, V.M. Shalaev, A. Boltasseva, Searching for better plasmonic materials. Laser Photonics Rev. **4**(6), 795–808 (2010)
38. A.V. Zayats, I.I. Smolyaninov, Near-field photonics: surface plasmon polaritons and localized surface plasmons. J. Opt. A Pure Appl. Opt. **5**, S16 (2003)

Part VII
Advanced Theoretical Studies: Nonlinear Optics

Chapter 14
High Harmonic Generation Assisted by Metal Nanostructures and Nanoparticles

Anton Husakou, Song-Jin Im, Kwang-Hyon Kim and Joachim Herrmann

Abstract We present a review of our theoretical studies of plasmonic field enhanced high harmonic generation in the vicinity of various metallic nanostructures, of rough metallic surfaces or in composites containing a mixture of a noble gas and metallic nanoparticles. First we present a semiclassical model for plasmon-enhanced high-harmonic generation (HHG) taking into account both the field inhomogeneity in the hot spots and electron absorption by the metal surface. Both effects play an important role in the HHG process and lead to the generation of even harmonics and to an twofold increased cutoff. Further alternative arrangements or mechanism for field enhancement enabling higher HHG efficiencies and a lower damage threshold are studied. We simulate field enhancement and HHG spectra in the vicinity of metallic rough surfaces and predict an increased interaction volume of hot spots in the case of grazing incidence of s-polarized pump pulses with an efficiency of plateau harmonics in the range of 10^{-7}. Finally, we investigate low-intensity high-harmonic generation enabled by the plasmonic electric field enhancement in a mixture of a noble gas with metal nanoparticles. In this case HHG efficiencies up to 10^{-6} are predicted.

14.1 Introduction

High-harmonic generation (HHG) has become an attractive light source for the generation of radiation in the extreme ultraviolet region. Most notable is the possibility to use HHG for the generation of attosecond pulses [1] opening the way to exciting opportunities to study attosecond-resolved fundamental electronic processes in atoms and molecules and providing a valuable tool for a variety of applications such as attosecond physics, nanolithography, etc. [2–5]. The main

A. Husakou (✉) · S.-J. Im · K.-H. Kim · J. Herrmann
Max-Born-Institut für Nichtlineare Optik und Kurzzeitspektroskopie, Max-Born-Str. 2a, 12489 Berlin, Germany
e-mail: gusakov@mbi-berlin.de

© Springer International Publishing Switzerland 2015

S. Sakabe et al. (eds.), *Progress in Nonlinear Nano-Optics*,
Nano-Optics and Nanophotonics, DOI 10.1007/978-3-319-12217-5_14

mechanism of HHG is described by the three-step model of tunneling ionization, electron acceleration in the strong electric field and its recombination with the parent ion, accompanied by the emission of energetic photons [6]. A number of applications of HHG would greatly benefit if pump lasers with a significant increased repetition rate can be developed or lower intensities of the pump pulses could be used. Recently for the realization of this aim a method for HHG at low pulses energies has been demonstrated based on the local field enhancement near a metallic bowtie-shaped gold nanoelement [7]. In the last decade metallic nanostructures became a subject of extensive theoretical and experimental research [8]. In particular, it has been shown that localization of light on a sub-wavelength nanometer scale and huge plasmonic field enhancements in the vicinity of these objects [9, 10] are possible. Based on this phenomenon, in [7] HHG has been demonstrated by nJ pulses directly from a laser oscillator. In the vicinity of metal nanostructures the incident laser intensity is enhanced by up to three orders of magnitude by the plasmons in so-called "hot spots". The strongly enhanced field ionizes noble gas atoms and accelerates the resulting electrons, which recollide with the parent ion transforming their kinetic energy into coherent high harmonic radiation. The elimination of complex and expensive amplifiers and the opportunity to perform HHG and attosecond experiments at MHz repetition rates can significantly extend the ability of extreme VUV generation and attosecond pump-probe spectroscopy. Later, the concept of plasmon-enhanced HHG was extended for the case of tapered hollow metallic waveguides [11].

A first theoretical investigation of HHG employing field enhancement by metallic nanostructures was provided in [12] using the finite-element method for the calculation of the spatial field distribution in the vicinity of nanostructures and a modified version of the Lewenstein model for the incorporation of the field inhomogeneity in the hot spots and electron absorption from the metal surfaces. It was shown that both field inhomogeneity and the electron absorption at the metal surface lead to the emission of even harmonics as well as to more than a twofold increase of the cut-off frequency. Later HHG by spatial inhomogeneous fields using the strong-field approximation [13, 14] or the 3D Schrödinger equation [15] has also been studied predicting a similar cutoff extension. Besides a theoretical study of HHG employing nanoplasmonic field enhancement of coupled ellipsoids was published in [16]. The generation of isolated attosecond pulses using polarization gating via HHG utilizing plasmon field enhancement in cross-bow-tie nanostructures has been theoretically studied in [17]. HHG in tapered hollow metallic waveguides has also been theoretically studied in [18]. After that, in several publications the quantum description of both the field inhomogeneity and electron absorption at surface was provided by several groups [13–15, 19–22], along with the study of the high-energy photon emission in plasmonic field [23], plasmon-assisted as-pulse generation without CEO-stabilization [24] and HHG in periodic bowtie arrays [25].

Though plasmonic field enhancement seems to be a promising route to low-energy excitation of HHG, there exist problems for its utilization under realistic experimental conditions. The two main problems are the possible damage of the

nanostructures and the low efficiency of 10^{-9} in the plateau region obtained up to now in [7]. Therefore the search of alternative arrangements or mechanism for field enhancement enabling higher efficiencies or a lower damage threshold is a crucial point in the further development of this method. Combined with a review of our previous contributions to this issue we present in this paper our recent results with a study of possible arrangements indicating a potential route towards this aim.

In Sect. 14.2 we describe the theory of plasmon-enhanced HHG in a noble gas taking into account both field inhomogeneity and the electron absorption at the metal surface. By using a Maxwell solver in Sect. 14.3 the spatial field distribution near a nanocone and a bowtie nanostructure, and the corresponding HHG spectra are calculated and its peculiarities are discussed. In Sect. 14.4 we study the possibility to use metallic rough surfaces for plasmonic field enhanced HHG with decreased threshold pump power due to an intensity enhancement factor more than 10^3. The potential of this structure for field-enhanced HHG with a higher efficiency is studied and an efficiency of 10^{-7} in the plateau region for grazing incidence of s-polarized pump pulses is predicted. Finally, in Sect. 14.5 we propose and theoretically study a third scheme for plasmon-assisted HHG with higher efficiencies consisting of a mixture of noble gas atoms and metal nanoparticles. For the example of a composite of silver metallic ellipsoids with suspended argon we calculate the field distribution, the enhancement factors and the HHG spectrum. It is shown that phase matching in the composite can be achieved by the significant contribution of the silver nanoparticles to anomalous dispersion. As a result we predict that in such systems harmonics up to the harmonic number of 70 can be generated with efficiencies near the cutoff in the range of 10^{-6}.

14.2 Theory of High-Harmonic Generation in the Vicinity of Metal Nanostructures

Besides the generation of higher harmonics in plasmon-enhanced HHG in a noble gas in the vicinity of metallic nanostructures two additional effects come into play. In the hot spot, electrons experience the inhomogeneous electric field, and some of them will hit the metal surface and never return to the parent ion. Both field inhomogeneity and the electron absorption at the metal surface play an important role in the HHG process.

We describe HHG in the framework of an modified Lewenstein model, and start with the description of the standard version of this semi-classical approach. In the first stage the strong electric field $\mathbf{E}(t)$ ionizes an atom at the time moment t_s and creates a free electron. It is accelerated by the oscillating field and for linearly polarized field is driven back to the parent ion after the field changes the direction. In the last stage the recombination with the parent ion at the moment t_f leads to the emission of a high-energy photon. The high-harmonic signal is determined by the field-induced time-depending dipole moment $d(t) = e\langle 0|x|\Phi_c(t)\rangle + c.c$ where $\langle 0|$ is

the ground atomic state and $|\Phi_c(t)\rangle$ the wavefunction tracing the evolution in the continuum state. Neglecting the Coulomb potential, one can represent the time-dependent high-harmonic dipole moment in direction of the field polarization x as [6]

$$d(t_f) = ie^2 \int_{-\infty}^{t_f} dt_s \int d^3p \langle 0|x|p - eA(t_f)\rangle e^{iS/\hbar} \times E(t_s)\langle p - eA(t_s)|x|0\rangle + c.c. \tag{14.1}$$

In this expression the integration is performed over all past ionization moments t_s and all canonical momenta $p = m_e v + eA$ which is a conserved quantity. Here $\langle p - eA(t_s)|x|0\rangle = d_x(p - eA(t_s))$ is the dipole moment for a transition from the ground state to the continuum with a kinetic momentum $p - eA(t_s)$, $A(t)$ is the vector potential with $\dot{A} \equiv dA(t)/dt = E(t)$. During the second stage this momentum state evolves influenced by the laser field and acquires a phase factor $\exp(-iS(t_f, t_s)/\hbar)$ where $S(t_f, t_s) = \int_{t_s}^{t_f} (I_p + (p - eA(t))^2/2m_e)dt$ is the classical action of the electron moving in the laser field, I_p being the ionization potential. Finally the electron recombines with the parent ion into the ground state with the amplitude $d_x^*(p - eA(t_f))$. In this case, as shown in [6], (14.1) can be simplified to

$$d(t_f) = i\frac{e}{2\omega_0^{5/2} m_e} \int_{-\infty}^{t_f} \left(\frac{\pi}{\varepsilon + i\Delta t/2}\right)^{3/2} H(t_f, t_s) \times d_x(p_{st} - eA(t_s)) \exp(-i\frac{S(t_f, t_s)}{\hbar}) \times d_x^*(p_{st} - eA(t_f))E(t_f)dt_s + c.c. \tag{14.2}$$

Here the canonical momentum is given by $p_{st} = e\Delta B/\Delta t$ with $\dot{B}(t) = A(t)$, $\Delta t \equiv t_f - t_s$, ε is an arbitrary small regularization parameter, ω_0 is the central laser frequency, m_e the electron mass, and the action is $S_0(t_f, t_s) = I_p\Delta t - 0.5e^2(\Delta B^2/\Delta t + \Delta C)/m_e$ where $\dot{C}(t) = A^2(t)$. For any function F we define $\Delta F \equiv F(t_f) - F(t_s)$. For the ground state of a hydrogen like atom the dipole matrix element is $d_x(p) = i2^{7.25}[\hbar\omega_0 m_e^2 I_p]^{5/4}\pi^{-1}p/(p^2 + \alpha)^3$, where $\alpha = 2m_e^{1/2}I_p^{1/2}$. In the unmodified Lewenstein model we have $H(t_f, t_s) \equiv 1$.

We extend the semiclassical HHG model accounting for the inhomogeneity of the field in the hot spot by adding the first-derivative term to the field $E(t, x) = E(t)(1 + x/d_{inh})$, and consider this derivative term as a perturbation, including only the first-order correction $x^{(1)}(t) = -e/(d_{inh}m_e)\int_{t_s}^{t} dt' \int_{t_s}^{t'} E(t'')x^{(0)}(t'')dt''$ to the zeroth-order electron trajectory $x^{(0)}(t)$. The second-order term is typically smaller than 25 % of the first-order one. As a result, the expressions for the momentum p_{st} and $S(t_f, t_s)$ are modified as follows:

$$p_{st} = e\left[A(t_s) + \frac{\Delta B - A(t_s)\Delta t + \beta(0.5(\Delta B)^2 - \Delta D + C(t_s)\Delta t)}{\Delta t - \beta(2\Delta G + \Delta t[B(t) + B(t_s)])}\right], \tag{14.3}$$

$$\begin{aligned} S(t_f, t_s) = S_0(t_f, t_s) + e2\beta m_e^{-1}\{p(t_s)^2[2\Delta G \\ + (B(t_f) + B(t_s))\Delta t] + p(t_s)[-\Delta C\Delta t \\ + 2\Delta D] + (C(t_f) + C(t_s))\Delta B - 2\Delta F\}, \end{aligned} \tag{14.4}$$

where $\dot{D}(t) = C(t)$, $\dot{F}(t) = C(t)E(t)$, $\dot{G}(t) = B(t)$, $\beta = e/(m_e d_{inh})$. Another modification of the model is described by the function $H(t, t_s)$ under the integral in (14.2). This function is equal to 1 unless the electron during the motion hits the metal surface positioned at d_{sur}, otherwise we assume that the electron is absorbed by the surface and set $H(t, t_s) = 0$.

To understand the effect of the inhomogeneity of the field and of the metal surface on the HHG process, in Fig. 14.1 we consider the HHG spectra for different parameters d_{inh} (Fig. 14.1a) and d_{sur} (Fig. 14.1b) for cw radiation with a typical intensity in the hot spot of 200 TW/cm^2. The inverse spatial symmetry, which exists in a homogeneous infinite gas, is broken even for a very low inhomogeneity characterized by $d_{inh} = 1,000$ nm, as shown in Fig. 14.1a. This leads to a qualitatively new effect: the generation of even harmonics (shown by the blue crosses). For larger inhomogeneities with $d_{inh} = 20$ nm the amplitude of the even harmonics approaches that of odd harmonics. Simultaneously, the harmonic cutoff shifts to higher harmonic numbers and become much less pronounced. Due to inhomogeneity, electrons have higher velocities when they reach the parent ion, leading to a higher kinetic energy and therefore to a higher cut-off frequency. The influence of the metal surface and the associated electron absorption is studied in Fig. 14.1b. One can see that for a distance to the surface $d_{sur} = 3$ nm, no electron reaches the surface, and correspondingly no modification in the dipole moment and no even harmonics appear. For shorter d_{sur}, some electrons will reach the surface. Since the function $H(t, t_s)$ introduces a sharp modulation in the temporal profile of the harmonics, an extension of the spectrum to higher harmonic numbers can be seen in Fig. 14.1b, combined with the emission of even harmonics. From Fig. 14.1 one can see that the combined effect of the field inhomogeneity and of the metal surface can increase the HHG cutoff by a factor larger than two.

14.3 Spatial Field Distribution and HHG in Gases Near a Metallic Tip and a Bow-Tie Nanostructure

In this Section we perform a realistic simulation of HHG in the vicinity of a silver nanocone as depicted in Fig. 14.2a. Such nanocone structure can be produced by silver deposition on a chemically created silicon needle without nanoscale lithographic control. The curvature radius of the nanostructure edges is the key

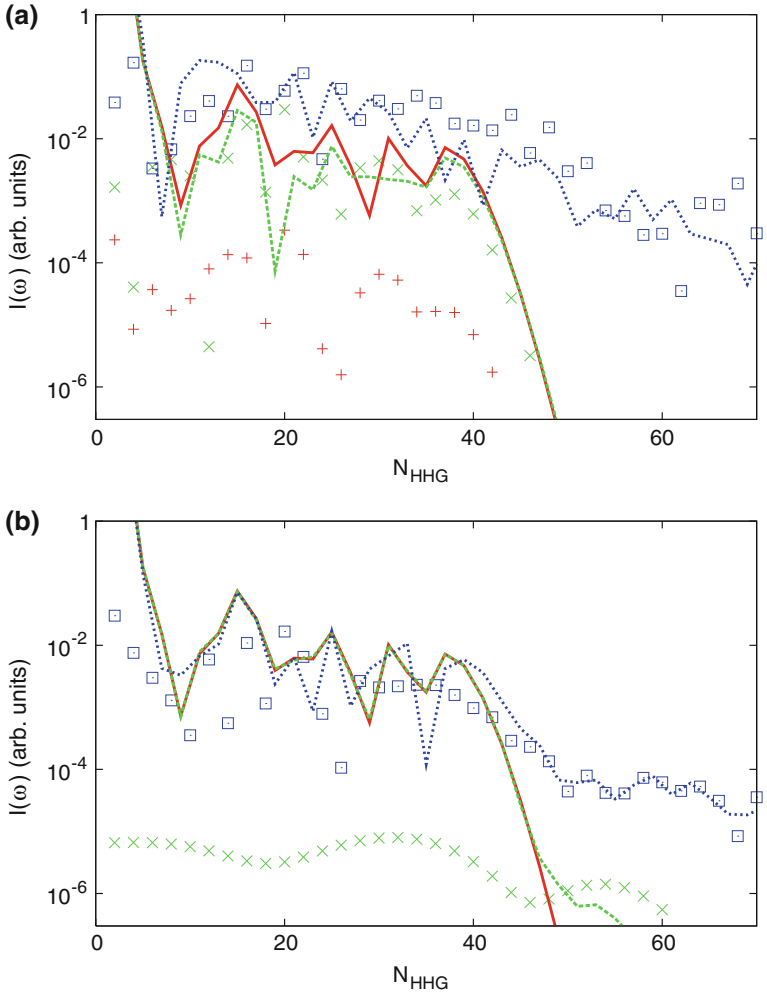

Fig. 14.1 Influence of the field inhomogeneity (**a**) and of the metal surface (**b**) on the HHG process. Odd harmonics are presented by *curves* while even harmonics are shown by *points*. In **a**, the field has the inhomogeneity scale d_{inh} of 1,000 nm (*red solid curve* and *red vertical crosses*), 20 nm (*green short-dashed curve* and *green diagonal crosses*), and 5 nm (*blue long-dashed curve* and *blue squares*). In **b**, the distance to the metallic surface d_{sur} is 3 nm (*red solid curve*), 2.62 nm (*green short-dashed curve* and *green diagonal crosses*), and 1.5 nm (*blue long-dashed curve* and *blue squares*). For both cases, cw radiation at 830 nm with intensity in the hot spot of 200 TW/cm^2 in argon is considered

parameter determining the maximum field enhancement, with optimum structure having the smallest curvature radius. We have assumed a radius of 5 nm, determined by the current state of the manufacturing technique.

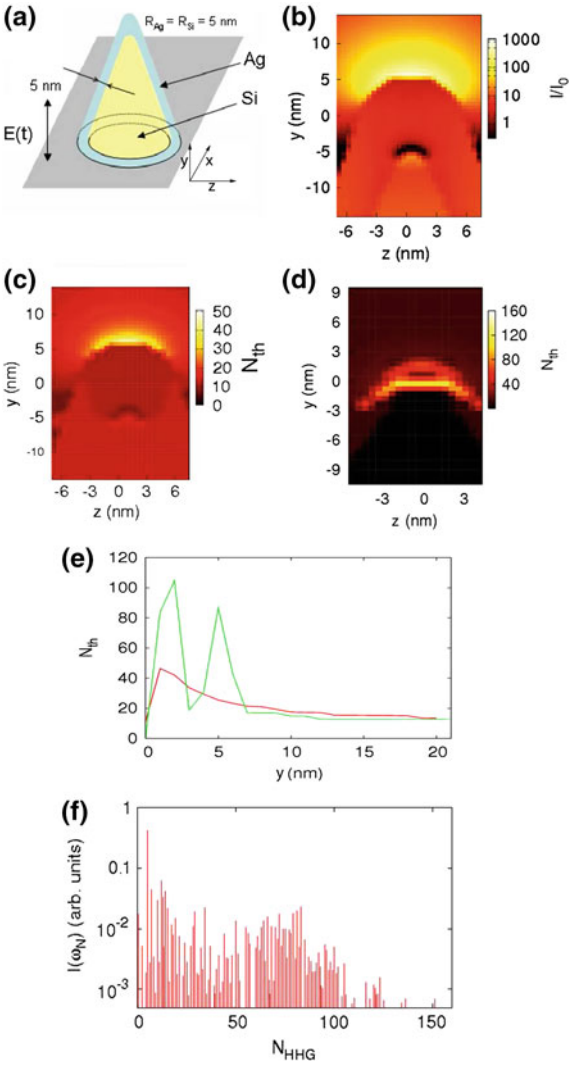

Fig. 14.2 High harmonic generation in the vicinity of a nanocone structure. In **a**, the scheme of the nanocone is shown. The curvature radii and the thickness of silver coating are 5 nm, the *y*-polarized field propagates along the *x* direction. In **b** the intensity enhancement is presented for the *zy* cross-section of the incident field at 830 nm. In **c** and **d**, the distribution of the harmonic cutoff is shown for the model without (**c**) and with (**d**) modifications by the field inhomogeneity and metal surface for 10-fs input pulses with 0.3 TW/cm^2 intensity and argon surrounding the tip. In **e** the cutoff for the modified (*green curve*) and unmodified (*red curve*) model is shown along the *y* axis, and in (**e**) the spectrum for cw excitation with the above parameters is shown

We have used the Maxwell solver JCM wave to model the plasmonic field enhancement in the vicinity of the nanostructure, taking into account the phenomenological complex-valued dielectric function of silver. For short input pulses we included the dispersion of silver and the wavelength dependence of the enhancement factor near the nanostructure. In this paper, we disregard depolarisation effects and the influence by next-nearest nanostructure, since the typical distance to them is much larger than the hot spot.

Typical intensities in the hot spots in the range of 10^{14}–10^{15} TW/cm^2 above the metal surface could lead to damage. However, the boundary condition for the electric field normal to the surface causes an intensity reduction of $1/|\varepsilon_{Ag}|^2 \sim 0.01$

to values below 5 TW/cm^2. Therefore for the considered parameters and a single pulse the damage threshold of metal or metal NPs of about 0.1 J/cm^2 [26] is not reached. For a pulse train, to avoid damage a good heat evacuation of the substrate is required. For moderate laser intensities lower than 10 GW/cm^2 harmonics up to the fifth order can be generated from the metal surface [27] but with efficiency very rapidly decreasing with the harmonic order. For higher intensities below the relativistic values no increase of high-harmonic efficiency was reported. On the other hand, plasma formation and the multiphoton photo effect [28] at the surface do not perturb the considered HHG process. They exhibit features clearly distinct from high harmonic spectra observed in the experiment [7] and in our simulations.

We note that according to the previous experimental results the nonlinear change of the metal dielectric function does not exceed the value of 2. The existence of the plasmonic modes is therefore not endangered by the optical metal nonlinearity, furthermore, it will only slightly affect the enhancement which mostly arises from the nonresonant "lightning-rod" effect.

The spatial field distribution around the nanocone structure is shown in Fig. 14.2b. With parameters given in the caption, it demonstrates intensity enhancement factors of up to 1,000 in the "hot spot" in the vicinity of the tip as well as only a weak azimuthal dependence. Note that the field is inhomogeneous on the scale below 10 nm in the "hot spot" which is located directly above the metal surface. The parameters $d_{inh}(x, y, z)$ and $d_{sur}(x, y, z)$ are calculated from this spatial distribution and are used for the HHG simulation by using the extended model as given by (14.2)–(14.4). In Fig. 14.2c, d we show the spatial distribution of the harmonic cutoff Nth for an excitation by 830-nm sech-shaped pump pulses with intensity of only 0.3 TW/cm^2, FWHM of 10 fs, and polarization and wavevector as indicated in Fig. 14.2a. The field enhancement in the "hot spot" increases the intensity to approximately 300 TW/cm^2, which for the chosen wavelength corresponds in the unmodified Lewenstein-model to a cut-off roughly at the 50th harmonic, as can be seen in Fig. 14.2c. However, caused by the effect of the field inhomogeneity and the presence of the metal surface, the cutoff increases up to the 105th harmonic, which correspond to the emission of 150-eV photons. In Fig. 14.2e a comparison between the extended model including the effects of the field inhomogeneity and metal surface and the unmodified Lewenstein model is drawn. The cut-off harmonic number reaches values of 105 for the modified model, while the unmodified predicts values of only 50. Further from the tip of the nanocone, the field become relatively homogeneous, and the distance to the metal surface is large, therefore both models coincide. Note that although the modifications of the Lewenstein model are important only in a small fraction of the volume, it is exactly this volume ("hot spot") which dominate the generation of high harmonics, making these modifications especially important. This is clearly visible in Fig. 14.2f, where we show the spectrum of the high harmonics emitted in the x direction integrated over the spatial position, with a significant emission of even harmonics as well as the extended and smoothed cutoff. We have also calculated the phases of the HHG harmonics separately for short and long electron trajectories, and found that the modification of phases due to the field inhomogeneity is negligible for short

trajectories but reaches $\pi/2$ for the long ones. This, however, will not influence the divergence of the HHG radiation, since the hot spot is smaller than the typically considered wavelength and acts as a point like source.

In order to compare the results of our model with experimental measurements, we have simulated high harmonic generation in the vicinity of a bowtie nanoantenna, such as used in [7]. Structure and parameters of the studied bowtie antennas is shown in Fig. 14.3a. It consists of two silver isosceles triangles with curvature radius and a distance between the vertices in the range of 10 nm. In Fig. 14.3b, the field enhancement by the bowtie antenna with parameters as given in the figure is presented, which shows a "hot spot" between the inner vortices of the triangles and a maximum enhancement of about 10^2. By using this field enhancement HHG is calculated by using the extended model. In Fig. 14.3c for incident 10-fs pulses with intensity of 0.5 TW/cm^2 the spatial distribution of the threshold harmonic number

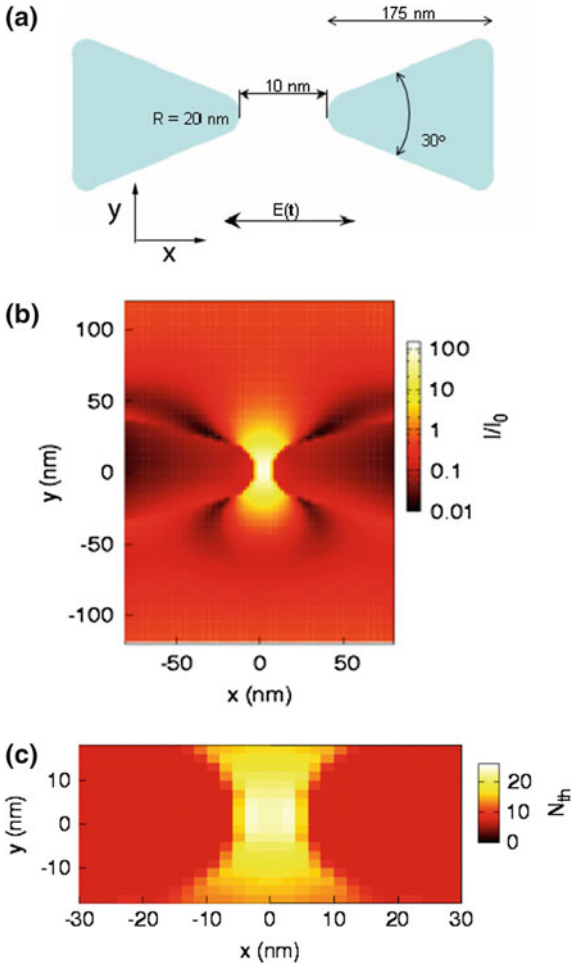

Fig. 14.3 High harmonic generation in the vicinity of a bowtie structure. In **a**, the scheme of the bowtie structure and its geometric parameters are shown, the *x*-polarized field propagates along *y* direction. In **b** the field enhancement is presented for the *xy* cross-section of the incident field at 830 nm; in **c**, the distribution of the harmonic cutoff is shown for 10-fs input pulses with 0.5 TW/cm^2 intensity for HHG in argon surrounding the bowtie structure

*N*th is presented. The calculated maximum harmonic number is 23, which corresponds to the wavelength of 36 nm. This is in good agreement with the experimental findings of [7], where harmonics down to 45 nm were observed. Note that both the parameters of the bowtie antenna and the input intensity are not exactly determined in [7] which can lead to deviations between theory and the experiment. In contrast to the nanocone, in the case of the considered bowtie antenna a relatively low field enhancement due to larger curvature radii leads to a smaller amplitude of electron motion which, together with a relatively homogeneous field distribution, makes the model modifications less important than in the case of the considered nanocone. Our calculations predict that the cutoff value has increased by only approximately 20 % due to the effects of the inhomogeneity and the metallic surface.

14.4 HHG in Noble Gases in the Vicinity of a Rough Metallic Surface with Fractal Properties

During the last three decades nonlinear optical processes (as e.g. surface-enhanced Raman scattering) on metallic rough surfaces have been extensively studied theoretically (see e.g. [29, 30]) as well as experimentally (see e.g. [31–33]). It was shown that signal intensities can be increased by more than 6 orders of magnitudes. This enables the observation of nonlinear and scattering processes at very low intensities. In principle metallic rough surfaces as an inexpensive and strongly field-enhancing element can be used for all the processes which require a relatively high threshold intensity. In this chapter we describe its possible use for the generation of low-intensity high harmonics [34].

We characterize a realistic metallic rough surface using the restricted solid-on-solid model [35, 36] which well describes the self-affine fractal structure typical for deposited metallic rough surfaces. The generated surface is characterized by a Hausdorff dimension of roughly 2.6. An example of the fractal-structured rough surface generated by using this model is presented in Fig. 14.4 for physical size of pixels 1 nm and the total size of 50 nm × 50 nm.

The enhanced field distribution determined by the discrete-dipole approximation [37] is shown in Fig. 14.4 by red cones and the 800-nm incident field by blue cone. The cone directions indicate the polarization and the cone sizes the field enhancement factor. The enhanced field is localized at random positions due to existence of localized modes on the fractal surface and is related to the Anderson localization. The simulation shows that the physical size of the elementary pixels does not affect to the maximum enhancement factor and the statistical characteristics of the field distribution.

For the full study of the HHG process on metallic rough surfaces in the noble gas environment, including the dispersion of the enhancement, we explore the field enhancement in the spectral range of the pump pulses. For the full coverage of the spectral range of few cycle pump pulses, we calculate the distribution of field

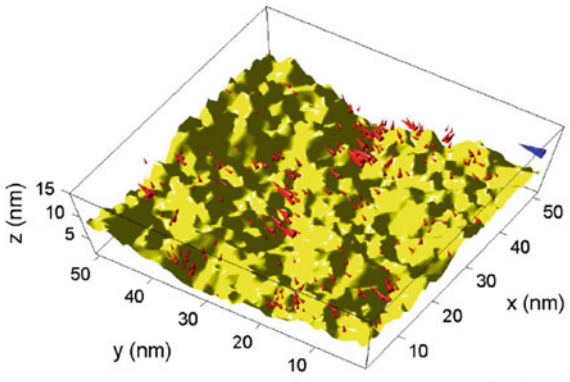

Fig. 14.4 (*Color online*) Structure of rough surface and enhanced field distribution. The surface structure is illustrated by *yellow color* and relative magnitudes and directions of enhanced field are shown by *red cones*. The *blue cone* shows the polarization of incident field at 800 nm

enhancement factors in the spectral range of $\sim$600 to $\sim$1,000 nm with steps of $\sim$12 nm.

In Fig. 14.5 we show the maximum enhancement factor distribution for different wavelengths. One can see that plasmonic hot-spots are formed at different places for different wavelengths which is one of the main features of fractal surfaces [38]. Intensity enhancement factors up to $\sim$5,000 are reached, with a density of "hot spots" which is higher for longer wavelengths.

Using the wavelength-dependent field enhancement factors and the pump pulse spectrum, we can apply the inverse Fourier transformation to reconstruct the temporal profile of the enhanced pulse. In Fig. 14.6 we show an example of a pulse shape at one of the "hot spots". The figure shows that the enhanced temporal pulse shape is delayed and stretched. This phenomenon is attributed to the dispersion of the plasmonic response on the surface. For the calculation of the HHG spectrum we apply the model as discussed in Sect. 14.2.

The main purpose of this study is to answer the question whether the HHG efficiency on metallic rough surfaces can be increased compared with bow-tie nanostructures. The HHG efficiency is approximately calculated by using the formula $\eta(N) = \omega^4 NT(12\pi\varepsilon_0 c^3)^{-1}\int|x(\omega)|^2 dV/\Phi$, where V is the volume of the space in consideration, $N = \omega/\omega_0$ is the harmonic order, ω_0 is the central frequency of the incident pulse, T is the time window of the numerical Fourier transformation, Φ is the total pulse energy incident on the rough surface of the metallic substrate sample, and $x(\omega)$ is the Fourier transform of the high-harmonic dipole moment. In the simulation, the environment is assumed to be filled with Ar gas at pressure of 0.18 atm. In Fig. 14.7 we show the calculated HHG efficiency as a function of harmonic order N. In the figure the efficiency is averaged over an ensemble of 20 samples. For harmonics in the plateau the efficiency is 10^{-8}–10^{-9}.

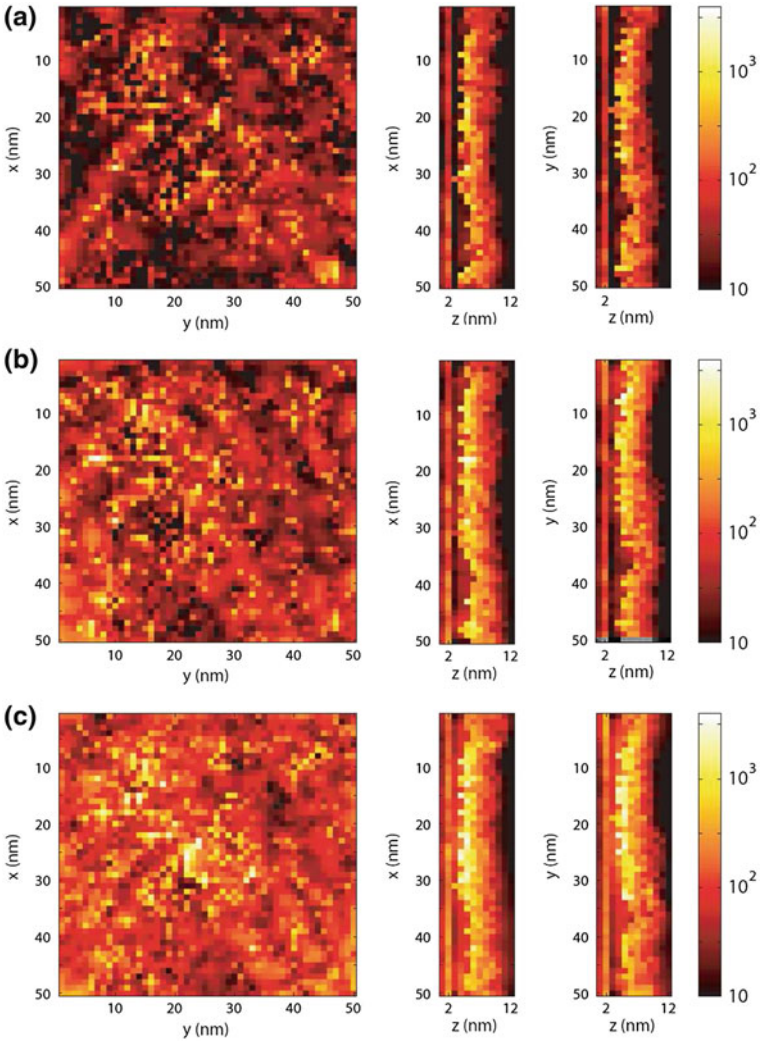

Fig. 14.5 Maximum intensity enhancement factor in different cross-sections for different wavelengths: 700 nm (**a–c**); 800 nm (**d–f**); 900 nm (**g–i**)

Finally, we investigate the dependence of the HHG efficiency on the incident angle. In Fig. 14.8 we show the dependence of the efficiency for different incident angles and polarizations on the given fractal surface sample of Ag under the same pump condition as in Fig. 14.7. In Fig. 14.8d, the efficiencies for harmonics in the plateau are determined by the average over the harmonic order in the spectral range

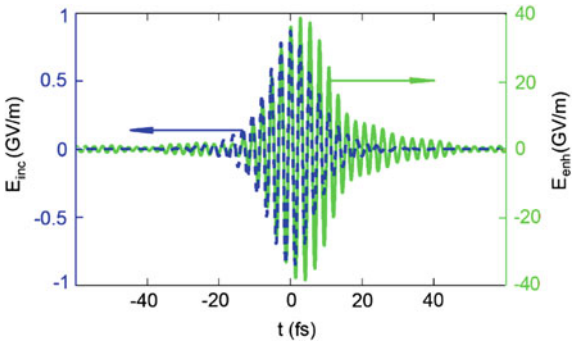

Fig. 14.6 Incident pulse (*blue dotted line*) and enhanced pulse (*yellow line*) profiles on the rough Ag surface for one of the realizations of random surface. Maximum field enhancement is more than 40 which corresponds to the instant intensity enhancement $\sim$2,000

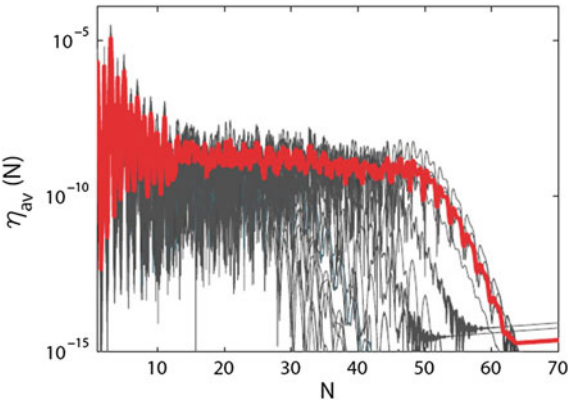

Fig. 14.7 The HHG efficiency $\eta_{av}(N)$ as a function of harmonic orders N averaged over 20 samples. The *gray curves* represent different samples, and the average efficiency is in *red*

of the plateau. The efficiency increases with the increase of the incident angle for *s*-polarization and decreases for *p*-polarization. For the *p*-polarized pump pulse with grazing incidence the main energy is contained in the component normal to the base plane of the sample [38], leading to low enhancement factors and low efficiency. On the other hand, for *s*-polarized pump with large incident angle, the pump pulses propagate in the highly field-enhanced area over a distance much longer than in the case of normal incidence. This effect contributes to the increase of the HHG efficiency, since the enhancement factors remain the same for grazing incidence. In the case of *s*-polarization, the efficiency for harmonics in the plateau is increased by more than 30 times for grazing incidence (incident angle of 89.9°) compared with the case of normal incidence. For an incident angle of 89.9°, the HHG efficiency in the plateau is around 1.1×10^{-7} which is approximately 2 orders of magnitudes larger than the result in [7].

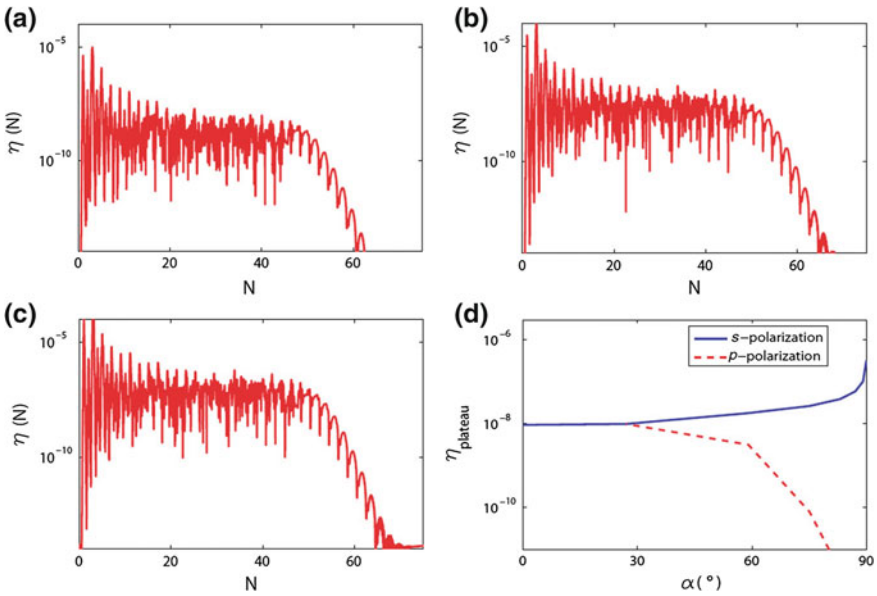

Fig. 14.8 (*Color online*) The dependence of HHG efficiency on the incident angle for *s*- (*blue curve*) and *p*- (*red curve*) polarizations of the pump beam: **a**, **b** and **c**- HHG efficiency spectra for incident angles 0°, 89° and 89.9° for *s*-polarization, respectively. In **d**, the HHG efficiencies in the range of plateau are shown

14.5 HHG in a Mixture of Nanoparticles and a Noble Gas

As a third possibility to increase the efficiency, we study HHG in a composite of silver ellipsoids suspended in a noble gas. For the simulation of the field distribution we used the ellipsoidal-harmonics formalism [39]. In this formalism, we assume that the ellipsoid is much smaller than the pump wavelength. In this case, the electrostatic solution can be used to describe the field enhancement. We consider ellipsoids with semidiameters $a > b > c$ oriented along the x, y, and z axes, correspondingly, in the external electric field with components E_x, E_y and E_z. The total potential of the field around the ellipsoid is given by

$$\Phi = \Phi_0 + \frac{(1-\varepsilon_r)abc}{3}\sum_{p=1}^{3} A_p F_1^p(\xi) E_1^p(\mu) E_1^p(\nu), \tag{14.5}$$

where $\Phi_0 = -xE_x - yE_y - zE_z$ is the potential of the external field, ε_r is the dielectric function of the ellipsoid, E_1^p and F_1^p are the Lame functions of the first and second kind, correspondingly, and the coordinates of the ellipsoidal coordinate system ξ, μ and ν are expressed through the cartesian coordinates by implicit relations $x^2 = \xi^2\mu^2\nu^2k^{-2}h^{-2}$, $y^2 = (\xi^2 - h^2)(\mu^2 - h^2)(h^2 - \nu^2)h^{-2}(k^2 - h^2)^{-2}$,

and $z^2 = (\xi^2 - k^2)(k^2 - \mu^2)(k^2 - \nu^2)k^{-2}(k^2 - h^2)^{-2}$. The parameters k and h are given by $k = \sqrt{a^2 - b^2}$ and $h = \sqrt{a^2 - c^2}$. Finally, the coefficients A_p are given by

$$A_1 = -\frac{E_x}{kh(1 + L_1(\varepsilon_r - 1))} \tag{14.6}$$

$$A_2 = -\frac{E_y}{h\sqrt{k^2 - h^2}(1 + L_2(\varepsilon_r - 1))} \tag{14.7}$$

$$A_3 = -\frac{E_z}{k\sqrt{k^2 - h^2}(1 + L_3(\varepsilon_r - 1))} \tag{14.8}$$

where L_i are the depolarization factors of the ellipsoid [39].

The results are illustrated in Fig. 14.9a, where the relative differential volume dV/dI (defined as the volume in which the intensity enhancement has a given value, normalized by the volume of the ellipsoid) is shown as a function of the enhancement I/I_0. One can see that for a 800 nm pump and an ellipticity of 6.5, the intensity enhancement reaches values up to 400. Note that the result shown in Fig. 14.9a was obtained after averaging over possible ellipsoid orientations. Here again we used the experimentally observed, complex-valued dielectric function of silver.

The polarization of high-harmonic generation in the mixture of randomly-oriented ellipsoids and the noble gas was calculated using the Lewenstein model described in Sect. 14.2. The propagation of the pump beam was simulated by a generalized unidirectional wave equation taking into account effective dispersion, effective loss, Kerr nonlinearity, and HHG polarization, with inclusion of the effects of the ionization and plasma formation. For the harmonic beam, only the linear losses and phase mismatch have to be taken into account in a separate equation.

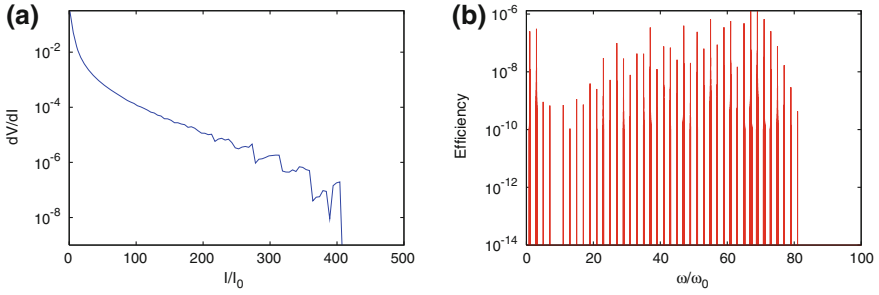

Fig. 14.9 Differential volume dV/dI (**a**) and efficiencies of the generated high-harmonics (**b**) for plasmonic enhancement by metallic ellipsoids. In **a**, the differential volume is normalized by the volume of a single ellipsoid, and 20-nm-long silver ellipsoids with ellipticity of 6.5 were considered. The pump wavelength is 800 nm, and the oscillations of the *curve* in (**a**) are a numerical artefact. In **b**, the efficiency of HHG after propagation of 400 μm in a composite of 1-atm argon filled with such ellipsoids at a volume filling factor of 10^{-4} is shown. The quasi-cw pump at 800 nm has an intensity of 1 TW/cm^2

For simplicity, plane-wave propagation is considered here. We consider the Fourier transform $\mathbf{E}(z,\omega)$ of the linearly-polarized pump field $\mathbf{E}(z,t)$ with z being the propagation coordinate. Substituting this ansatz into the wave equation and neglecting weak back reflected field components the following system of first-order differential equations can be derived written as [40]

$$\frac{\partial E(z,\omega)}{\partial z} = i\beta(\omega)E(z,\omega) - \frac{\alpha_j}{2}(\omega)E(z,\omega) + \frac{i\omega^2}{2c^2\varepsilon_0\beta_j(\omega)}P_{NL}(z,\omega) \tag{14.9}$$

where $\beta(\omega)$ and $\alpha(\omega)$ are the wavenumber and the loss and $P_{NL}(z,\omega)$ is the nonlinear polarization.

The quantities $\beta(\omega)$ and $\alpha(\omega)$ are calculated including the dispersion due to the linear polarization of the argon atoms as well as the contribution from the composite of the randomly oriented ellipsoids. They are related to the dielectric function $e_{eff} = c^2(\beta(\omega) + i\alpha(\omega))^2/\omega_0^2$ which is given by

$$\varepsilon_{eff} = \varepsilon_{Ar} + f\varepsilon_{Ar}(\varepsilon_{Ag} - \varepsilon_{Ar})\sum_{j=1} 3\frac{\varepsilon_{Ar}}{\varepsilon_{Ar} + L_j(\varepsilon_{Ag} - \varepsilon_{Ar})}, \tag{14.10}$$

where f is the volume filling factor and the ε_{Ar} and ε_{Ag} are the dielectric functions of argon and silver, correspondingly.

The local nonlinear polarization $P_{NL}(z,r,t)$ includes three terms: the Kerr nonlinearity, the plasma-induced refraction index change and absorption due to ionization:

$$P_{NL}(z,t) = \varepsilon_0\chi_3 E^3(z,t) - \rho(z,t)ed(z,t) - E_g\varepsilon_0 c\int_{-\infty}^{t}\frac{E(z,t)}{\widetilde{I}(z,t)}\frac{\partial\rho(z,t)}{\partial t}dt \tag{14.11}$$

where $\chi_3 = (4/3)c\varepsilon_0 n_2$ is the third-order polarizability of the gas and $\widetilde{I}(z,r,t)$ is the intensity averaged over few optical periods. For argon we have $n_2 = 1\times10^{-19}$ cm^2/W at 1 atm, E_g is the ionization potential, $\rho(z,t)$ is the electron density and $d(z,t)$ is the mean free-electron displacement in the electric field. The evolution of the two latter quantities is described by

$$\frac{\partial\rho(z,t)}{\partial t} = (N_0 - \rho(z,t))\Gamma(\widetilde{I}(z,t)) \tag{14.12}$$

$$\frac{\partial^2 d(z,t)}{\partial t^2} = -eE(z,t)/m_e - \frac{\partial_t d(z,t)}{\rho(z,t)}\frac{\partial\rho(z,t)}{\partial t} \tag{14.13}$$

where $\Gamma(\widetilde{I}(z,t))$ is the photoionization rate calculated from the Keldysh-Faisal-Reiss model [41] which describes both the multiphoton and tunnelling regime and N_0 is the initial argon density. In the case of a composite, the nonlinear response is averaged around the vicinity of the metal ellipsoid when calculating the propagation of the pump field.

Note that the phase mismatch between the high harmonic and pump beam, as well as harmonic reabsorption in both argon and silver, were taken into account. Phase matching in the mixture can be achieved by the significant contribution of the silver NPs to anomalous dispersion. In contrast to HHG in a noble gas this contribution enables phase matched HHG at high pressures. The harmonic spectrum is displayed in Fig. 14.9b for parameters listed in the caption. Generation of harmonics up to harmonic number of 70 is predicted, with efficiencies near the cutoff slightly below 10^{-6}. This value is three order of magnitudes higher compared with the experimentally realized efficiency in bowtie nanostructures [7]. The optimization of the ellipsoid shape and other parameters possesses the potential to further increase the efficiency.

Acknowledgments A. H. acknowledges financial support from German Research Council, Projekt Hu 1593/2-1.

References

1. M. Hentschel et al., Nature **414**, 509 (2001)
2. P.B. Corkum, F. Krausz, Nat. Phys. **3**, 381 (2007)
3. A. Paul et al., Nature **421**, 51 (2003)
4. F. Krausz, M. Ivanov, Rev. Mod. Phys. **81**, 163 (2009)
5. G. Sansone et al., Nature **465**, 763 (2010)
6. M. Lewenstein, P. Balcou, M.Y. Ivanov, A. L'Huillier, P.B. Corkum, Phys. Rev. A **49**(3), 2117–2132 (1994)
7. S. Kim et al., Nature **453**, 757 (2008)
8. S.A. Maier, *Plasmonics: Fundamentals and Applications* (Springer, Berlin, 2007)
9. S. Nie, S.R. Emory, Science **275**, 1102 (1997)
10. M.I. Stockman, *Nonlinear Optical Materials* (Springer, New York, 1998)
11. I.-Y. Park et al., Nat. Photonics **5**, 678 (2011)
12. A. Husakou, S.-J. Im, J. Herrmann, Phys. Rev. A **83**(4), 043839 (2011)
13. M.F. Ciappina et al., Phys. Rev. A **85**, 033828 (2012)
14. T. Shaaran et al., Phys. Rev. A **86**, 023408 (2012)
15. I. Yavuz et al., Phys. Rev. A **85**, 013416 (2012)
16. S.L. Stebbings et al., New J. Phys. **13**, 073010 (2011)
17. A. Husakou, F. Kelkensberg, J. Herrmann, M.J.J. Vrakking, Opt. Express **19**, 25346 (2011)
18. J. Choi et al., New J. Phys. **14**, 103038 (2012)
19. M.F. Ciappina et al., Opt. Express **20**, 26261 (2012)
20. I. Yavuz, Phys. Rev. A **87**, 053815 (2013)
21. M.F. Ciappina, T. Shaaran, M. Lewenstein, Ann. Phys. **525**, 97 (2013)
22. B. Fetic, K. Kalajdzic, D.B. Milosevic, Ann. Phys. **525**, 107 (2013)
23. J.A. Perez-Hernandez et al., Phys. Rev. Lett. **110**, 053001 (2013)
24. J. Luo et al., J. Phys. B **46**, 145602 (2013)

25. N. Pfullmann et al., New J. Phys. **15**, 093027 (2013)
26. K. Furusawa et al., Appl. Phys. A **69**, S359 (1999)
27. Farcas et al., Phys. Rev. A **46**, R3605 (1992)
28. F. Banfi et al., Phys. Rev. Lett. **94**, 037601 (2005)
29. V.M. Shalaev, *Nonlinear Optics of Random Media: Fractal Composites and Metal-Dielectric Films* (Springer, Berlin, 2000)
30. E.Y. Poliakov, V.A. Markel, V.M. Shalaev, R. Botet, Phys. Rev. B **57**(23), 14901–14913 (1998)
31. C.K. Chen, A.R.B. de Castro, Y.R. Shen, Phys. Rev. Lett. **46**(2), 145–148 (1981)
32. K.A. O'Donnell, R. Torre, C.S. West, Phys. Rev. B **55**(12), 7985–7992 (1997)
33. E.M. Kim, S.S. Elovikov, T.V. Murzina, A.A. Nikulin, O.A. Aktsipetrov, M.A. Bader, G. Marowsky, Phys. Rev. Lett. **95**(22), 227402 (2005)
34. K.-H. Kim, A. Husakou, J. Herrmann, Opt. Express **19**, 20910–20915 (2011)
35. P. Meakin, P. Ramanlal, L.M. Sander, R.C. Ball, Phys. Rev. A **34**(6), 5091–5103 (1986)
36. J.M. Kim, J.M. Kosterlitz, Phys. Rev. Lett. **62**(19), 2289–2292 (1989)
37. B.T. Draine, P.J. Flatau, J. Opt. Soc. Am. A **11**(4), 1491–1499 (1994)
38. V.M. Shalaev, R. Botet, J. Mercer, E.B. Stechel, Phys. Rev. B **54**(11), 8235–8242 (1996)
39. J.C.-E. Sten, J. Electrostat. **64**, 647–654 (2005)
40. A. Husakou, J. Herrmann, Opt. Express **17**, 12481–12492 (2009)
41. H.R. Reiss, Phys. Rev. A **22**, 1786–1813 (1980)

Index

A
Ablation, 79, 142
Ablation threshold, 111
Absorption, 12
Absorptive transition, 176
Adaptive refinement, 232
Aluminium, 240
Angle of incidence, 21, 22
Angle-resolved spectral interferometry, 124
Anisotropic energy transfer, 16
Anisotropic excitation, 15, 27
Anisotropic light scattering, 50
Anisotropy parameter, 19
Anomalous dispersion, 267
Anti-crossing behavior, 128
Applications, 145

B
Benzophenone, 142
Bessel-Gauss beam, 35
Bio-compatible TiO_2 surfaces, 82
Biodegradable polymers, 144
Biopolymers, 144
Birefringence, 52, 64
Birefringent, 32, 33, 40, 42
Bowtie antenna, 163
Bowtie nanostructure, 253, 259

C
Catalyst, 196
Cavity, 56
CdS, 143
Characteristic time, 25
Charge transfer, 208
Chemical bath deposition (CBD), 194, 195, 197, 199–204
Chitosan, 143
Classical approach, 6
Coarsening, 25
Coherence, 239
Coherent coupling, 121
Coherently linked ripples, 75
Complex eigenenergies, 128
Composite, 264, 266
Conclusion, 191
Control of electron trajectories, 189
Control parameter, 20
Convergence, 232
Corrugated layer, 12
Corrugated surface, 9
Coulomb-explode, 107
Coulomb explosion, 110
Coupling of the laser pulse to the SPP, 80
Crossover time, 23
Cross section, 142, 229
Cutoff energy with wavelength, 189
Cylindrical vector beams, 34, 36
Cytotoxicity, 145

D
Damage threshold, 79
Damped driven harmonic oscillator, 228, 241
Damping, 228
Density matrix formalism, 127
Dephasing time, 169
Depth parameter, 19
Desorption, 12
Dielectric function, 266
Differential reflectivity spectrum, 132
Differential volume, 265
Diffraction limit, 139
Diffusion-assisted DLW, 140
Dimer nanoantennas, 161
3D inkjet printing, 137

© Springer International Publishing Switzerland 2015

S. Sakabe et al. (eds.), *Progress in Nonlinear Nano-Optics*,
Nano-Optics and Nanophotonics, DOI 10.1007/978-3-319-12217-5

Dipole approximation, 227
Dipole-dipole interaction, 120
Dipole mode, 234
Direct fs Laser Writing (DLW), 137
Discrete-dipole approximation, 260
Disorder-broadening, 130
Dispersion relation, 226
Double-fs-pulse irradiation, 91
Double pulse experiment, 62
Drude model, 78
3D structures, 137

E
E-beam lithography, 138
E'-center, 62
Egg albumen, 211, 214
Electric dipole approximation, 159
Electroless plating, 146
Electron absorption, 253, 255
Electron beam lithography, 158, 161
Electronic density oscillations, 224
Ellipsoidal-harmonics formalism, 264
Energy transfer, 15
Enhancement, 261, 265
Equation of motion, 17
Erosion, 9, 13
Erosion rate, 16
Erosion velocity, 14, 17
Even harmonics, 255
Exciton, 120, 194, 199
Experimental photoelectron spectra, 188

F
Fano, 129
Far field, 228
Femtosecond laser ablation, 3
Femtosecond laser oscillator, 51
Femtosecond lasers, 149
Femtosecond LIPSS, 104
Femtosecond pump-probe spectrometer, 125
Fibre lasers, 139
Field enhancement, 156, 157, 252, 258, 259
Field inhomogeneity, 253
Finite element method, 231
Fixed focus method, 74
Fluence dependence of LIPSS, 88
Focussed Ion Beam, 53, 56, 57
Form birefringence, 52
Forward scattering, 242
Fractal, 260
Free electrons, 227
Free radicals, 142
Frequency resolved optical gating (FROG), 197, 203
Fs, 195, 197, 200, 201, 203, 204
Fused silica, 57, 88

G
Gap nonlinearity, 164
Gap size, 163
Gold, 240
Grazing incidence, 263

H
Harmonic cutoff, 255
Harmonic oscillator model, 170
Hausdorff dimension, 260
Heat accumulation, 58
Herring sperm DNA, 211, 214
HHG efficiency, 261
High harmonic generation, 251
High-spatial-frequency LIPSS (HSFL), 86, 89
High-speed processing, 75
Hot spot, 161, 258
Hybrid materials, 142, 143
Hybrid mode energies, 128
Hybrid nanostructures, 124
Hydrofluoric acid, 53
Hydrogels, 144

I
Incoherent exchange, 120
Inhomogeneity of the field, 254
Inhomogeneous broadening, 131
Instability, 8, 15
Interband transitions, 240
interferometric frequency resolved optical gating (iFROG), 195, 197, 200–204
Interpulse changes of the optical properties, 91
Inversion symmetric, 159
Ion-beam sputtering, 9

J
J-aggregate, 121

K
Keldysh-parameter, 187
Kinetic roughening, 25

L
Large-area nanostructuring, 74
Laser, 195, 197, 200, 201, 203, 204
Laser ablation threshold, 111
Laser fluence, 111
Laser-induced periodic surface structures (LIPSS), 73, 85, 86, 104, 208, 209
Laser polarization, 13, 27
Laser sintering, 137
Layer interface, 242
Lewenstein model, 253
Light emitting diode (LED), 228
Lightning rod effect, 240
Lindblad formalism, 127
Linear, 194, 197, 204
Linear response, 177
Linear stability analysis, 19
Lineshape, 237
Line spacing, 107
Linewidth, 169
LIPSS experiments, 212
LIPSS in rough surface, 76
LIPSS mechanism, 209
Lithography (LIGA), 143
Localised surface plasmon resonance, 226
Localized plasmonic modes, 133
Lorentzian line shape, 131
Lorentzian-type resonances, 126
Lower polariton (LP), 123
Low-spatial-frequency LIPSS (LSFL), 86, 89
Lycurgus cup, 223

M
Maxwell's equations, 232
Medium, 241
MEH-PPV, 143
Metal alkoxides, 144
Metallic LIPSS substrates, 211
Metallization, 146
Metal nanostructures, 251
Metal surface, 255
Metamaterials, 143
Michelson-interferometer (MI), 87
Microfluidic, 138, 145, 149
Microfluidic systems, 147
Micromechanical, 147
Micro-SERS, 211
Microvalve, 147
Mie theory, 229
Mode-locked Ti:sapphire laser, 76
Morphology, 20
Multiphoton absorption, 138
Multiphoton-induced plasmons, 74
Multiphoton polymerization (MPP), 137, 139
Multipole, 235

N
Nanocone, 255, 258
Nano-grains, 80
Nanograting inscription, 51
Nanogratings, 31, 32, 36, 37, 39, 40, 42, 44, 49
Nanogratings period, 56, 60
Nanoparticles, 251, 264
Nanoplasmonic model, 50, 61
Nanoripples, 210
Nanorod, 194, 195, 197–199, 200–204
Nanostructures, 58
Near-field effect, 111
Near-field light, 108
Near-fields, 230
Non-bridging oxygen hole center, 62
Non-collinear optical parametric amplifier (NOPA), 125
Nonequilibrium, 11
Nonlinear, 194, 195, 197, 201, 203, 204
Nonlinear behavior, 23
Nonlinear interaction, 95
Nonlinear mechanisms, 8
Nonlinear optical response, 161
Nonlinear oscillator model, 172
Non-radiative processes, 127
Normalised cross section, 229
Normal mode splitting, 133

O
Optical axis, 52
Optical Bloch equations, 127
Optical density of states, 242
Optical field emission, 187
Optical memory, 41, 42
Optical properties of nanostructures, 185
Optical vortex, 37, 39, 40, 44, 65
Optimization, 232
Orientation, 20
ORMOCER, 144
Oscillator strength, 177
Oxides, 241

P
Pancharatnam-Berry geometrical phase, 38, 44
Parametric process, 109
Particle, 227
Particle plasmon, 226

Particle radius, 234
Pattern formation, 3, 27
Pattern orientation, 13
Perfectly matched layer, 234
Phase elements, 63
Phase mismatch, 267
Photocatalysis, 81
Photodetectors, 228
Photo-excited carrier density, 79
Photoinitiator, 140–142
Photoluminescence (PL), 194, 195, 197, 199, 202, 204
Photonic bandgap, 145
Photonic crystal, 145, 146
Photonics, 138, 149
Photopolymerization, 138, 139, 142
Photopolymers, 142
Photovoltaic, 243
Plasma, 61, 224
Plasma frequency, 224
Plasma separation, 149
Plasma waves, 107, 108
Plasmon hybridization model[2], 156
Plasmonic, 155
Plasmonic materials, 241
Plasmonic sensing, 156
Polariton branches, 133
Polarization, 21, 24, 32–44, 227
Polarization-coded wave plates, 67
Polarization contrast intensity, 61
Polarization contrast microscopy, 52
Polarization converter, 65
Polarization degree, 23
Polarization ellipse, 24
Polarization parameter, 19–21
Population damping, 127
Porod Invariant, 54, 55
Processing parameter for nanograting formation, 57
Proteins, 144
Pulse, 195, 197, 200–204
Pulse number dependence of LIPSS, 89

Q

Quadrupole, 231
Quality factor, 174
Quantum yield, 142
Quartz, 195, 196, 200, 201, 203

R

Rabi frequency, 127
Rabi oscillations, 121
Rabi splitting, 129
Radial polarization, 32–34, 38, 44
Radiative processes, 127
Redshift, 239
Refractive index, 79
Refractive index contrast, 52, 64
Relaxation, 11
Resists, 142
Resonance dipole strength, 169
Resonant excitation, 174
Resonant nonlinearities, 175
Retardance, 33, 36, 39, 40, 42–44
Retardation, 53, 64, 235
Retardation control, 63
Ripple, 31, 32
Ripple wavelength, 25
Rough surfaces, 260
Rutile-type single crystal TiO2, 76

S

Scaling of LIPSS Line Spacing, 111
Scanning electron microscopy, 53
Scanning focus method, 74
Scattering intensity, 54
Scattering loss, 65
Scattering vector, 54
Self-diffusion, 10
Self-focusing, 64
Self-organization, 103, 104
Self-organization mechanism, 3
Self-organization model, 6
Self-organized grating structures, 104
Self-organized nanogratings, 104
Self-organized patterns, 7
Self-organized periodic grating structures, 104
Self-organized structures, 50, 104
Self trapped exciton, 61
SERS substrates, 210
Short trajectories, 258
Silicate, 143
Silicon (Si), 95, 195, 196, 199
Silver, 240
Single-crystalline synthetic quartz, 87
Slow axis, 40
Slow axis orientation, 36, 42
Small Angle X-ray scattering, 53, 55
Smoothing, 13
Solar cell, 243
Solid-on-solid model, 260
Spatial light modulators, 33
Spectral overlap, 173
Split ring resonators, 158
Spontaneous pattern formation, 9
Sputtering, 78

Stages of nanograting growth, 58
Stereolithography, 137
Stimulated-emission-depletion (STED) fluorescence microscopy, 140
Strong coupling, 123
Strong-field regime, 185
Structured illumination, 67
Structure size of nanogratings, 55
SU-8, 143
Sub-100-nm HSFL, 78
Sub-cycle regime, 190
Sub-radiant, 121
Substrate, 242
Super-Gaussian profile, 105
Super-radiant, 121
Surface corrugation, 17
Surface curvature, 239
Surface enhanced Raman spectroscopy (SERS), 208, 230
Surface enhanced THG (STHG), 200, 201, 204
Surface nonlinearities, 157
Surface plasma, 108
Surface plasmon polaritons (SPPs), 96, 120, 226
Surface profile, 10
Surface scattered electromagnetic wave, 96
Symmetry breaking, 159

T
Temporally distributed deposition of optical energy, 92
Temporal pulse shaping, 87
TH conversion efficiencies, 166
Thin liquid films, 15
Third harmonic, 194, 204
Third harmonic generation (THG), 160, 200, 201, 204
Third order polarizability, 172
Third-harmonic (TH) spectrum, 163
Time evolution, 25
Time-resolved experiments, 130
TiO_2, 143, 210
TiO_2 films, 78
Ti:Sapphire, 139, 143
Tissue engineering, 137, 144, 145
Total internal reflection, 242
Transfer matrix formalism, 126
Transfer of nanostructures, 217
Transient population, 134
Transient $\Delta R/R$ measurements, 124
Transition from multiphoton to strong-field photoemission, 186
Two-dimensional Fast Fourier Transform, 75

U
Ultrafast, 195, 204
Uniformity over the whole processed area, 80
Upper polariton (UP), 123

V
Vacuum field fluctuations, 120
Vapour-liquid-solid (VLS), 196
Vapour phase transport (VPT), 194–204
Variational problem, 231
Vector beams, 65
Volume nonlinearities, 157

W
Wave plate, 65
Wet chemical growth, 158

X
X-SPP system, 133

Z
Zero detuning, 123, 133
ZnO, 194–204